2010-02-03

The Heat Capacity and Thermodynamic Properties of the Iron Oxides and Their Relation to the Mineral Core of the Iron Storage Protein Ferritin

Claine Lindsey Morton Snow
Brigham Young University - Provo

The Heat Capacity and Thermodynamic Properties of the Iron Oxides and their Relation to the Mineral Core of the Iron Storage Protein Ferritin

Claine L. Snow

A dissertation submitted to the faculty of
Brigham Young University
in partial fulfillment of the requirements for the degree of

Doctor of Philosophy

Brian F. Woodfield
Juliana Boerio-Goates
Roger G. Harrison
Branton J. Campbell
James E. Patterson

Department of Chemistry and Biochemistry

Brigham Young University

April 2010

ABSTRACT

The Heat Capacity and Thermodynamic Properties of the Iron Oxides

and their Relation to the Mineral Core of the Iron

Storage Protein Ferritin

Claine L. Snow

Department of Chemistry and Biochemistry

Doctor of Philosophy

The iron oxides are a group of materials with geological, biological, and technological importance. A thermodynamic understanding of these materials is important because it provides information about their relative stabilities, chemical reactivity, and transformations. This study provides the heat capacity of a nanocrystalline magnetite (Fe_3O_4) sample, bulk hematite (α-Fe_2O_3), nanocrystalline hematite, akaganéite (β-FeOOH), and lepidocrocite (γ-FeOOH) at temperatures as low as 0.5 K. These measurements were fit to theoretical functions at temperatures lower than 15 K, and the respective thermophysical properties of these materials are discussed. Also the molar entropies of bulk hematite and hydrous nanocrystalline hematite as well as hydrous akaganéite are given.

Finally, a ferritin protein powder was prepared for heat capacity measurements by reconstituting the iron core in the presence of an imidazole buffer. This method allowed the introduction of almost 3000 iron atoms into each protein. Heat capacity measurements of apoferritin and the reconstituted ferritin sample are anticipated in the near future with plans to compare the heat capacity of the mineral core to that of other nanocrystalline iron oxides and oxyhydroxides.

Keywords: Heat Capacity, Iron, Ferritin

ACKNOWLEDGEMENTS

The story of my graduate experience has seen the entrance and exit of quite a few important characters. However with me through every second of it all has been the divine support of my Heavenly Father. To him I owe my thanks first for the blessings of aptitude and the wherewithal to complete such a rigorous course as physical chemistry. Many times I have had timely moments of inspiration which have proven to be successful. Those characters who are also deserving of my gratitude have been placed in my life by Him and to Him goes the first placement of thanks.

I must then take the occasion to thank my family who has suffered the most throughout this ordeal. This degree belongs as much to them as it does to me. My wife, Necia, has held down the fort and taken up the slack that I necessarily had to leave behind. I could not have done this without her support. I thank my children for all their understanding, and their developing love for science and learning. I thank, Xion, my oldest son, for his suggestions to write on Elephant Toothpaste and Floating Magnets. Even though I didn't use them he was eager to contribute. Also, to Ariah my only daughter for the 10,000 hugs I got when coming and going, and to Bryce my youngest for just making that last year even more difficult with sleepless nights, which were already sleep deprived. If Shakespeare had attended graduate school, I'm sure his words would have been "To graduate, to sleep once more."

Then I must profusely thank my graduate advisor Dr. Brian Woodfield for his patience and outright forgiveness for the many expensive mistakes (which I do not care to repeat) I made along the way. Also, I wish to thank him for his kindness and for setting the bar far higher than I ever thought I could reach, which consequently allowed me to make the most out of my small potential. I also appreciate his teaching style which has inspired me as I develop my own teaching philosophy.

On par with Dr. Woodfield is his chief collaborator Dr. Juliana Boerio-Goates who has perhaps the most pure approach to scientific research I have seen in my limited experience. Still, I do believe it would be difficult to find a person who enjoys the smallest detail in the pursuit of knowledge as much as she does. She has been most generous to us all in the lab as the great

benefactor of many a pizza party – root beer and liquid nitrogen ice cream included. Not to take away from my advisor, but because of her, I have had some important experiences that I would not have had with Dr. Woodfield alone.

I wish also to thank my committee for their patience in scheduling and for the constructive criticism at the many reviews and presentations they've attended. Outside of my committee I wish to thank Dr. Richard Watt for all of his help with ferritin and its preparation. He is probably one of the easiest professors to work with, especially as I was a physical chemist attempting to work in a biochemistry lab. Also, to Dr. Eric Sevy who taught more of my graduate classes than any other professor, and also offered great advice along with Dr. Matthew Asplund about the postdoc search and interviewing as well as interesting conversation on many a "pizza day."

There have been many undergraduates, graduates, and postdocs who have taught me invaluable skills in the lab. Thanks to Drs. Brian Lang and Shengfeng Liu for teaching me the skills of semi-adiabatic calorimetry and to Tyler Meldrum, Trent Walker, and Tom Parry for teaching me adiabatic calorimetry. Tyler was an especially good friend who helped me adapt to life in the lab with his good work ethic and positive attitude. Also, thanks to Stacey Smith who helped me to learn methods for analyzing heat capacity data. There have been many others who have helped as well: Baiyu Huang, Betsy Olsen, David Selck, Jessica Paul, Curtis Simmons, McKay Ritting, Katie Andrus, and Naomi Handly Martineau. Most recently, Dr. Quan Shi has helped immensely with the measurement of heat capacities on the PPMS.

One final thanks goes to my mother and father, Bruce and Nancy Snow for raising me in a loving home and instilling in me good values. It was on the foundation they laid, that I have built my life.

Brigham Young University

SIGNATURE PAGE

of a dissertation submitted by

Claine L. Snow

The dissertation of Claine L. Snow is acceptable in its final form including (1) its format, citations, and bibliographical style are consistent and acceptable and fulfill university and department style requirements; (2) its illustrative materials including figures, tables, and charts are in place; and (3) the final manuscript is satisfactory and ready for submission.

Date	Brian F. Woodfield, Chair
Date	Juliana Boerio-Goates
Date	Roger G. Harrison
Date	Branton J. Campbell
Date	James E. Patterson
Date	Matthew R. Linford Graduate Coordinator
Date	Thomas W. Sederberg, Associate Dean College of Physical and Mathematical Sciences

Contents

List of Tables

List of Figures

Chapter 1

Introduction to the Iron Oxides

Iron is among the most abundant elements in the earth's crust and has found applications in many different capacities.[1, 2] Biologists, chemists, physicists, geologists, and engineers have all displayed interest in understanding iron and the compounds that it forms. Biologically, iron is vital and employed in ATP production, oxygen transport, nitrogen fixation and more. Geologists study the properties of iron-containing minerals and their relation to the water systems found throughout the earth[1] while chemists have used iron in synthetic processes, catalysis, and oxidation-reduction reactions. In both its elemental and ionic states, iron displays electrical and magnetic properties that interest physicists and materials scientists. Also, iron has a long technological history and those civilizations that understood it best went on to shape the world. Contemporary studies on iron are multidisciplinary in nature,[2] and in all of these studies a fundamental understanding of the thermodynamic behavior of iron is essential.[1, 5, 6]

Table 1.1 A summary of the Iron Oxides and their structure[2]

Mineral Name	Chemical Formula	Crystal Structure
Hematite	Fe_2O_3	Hexagonal
Magnetite	Fe_3O_4	Cubic
Maghemite	γ-Fe_2O_3	Cubic
Wüstite	FeO	Cubic
Goethite	α-FeOOH	Orthorhombic
Lepidocrocite	γ-FeOOH	Orthorhombic
Akaganéite	β-FeOOH	Monoclinic
Ferrihydrite	$FeOOH \cdot xH_2O$	Hexagonal

Much emphasis has been placed on the iron oxides and oxyhydroxides since these compounds exhibit a diversity of structure and properties.[2] A list of the compounds that comprise this family and their structures is found in Table 1.1. Of these materials, this study will focus on α-Fe_2O_3 (hematite), Fe_3O_4 (magnetite), γ-FeOOH (lepidocrocite), β-FeOOH (akaganéite), and FeOOH (ferrihydrite).

The study of these species aims to achieve three goals. First we wish to provide a detailed description of the iron oxides and oxyhydroxides through the measurement and analysis of the constant-pressure heat capacity for these compounds. Second, for those compounds that exist on the bulk-scale (large crystal size) we wish to describe the changes that can be observed through heat capacity as the crystal size decreases to the nanoscale. Finally, this knowledge can be used to understand the physical and structural properties of iron as it is found in the biological storage protein, ferritin.

As this study is thermodynamic in nature, it will be important to provide an overview of the basic principles of the acquisition and analysis of heat capacities. An introduction to the iron oxides and oxyhydroxides can then be given in the proper context of their thermodynamic and physical properties. The rest of this chapter will proceed as follows: first a brief description of heat capacities and how they relate to this study, second a review of the thermodynamics of the iron oxide and oxyhydroxide polymorphs as found in the scientific literature, and finally an overview of this project with the specific aims involved therein.

1.1 The Heat Capacity of Solids

The purpose of this section is to provide a description of the fundamentals of heat capacity as well as a description of the principal methods we use in its acquisition. Many previous authors have provided detailed descriptions of these topics, and it is beyond the scope of this report to discuss heat capacities with the same level of detail.[8-10] The objective here is to give a sufficient familiarity of these concepts as they are relevant to the overall goals of this work.

The heat capacity is often described as a bulk property, and classically it is defined as the amount of energy required to raise the temperature of a substance. Written in equation form the definition appears as:

$$C = \frac{Q}{\Delta T}.$$

where C is the heat capacity, Q heat, and T temperature.

While this classical definition fits, it is generalized. With significant fine detail, the heat capacity of a substance is determined by the various energetic states available to it at a given temperature. Contributions to the heat capacity can come from atomic vibrations, conduction electrons, or magnetic interactions as well as other physical phenomena. As temperature increases the magnitude of these contributions varies with vibrations in the crystalline lattice generally making the largest contribution to the heat capacity at temperatures greater than 10 K. Below this temperature the lattice contribution is small enough that contributions from other sources are more easily discerned. The sum of the various contributions exhibited by a material will equal the total heat capacity as it is obtained from experimental measurements. This concept makes the measurement of heat capacities a powerful tool to test the theoretical model of a system. The more common physical models that contribute to the heat capacity are described below.

1.1.1 Anomalies in the Heat Capacity

Certain modes of energy exist over a short temperature range.[8] The corresponding magnitude of the heat capacity can be significant in comparison to the other contributions over that same restricted temperature range which produces the effect of a local maximum when viewing a plot of heat capacity against temperature. This behavior is referred to as an anomaly in the heat capacity and a good example is shown in Figure 1.1.[11] Some physical origins of heat capacity anomalies include the alignment of magnetic dipoles, phase changes, and electrical transitions from superconducting to insulating.

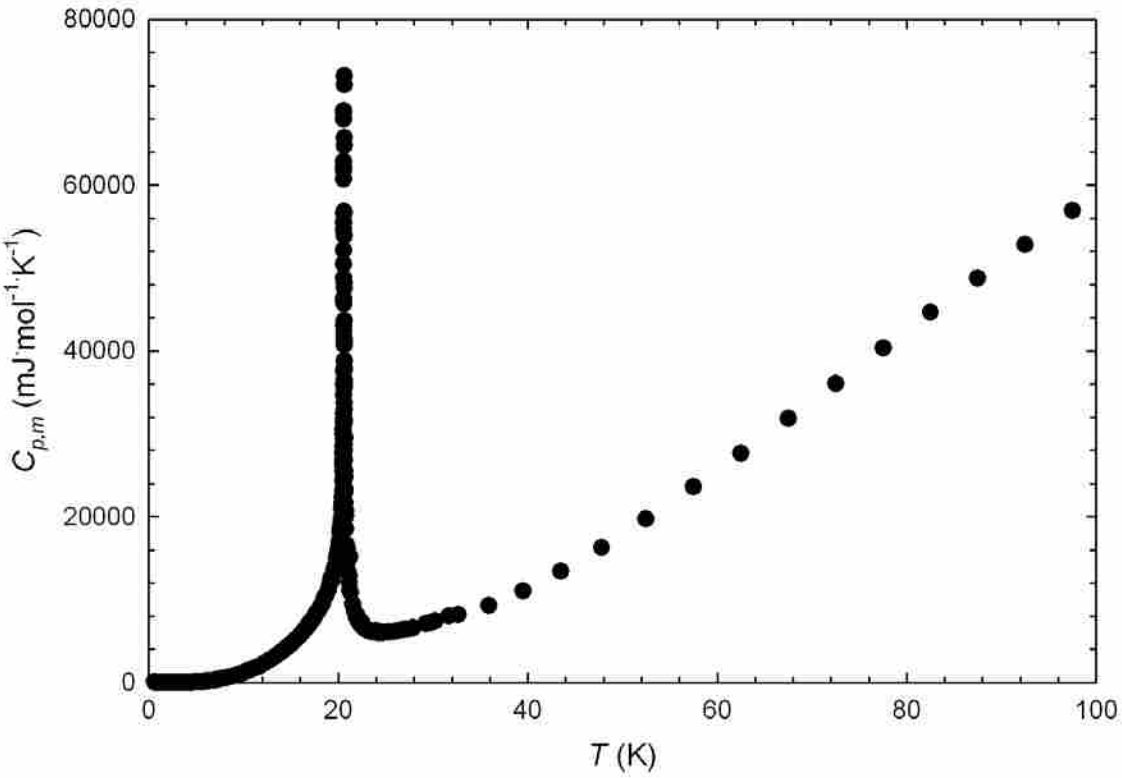

Figure 1.1 An Anomaly due to the frustrated antiferromagnetic transition in the Heat capacity of $GeCo_2O_4$[11, 12].

1.1.2 The Lattice Heat Capacity

Generally, the largest contribution to the heat capacity of solids stems from the vibrational motion of its atoms. Because the heat capacity is determined by the various energetic states available at a given temperature it is able to give insight into the microscopic behaviors in a system. The heat capacity curve for a simple solid in which the lattice is the principal contributor (Figure 1.2)[4] displays a dramatic increase in the low-temperature region while it behaves nearly linearly in the high-temperature limit.

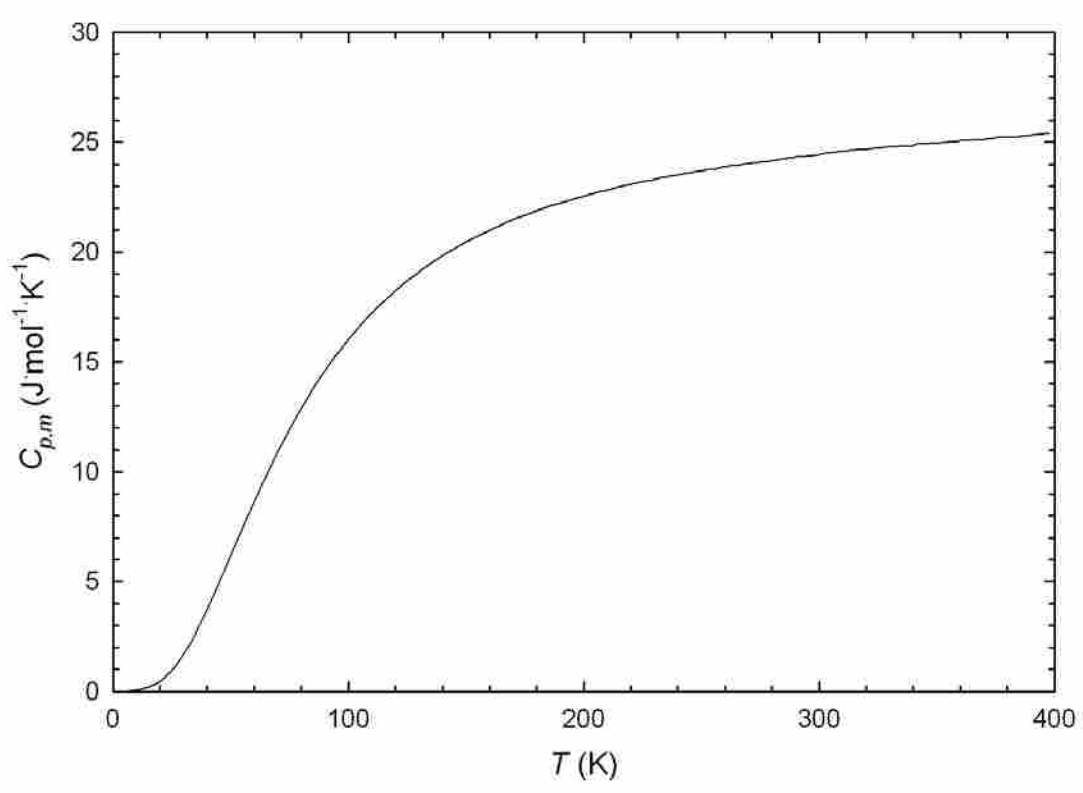

Figure 1.2 The Heat Capacity of Copper[4]

Heat capacity models attempting to represent the vibrational motion of atoms in a solid can be tested by comparing them with experimental results, and should match such temperature-dependent behavior. The degree to which a model agrees with experimental data determines the accuracy of the theories used to propose that model. Once a dependable model is developed it can provide insight into the microscopic behavior of the energetic modes in a solid. Like the lattice heat capacity other contributions and anomalous behavior can also be modeled and matched with experiment giving valuable information in regards to the energetic modes in a solid.

The first model to describe the lattice heat capacity invoked classical physics and the equipartition[8, 10] theorem, which assumes that on average each mode of atomic oscillation has the same amount of thermal energy having the value k_BT, where k_B is Boltzmann's constant. Since each atom has three degrees of freedom, a crystal containing N atoms will have a total of $3N$ modes of oscillation, and the total thermal energy in the crystal is

$$E = 3Nk_BT$$

Putting a small amount of heat into the sample raises its thermal energy by $dQ = dE = 3Nk_BdT$. Or solving for $Q/\Delta T$ we obtain

$$C = 3Nk_B$$

This expression is a rough approximation of the heat capacity of most solids at high temperatures, and some differences between this theory and experiment are readily observed. First, as can be seen in figure 1.3 the equipartition theorem predicts a constant linearity with no temperature dependence, and thus ignores the dramatic decrease in the heat capacity at low temperatures. A second discrepancy can be seen in the quantitative disagreement between the theory and experiment. The problem is that this theory does not include quantum mechanics which postulates that there are only certain allowable vibrational states. Thus the vibrational levels are populated according to Maxwell-Boltzmann statistics for a given thermal energy. Only a small fraction of those modes found to be of higher energy than the given thermal energy will be populated. As the thermal energy increases, these modes begin to be completely filled and the heat capacity approaches $3Nk_B$. The two most common models that use this quantum mechanical approach are the Einstein and the Debye models.

1.1.3 The Einstein Model of Lattice Heat Capacity

Einstein[8, 10] proposed a basic model for the lattice vibrations in which each atom vibrates independently from one another with the same frequency. Applying the quantum mechanical model of the harmonic oscillator and statistical mechanics the relationship among the lattice heat capacity, temperature, and fundamental frequency is derived as:

$$C_{V,Vib} = 3Nk_B\left(\frac{h\nu}{k_BT}\right)^2 \frac{e^{-h\nu/k_BT}}{\left(1-e^{-h\nu/k_BT}\right)^2}.$$

The Einstein model turned out to be too simplistic as evidenced by quantitative disagreement for even simple monatomic solids. In a lattice, which is a coupled system, the vibrations of one atom affect the vibrations of its neighbors, which in turn affect their

neighbors and so on. As a result of these interactions every atom can vibrate with several available frequencies. The Einstein model was somewhat successful however as it was the first model put forth to map out the decreasing trend in heat capacity at low temperatures. This qualitative agreement solidified the theory that the decrease of heat capacities at low temperatures was indeed a quantum phenomenon.

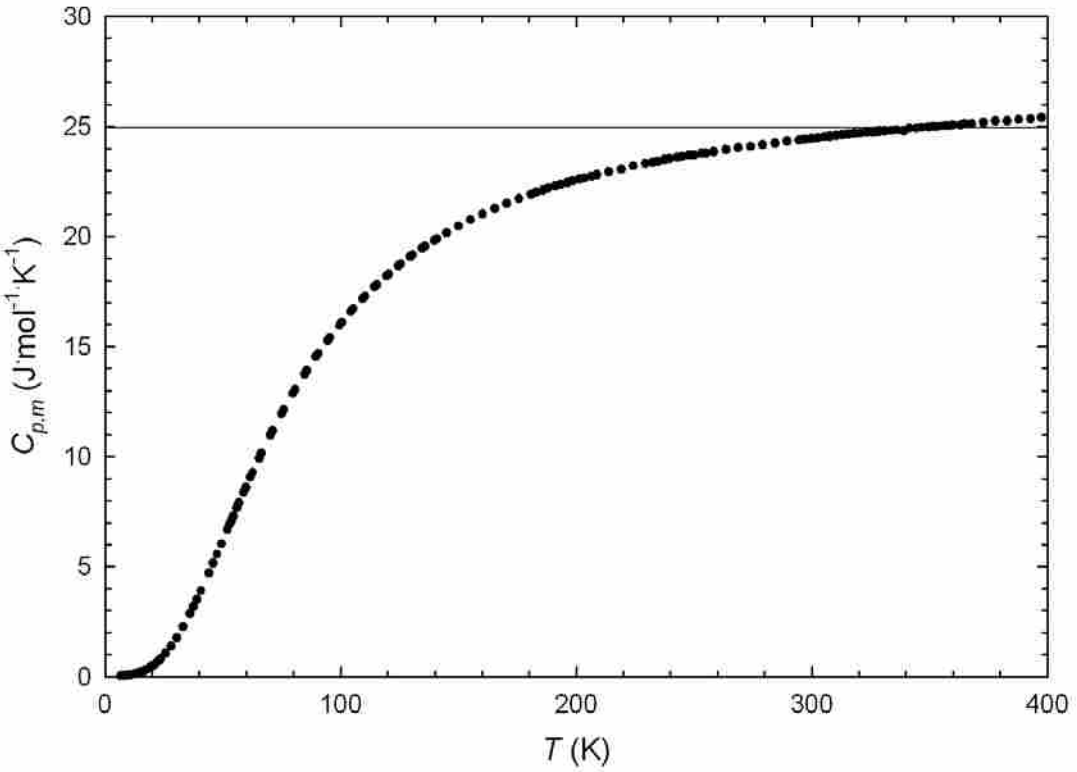

Figure 1.3 Heat Capacity Curve for Copper (black circles) with a comparison of that predicted by the equipartition theorem (straight line).[4]

1.1.4 The Debye Model of Lattice Heat Capacity

Debye[8, 10] built upon Einstein's quantum mechanical description of the vibrations in solids but differed in describing them in terms of a finite range of frequencies, v. Each frequency has a number of modes associated with it starting with the lowest frequency $v = 0$. Mathematically the number of modes between two frequencies near this minimum frequency is proportional to v^2, and Debye's approximation extends this trend to higher frequencies until a characteristic frequency v_D is obtained. No modes exist above v_D or in other words the total number of modes is equal to those found between $v = 0$ and v_D. The

characteristic frequency is more often expressed as the Debye temperature or $\theta_D = h\nu_D/k_B$. Applying statistical mechanics to this model the heat capacity relationship is derived as:

$$C_{v,vib} = 9Nk_B\left(\frac{T}{\theta_D}\right)^3 \int_0^{\theta_D/T} \frac{x^4 e^x dx}{\left(e^x - 1\right)^2}.$$

For temperatures much smaller than the Debye temperature, or $T < \theta_D/50$, the upper limit of the integral can be extended to infinity and the solution for the expression becomes:

$$C_{v,vib} = \frac{12\pi^4 Nk_B T^3}{5\theta_D^3}.$$

Thus at low temperatures the lattice heat capacity typically obeys a T^3 law while at progressively higher temperatures it follows an odd powers expansion ($T^3 + T^5 + T^7$ …).[13] The Debye model is most accurate for $\theta_D/50 > T > \theta_D/2$,[8] but outside of these regions the model does not agree well with experimental results. The main source of error comes from modeling of higher frequencies to be the same as lower frequencies. In spite of its shortcomings, the Debye model is still applied in modeling the heat capacity of solids especially at temperatures below 10 K. A more exact calculation of the vibrational heat capacity can be made from the density of states, the number of states between two frequencies, which is calculated from neutron scattering data. Unfortunately there are only a few high energy neutron sources available throughout the world so the data to perform such calculations is limited. Some alternatives have been found in computations using the Debye and Einstein models to approximate the true density of states.

1.1.5 The Electronic Heat Capacity

Electrically conducting solids have an electronic heat capacity.[8, 10] The quantum mechanical behavior of conduction electrons is best described through Fermi-Dirac statistics, which gives a mathematical model of the probability that an electronic state of energy E will be occupied. The Pauli exclusion principle dictates that all electrons must occupy a different energy state and consequently a proportional number of energy states is needed to accommodate all of the conduction electrons. Through application of these principles and statistical mechanics the electronic heat capacity is derived as

$$C_{v,electronic} = \frac{\pi^2 Nk_B^2 T}{2E_F},$$

where E_F is the Fermi energy or the energy of the highest occupied electronic state. This model yields an electronic heat capacity that is linearly dependent on temperature. Thus the electronic heat capacity will become important at temperatures lower than 10 K and will be almost negligible at room temperature. A low-temperature model of the total heat capacity often appears as $C = \gamma T + \beta_3 T^3$, and a plot of C/T against T^2 should display linear behavior. The slope of this fit provides β_3 (sometimes represented as α), which can be used to evaluate the Debye temperature, while γT is the electronic contribution obtained from the intercept.

1.1.6 The Magnetic Heat Capacity

Magnetic phenomena are observed in solids in which there are unpaired electrons. In a paramagnetic solid each magnetic dipole is randomly oriented, but will align with an external magnetic field. For ferromagnetic solids, the magnetic dipole will align in the same direction as its nearest neighbor, producing a net magnetization. In contrast, antiferromagnetic solids have nearest neighbors aligning in opposite direction and no net magnetization is observed. A ferrimagnetic solid behaves like an antiferromagnet with neighbors aligning in opposite directions, but one dipole is stronger than the other and a net magnetization is observed. Most magnetic solids order below a critical temperature T_C, above which the sample is paramagnetic. For ferromagnetic solids this temperature is referred to as the Curie temperature (T_C) while for antiferromagnets and ferrimagnets it is called the Néel temperature (T_N).

Magnetic interactions contribute to the heat capacity[8, 10] in more than one way. As the temperature approaches the critical temperature a cooperative transition takes place in which the magnetic spins go from an ordered to a disordered state. Such a process is accompanied by a large entropy change that can often be represented by:

$$S_M = R \ln(2s+1),$$

where s is the magnetic spin quantum number. This transition appears in the heat capacity as a spike or peak at the critical temperature.

The magnetic contributions to the heat capacity are also observed at temperatures near absolute zero as a result of the periodicity of the magnetic spins in the lattice. This periodicity, referred to as spin waves or magnons, is modeled based on the type of

magnetic ordering. The low temperature heat capacity for ferrimagnetic and ferromagnetic magnons is proportional to $T^{3/2}$. Antiferromagnetic spin wave models show the associated heat capacity as proportional to T^3, which makes such contributions difficult to separate from the lattice heat capacity. In spite of this, heat capacity measurements have proven useful in the characterization of magnetic materials since they are often more sensitive to magnetic ordering than magnetic susceptibility measurements. This is especially true in the case of antiferromagnetic transitions where the order in the system changes, but the net magnetic field shows no dramatic change.

1.1.7 The Schottky Effect

The Schottky effect is based on the thermal population of non-interacting energy levels. The heat capacity in solids due to this phenomenon comes from the thermal population of electronic and nuclear energy levels.[8, 10, 14] For instance, in compounds containing transition metals, the neighboring atoms can split the electronic states into separate energies. For the transition metals, the five degenerate *d*-orbitals are separated into two energy levels with degeneracies of 2 and 3, respectively. Atomic nuclear energy levels can also be split by a magnetic field if the nucleus has a magnetic moment and a non-zero spin. Commonly called a nuclear hyperfine, this behavior is of small energy and is only observable below 2 K. In contrast, the electronic energy levels are considerably larger and thus the electronic Schottky effect can occur at higher temperatures.

The energy of the ground state is ε_0 and each successive level is given relative to the ground state as ε_i with $i = 1,2,3 \ldots,n$. These energy levels have a specific degeneracy represented as g_i. Because these phenomena are non-interacting, or each nuclear moment and electronic splitting is independent of one another, the population of these levels can be described by a Boltzmann distribution. Therefore the probability of a particle occupying the *i*th energy level is:

$$P_i = \frac{g_i e^{-\varepsilon_i / k_B T}}{\sum_{j=1}^{n} g_j e^{-\varepsilon_j / k_B T}}.$$

At the lowest thermal energy, $k_B T = 0$, all quanta will be in the ground state. With increasing thermal energy, these non-interacting particles will begin to occupy the

available energy levels, and the internal energy of the system increases. A corresponding change in the overall heat capacity results from this excitation. For a two-level system the heat capacity is:

$$C_{Schottky} = R\left(\frac{\theta_S}{T}\right)^2 \frac{g_0}{g_1} \frac{e^{-\theta_S/T}}{\left(1-(g_0/g_1)e^{-\theta_S/T}\right)^2}$$

where θ_S is the Schottky temperature which describes the energy separation in temperature, $\theta_S = \varepsilon/k_B$. The contribution to the heat capacity for the electronic Schottky appears as an anomaly in the heat capacity curve that exponentially rises to the maximum while the the curve decays in proportion with T^{-2} in the high-temperature limit. The nuclear hyperfine usually appears in heat capacity as just the high-temperature side of this function and the heat capacity can be modeled by:

$$C_{Sch} = \chi A T^{-2}$$

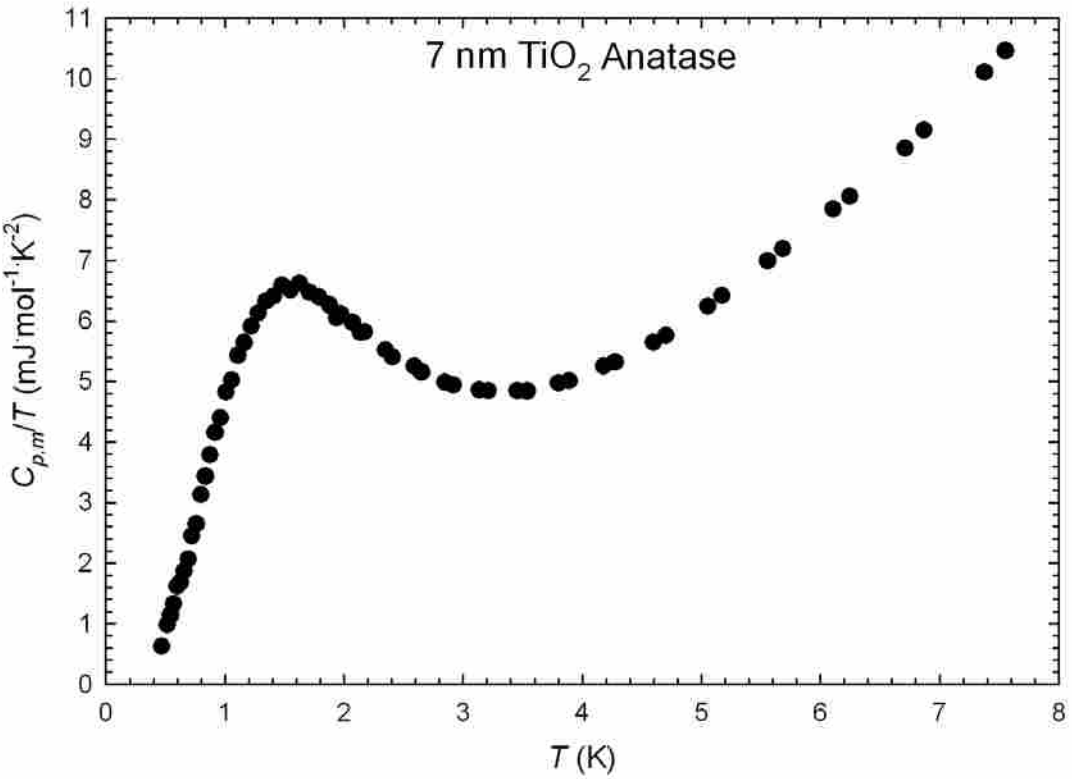

Figure 1.4 A Schottky Anomaly in the Heat Capacity of a 7 nm Anatase TiO_2 polymorph. The anomaly has not been published, but details of the sample and the measurement of its heat capacity have.

where A is a factor related to the hyperfine splitting, while χ is the mole fraction of nuclei having a magnetic moment. An example of a Schottky anomaly can be seen in Figure 1.4 in the heat capacity of a nanocrystalline sample of anatase TiO_2.

1.1.8 Thermodynamic Relationships of the Heat Capacity

In the preceding discussion, it was shown how a given physical phenomena has a corresponding temperature-dependent heat capacity contribution. The equations derived from modeling these phenomena describe the heat capacity as a function of temperature, and a comparison of these equations reveals similarities and differences in their temperature dependence. For instance the lattice contribution grows as T^3 and antiferromagnetism also has a T^3 dependence to it. In contrast, electronic heat capacity is linear in T, while ferromagnetism is $T^{3/2}$ and the Schottky effect requires an exponential term. Experimental heat capacity can be fit to a polynomial function of temperature which may include a combination of these models. Through this process the heat capacity is broken down into components representing the energetic states that represent the system mathematically written as:

$$C_{total} = C_{lattice} + C_{electronic} + C_{magnetism} + C_{other}.$$

Calorimetric techniques are derived from the classical thermodynamic properties

$$C_V = \left(\frac{\partial U}{\partial T}\right)_V \qquad C_p = \left(\frac{\partial H}{\partial T}\right)_p$$

where C_V represents the heat capacity with constant volume while C_p represents the heat capacity at constant pressure. The pressures required to maintain a solid at constant volume are for the most part impractical and nearly all heat capacity measurements provide C_p. The previous heat capacity contributions described by models are related to C_V. While the majority of experimental heat capacity yields C_p, corrections from $C_p$to C_V in solids can be made by the relationship:

$$C_P = C_V + BV_m\alpha^2 T$$

where B is the bulk modulus, V_m is the molar volume, and α is the coefficient of thermal expansion. Typically for temperatures below 20 K the difference between C_p and C_V is almost insignificant and this discrepancy gets ignored when applying the low-temperature theoretical models.

Not only can the heat capacity be used to test the physical models of a system, but the entropy of a system is readily obtained from constant pressure heat capacity. This calculation is done by the relationship:

$$S_{m,T} = \int_0^T \frac{C_{p,m}}{T} dT \, .$$

Combined with enthalpy, the entropy of a system allows the calculation of free energies and consequently provides predictive powers in relation to a system. However, heat capacity cannot yield the free energy or enthalpy in an absolute form. This is not to say that these two quantities do not have useful relationships with the heat capacity. While the absolute enthalpy and free energy cannot be obtained, values relative to the absolute enthalpy and free energy at 0 K can be obtained. The enthalpy is related to the heat capacity at constant pressure in the equation:

$$\left(\frac{\partial H_m}{\partial T} \right) = C_{p,m} \, .$$

From this equation we can derive the relationship:

$$H_{m,T} - H_{m,0} = \int_0^T C_{p,m} dT + \sum \Delta_{pc} H_m$$

Where $H_{m,0}$ is the enthalpy at 0 K, and the latter term in this equation ($\Delta_{pc} H_m$) is given to adjust for any phase transitions. The enthalpy at standard state conditions and at 298.15 K is of particular interest since 298.15 K is the reference temperature for most thermodynamic data.

The Gibbs free energy is related to the entropy using the equation:

$$\left(\frac{\partial G_m}{\partial T} \right)_p = -S_m \, .$$

Rearrangement and integration gives the relationship:

$$G_{m,T} - G_{m,0} = -\int_0^T S_m dT \, .$$

In this expression $G_{m,0}$ is the free energy at 0 K, and when the enthalpy and Gibbs free energy are taken at the standard state, $G_{m,0} = H_{m,0}$. For practical purposes these functions are usually calculated directly from the heat capacity using:

$$G^{\circ}_{m,T} - H^{\circ}_{m,0} = \int_0^T C_{p,m}\,dT - T\int_0^T \frac{C_{p,m}}{T}\,dT\,.$$

A standard practice among calorimetrists is to provide calculations of these thermodynamic functions when reporting heat capacity in the scientific literature. As long as heat capacity data is available, these relationships allow the calculation of the entropy, enthalpy, and Gibbs free energy at any temperature and not just the standard reference temperature listed in basic thermodynamic tables. In turn, these values are important when determining the favorability and equilibrium conditions of chemical reactions under different conditions.

1.1.9 Experimental Measurement of Heat Capacities

The calorimetric techniques employed in this study use the adiabatic or semi-adiabatic pulse method.[4, 9, 14-16] As the name implies this technique requires the net heat flow from the system to the surrounding or vice versa to be equal. The calorimeter or sample platform is maintained in a high vacuum, which serves to prevent heat flow between the system and surroundings. In the adiabatic method a series of shields surround the calorimetric vessel. The temperature of these shields is monitored with respect to that of the calorimeter and adjusted so that the two temperatures are equal at all times. When the system is in thermal equilibrium a known quantity of heat (Q) is added and the system is subsequently brought to a new equilibrium or drift. The heat is divided by the change in temperature (ΔT) in accordance with the relationship $C = Q/\Delta T$ and the average heat capacity is obtained at the midpoint of the temperature. This method of establishing a thermal equilibrium and then adding heat (pulse) to the system is done in a series (see Figure 1.5) and the temperature variation of the heat capacity is obtained in this manner.

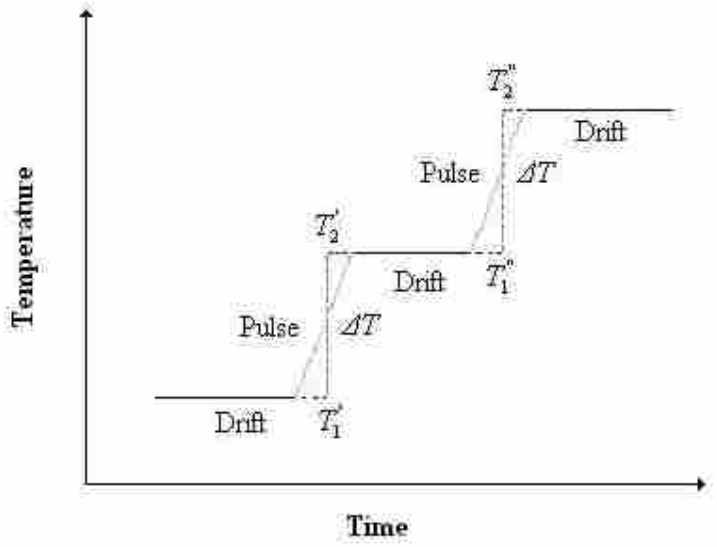

Figure 1.5 Ideal Adiabatic Pulse

The semi-adiabatic pulse is similar to the adiabatic technique in that the sample undergoes a series of drifts and pulses. However the sample and the surrounding are not kept at the same temperature. In general, the surroundings are kept at a lower temperature than the sample, and there is a thermal gradient resulting a in a heat loss from the sample to the surroundings. To compensate for this heat loss a known amount of heat is added back into the sample during the drift portion of the heat capacity measurement. In an ideal measurement system there would be no net heat flow between the sample and the surroundings, but in practice there is almost always some heating or cooling during the drift for semi-adiabatic measurements. The semi-adiabatic technique works best for heat capacity measurements below 20 K where heat loss due to blackbody radiation is minimal. With care this technique can yield results with an accuracy of 0.25% and a precision of 0.1%.

1.2 Heat Capacity of the Iron Oxides: A Literature Review

As iron compounds have always been of technological importance, iron oxide minerals were among the earliest materials to be studied through heat capacity. Heat capacity data beginning at low temperatures for the iron oxides gives direct information on the absolute entropy and the relative changes to the enthalpy and Gibbs free energy.

The thermodynamic relationships with the heat capacity discussed previously allow us to make thermodynamic calculations at any temperature for which we have data and not just at the standard reference temperature (298.15 K) listed in basic thermodynamic tables. These values are an important factor in determining the spontaneity and equilibrium conditions of reactions under varying conditions. Also, the physical properties exhibited in these compounds such as magnetism and electrical conductivity can be described in terms of their contributions to the total heat capacity. Thus heat capacity for all of the iron oxide polymorphs can facilitate scientific investigations involving these compounds in chemical reactions and synthesis, technological research and development, and materials characterization.

As seen in Table 1.1 there is a wide array of iron oxide and iron oxyhydroxide polymorphs. While similar in chemical formula, these polymorphs are diverse in their physical properties and relative stability.[2, 17] This study will focus on the heat capacity of magnetite, hematite, goethite, lepidocrocite, akaganéite, and ferrihydrite. Also it will include an investigation of ferritin, the biological protein responsible for iron storage. While hematite and magnetite were first studied many years ago and have been revisited over the years, the iron oxyhydroxides have only gained attention in more recent years. With growth in the field of nanotechnology, the iron compounds are once again candidates for heat capacity studies as this family displays a wide variety of physical phenomena. The physical properties of solids have been shown to be different in nano-sized crystallites[18] as compared to their bulk-phase properties, and these differences can be observed through heat capacity. Also, a comparison of the heat capacity of nano-sized iron oxide polymorphs to the heat capacity of the iron core of ferritin can yield information about the core's physical properties and thermodynamic stability. The following discussion is an introduction to the iron oxide polymorphs and ferritin, which includes a survey of the scientific literature as it relates to their respective heat capacities.

1.2.1 Magnetite

Found in lodestone, Fe_3O_4, or magnetite, was used as a primitive magnet for compasses. It was discovered over 2,500 years ago and thought to have "magic" properties. In modern times, magnetite has been applied in ferrofluids, pharmaceutics,

magnetic refrigerants, and photocatalysis. Magnetite is also an important mineral in the study of plate tectonics because it is the main magnetic signature in rocks. Biologically, it is found in the brains of bees, termites, some birds, and humans, and is thought to aid in navigation and the ability to sense the polarity of the Earth's magnetic field.[2, 19]

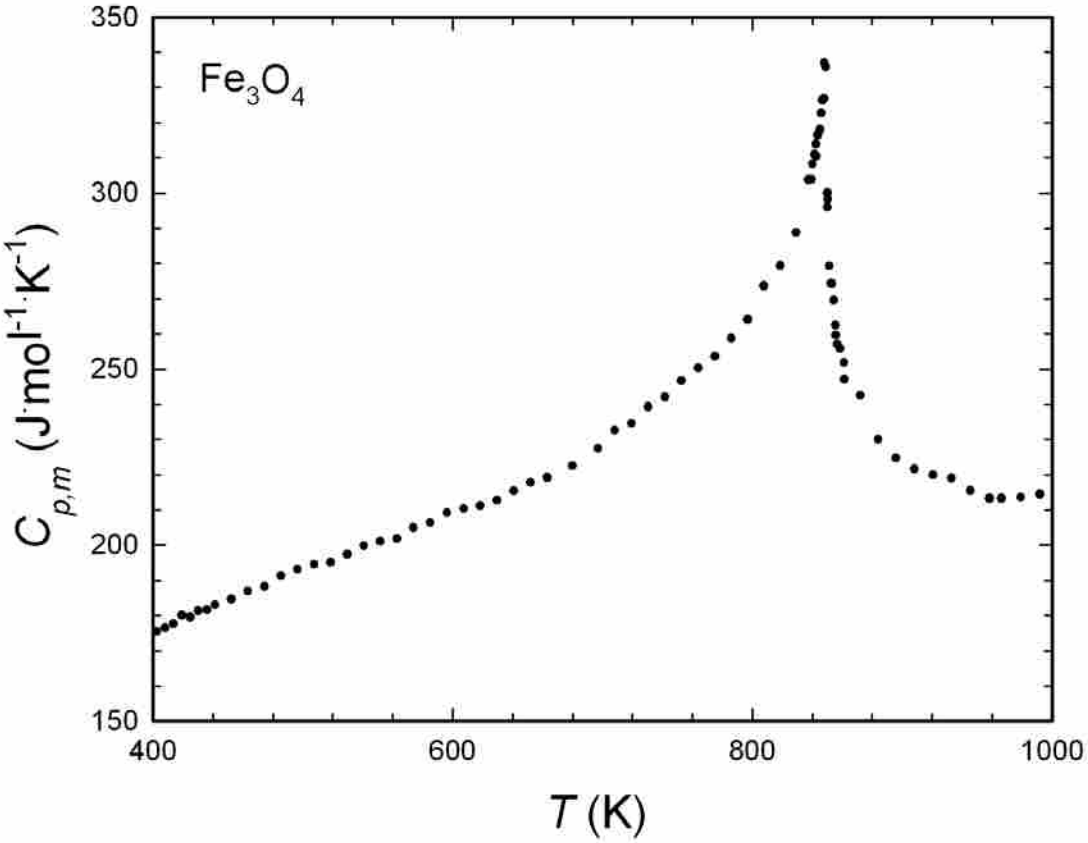

Figure 1.6 The paramagnetic to ferrimagnetic transition at the Curie temperature of magnetite.[3]

Magnetite is a ferrimagnetic solid that crystallizes in the inverse spinel structure. It has a Curie Temperature of 575 K (see Figure 1.6), and it is by far the most studied of all spinel compounds.[20] A low-temperature transition occurs in magnetite from a semi-metallic, cubic phase to either a monoclinic or triclinic insulating phase. A model for this transition in the area of 120 K (T_v) was first put forth by Verwey and the transition has since been called by his name.[21-23] Originally the underlying model was described as an order-disorder transition described by delocalized charges above T_v and ordering of

charge below T_v. A comprehensive review of the Verwey transition was put forth in 2004 that showed the discrepancy between this model and experimental results.[24] Newer theoretical studies suggest that the anomaly might arise from electron-phonon coupling, however it is not a foregone conclusion.[25-30]

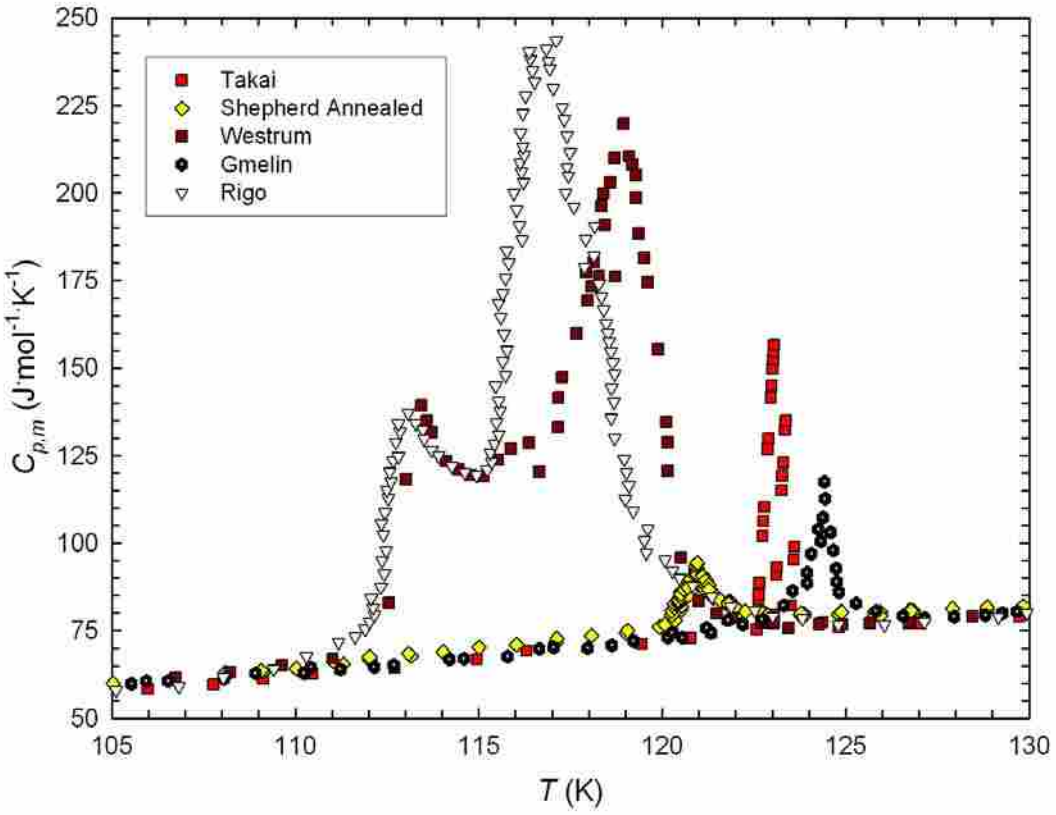

Figure 1.7 The anomaly in the heat capacity of magnetite due to the Verwey transition reported by various groups. [31-35]

This confusion regarding the mechanism of the Verwey transition is also exhibited calorimetrically (Figure 1.7); some heat capacity measurements show a bifurcated anomaly while other studies show a single peak. For instance, Westrum *et al.* characterized the Verwey transition on a polycrystalline sample and observed a bifurcated anomaly in the heat capacity over the temperature range 110-120 K.[35, 36] On the theory that the two peaks might be caused by stress in the crystal, Rigo *et al.* used an annealed sample but still observed the double peaks.[33, 37] In contrast, Gmelin *et al.*[31, 38] and Shepherd *et al.*[39, 40] observed a single anomaly for annealed samples.

Matsui and his collaborators performed a detailed analysis with stressed, stress-released, and annealed samples.[7] The results (Figure 1.8) display two peaks for stressed and stress-released samples, which are replaced with a single peak for the annealed sample.

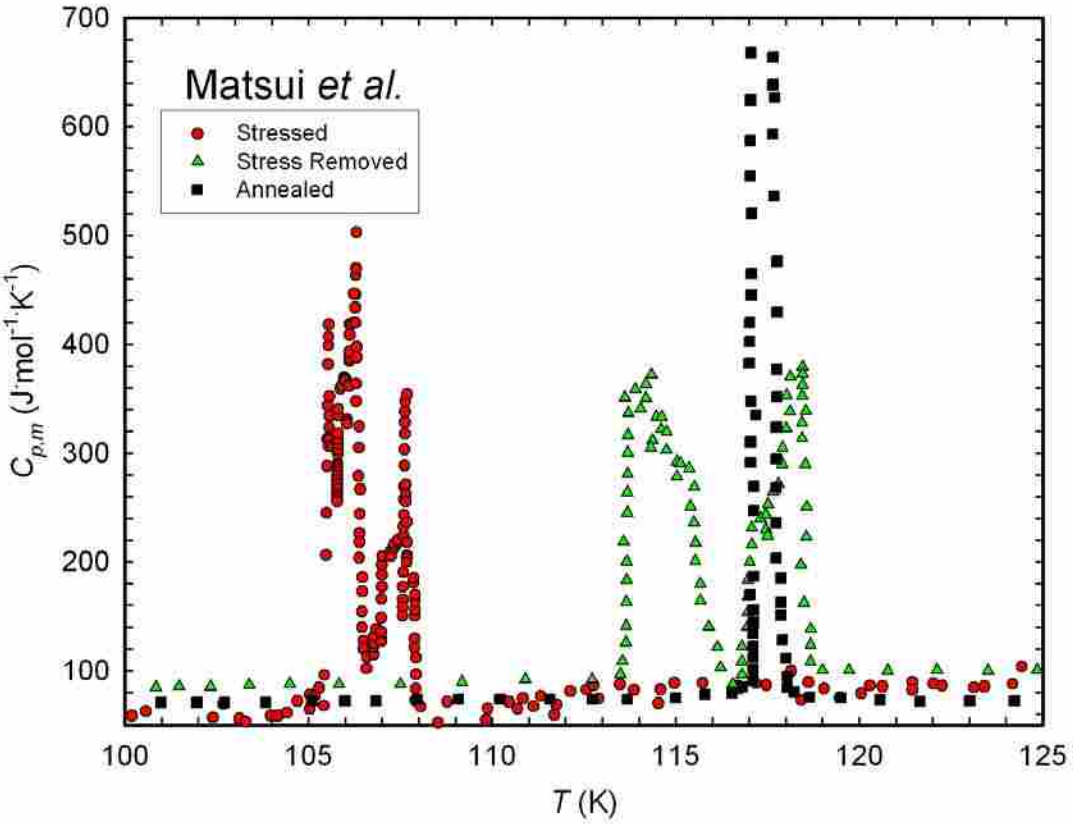

Figure 1.8 Heat capacity study of the Verwey transition in magnetite by Matsui *et al.* on stressed, stress-released, and annealed samples.[7]

Stoichiometry was also brought into question by Shepherd *et al.* who found that the temperature of the Verwey transition decreased from $T = (121.0 \pm 0.1)$ K for $\delta = -0.0002$ to $T = (110.2 \pm 0.5)$ K for $\delta = 0.0035$ in $Fe_{3(1-\delta)}O_4$.[34, 41-43] In later years, Tōdō *et al.* reported another anomaly in the heat capacity at 10 K.[44] However, Shepherd and his colleagues reported no anomaly at that temperature.[32] Currently no consensus as to the origin of these phenomena has been reached, but evidence does show that stress, stoichiometry, and quality of the crystal all play a role in the nature of the Verwey transition.

In all these studies, crystallite size has not been considered as a variable that could affect the Verwey transition. However, as the understanding of nanomaterials increases, it has been observed that physical properties change as particle size decreases. Only one study on the heat capacity of nanocrystalline magnetite is found in the scientific literature.[45] This was done in the narrow region from 253 K to 283 K in a variety of suspensions whose respective contributions were later subtracted. This study was also carried out varying the magnetic field from 0 to 0.7 T, and the authors report that the error in this experiment is ± 1.5%. This data is insufficient to calculate the entropy associated with nanocrystalline magnetite and the authors state that their research purpose was to study the magnetocaloric effect in nanosystems.

1.2.2 Hematite

Hematite is the main source of iron ore used in the production of iron metal. In synthetic chemistry, hematite is applied as the catalyst for Fisher-Tropsch production of hydrocarbons and in the oxidation of alcohols to aldehydes and ketones. When reacted with Al(s) in the Thermite reaction hematite is reduced to liquid Fe which is then used to weld iron rails.[2] Hematite or α-Fe_2O_3 is a common mineral which is paramagnetic above its Neel temperature of 950 K. Below this temperature it displays varying degrees of ferromagnetism depending on the crystallite size, and below the Morin transition temperature of 260 K it becomes antiferromagnetic.[46-49] It has a band gap of about 2.2 eV categorizing it as a semiconductor.[50]

The heat capacity of hematite was first measured by Parks and Kelley in 1926 over four narrow regions from 90 K to 290 K.[51] In 1958, Westrum and Gronvold improved upon these measurements covering the range from 5 K to 350 K.[52] This study and another later series of measurements in 1985 by Jayasuriya *et al.* showed no anomaly due to the Morin transition.[53]

Complementary methods such as static or ultrafast optical spectroscopies, x-ray and Mössbauer spectroscopy, neutron scattering, and tests of photochemical or catalytic reactivity have been used to study the chemical and physical properties of iron oxide particles as a function of particle size.[54] Nanocrystalline hematite heat capacities were measured in the temperature range 253 K to 283 K with an accuracy of ± 1.5%.[45] This

data like that of nano-magnetite is insufficient to provide standard entropies and other thermodynamic functions.

1.2.3 The Iron Oxyhydroxides

The iron oxyhydroxides have the general chemical formula of FeOOH. There are many crystal structures associated with this formula in its purity while dopants like Al are common in naturally occurring iron oxyhydroxides. The four most prevalent of these compounds, goethite (alpha phase), lepidocrocite (gamma phase), akaganéite (beta phase), and ferrihydrite (semi amorphous), will be discussed in this section.[2]

Goethite is the most thermodynamically stable phase of FeOOH. It has a yellow-brown color and has found applications as a pigment. It crystallizes in the orthorhombic system as part of the diaspore family with half of it octahedral sites occupied.[2, 17, 55] Goethite has a Néel temperature of 380 K, below which it is antiferromagnetic,[56-58] and electronically it is a semiconductor with a band gap of 2.5 eV.[47, 48] While natural goethites are usually found to be of micron length some macroscopic crystals can be up to several mm in length. In contrast, synthetic goethite samples have dimensions less than 100 nm. Thus goethite, as well as some other iron oxyhydroxides, is most commonly found in the borderline region between bulk and nanocrystallites.

The heat capacity of goethite was first reported by King and Weller[59] in 1970 in the temperature range 50 K to 298 K. In this study the authors extrapolated the data to zero and calculated the standard entropy of goethite. More recent measurements by Majzlan *et al.*[1, 5, 6, 60-62] reported in 2003 extended the available range down to 0.5 K and went as high as 400 K, revealing an anomaly in the heat capacity for the Néel transition. The entropy calculated from the two data sets are similar as Majzlan reported a value of 59.7 ± 0.2 J/(mol·K) while King reported 60.4 J/(mol·K). Arguably the value given by Majzlan *et al.* is more reliable as this group used experimental data over a larger range with no extrapolations for data lower than 50 K. Using this entropy value and enthalpy values from drop solution and acid-solution calorimetry, the Gibbs free energy was calculated to be – 489.8 ± 1.2 kJ/mol.

Lepidocrocite (γ-FeOOH) is the second most common phase of FeOOH after goethite.[2] Similar to goethite, lepidocrocite is orthorhombic and is isostructural to

Boehmite (γ-AlOOH).[17, 63] The name comes from the Greek word lepidos meaning flake, which is a fitting description as this solid is layered. The second half of the word comes from krokoeis meaning saffron-colored, but orange is a more common description. Lepidocrocite is naturally formed as an oxidation product of Fe^{2+} in biomes, soils, and rust. It is paramagnetic at room temperature, but becomes antiferromagnetic at its Néel temperature of 77 K[56, 64] and has a slightly smaller band gap than goethite at 2.4 eV.[47, 48] With slow crystallization, plates of lepidocrocite of 0.5-1.0 μm in length, 0.1-0.2 μm wide, and < 0.1 μm thick can be grown. Low-temperature heat capacity for lepidocrocite[5, 6, 65] was first published by Majzlan *et al.* in 2003 in the temperature range 10 K to 300 K. The sample used in this study had an average crystallite size of 30 nm as determined by powder x-ray diffraction (XRD). The small particle size creates the effect of a broad anomaly in the heat capacity around the Néel transition at 68 K. Mössbauer spectroscopy studies by Murad and Schwertmann[66] found that antiferromagnetic and paramagnetic lepidocrocite co-exist over a large temperature range, which is consistent with the observation of a broad anomaly in the heat capacity. Majzlan reported the standard entropy for lepidocrocite to be 65.08 ± 0.16 J/(mol·K). After the enthalpy of formation was obtained, the Gibbs free energy of formation was calculated to be – 480.1 ± 1.4 kJ/mol, showing lepidocrocite to be less thermodynamically stable than goethite under standard conditions.

Akaganéite, (β-FeOOH) is rarely found in nature. It mostly occurs in chloride-rich environments such as hot brines or in acid mine waters and has a brown to bright yellow color.[2] In contrast to the other FeOOH phases, it has a structure based on body centered cubic close packing of the anions and necessarily includes trace levels of chloride.[17, 67] It is classified in the monoclinic crystallographic system and patterned after the hollandite ($BaMn_8O_{16}$) structure.[1, 2] This structure is less dense than those of goethite and lepidocrocite and contains one tunnel per unit cell. These tunnels are the location of a significant amount of zeolitic water as well as the chloride anions. Akaganéite has a Néel temperature that lies close to room temperature at 290 K,[68] and thus it is called either a paramagnet or antiferromagnet under ambient conditions. Akaganéite is a semiconductor like goethite and lepidocrocite although with a smaller band gap of 2.12 eV.[47, 48]

The heat capacity for akaganéite has not been published but does appear in the dissertation of B. Lang[69] for two samples of akaganéite with varying degrees of hydration. These measurements were performed adiabatically in the range 12 K to 320 K. No noticeable anomaly could be seen in the heat capacity, but an inflection was observed that put the Néel temperature between 290 and 295 K. From the resulting entropy and enthalpy values from the literature, the standard Gibbs free energy was reported as -481.7 ± 1.3 kJ·mol^{-1}. An in depth literature search for heat capacity studies of akaganéite failed to produce any other sources than the study carried out by Lang.[69]

Ferrihydrite is perhaps the most intriguing of the iron oxyhydroxides. It is a poorly ordered, reddish-brown mineral that easily transforms into more stable members of the group.[2] It has attracted attention as it is naturally abundant in surface environments and is believed to be the structure of the iron core of the biological storage protein, ferritin.[17, 70] Studies and discussion still continue in trying to establish both the structure and the chemical formula of this compound.[55, 71-78] Its structure most resembles that of hematite with a hexagonal system, while the degree of ordering in ferrihydrite varies with the least ordered referred to as 2-line and the highest ordered as 6-line. These names originated because the XRD patterns display a range from two to six reflections. One of the reasons for the difficulty in solving the structure of ferrihydrite is that it only exists as a nanoparticle with diameters less than 8 nm. XRD spectra of nanopowders result in broad lines which are harder to resolve. In spite of this debate it has been well established that ferrihydrite is an antiferromagnet with a Néel temperature placed at 330 K but with an uncertainty of ± 20 K due to the poor intensity of the scattered neutrons used in its magnetic characterization.[79-81] Electronically ferrihydrite is a quantum dot whose band gap varies from 1.3 eV at a particles size of 2 nm to values greater than 2.5 eV when the particle size is larger than 8 nm.[82]

Acid solution calorimetry experiments on 2-line and 6-line ferrihydrite by Majzlan *et al.* give insight into its thermodynamic nature.[83] In this study the authors concluded that ferrihydrite samples become more stable with increasing crystallinity and showed ferrihydrite to be a metastable compound with respect to hematite in water. Using equilibrium constants the Gibbs free energy of formation was calculated to be in the range -708.5 to -711.0 ± 2.0 kJ/mol with 6-line ferrihydrite displaying the latter value.

The entropy of the sample was then obtained from the free energy and enthalpy and shown to have values in the range 122.2 to 133.0 J/(mol·K). In spite of this valuable thermodynamic information, no studies could be found that provide low-temperature heat capacity or an entropic description of the magnetic properties of ferrihydrite.

1.2.4 Ferritin

The processes of life demonstrate a multitude of paradoxes. For instance, unregulated iron is toxic to organisms because of its contribution to oxidative damage. Simultaneously, iron is essential to vital processes like oxygen transport, nitrogen fixation, and ATP production. To mediate these opposing processes, almost all organisms possess an efficient system for regulating the various metabolic processes of which iron is a part.[84]

A common component for all metabolic pathways involving iron is ferritin, the protein responsible for its storage.[85] Apoferritin, the protein with no iron, is made up of 24 subunits designated as either H- or L-chain according to their primary structure. These subunits are then arranged into a hollow shell having an outer diameter of 12 to 13 nm, an inner diameter of 7 to 8 nm, and a molecular weight of about 460 kDaltons. When iron is taken into the protein, it undergoes an oxidation from the ferrous to the ferric ion, and a nanoparticulate, ferric oxyhydroxide core is formed inside the shell that most resembles ferrihydrite. The ferritin molecule holds up to 4500 Fe(III) atoms, however native ferritin on average is found holding about 2000.

A large number of diseases of the central nervous system (CNS) are correlated to abnormal iron metabolism.[86, 87] Alzheimer's Disease (AD), which is found in 5% of men and women between the ages of 65 and 74 years old is linked to alterations in the levels of iron and distribution of iron-related proteins in specific areas of the brain.[88, 89] Oxidative stress and iron mismanagement appear to be important factors in Parkinson's Disease (PD). The primary site of neurodegeneration in PD is the substantia nigra pars compacta and most studies show increased iron in this region for individuals with severe PD.[90-93] Multiple Sclerosis (MS) is a neurological disorder that results from the demyelination of neurons. It is now widely accepted that iron acquisition by oligodendrocytes (cells that myelinate neurons of the CNS) is essential for myelination.[94,

[95] There is evidence that the expression of transferrin and ferritin in oligodendrocytes, as well as the cellular and regional distribution of iron is altered in MS.

Ferritin has also proven itself as a candidate in nanotechnological research. With its cage-like structure it has been used as a template in the size-controlled production of various inorganic materials.[96] Furthermore, ferritin has shown the ability to be immobilized on various substrates and functionalized by the addition of ligands. These properties have attracted much attention to ferritin from researchers outside of the traditional biochemical sciences.[97, 98]

Very little low-temperature heat capacity exists for proteins, including ferritin. One reason for this is that it is expensive and difficult to acquire proteins in large enough quantities to make such measurements with more traditional instrumentation. Most heat capacity studies on proteins have been carried out in the temperature range 260 to 400 K using differential scanning calorimetry (DSC), a technique which can be applied to proteins because it does not require large amounts of sample.[99-101] In these studies, the unfolding of proteins has been of key interest. Some data does exist for proteins at lower temperatures including albumin,[102] collagen,[103] ribonuclease-A,[103] insulin,[104] lysozyme,[105, 106] ovalbumin,[106] and lactoglobulin.[106] These studies make up a small fraction of the many interesting proteins that could be studied through low-temperature heat capacity measurements. With newer devices such as the physical properties measurement system (PPMS), which require sample sizes as small as ten mg,[107] it is possible that more heat capacity studies will be undertaken on proteins. Low-temperature heat capacity could provide insight into the stability of protein structural motifs, the energetic relationship between enzymes and their cofactors, and a thermodynamic description of bonding, atomic and molecular motion, and other physical phenomena. With ferritin specifically, heat capacity will help to give insight into the nature of the iron core and its thermophysical properties in addition to the relationship between the mineral core and the protein shell. This can be accomplished by fitting the core's heat capacity to a combination of the various models described above and determining which of these physical properties are relevant. While some studies have shown that the mineral core is some form of ferrihydrite,[108-110] a detailed study by Galvez *et al.* suggests that the ferritin iron core consists of a polyphasic structure with ferrihydrite, hematite, and magnetite

coexisting within the protein shell.[110, 111] This group was also able to demonstrate that these phases vary as iron is removed from the complex. Since the heat capacity of the mineral core can be separated into its various contributions, there is a possibility that it can be modeled as a combination of the three phases reported. Such a combination can then be a means of validation of the polyphasic model suggested by Galvez and coworkers.

1.3 Overview of the Dissertation

The previous description provides a background of the iron oxide and oxyhydroxide polymorphs as they relate to the heat capacity. With the goal of providing a thermodynamic description of these compounds through heat capacity and its corresponding thermodynamic relationships, an overview of this dissertation is given below. Overall, this work will provide the heat capacity for iron compounds for which no data exists, and complement existing data for bulk magnetite and hematite with heat capacity for their nanocrystalline counterparts.

Magnetite has been well studied on the bulk scale with special attention given to the Verwey transition and how it is affected by crystal quality and stoichiometry. Limited attention has been given to the effect of particle size on the heat capacity of magnetite and its effects on the Verwey transition. Chapter 2 contains a report on the heat capacity of a magnetite powder with an average diameter of 12 nm synthesized at Brigham Young University. This study was carried out in the temperature range 0.5 to 350 K, and the standard entropy and relative enthalpy and Gibbs free energy are also reported. Comparisons are made between these values and those reported in the scientific literature for bulk magnetite.

Entropic values obtained through heat capacity for hematite have relied on extrapolating the temperatures down to 0 K, and little reliable data exists below 10 K. Data from the one study performed on nanocrystalline hematite displayed a large error when compared to the accuracy that is achievable through adiabatic calorimetry. Additionally, these studies were over a limited range of temperature, and the data is insufficient to calculate third law entropy values. As we seek to understand the physical changes that are observed in nanocrystalline iron oxides, the heat capacity of two samples

of hematite have been measured. The first sample is a bulk hematite powder which was measured in the range 2 to 300 K and a discussion is given in Chapter 3. This data was used to calculate new entropy, relative enthalpy, and relative Gibbs free energy values which were compared to those reported by Westrum and Gronvold. The second sample is a nanocrystalline hematite powder synthesized at Brigham Young University with an average diameter of 13 nm. The heat capacity of the 13 nm sample was measured in the temperature range 0.5 to 350 K, and its corresponding thermodynamic functions are reported with a comparison to those reported for the bulk hematite in Chapter 4.

Chapter 5 is an extension of the work of Lang and Majzlan with respect to the iron oxyhydroxide compounds akaganéite and lepidocrocite. Semi-adiabatic calorimetric measurements yielded heat capacity for these compounds in the region 0.5 to 38 K. The akaganéite used in these low temperature experiments came from the same sample batch used in Lang's study and the lepidocrocite likewise came from the batch used by Majzlan. A discussion of the low-temperature physical behavior is given and the new data is merged with previously reported data and new calculations of thermodynamic functions are made based on this more complete data set.

Ferrihydrite has yet to be studied through heat capacity measurements, which should be interesting in that this compound shows a large degree of disorder. Also, as this compound most closely resembles the structure of the ferritin core a comparison between the heat capacity of ferrihydrite and that of the ferritin core will be useful in describing the nature of iron storage in ferritin. Heat capacity studies on 2-line ferrihydrite have begun in our laboratory, but will not be included in this study.

We have also begun measurements of the heat capacity of apoferritin, ferritin, and the iron core as obtained by subtracting the protein contribution from the ferritin data. Measurements have been obtained semi-adiabatically in the temperature region 0.5 to 38 K, but will not be discussed until further analysis can be made with the addition of higher temperature measurements. However, Chapter 6 describes the preparation of apoferritin and reconstituted ferritin for heat capacity measurements with a discussion on the effects of buffers on the iron-loading capacity of ferritin.

References

1. Navrotsky, A.; Mazeina, L.; Majzlan, J., *Science (Washington, DC, U. S.)* **2008,** *319* (5870), 1635-1638.
2. Cornell, R. M.; Schwertmann, U.; Editors, *The Iron Oxides: Structure, Properties, Reactions, Occurrence and Uses*. VCH: Weinem, 1996; p 573.
3. Coughlin, J. P.; King, E. G.; Bonnickson, K. R., *J. Am. Chem. Soc.* **1951,** *73*, 3891-3.
4. Stevens, R.; Boerio-Goates, J., *J. Chem. Thermodyn.* **2004,** *36* (10), 857-863.
5. Majzlan, J.; Grevel, K.-D.; Navrotsky, A., *Am. Mineral.* **2003,** *88* (5-6), 855-859.
6. Majzlan, J.; Lang, B. E.; Stevens, R.; Navrotsky, A.; Woodfield, B. F.; Boerio-Goates, J., *Am. Mineral.* **2003,** *88* (5-6), 846-854.
7. Matsui, M.; Todo, S.; Chikazumi, S., *J. Phys. Soc. Jpn.* **1977,** *42* (5), 1517-24.
8. Gopal, E. S. R., *Specific Heats at Low Temperatures (International Cryogenics Monograph Series)*. Plenum Press: New York, 1966; p 226
9. Boerio-Goates, J.; Stevens, R.; Lang, B.; Woodfield, B. F., *J. Therm. Anal. Calorim.* **2002,** *69* (3), 773-783.
10. Ott, J. B.; Boerio-Goates, J., *Chemical Thermodynamics: Principles and Applications*. 2000; p 360 pp.
11. Stevens, R.; Woodfield, B. F.; Boerio-Goates, J.; Crawford, M. K., *J. Chem. Thermodyn.* **2004,** *36* (5), 359-375.
12. Lashley, J. C.; Stevens, R.; Crawford, M. K.; Boerio-Goates, J.; Woodfield, B. F.; Qiu, Y.; Lynn, J. W.; Goddard, P. A.; Fisher, R. A., *Phys. Rev. B: Condens. Matter Mater. Phys.* **2008,** *78* (10), 104406/1-104406/18.
13. Phillips, N. E., *Crit. Rev. Solid State Sci.* **1971,** *2* (4), 467-553.
14. Lang, B. E.; Boerio-Goates, J.; Woodfield, B. F., *J. Chem. Thermodyn.* **2006,** *38* (12), 1655-1663.
15. Boerio-Goates, J.; Callanan, J. E., **1992,** *6*, 621-717.
16. Woodfield, B. F. Specific-heat of high-temperature superconductors: apparatus and measurements (magnetic field, yttrium barium copper oxide, mercury barium copper oxide, barium potassium bismuth oxide). 1995.
17. Schwertmann, U., *NATO ASI Ser., Ser. C* **1988,** *217* (Iron Soils Clay Miner.), 267-308.
18. Stix, G., *Sci Am* **2001,** *285* (3), 32-7.
19. Chang, S. B. R.; Kirschvink, J. L., *Annu. Rev. Earth Planet. Sci.* **1989,** *17*, 169-95.
20. Iida, S.; Mizushima, K.; Mizoguchi, M.; Mada, J.; Umemura, S.; Yoshida, J.; Nakao, K., *J. Phys. (Paris), Colloq.* **1977,** (1), 73-7.
21. Verwey, E. J. W., *Nature (London, U. K.)* **1939,** *144*, 327-8.
22. Verwey, E. J. W.; Haayman, P. W., *Physica (The Hague)* **1941,** *8*, 979-87.

23. Verwey, E. J. W.; Haayman, P. W.; Romeijn, F. C., *J. Chem. Phys.* **1947,** *15*, 181-7.
24. Garcia, J.; Subias, G., *J. Phys.: Condens. Matter* **2004,** *16* (7), R145-R178.
25. Kakol, Z.; Kozlowski, A., *Solid State Sci.* **2000,** *2* (8), 737-746.
26. Koo, J. H.; Kim, J.-H.; Jeong, J.-M.; Cho, G., *Mod. Phys. Lett. B* **2009,** *23* (14), 1791-1797.
27. Leonov, I.; Yaresko, A. N., *J. Phys.: Condens. Matter* **2007,** *19* (2), 021001/1-021001/3.
28. Piekarz, P.; Parlinski, K.; Oles, A. M., *Phys. Rev. Lett.* **2006,** *97* (15), 156402/1-156402/4.
29. Piekarz, P.; Parlinski, K.; Oles, A. M., *J. Phys.: Conf. Ser.* **2007,** *92*, No pp given.
30. Piekarz, P.; Parlinski, K.; Oles, A. M., *Phys. Rev. B: Condens. Matter Mater. Phys.* **2007,** *76* (16), 165124/1-165124/16.
31. Gmelin, E.; Lenge, N.; Kronmueller, H., *Philos. Mag. B* **1984,** *50* (3), L41-L44.
32. Koenitzer, J. W.; Keesom, P. H.; Honig, J. M., *Phys. Rev. B: Condens. Matter Mater. Phys.* **1989,** *39* (9), 6231-3.
33. Rigo, M. O.; Mareche, J. F.; Brabers, V. A. M., *Philos. Mag. B* **1983,** *48* (5), 421-30.
34. Shepherd, J. P.; Aragon, R.; Koenitzer, J. W.; Honig, J. M., *Phys. Rev. B: Condens. Matter Mater. Phys.* **1985,** *32* (3), 1818-19.
35. Westrum, E. F. F.; Groenvold, F., *J. Chem. Thermodyn.* **1969,** *1* (6), 543-57.
36. Groenvold, F.; Sveen, A., *J. Chem. Thermodyn.* **1974,** *6* (9), 859-72.
37. Rigo, M. O.; Kleinclauss, J., *Philos. Mag. B* **1980,** *42* (3), 393-407.
38. Gmelin, E.; Lenge, N.; Kronmueller, H., *Phys. Status Solidi A* **1983,** *79* (2), 465-75.
39. Shepherd, J. P.; Koenitzer, J. W.; Aragon, R.; Sandberg, C. J.; Honig, J. M., *Phys. Rev. B: Condens. Matter Mater. Phys.* **1985,** *31* (2), 1107-13.
40. Shepherd, J. P.; Koenitzer, J. W.; Sandberg, C. J.; Aragon, R.; Honig, J. M., *Mol. Cryst. Liq. Cryst.* **1984,** *107* (1-2), 191-4.
41. Aragon, R.; Rasmussen, R. J.; Shepherd, J. P.; Koenitzer, J. W.; Honig, J. M., *J. Magn. Magn. Mater.* **1986,** *54-57* (3), 1335-6.
42. Aragon, R.; Shepherd, J. P.; Koenitzer, J. W.; Buttrey, D. J.; Rasmussen, R. J.; Honig, J. M., *J. Appl. Phys.* **1985,** *57* (8, Pt. 2A), 3221-2.
43. Shepherd, J. P.; Koenitzer, J. W.; Aragon, R.; Spalek, J.; Honig, J. M., *Phys. Rev. B: Condens. Matter Mater. Phys.* **1991,** *43* (10-B), 8461-71.
44. Todo, S.; Chikazumi, S., *J. Phys. Soc. Jpn.* **1977,** *43* (3), 1091-2.
45. Korolev, V. V.; Arefyev, I. M.; Blinov, A. V., *J. Therm. Anal. Calorim.* **2008,** *92* (3), 697-700.
46. Hill, A. H.; Jiao, F.; Bruce, P. G.; Harrison, A.; Kockelmann, W.; Ritter, C., *Chem. Mater.* **2008,** *20* (15), 4891-4899.
47. Sherman, D. M., *Geochim. Cosmochim. Acta* **2005,** *69* (13), 3249-3255.
48. Sherman, D. M.; Todd, E. C.; Purton, J. A., *Abstracts of Papers, 223rd ACS National Meeting, Orlando, FL, United States, April 7-11, 2002* **2002**, GEOC-137.
49. Willis, B. T. M.; Rooksby, H. P., *Proc. Phys. Soc., London* **1952,** *65B*, 950-4.

50. Gilbert, B.; Frandsen, C.; Maxey, E. R.; Sherman, D. M., *Phys. Rev. B: Condens. Matter Mater. Phys.* **2009,** *79* (3), 035108/1-035108/7.
51. Parks, G. S.; Kelley, K. K., *J. Phys. Chem.* **1926,** *30*, 47-55.
52. Gronvold, F.; Westrum, E. F., Jr., *J. Am. Chem. Soc.* **1959,** *81*, 1780-3.
53. Jayasuriya, K. D.; Stewart, A. M.; Campbell, S. J., *J. Phys. Chem. Solids* **1985,** *46* (5), 625-9.
54. Morris, R. V.; Lauer, H. V., Jr.; Lawson, C. A.; Gibson, E. K., Jr.; Nace, G. A.; Stewart, C., *J. Geophys. Res., B* **1985,** *90* (B4), 3126-44.
55. Penn, R. L.; Banerjee, S.; Berquo, T. S.; Erbs, J. J.; Jentzsch, T. L.; Tanaka, K., *Abstracts of Papers, 233rd ACS National Meeting, Chicago, IL, United States, March 25-29, 2007* **2007**, GEOC-009.
56. Hall, P. G.; Clarke, N. S.; Maynard, S. C. P., *J. Phys. Chem.* **1995,** *99* (15), 5666-73.
57. Lee, G. H.; Kim, S. H.; Choi, B. J.; Huh, S. H.; Chang, Y.; Kim, B.; Park, J.; Oh, S. J., *J. Korean Phys. Soc.* **2004,** *45* (4), 1019-1024.
58. Yamamoto, N., *Bull. Inst. Chem. Res., Kyoto Univ.* **1968,** *46* (6), 283-8.
59. King, E. G.; Weller, W. W. *Low-temperature Heat Capacities and Entropies at 298.15^{o} K of Goethite and Pyrophyllite*; Bur. of Mines,Washington,DC,USA.: 1970; p 10 pp.
60. Majzlan, J.; Navrotsky, A.; Woodfield, B. F.; Lang, B. E.; Boerio-Goates, J.; Fisher, R. A., *J. Low Temp. Phys.* **2003,** *130* (1/2), 69-76.
61. Mazeina, L.; Navrotsky, A., *Clays Clay Miner.* **2005,** *53* (2), 113-122.
62. Mazeina, L.; Navrotsky, A., *Chem. Mater.* **2007,** *19* (4), 825-833.
63. Ewing, F. J., *J. Chem. Phys.* **1935,** *3*, 420-4.
64. Hirt, A. M.; Lanci, L.; Dobson, J.; Weidler, P.; Gehring, A. U., *J. Geophys. Res., [Solid Earth]* **2002,** *107* (B1), EPM5/1-EPM5/9.
65. Majzlan, J.; Mazeina, L.; Navrotsky, A., *Geochim. Cosmochim. Acta* **2007,** *71* (3), 615-623.
66. Murad, E.; Schwertmann, U., *Mineral. Mag.* **1984,** *48* (349), 507-11.
67. Childs, C. W.; Goodman, B. A.; Paterson, E.; Woodhams, F. W. D., *Aust. J. Chem.* **1980,** *33* (1), 15-26.
68. Chambaere, D.; De Grave, E., *J. Magn. Magn. Mater.* **1984,** *42* (3), 263-8.
69. Lang, B. E. Specific Heat and Thermodynamic Properties of Metallic Systems: Instrumentation and Analysis. 2005.
70. Jambor, J. L.; Dutrizac, J. E., *Chem. Rev. (Washington, D. C.)* **1998,** *98* (7), 2549-2585.
71. Carta, D.; Casula, M. F.; Corrias, A.; Falqui, A.; Navarra, G.; Pinna, G., *Mater. Chem. Phys.* **2009,** *113* (1), 349-355.
72. Cismasu, C.; Michel, F. M.; Stebbins, J. F.; Tcaciuc, A. P.; Brown, G. E., *Abstracts of Papers, 237th ACS National Meeting, Salt Lake City, UT, United States, March 22-26, 2009* **2009**, GEOC-100.
73. Ford, R. G.; Michel, F. M.; Thompson, J., *Abstracts of Papers, 235th ACS National Meeting, New Orleans, LA, United States, April 6-10, 2008* **2008**, GEOC-174.
74. Hiemstra, T.; Van Riemsdijk, W. H., *Geochim. Cosmochim. Acta* **2009,** *73* (15), 4423-4436.

75. Jansen, E.; Kyek, A.; Schafer, W.; Schwertmann, U., *Appl. Phys. A: Mater. Sci. Process.* **2002,** *74* (Suppl., Pt. 2), S1004-S1006.
76. Michel, F. M.; Antao, S. M.; Celestian, A. J.; Schoonen, M. A.; Parise, J. B.; Liu, G.; Strongin, D. R.; Lee, P. L.; Chupas, P. J., *Abstracts of Papers, 232nd ACS National Meeting, San Francisco, CA, United States, Sept. 10-14, 2006* **2006**, GEOC-133.
77. Michel, F. M.; Ehm, L.; Antao, S. M.; Lee, P. L.; Chupas, P. J.; Liu, G.; Strongin, D. R.; Schoonen, M. A. A.; Phillips, B. L.; Parise, J. B., *Science (Washington, DC, U. S.)* **2007,** *316* (5832), 1726-1729.
78. Penn, R. L., *Science (Washington, DC, U. S.)* **2007,** *316* (5832), 1704-1705.
79. Duarte, E. L.; Itri, R.; Lima, E., Jr.; Baptista, M. S.; Berquo, T. S.; Goya, G. F., *Nanotechnology* **2006,** *17* (22), 5549-5555.
80. Murad, E.; Schwertmann, U., *Am. Mineral.* **1980,** *65* (9-10), 1043-8.
81. Seehra, M. S.; Babu, V. S.; Manivannan, A.; Lynn, J. W., *Phys. Rev. B: Condens. Matter Mater. Phys.* **2000,** *61* (5), 3513-3518.
82. Liu, G.; Debnath, S.; Paul, K. W.; Han, W.; Hausner, D. B.; Hosein, H.-A.; Michel, F. M.; Parise, J. B.; Sparks, D. L.; Strongin, D. R., *Langmuir* **2006,** *22* (22), 9313-9321.
83. Majzlan, J.; Navrotsky, A.; Schwertmann, U., *Geochim. Cosmochim. Acta* **2004,** *68* (5), 1049-1059.
84. Hower, V.; Mendes, P.; Torti, F. M.; Laubenbacher, R.; Akman, S.; Shulaev, V.; Torti, S. V., *Mol. BioSyst.* **2009,** *5* (5), 422-443.
85. Arosio, P.; Ingrassia, R.; Cavadini, P., *Biochim. Biophys. Acta, Gen. Subj.* **2009,** *1790* (7), 589-599.
86. Harvey, J. W., *Clin. Biochem. Domest. Anim. (6th Ed.)* **2008**, 259-285.
87. Mascitelli, L.; Pezzetta, F.; Goldstein, M. R., *Cell. Mol. Life Sci.* **2009,** *66* (17), 2943.
88. Bartzokis, G.; Beckson, M.; Hance, D. B.; Marx, P.; Foster, J. A.; Marder, S. R., *Magn. Reson. Imaging* **1997,** *15* (1), 29-35.
89. Cornett, C. R.; Markesbery, W. R.; Ehmann, W. D., *Neurotoxicology* **1998,** *19* (3), 339-45.
90. Bartzokis, G.; Cummings, J. L.; Markham, C. H.; Marmarelis, P. Z.; Treciokas, L. J.; Tishler, T. A.; Marder, S. R.; Mintz, J., *Magn. Reson. Imaging* **1999,** *17* (2), 213-22.
91. Dexter, D. T.; Carayon, A.; Vidailhet, M.; Ruberg, M.; Agid, F.; Agid, Y.; Lees, A. J.; Wells, F. R.; Jenner, P.; Marsden, C. D., *J. Neurochem.* **1990,** *55* (1), 16-20.
92. Sofic, E.; Paulus, W.; Jellinger, K.; Riederer, P.; Youdim, M. B. H., *J. Neurochem.* **1991,** *56* (3), 978-82.
93. Riederer, P.; Sofic, E.; Rausch, W. D.; Schmidt, B.; Reynolds, G. P.; Jellinger, K.; Youdim, M. B. H., *J. Neurochem.* **1989,** *52* (2), 515-20.
94. Connor, J. R.; Menzies, S. L., *Glia* **1996,** *17* (2), 83-93.
95. Craelius, W.; Migdal, M. W.; Luessenhop, C. P.; Sugar, A.; Mihalakis, I., *Arch Pathol Lab Med* **1982,** *106* (8), 397-9.
96. Iwahori, K.; Yamashita, I., *Recent Res. Dev. Biotechnol. Bioeng.* **2005,** *7*, 41-68.

97. King, G. C.; Choi, S. H.; Chu, S.-H.; Kim, J.-W.; Park, Y.; Lillehei, P. T.; Watt, G. D.; Davis, R. C.; Harb, J. N., *Proc. SPIE-Int. Soc. Opt. Eng.* **2004,** *5389* (Smart Electronics, MEMS, BioMEMS, and Nanotechnology), 461-467.
98. Klem, M. T.; Young, M.; Douglas, T., *Mater. Today (Oxford, U. K.)* **2005,** *8* (9), 28-37.
99. Lopez, M. M.; Makhatadze, G. I., *Methods Mol. Biol. (Totowa, NJ, U. S.)* **2002,** *173* (Calcium-Binding Protein Protocols, Volume 2), 113-119.
100. Prabhu, N. V.; Sharp, K. A., *Annu. Rev. Phys. Chem.* **2005,** *56*, 521-548.
101. Privalov, G. P.; Privalov, P. L., *Methods Enzymol.* **2000,** *323* (Energetics of Biological Macromolecules, Part C), 31-62.
102. Shinyashiki, N.; Yamamoto, W.; Yokoyama, A.; Yoshinari, T.; Yagihara, S.; Kita, R.; Ngai, K. L.; Capaccioli, S., *J. Phys. Chem. B* **2009,** *113* (43), 14448-14456.
103. Mrevlishvili, G. M., *Thermochim. Acta* **1998,** *308* (1-2), 49-54.
104. Hutchens, J. O.; Cole, A. G.; Stout, J. W., *J. Biol. Chem.* **1969,** *244* (1), 26-32.
105. Miyazaki, Y.; Matsuo, T.; Suga, H., *J. Phys. Chem. B* **2000,** *104* (33), 8044-8052.
106. Zhang, G.; Wunderlich, B., *J. Therm. Anal.* **1997,** *49* (2), 823-829.
107. Lashley, J. C.; Hundley, M. F.; Migliori, A.; Sarrao, J. L.; Pagliuso, P. G.; Darling, T. W.; Jaime, M.; Cooley, J. C.; Hults, W. L.; Morales, L.; Thoma, D. J.; Smith, J. L.; Boerio-Goates, J.; Woodfield, B. F.; Stewart, G. R.; Fisher, R. A.; Phillips, N. E., *Cryogenics* **2003,** *43* (6), 369-378.
108. Bou-Abdallah, F.; Carney, E.; Chasteen, N. D.; Arosio, P.; Viescas, A. J.; Papaefthymiou, G. C., *Biophys. Chem.* **2007,** *130* (3), 114-121.
109. Pan, Y.; Brown, A.; Brydson, R.; Warley, A.; Li, A.; Powell, J., *Micron* **2006,** *37* (5), 403-411.
110. Pan, Y.-H.; Sader, K.; Powell, J. J.; Bleloch, A.; Gass, M.; Trinick, J.; Warley, A.; Li, A.; Brydson, R.; Brown, A., *J. Struct. Biol.* **2009,** *166* (1), 22-31.
111. Galvez, N.; Fernandez, B.; Sanchez, P.; Cuesta, R.; Ceolin, M.; Clemente-Leon, M.; Trasobares, S.; Lopez-Haro, M.; Calvino, J. J.; Stephan, O.; Dominguez-Vera, J. M., *J. Am. Chem. Soc.* **2008,** *130* (25), 8062-8068.

Chapter 2

Heat Capacity Studies of Nanocrystalline Magnetite (Fe_3O_4)

2.1 Introduction

The Verwey transition in magnetite (Fe_3O_4) was first discovered as a discontinuity in the electrical resistance at $T = 120$ K, and has been the cause of scientific debate for almost 70 years.[3] It has been extensively investigated which can be seen by the wide array of experimental tools employed in its characterization. As a result of extensive characterization, it is now known that, in addition to the sudden increase in the electrical resistance by two orders of magnitude, magnetite undergoes a phase transition from the cubic inverse spinel to either a tetragonal or orthorhombic phase.[2, 4, 5] In spite of these studies the microscopic origin of the Verwey transition is not well-established. Verwey originally proposed a charge-ordering model[6, 7] in which electrons become localized on specific sites, but decades of research would provide evidence supporting and refuting this theory.[8] As evidence has been gathered, other models have also been put forth with those proposing electron-lattice interactions gaining more acceptance.[9-14]

The measurement of heat capacities has been applied in several studies of the Verwey transition[15] which generally appears as an anomaly in the heat capacity around $T = 120$ K (T_v). Some controversy surrounds the exact form of the anomaly with some authors reporting a single peak[16-18] in this region while others have observed two or more.[1, 15, 19, 20] Those papers reporting two peaks disagreed as well with some showing peaks separated by several degrees and others showing overlap. The peaks have also appeared as broad or sharp anomalies while their temperature also varies with values reported as low as $T = 113.0$ K and as high as $T = 125.0$ K.[21]

Many studies have been designed to gain a better understanding of these discrepancies in the heat capacity of magnetite at the Verwey transition. The central

question in these studies has involved sample preparation and characterization and how they affect the form of the anomaly. Attempts to resolve the inconsistencies reported for the Verwey transition in the literature can be separated into three categories: i) the effect of dopants and impurities, ii) studies involving crystal quality, and iii) the effect of oxygen stoichiometry. A brief review of theses studies is given below.

Studies involving the effects of dopants on the low-temperature transition of magnetite have been carried out by more than one group.[19, 22-26] These experiments varied the exact amount of dopants which included Cd, Zn, Mn, Ti, Co, Ni, Cu, and Al, and the results of these studies agreed in many ways. It was shown that increased doping resulted in a change in the Verwey transition from first to second order and was accompanied by a decrease in entropy. Also, only one of the many samples studied exhibited a bifurcated anomaly whereas the others showed a single peak.

While studies describe the effects of crystal quality[27, 28] on the heat capacity of magnetite, a report by Matsui *et al.*[29] provides the most detailed study involving defects in crystal structure and their relation to the Verwey transition. The first sample in this report is a polycrystalline, "stressed" magnetite compact whose corresponding heat capacity reveals several peaks found 12 K below T_v and extending over a temperature range of ~3 K. This polycrystalline sample was then squeezed with aluminum rings to "remove the stress" which can be observed through the convergence of the several peaks into two which are found 2 K below T_v, yet over a broader range of ~ 4 K. After this "stress-released" sample was annealed at 700°C for 10 days a narrow, single anomaly was observed at T = 117.2 K.

The question of oxygen stoichiometry[27, 30-32] was also investigated through heat capacity measurements by many groups. Like studies involving dopants, experiments investigating the effects of non-stoichiometry in $Fe_{3(1-\delta)}O_4$ have been insightful. When the value of δ increases from 0 to 0.0039 the Verwey transition is first-order and the transition temperature progressively decreases to 109 K. For values of δ in the range 0.0039-0.012 the anomaly takes the shape of a "hump" indicating a change to a second-order transition, and the temperature of the peak's maximum decreases to 80 K.

It is clear from these studies that the Verwey transition in magnetite is affected by sample composition including such factors as crystal quality, sample purity, and

stoichiometry. The anomaly in the heat capacity due to the Verwey transition appears as one peak when the sample is of the highest crystal quality and stoichiometric while two or more peaks are observed when there are defects in the crystal. Also, impurities in the sample and higher oxygen content can decrease the temperature of the transition by as much as 40 K.

Although the effects of crystal defects on the Verwey transition have been studied, there have been no experiments attempting to describe its relationship with crystal size. Heat capacity studies on magnetite at the nanoscale can provide information on the size-dependence of the Verwey transition. The heat capacity of nanocrystalline magnetite has been reported in the small temperature range from 253 to 283 K and was carried out varying the magnetic field from 0 to 0.7 T.[33] As these measurements are over 100 K above T_v they cannot provide insight into the microscopic origin of the Verwey transition. However, the goal of this study was to investigate the magnetocaloric effect in nanosystems, and thus understanding the Verwey transition was never within in its scope. If the size-dependence of the Verwey transition is to be studied through heat capacity, new measurements will need to be made on magnetite at the nanoscale.

In addition to the insights it can provide regarding the Verwey transition, heat capacity can also yield information about the physical properties of nanocrystalline magnetite. Some of the physical properties that can be studied through heat capacity include magnetic ordering, electrical conductivitiy, and the vibrational motion of atoms.[34] By comparing the heat capacity of nanocrystalline magnetite to that of its bulk counterpart, the size-dependence of these properties can be studied. In particular, the magnetic properties of nanocrystalline magnetite compared to those of the bulk are of key interest.

The magnetic properties of nanocrystalline magnetite samples have been extensively studied using other methods which show that magnetite nanoparticles have superparamagnetic properties.[35-38] Superparamagnetism occurs in nanoparticles that consist of a single magnetic domain with a diameter between 3 and 50 nm. Unlike the effects of paramagnetism which are usually observed above the Curie temperature, superparamagnetism occurs below this point.[39, 40] This magnetic behavior is characterized by the entire nanoparticle acting as a single magnetic moment which can randomly flip

direction under the influence of temperature. Superparamagnetism can be manifest as a dipolar contribution to the heat capacity due to the interaction of each cluster spin with the dipolar field created by all the other neighbors. This dipolar field depends on the spin configuration of the neighboring spins, which is dependent on the overall magnetization. In the absence of a magnetic field the probability distribution of the internal fields is centered at zero.[39] The heat capacity of ideal superparamagnets frequently exhibits an upturn[41] in the heat capacity at temperatures lower than 1 K as shown in reports by Triplett and Phillips.[42] Livingston and Bean[40, 43] proposed that superparamagnetic effects might make a measurable contribution to γ, the linear temperature coefficient of the specific heat. This model is limited by its neglect of interactions between particles, yet experimental results support the need for a large linear term in other superparamagnetic systems.[41, 42]

Most studies characterizing magnetite nanoparticles as a superparamagnet are carried out in solutions where particles are dispersed using a surfactant and interactions between particles are weak.[35-37] It has been observed that as nanoparticle concentration increases a superparamagnet may evolve into a spin-glass.[39] Recent studies by Suzuki *et al.*[44] indicate that nanocrystalline magnetite may exhibit a superspin-glass phase below a freezing temperature of T_f= 30.6±1.6 K. Heat capacity models of the transition from a paramagnet (or superparamagnet) to a spin glass display a broad anomaly at the transition temperature,[45, 46] and the limiting low-temperature form of the spin-glass heat capacity can be approximated by $C = \gamma T + B_2 T^2$.[47] Claims of spin-glass behavior versus superparamagnetism create some uncertainty in the understanding of magnetic behavior in nanocrystalline magnetite, and low-temperature heat capacity measurements can help discern between superparamagnetic and spin-glass behavior in nanocrystalline magnetite

The heat capacity of bulk $Fe_{(3-\delta)}O_4$ (δ = 0 and 0.0049) has been measured from 0.3 to 10 K by Koentizer *et al.* using a ^{3}He adiabatic technique which had an error of ±3%.[48] These measurements were successfully fit to the expression $C = LT^{3/2} + \alpha T^3$, showing that bulk magnetite orders ferrimagnetically.[48] On the other hand magnetization, Mossbauer, and theoretical studies of magnetite nanoparticles with a single domain have shown anisotropic behavior in their spin-wave spectrum.[49-53] Low-temperature heat capacity studies using semi-adiabatic calorimetry of samples having magnetic anisotropy

required a modified spin-wave term of the form $T^{3/2}e^{-\Delta/T}$ where delta represents a gap in the spin-wave spectrum in units of K.[54-56] Heat capacity measurements at low-temperature of nanocrystalline magnetite can be fit using a spin-wave term or an anisotropic spin gap, and these fits can be compared to see which most accurately models the heat capacity. Through this approach low-temperature heat capacity measurements of nanocrystalline magnetite can provide insight into its magnetic properties as compared to the bulk.

This study provides the heat capacity for a nanocrystalline sample of magnetite in the temperature range 0.5 to 350 K. A discussion is given on the implications this data has with respect to the Verwey transition with a description of nanocrystalline magnetite's physical properties as they relate to low-temperature heat capacity.

2.2 Experimental

A nanocrystalline sample was prepared following the method outlined by Wang.[57, 58] An aqueous solution of 0.5 M Fe^{3+} was prepared by combining 135.16 g $FeCl_3 \cdot 6H_2O$ (99% pure) and 18 MΩ water in a 1 L solution. Likewise a 0.5 M Fe^{2+} solution was prepared by dissolving 50.71 g $FeCl_2 \cdot 4H_2O$ (99.99% pure) in 18 MΩ water using a 500 mL volumetric flask. These solutions were then filtered to remove any insoluble materials before combining them in a 1.75:1 Fe^{3+}/Fe^{2+} molar ratio. This solution was titrated under constant stirring with 306.36 mL of 50 % aqueous NH_4OH until the final pH was 8.0. The mixture was stirred for an additional 5 minutes then covered and stored in the mother liquid for 24 hours. The supernatant was removed and the precipitate was treated twice with 1.8 L boiling water. The black powder was then rinsed with 18 MΩ H_2O by centrifugation. This rinsing step was repeated until Cl^- could no longer be detected by the addition of Ag^+ to the supernatant. The product was then dried in air at 40°C for 24 hours.

The sample was characterized by powder x-ray diffraction (XRD) on a Scintag Diffractometer (Cu-Kα radiation, λ = 1.54176 nm) at a scanning rate of 0.1 2θ/min at a power of 15 kW over the range 10-90°. The resulting pattern (Figure 2.1) showed the product to be pure magnetite in agreement with JCPDS card number 00-001-1111. Using

the full peak width at half the maximum intensity and the Scherrer formula, the average crystallite diameter was calculated to be 13.0 nm.

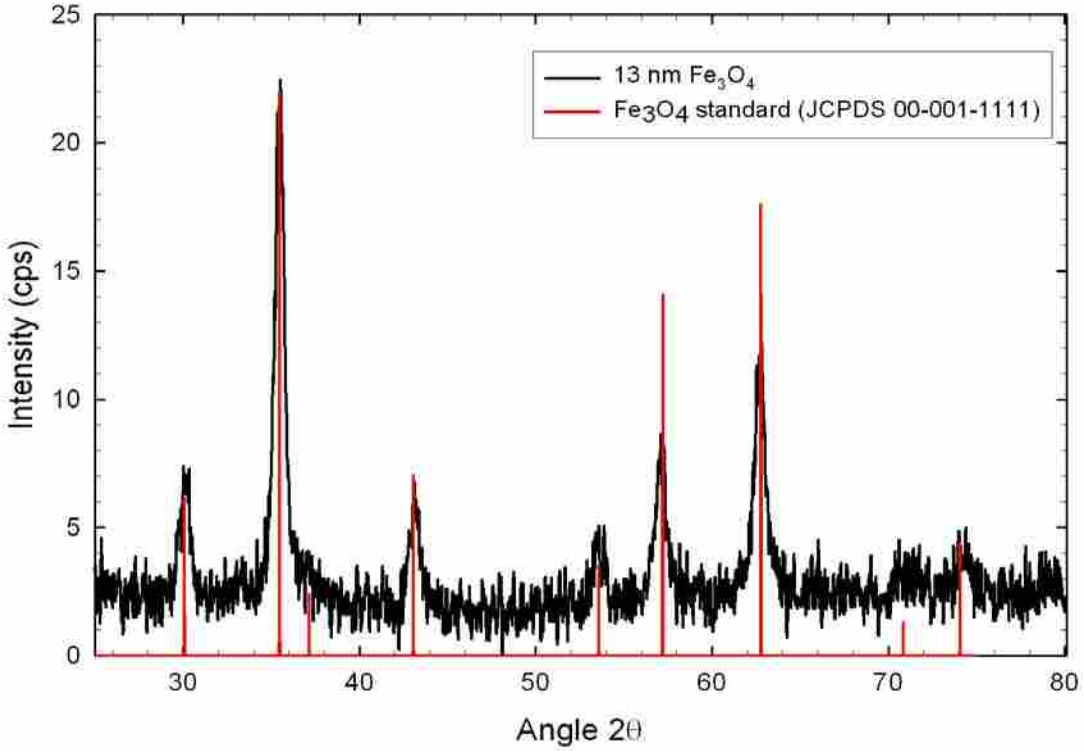

Figure 2.1. Powder X-ray Diffraction spectrum of magnetite powder.

A specimen was prepared for transmission electron microscopy (TEM) by dispersing a small amount of the powder in ethanol and grinding with an agate mortar and pestle. The mixture was allowed to rest for 24 hours in a glass test tube before drawing off the supernatant. A drop of this suspension was then placed on a copper grid with 3 nm carbon backing and microscopy images were acquired using a Tecnai F30 TEM. Micrographs of the magnetite powder can be seen in Figure 2.2. These images reveal spherical particles in the range of 9-15 nm which is consistent with the results given by XRD. Also, ordered atomic planes can be observed in some of the particles indicating that the sample has good crystal quality.

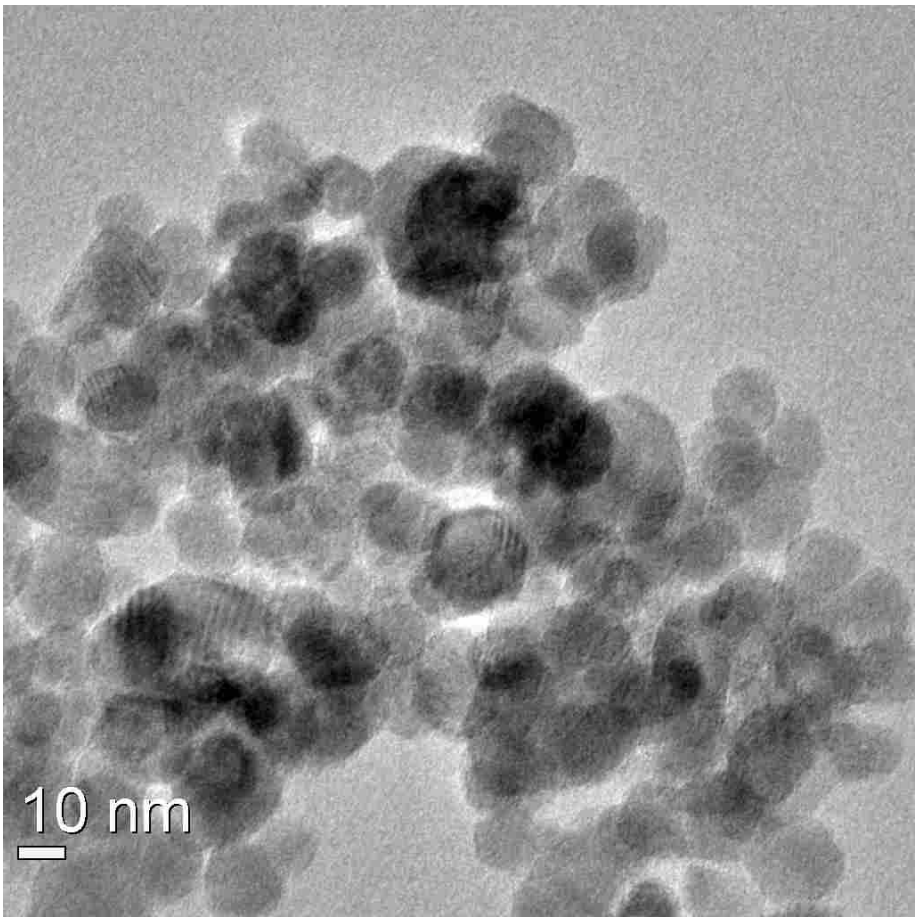

Figure 2.2. Transmission Electron Micrograph of magnetite powder at 115 kX magnification.

Analysis of chemical impurities was performed using a Perkin-Elmer inductively coupled plasma optical emission spectrometer (ICP-OES) Optima 4300 DV. A sample solution for ICP was prepared by dissolving 246.1 mg of the magnetite powder in 100 mL of 5% HNO_3. Qualitative analysis of this sample revealed the presence of Na, Ca, Cr, K, and Zn. Quantitative analysis using standard concentrations of these species showed the total impurities to be less than 0.025% of the sample mass making the sample 99.975% pure on a metals basis. An analysis of carbon, nitrogen, and hydrogen by combustion at Galbraith Laboratories showed no nitrogen residue from the NH_4OH while there was a 0.75% carbon content and 0.60% hydrogen impurity. Although no carbon compounds were used in the synthesis of the magnetite powder studies have shown that magnetite can readily absorb carbon dioxide and that nanoparticles in general have water on the surface.[59-63]

Thermal gravimetric analysis (TGA) of the sample was carried out in corundum crucibles using a Netzsch 409 TGA/DSC system. The sample was heated at a rate of 7.0 K/min up to 1000°C in He(g) resulting in a 5.41% mass loss. Assuming all the mass lost to be water this equates to a percent mass of hydrogen to be 0.605% which agrees well with the Galbraith results of 0.60%. Using the value of water from TGA the chemical formula of the magnetite powder is given as $Fe_3O_4 \cdot 0.735H_2O$ and a molecular weight of M = 244.78 g/mol.

The sample was prepared for adiabatic calorimetry by compressing the powder into pellets of 3/8" diameter which were then broken and placed in the calorimetric vessel described by Stevens and Boerio-Goates.[64] This container was evacuated and refilled with 0.335 mmoles of dry He(g). The calorimeter was then sealed by pressing a 0.7620 g gold gasket against a stainless steel knife edge located at the top of the vessel. Heat capacity measurements were made on this system over the temperature range 50 to 350 K.

The heat capacity of this sample was measured in the temperature range 0.5 to 38 K using a semi-adiabatic calorimeter described by Lashley *et al.*[65] This was done using a 0.2116 g sample wrapped in a 0.0683 g copper foil to provide greater thermal conductivity. A second sample of 0.2142 g with 0.1012 g Cu was measured in the temperature range 0.5 to 60 K. For both samples the copper and magnetite were compressed into a pellet of 3/8" diameter and 1/8" thickness which was then attached to the sample platform of the apparatus using Apiezon N grease. The contributions of the copper, grease, and addenda were subtracted to obtain the molar heat capacity of nanocrystalline magnetite.

2.3 Results

The heat capacity results of 13 nm magnetite using the formula $Fe_3O_4 \cdot 0.735H_2O$ are shown in Tables 2.1-2.3 where each table represents the different measurements. In these tables no correction has been made at this point for the water adsorbed onto the surface of nanocrystalline magnetite. The first measurements of the heat capacity of 13 nm magnetite were obtained semi-adiabatically, and these results can be found in Table 2.1. This sample (Load 1) was quickly cooled from 273 to 77 K under an atmosphere of

0.8 Torr of N_2(g). At 77 K the N_2(g) was evacuated and the sample was cooled to liquid helium temperatures. As the adiabatic measurements (Table 2.2) were

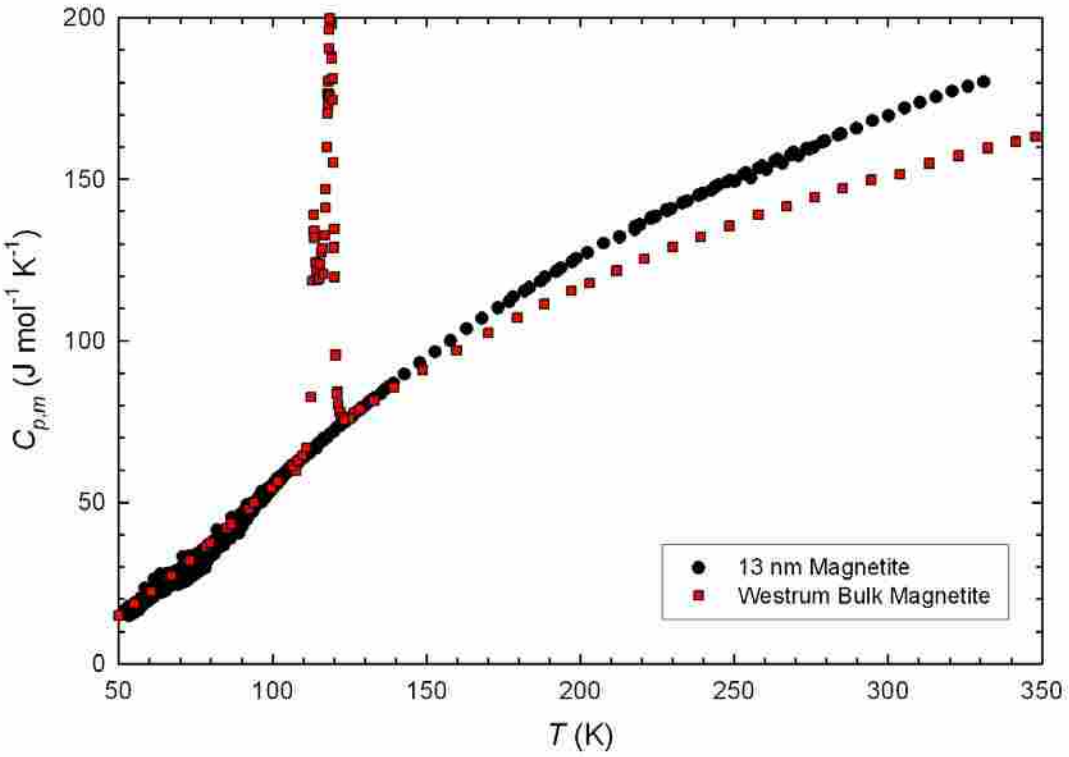

Figure 2.3. Plot of adiabatic measurements of nanocrystalline magnetite heat capacity with a comparison to bulk measurements by Westrum[1, 2]

obtained, it was realized that the cooling rate and time had an effect on the heat capacity of the sample, and a second set of semi-adiabatic measurements were made. Table 2.3 contains the results for the second sample used in semi-adiabatic measurements (Load 2) which was cooled from room temperature to liquid helium temperatures over a period of 72 hours under a vacuum of 0.1 mTorr.

A graph of the heat capacity of 13 nm magnetite can be seen with a comparison to measurements of bulk magnetite by Westrum[1] in Figure 2.3. An inspection of the heat capacity of 13 nm magnetite shows no anomaly for the Verwey transition, which can be seen as a tall anomaly in Westrum's measurements. Above T_v, the heat capacity of 13 nm magnetite is significantly larger than that of the bulk while below the transition the two sets of measurements appear to converge on the scale shown in the figure.

The heat capacity of 13 nm magnetite is shown below 10 K for Loads 1 and 2 in

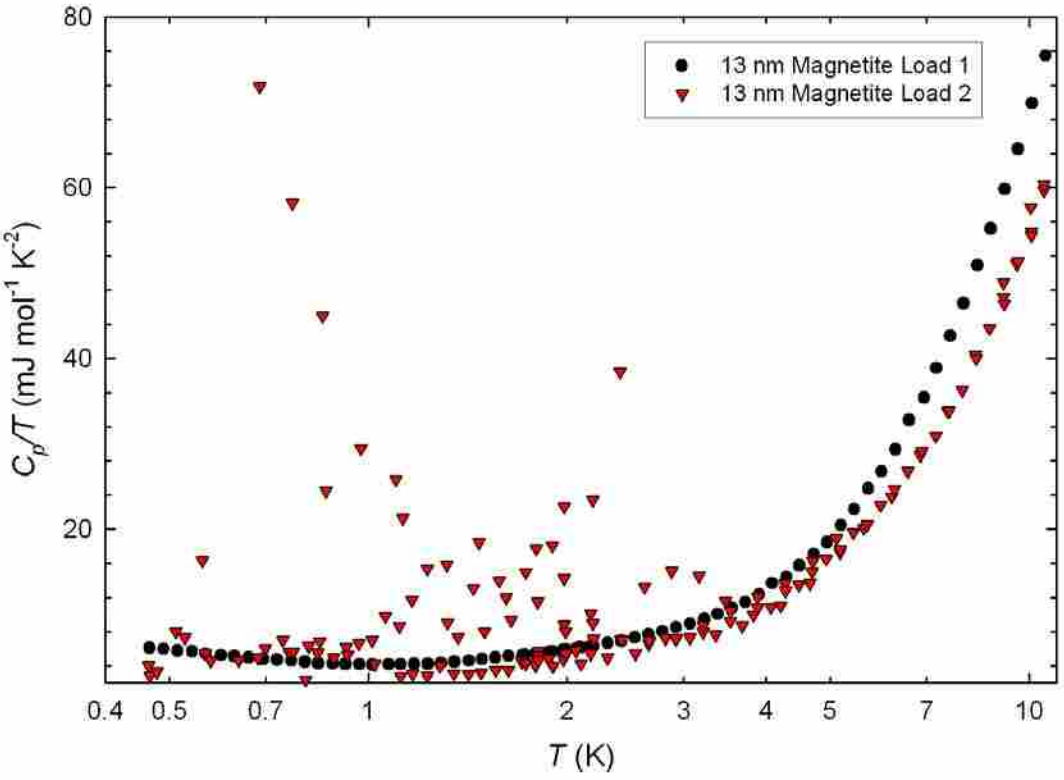

Figure 2.4. Low-temperature heat capacity of 13 nm magnetite. Two sets of measurement are represented and temperature is on a log-scale. Black circles are the quickly cooled sample and red inverted triangles represent the slow-cooled sample.

Figure 4. An upturn can be seen below 1 K in the heat capacity measurements of Load 1,

which shows good reproducibility. Conversely, Load 2 shows irreproducible anomalous behavior below 4 K while above 4 K Load 2 has better precision. The heat capacity of Load 1 is generally higher than that of Load 2, which confirms the importance of cooling rate and time.

Another interesting observation in the heat capacity of 13 nm magnetite can be seen in Figure 2.5 which shows the region of overlap between Load 2 and the adiabatic measurements. It can be seen that the heat capacity of Load 2 exceeds that of the adiabatic measurements by at least 7 $J \cdot mol^{-1} \cdot K^{-1}$, and this lack of overlap makes it difficult to calculate the standard molar entropy of 13 nm $Fe_3O_4.0.735\ H_2O$. Also, the adiabatic measurements in this region show low precision between each cooling of the sample,

with the data converging above 90 K. The significance of these observations is discussed below.

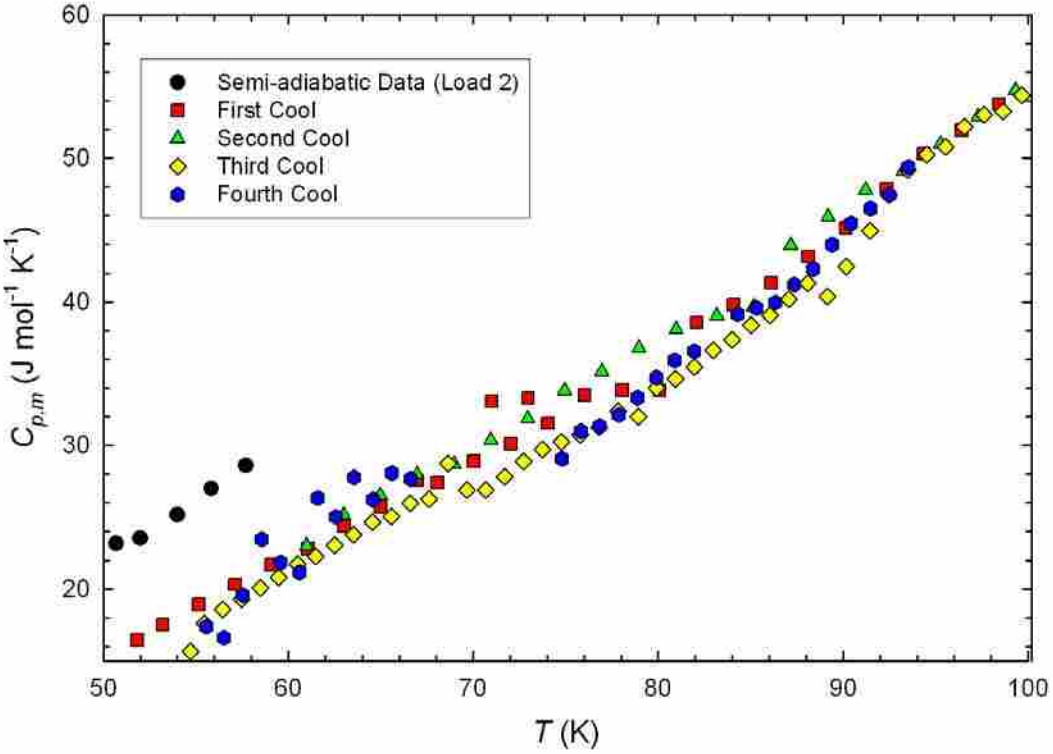

Figure 2.5. The region of overlap between the heat capacity of 13 nm magnetite measured semi-adiabatically (Load 2) and adiabatically.

Table 2.1. Molar heat capacity of 13 nm magnetite ($Fe_3O_4 \cdot 0.735H_2O$) from semi-adiabatic measurements Load 1 . M = 244.78 g/mol

T*/K	$C_{p,m}$ mJ·K^{-1}·mol^{-1}	ΔT/K	T*/K	$C_{p,m}$ mJ·K^{-1}·mol^{-1}	ΔT/K	T*/K	$C_{p,m}$ mJ·K^{-1}·mol^{-1}	ΔT/K
	Series 1		1.797	9.605	0.176	7.602	324.23	0.723
1.729	8.862	0.164	1.979	11.253	0.190	8.359	425.49	0.792
1.903	10.98	0.184	2.176	13.005	0.211	9.192	549.98	0.873
2.092	12.88	0.205		*Series 3*		10.110	706.75	0.966
2.304	15.40	0.221	9.194	561.63	0.882		*Series 5*	
2.533	18.57	0.246	10.111	719.52	0.975	0.494	2.786	0.042
2.789	22.38	0.276	11.124	918.62	1.071	0.661	3.419	0.074
3.070	27.35	0.298	12.236	1157.89	1.167	0.729	3.286	0.076
3.379	34.05	0.326	13.447	1434.65	1.287	0.804	3.546	0.079
3.720	42.57	0.351	14.797	1786.63	1.413	0.884	3.770	0.090

4.089	55.91	0.392	16.281	2200.29	1.556	0.972	4.050	0.100
4.497	70.91	0.428	17.911	2696.66	1.706	1.074	4.493	0.113
4.945	91.29	0.473	19.700	3296.90	1.879	1.177	4.964	0.114
5.440	121.44	0.516	21.669	4008.67	2.063	1.292	5.739	0.123
5.983	160.05	0.571	23.836	4889.67	2.274	1.422	6.586	0.136
6.585	215.86	0.618	26.207	5947.93	2.475	1.559	7.479	0.149
7.237	281.30	0.693	28.814	7229.91	2.740	1.715	8.836	0.167
7.960	369.80	0.751	31.695	8815.54	3.020	1.885	10.63	0.187
8.753	483.22	0.834	34.861	10891.14	3.313	2.071	12.55	0.210
9.631	621.56	0.922	37.682	12779.22	2.334		*Series 6*	
10.594	799.33	1.004		*Series 4*		9.651	632.24	0.920
	Series 2		1.816	9.459	0.174	10.615	807.51	1.013
0.471	2.679	0.042	1.998	11.273	0.196	11.677	1027.53	1.121
0.518	3.060	0.051	2.199	13.562	0.218	12.838	1283.22	1.217
0.570	3.220	0.060	2.420	16.386	0.238	14.119	1599.41	1.359
0.629	3.307	0.063	2.662	19.833	0.261	15.538	1980.07	1.488
0.694	3.322	0.072	2.932	24.443	0.285	17.093	2427.85	1.624
0.766	3.396	0.081	3.225	30.616	0.318	18.805	2975.11	1.799
0.841	3.854	0.089	3.550	38.127	0.349	20.688	3618.32	1.966
0.926	4.032	0.098	3.905	48.249	0.377	22.757	4419.60	2.172
1.017	4.360	0.106	4.294	61.898	0.410	25.024	5367.16	2.367
1.120	4.885	0.111	4.722	80.510	0.452	27.510	6572.23	2.605
1.233	5.387	0.116	5.192	106.18	0.492	30.246	8033.44	2.876
1.353	6.191	0.128	5.710	141.40	0.548	33.266	9841.57	3.184
1.485	7.122	0.141	6.278	184.12	0.593	36.270	11924.74	2.845
1.633	8.253	0.162	6.940	245.51	0.603			

Table 2.2. Molar heat capacity data for 13 nm magnetite ($Fe_3O_4 \cdot 0.735H_2O$) from adiabatic measurements. M = 244.78 g/mol.

T*/K	$C_{p,m}$ J·K^{-1}·mol^{-1}	ΔT/K	T*/K	$C_{p,m}$ J·K^{-1}·mol^{-1}	ΔT/K	T*/K	$C_{p,m}$ J·K^{-1}·mol^{-1}	ΔT/K
	Series 1		59.080	20.508	1.975	73.729	28.129	1.0120
82.069	39.078	4.627	61.049	21.586	1.985	74.744	28.636	1.0144
86.810	42.762	4.850	63.016	23.055	1.979	75.761	29.074	1.0202
91.675	46.549	4.879	64.993	24.347	1.994	76.785	29.575	1.0247
96.569	50.425	4.907	66.980	26.063	2.000	77.810	30.620	1.0183
101.491	54.278	4.934	70.995	31.285	1.960		*Series 20*	
106.437	58.117	4.956	72.963	31.486	2.000	78.909	30.253	1.017
111.404	61.856	4.976		*Series 11*		79.918	32.141	0.993
116.389	65.734	4.992	68.049	25.925	2.002	80.925	32.756	1.021
121.391	69.439	5.009	70.032	27.314	1.982	81.945	33.530	1.021
126.407	73.103	5.021	72.026	28.474	2.029	82.969	34.624	1.026

131.436	76.715	5.034	74.033	29.832	2.000	83.992	35.326	1.023
136.478	80.264	5.046	76.030	31.712	2.023	85.016	36.289	1.028
	Series 2		78.047	32.024	2.032	86.042	36.962	1.025
274.34	150.70	5.288	80.076	31.997	2.055	87.065	38.020	1.022
279.56	153.00	5.152	82.077	36.453	1.967	88.090	39.061	1.031
284.71	155.16	5.156	84.074	37.622	2.036	89.128	38.183	1.042
289.87	156.83	5.167	86.100	39.084	2.031	90.151	40.176	1.006
295.03	158.97	5.156	88.122	40.824	2.035		*Series 21*	
300.19	160.52	5.167	90.141	42.705	2.021	91.462	42.533	1.000
305.35	162.74	5.162		*Series 12*		92.461	44.852	1.020
310.52	164.42	5.168	92.350	45.300	2.038	93.483	46.500	1.030
315.68	165.95	5.168	94.372	47.560	2.005	94.516	47.534	1.030
320.85	167.60	5.172	96.394	49.129	2.030	95.545	48.049	1.025
326.02	169.10	5.170	98.428	50.840	2.031	96.574	49.358	1.029
331.19	170.36	5.174	100.457	52.919	2.028	97.604	50.132	1.022
	Series 3		102.492	54.626	2.034	98.627	50.380	1.026
176.87	106.09	5.143	104.529	56.558	2.032	99.654	51.431	1.028
181.99	109.09	5.102	106.567	58.116	2.035	100.685	52.491	1.030
187.10	112.00	5.109	108.607	59.623	2.042	101.714	52.894	1.029
192.21	114.84	5.115	110.648	61.314	2.039	102.741	54.134	1.026
197.33	117.64	5.119	112.691	62.765	2.044		*Series 22*	
202.45	120.38	5.124	114.736	64.344	2.044	55.564	16.442	0.982
207.57	123.10	5.125		*Series 13*		56.530	15.706	1.009
212.71	124.76	5.146	116.785	65.906	2.043	57.548	18.505	1.029
217.85	127.00	5.134	118.832	67.388	2.050	58.546	22.201	0.969
222.97	130.63	5.117	120.881	68.945	2.047	59.583	20.659	1.074
228.10	132.77	5.141	122.930	70.474	2.050	60.609	20.017	0.983
233.24	134.83	5.147	124.980	71.866	2.049	61.584	24.912	0.971
	Series 4		127.031	73.517	2.053	62.557	23.670	1.037
219.38	128.61	5.102	129.083	74.921	2.051	63.556	26.267	1.028
224.50	131.04	5.139	131.135	76.370	2.053	64.587	24.799	1.056
229.64	133.26	5.141	133.190	77.874	2.054	65.603	26.550	1.033
234.78	135.50	5.143	135.245	79.088	2.057	66.629	26.167	1.053
239.92	137.68	5.147	137.300	80.851	2.053		*Series 23*	
245.06	140.10	5.144	139.355	82.187	2.057	74.793	27.503	1.041
250.22	141.24	5.168		*Series 14*		75.821	29.320	1.017
255.40	142.29	5.167	142.851	84.663	4.849	76.845	29.640	1.037
260.57	144.59	5.129	147.806	88.055	5.062	77.867	30.397	1.009
265.72	146.55	5.141	152.876	91.383	5.076	78.882	31.520	1.022
270.87	148.86	5.134	157.954	94.662	5.081		*Series 24*	
276.02	151.23	5.137	163.037	98.025	5.085	79.905	32.835	1.004
	Series 5		168.130	101.045	5.102	80.908	33.984	1.002
242.64	138.55	5.224	173.230	104.152	5.097	81.936	34.568	1.048
247.82	141.04	5.133	178.330	107.363	5.104		*Series 25*	
252.95	143.26	5.150	183.437	110.113	5.113	84.300	37.025	0.994
258.10	145.17	5.151	188.551	113.163	5.115	85.316	37.423	1.030
263.25	147.15	5.154	193.667	115.789	5.119	86.350	37.788	1.028
268.41	149.04	5.162	198.788	118.672	5.121	87.368	38.967	1.006

273.57	150.82	5.161		*Series 15*		88.382	39.989	1.024
278.72	152.69	5.160	60.986	21.750	1.992	89.409	41.598	1.029
283.88	154.67	5.164	62.978	23.778	1.992	90.442	42.987	1.027
	Series 6		64.973	25.074	1.992	91.474	43.974	1.016
212.78	125.14	5.141	66.964	26.439	1.983	92.500	44.891	1.010
217.91	128.00	5.116	68.956	27.166	1.996	93.524	46.713	1.012
223.03	130.35	5.138	70.952	28.726	1.989		*Series 26*	
228.17	132.67	5.138	72.943	30.114	1.993	53.311	13.984	0.923
233.31	134.87	5.141	74.940	31.998	2.000	54.281	14.647	1.014
238.45	137.12	5.144	76.942	33.219	2.005	55.288	15.238	0.998
243.59	139.34	5.147	78.954	34.761	2.015	56.289	15.700	1.006
248.74	141.48	5.148	80.971	36.005	2.013	57.283	16.893	0.992
253.88	143.62	5.150		*Series 16*		58.293	17.431	1.027
259.03	145.68	5.155	83.165	36.904	1.960	59.312	18.105	1.010
264.18	147.79	5.154	85.157	37.484	2.023	60.320	18.980	1.006
269.34	149.80	5.161	87.163	41.534	1.988	61.330	19.504	1.014
	Series 7		89.174	43.440	2.022	62.340	20.269	1.006
95.850	49.073	1.873	91.206	45.169	2.017	63.349	20.924	1.014
97.809	50.617	2.113	93.238	46.408	2.018	64.370	21.026	1.025
99.897	52.003	2.070	95.256	48.230	2.011		*Series 27*	
101.948	53.729	2.040	97.278	50.024	2.029	65.415	21.640	1.034
103.983	55.309	2.040	99.312	51.760	2.030	66.431	22.804	0.999
106.020	56.836	2.045	101.343	53.638	2.029	67.441	22.932	1.022
108.059	58.605	2.048	103.379	55.385	2.037	68.456	24.290	1.011
110.102	60.303	2.045	105.423	57.046	2.036	69.483	23.229	1.039
112.149	61.829	2.054		*Series 17*		70.535	23.681	1.028
114.200	63.020	2.047	107.602	58.497	2.041	71.543	24.601	0.986
116.240	65.149	2.037	109.639	60.344	2.030	72.555	24.382	1.030
	Series 8		111.677	61.856	2.041	73.579	25.459	1.017
88.411	42.378	1.301	113.722	63.317	2.044	74.595	26.015	1.014
90.076	44.044	2.038	115.767	64.982	2.045	75.614	26.746	1.022
92.101	46.061	2.031	117.813	66.396	2.044	76.639	27.298	1.026
94.130	47.421	2.037	119.860	68.013	2.049		*Series 28*	
96.158	49.246	2.035	121.910	69.560	2.049	78.128	28.175	1.012
98.190	50.930	2.040	123.961	71.025	2.052	79.132	30.453	0.998
100.226	52.496	2.041	126.013	72.570	2.049	80.133	31.566	1.007
102.262	54.135	2.043	128.063	74.018	2.052	81.154	32.110	1.034
104.300	55.624	2.045	130.116	75.503	2.052	82.177	33.804	1.013
106.339	57.200	2.047		*Series 18*		83.206	34.322	1.030
108.381	58.709	2.050	54.700	14.810	0.534	84.232	34.793	1.013
110.423	60.506	2.050	55.458	16.647	0.983	85.251	36.344	1.022
	Series 9		56.451	17.551	1.003	86.281	36.767	1.028
91.157	44.658	2.042	57.458	18.265	1.007	87.300	38.870	1.010
93.178	47.010	2.023	58.469	18.997	1.011	88.323	40.022	1.024
95.211	48.001	2.051	59.476	19.677	1.000	89.354	42.149	1.013
97.242	49.977	2.032	60.481	20.556	1.009	90.396	40.977	1.028
99.269	51.941	2.037	61.493	21.061	1.013		*Series 29*	
101.307	53.324	2.044	62.507	21.813	1.013	91.474	42.034	1.015

103.348	54.906	2.047	63.520	22.485	1.012	92.488	43.715	1.014
105.391	56.335	2.047	64.534	23.338	1.014	93.510	44.486	1.028
107.430	58.248	2.040	65.549	23.685	1.015	94.535	46.022	1.023
109.467	60.051	2.040		*Series 19*		95.559	46.824	1.027
111.507	61.465	2.046	66.583	24.567	1.011	96.589	47.256	1.032
113.551	62.984	2.051	67.592	24.850	1.019	97.626	48.512	1.039
	Series 10		68.610	27.202	1.011	98.652	49.832	1.014
51.827	15.547	0.816	69.646	25.419	1.038	99.673	50.801	1.026
53.212	16.564	1.970	70.679	25.440	1.013	100.699	51.908	1.026
55.163	17.909	1.956	71.694	26.314	1.011	101.727	52.793	1.028
57.117	19.195	1.973	72.712	27.336	1.017	102.757	53.682	1.029

Table 2.3. Molar heat capacity of 13 nm magnetite ($Fe_3O_4 \cdot 0.735H_2O$) semi-adiabatic measurements Load 2. M = 244.78 g/mol

T*/K	$C_{p,m}$ mJ·K^{-1}·mol^{-1}	ΔT/K	T*/K	$C_{p,m}$ mJ·K^{-1}·mol^{-1}	ΔT/K	T*/K	$C_{p,m}$ mJ·K^{-1}·mol^{-1}	ΔT/K
	Series 1		24.949	4968.39	2.329	3.8837	41.856	0.3618
1.7316	7.3940	0.1777	27.353	6094.67	2.727	4.2760	54.740	0.4015
1.9027	7.5371	0.1800	30.075	7245.63	2.981	4.6987	70.598	0.4566
2.0958	8.8880	0.1916	33.184	9364.65	3.071	5.1711	89.306	0.4949
2.3031	11.3150	0.1985	36.049	11337.83	2.984		*Series 9*	
2.5344	13.7469	0.2148		*Series 5*		37.0281	11952.59	2.1177
2.8130	20.2820	0.2930	1.8086	10.322	0.1674	39.1394	13320.26	1.9956
3.0675	22.4133	0.2883	1.9788	17.413	0.1968	40.6704	14717.95	2.7408
3.3546	25.5849	0.2737	2.1688	21.981	0.2312	42.9966	16543.13	2.0763
3.6835	31.9572	0.2971	2.4025	92.371	0.3114	44.9785	17795.30	2.1081
4.0672	44.2142	0.3583	2.6165	34.648	0.3017	47.0495	19970.55	1.9783
4.4772	60.3806	0.4196	2.8767	43.335	0.3345	48.9742	21543.71	2.0605
4.9265	81.2801	0.4638	3.1651	45.885	0.3706	50.6917	23176.77	2.0482
5.4176	106.3397	0.5173	3.4721	40.236	0.3783		*Series 10*	
5.9626	135.8880	0.5709	3.8238	38.070	0.3877	52.0000	24266.78	2.1529
6.5584	175.7331	0.6347	4.2123	46.382	0.4021	53.9876	25942.36	2.1073
7.2156	223.0314	0.6957	4.6578	63.667	0.4612	55.8255	27809.22	2.4519
7.9319	287.7991	0.7514	5.1127	96.674	0.5703	57.6984	29462.74	2.6889
8.7225	379.5274	0.8368	5.6166	113.042	0.5966		*Series 11*	
9.5923	489.8604	0.9335	6.2003	147.395	0.6216	0.4672	1.3285	0.0470
10.5432	629.0351	1.0185	6.8404	195.978	0.6672	0.5142	0.3122	0.0422
	Series 2		7.5368	255.301	0.7350	0.5665	3.0944	0.0482
9.1607	425.025	0.8900	8.3047	335.245	0.8046	0.6724	0.8864	0.0546
10.0712	552.118	1.0010	9.1456	431.531	0.8905	0.6724	0.8864	0.0546
11.0660	722.831	1.1163	10.0729	548.012	0.9705	0.7413	5.2062	0.0670

12.1718	919.843	1.2056		*Series 6*		0.8114	5.1158	0.0748
13.3980	1179.72	1.2872	0.4685	0.2534	0.0440	0.8858	4.3816	0.0736
14.7181	1590.69	1.4361	0.5163	0.5646	0.0495	0.9678	6.4291	0.0845
16.2065	1798.46	1.5784	0.5685	0.9001	0.0551	1.0612	10.4057	0.0963
17.8427	2356.33	1.6920	0.6263	1.2253	0.0598	1.1626	13.5789	0.1047
19.6185	2901.49	1.8850	0.6817	3.3699	0.0900	1.3193	11.9819	0.1215
21.5730	3642.38	2.0794	0.7581	4.2500	0.0992	1.4434	18.8669	0.1263
23.7126	4328.99	2.3048	0.8379	4.5968	0.0882	1.5789	22.0379	0.1450
26.0822	5325.37	2.4871	0.9301	4.9009	0.1106	1.7315	25.8900	0.1616
28.6853	6628.17	2.7234	1.0240	4.2867	0.1102	1.9005	34.3093	0.1772
31.5444	8527.86	3.0083	1.1207	3.1045	0.1027		*Series 12*	
34.6762	10248.02	3.3758	1.2284	3.4416	0.1078	0.4647	1.860	0.0484
37.5267	12087.54	2.3517	1.3469	4.1247	0.1266	0.5117	4.093	0.0452
	Series 3		1.4819	4.7177	0.1424	0.5606	9.153	0.0645
1.8095	9.3427	0.1710	1.6291	5.6918	0.1541	0.6848	49.187	0.0615
1.9873	15.8824	0.1876	1.7919	7.2253	0.1701	0.7670	44.657	0.0713
2.1887	19.6373	0.2319	1.9721	9.3463	0.1887	0.8516	38.297	0.0760
2.4213	16.9279	0.2312	2.1703	11.7594	0.2082	0.8621	21.115	0.0844
2.6611	18.3673	0.2499		*Series 7*		0.9753	28.687	0.0925
2.9245	21.0518	0.2721	0.4908	0.4544	0.0497	1.1016	28.477	0.1038
3.2133	28.0864	0.2970	0.5415	0.4382	0.0557	1.1278	23.995	0.1093
3.5324	36.8082	0.3425	0.5993	0.3367	0.0531	1.3146	20.756	0.1248
3.8857	46.8648	0.3741	0.6600	0.4755	0.0532	1.4718	27.131	0.1428
4.2750	58.2162	0.4124	0.7269	0.7498	0.0660	1.6179	19.375	0.1444
4.7042	76.3136	0.4482	0.8042	1.8961	0.0735	1.7938	31.835	0.1638
5.1739	91.1241	0.4908	0.8763	0.8185	0.0706	1.9777	44.743	0.1765
5.6898	116.950	0.5385	0.9646	1.3602	0.0770	2.1843	51.170	0.1965
6.2577	154.498	0.5956	1.0551	2.0742	0.0990		*Series 13*	
6.8821	200.308	0.6569	1.1659	3.5379	0.1081	0.4784	1.575	0.0484
7.5679	255.852	0.7232	1.2819	5.1156	0.1238	0.5274	3.841	0.0452
8.3238	332.816	0.7912	1.4184	4.2557	0.1289	0.5778	2.648	0.0645
9.1523	447.486	0.8687	1.5579	5.4584	0.1362	0.6369	2.959	0.0615
10.0666	580.303	0.9663	1.7075	7.7064	0.1591	0.6987	4.204	0.0713
	Series 4		1.8775	8.8993	0.1822	0.7688	4.329	0.0760
9.6227	493.946	0.9201	2.0643	11.8333	0.2002	0.8440	5.799	0.0844
10.5469	636.424	1.0829		*Series 8*		0.9267	5.748	0.0925
11.5713	834.318	1.2861	1.8102	8.4550	0.1716	1.0144	7.051	0.1038
12.7157	1079.831	1.4122	1.9904	10.7277	0.1912	1.1139	9.583	0.1093
13.9645	1395.634	1.4702	2.1919	15.6135	0.2138	1.2291	18.894	0.1248
15.6066	1809.137	1.2638	2.4119	17.1526	0.2281	1.3658	10.034	0.1428
16.9926	2246.445	1.7136	2.6563	17.4271	0.2474	1.5006	11.993	0.1444
18.7508	2718.666	1.8024	2.9221	20.7730	0.2742	1.6448	15.367	0.1638
20.5424	3228.366	2.1206	3.2125	25.5018	0.3096	1.8051	20.687	0.1765
22.6750	3896.170	2.1574	3.5363	32.5759	0.3393	1.9804	28.225	0.1965

2.4 Discussion

2.4.1 The Verwey Transition

As seen in Figure 2.3, the Verwey transition does not appear as a sharp peak in the heat capacity of 13 nm magnetite. However, there is evidence that the sample undergoes a transition at lower temperatures. This can be seen in the heat capacity of 13 nm magnetite in the region 50 to 100 K where the data is irreproducible among the several series. A careful inspection of this region shows that the data can be divided into four groups according to the thermal history of the sample. These groups are separated by successive coolings of the sample and are respectively series 10-12 (First Cool), 15-17 (Second Cool), 18-21 (Third Cool), and 22-25 (Fourth Cool). As seen in Figure 2.6 there is good agreement among series in the same group which suggests that the heat capacity in this region is dependent on cooling rate and time. Above 90 K these four groups show good agreement, and it can be concluded that, if there is a transition, it begins below this temperature.

The data collection process provides some evidence of a transition. The time required to reach thermal equilibrium after a pulse of heat was unusually large in the range of 50 to 100 K, and Figure 2.7 shows how this time changed with temperature. One key feature of this graph is that the equilibrium time quickly decreases after the broad maximum between 80 -90 K. Typically, long equilibrium times are associated with heat capacity anomalies, and these long equilibrium times also suggest that the sample has a low thermal conductivity in this region.

The irreproducible region from 50 to 90 K is not necessarily associated with the Verwey transition, yet it does suggest the onset of some physical phenomena not present at higher temperatures. It is important to note that the 13 nm magnetite sample used in these studies was extensively characterized and found to be chemically pure (except for adsorbed water impurity), phase pure, and highly crystalline. While it is not certain that this anomalous behavior is related to the Verwey transition, it is observed that the heat capacity of 13 nm magnetite does not have the anomaly at T_v seen in the heat capacity of bulk magnetite.[19, 20, 28, 66] In spite of this uncertainty it can be concluded that crystal size

is an important factor as it is the only variable that has significantly changed between this study and other studies of pure magnetite.

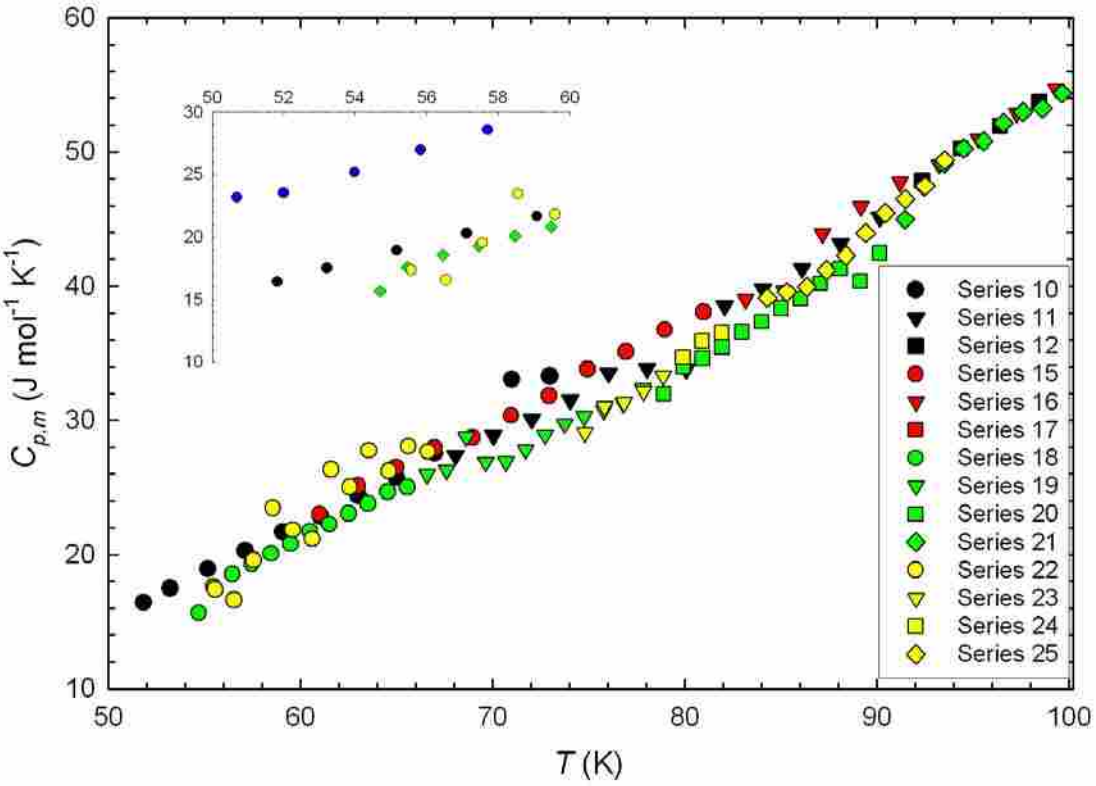

Figure 2.6. Heat capacity of 13 nm magnetite in the region characterized by unusually long equilibrium times. The inset shows the region of overlap between Load 2 (blue circles) and adiabatic measurements. Each color represents a different cooling of the sample.

The Verwey transition is associated with a structural change, and a natural energy barrier exists for this change.[4] If the system is cooled too quickly, there may not be enough thermal energy available to complete the structural transition, and consequently the sample gets "locked" into the higher temperature phase. To find the temperature of this structural change, the rate of cooling was measured with the calorimeter isolated from the surroundings. This data was then inspected for a break or discontinuity in the curve. Figure 2.8 displays the cooling rate of 13 nm magnetite which shows a continuous decrease. The lack of discontinuity in this curve indicates that there is no exact transition temperature. This phenomenon could stem from two possibilities: (1.) No structural transition is occurring or (2.) The structural transition occurs over a wide temperature range. Because long equilibrium times are associated with heat capacity anomalies it is more probable that the structural transition is occurring over a wide temperature range.

Temperature-dependent XRD measurements of nanocrystalline magnetite will be needed to provide more information on the origin of its low-temperature behavior.

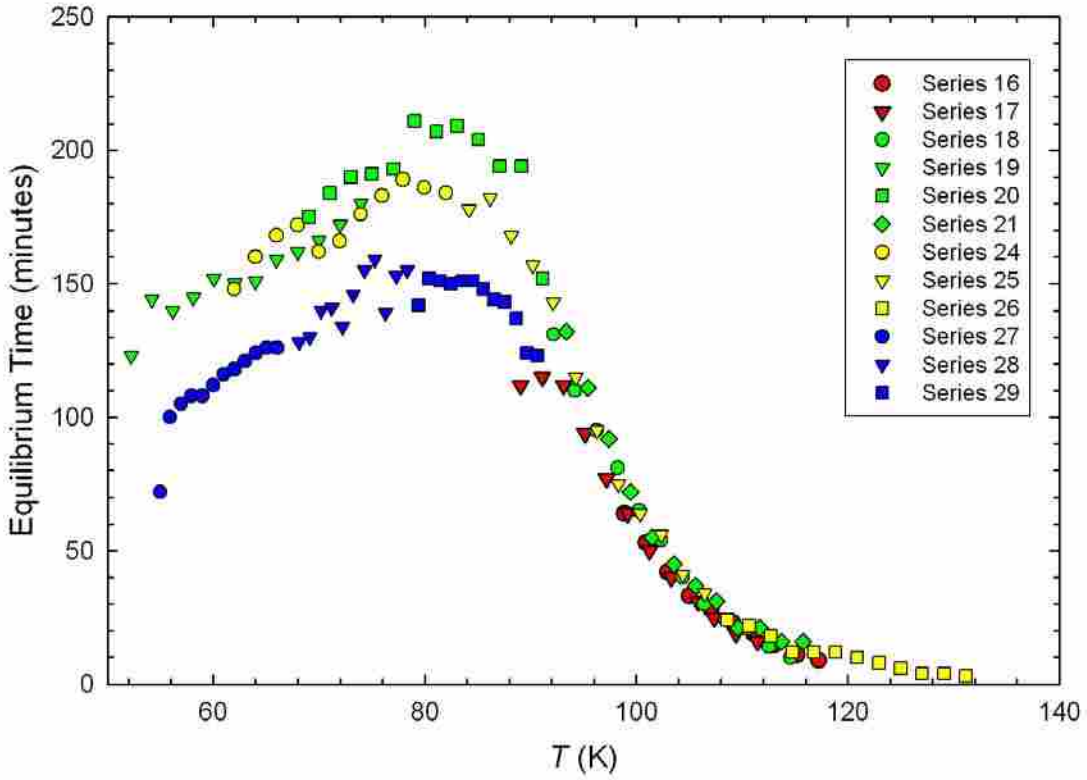

Figure 2.7. The temperature dependence of time required to reach thermal equilibrium during the measurement of the heat capacity of 13 nm magnetite. Each color represents a different cooling of the sample.

As seen in the inset of Figure 2.6 the higher temperature portion of Load 2 data is significantly larger than that measured adiabatically. Once again, this is attributed to the variation in cooling rate and thermal history. This discontinuity and the irreproducibility in the anomalous region from 50-100 K make it difficult to calculate the standard entropy and thermodynamic values for nanocrystalline magnetite. In spite of this setback, this data is insightful in that it reveals that crystal size is an important factor in the Verwey transition, and heat capacity studies of the Verwey transition as a function of particle size could provide valuable insight into its mechanism.

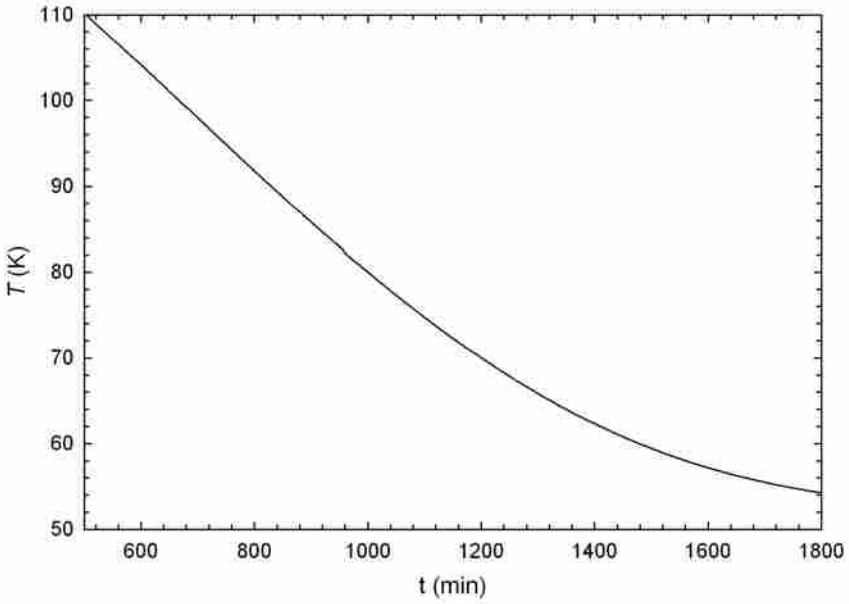

Figure 2.8. Plot of temperature vs. time as the sample was cooled. No discontinuity is observed.

2.4.2 Heat Capacity of 13 nm Magnetite Below 15 K

At temperatures below 15 K the heat capacity is amenable to theoretical modeling which can provide valuable insight into the physical properties of solids.[34] Before a discussion can be given of the various physical properties of 13 nm magnetite, it will be necessary to fit its heat capacity to theoretical functions. The total molar heat capacity can be viewed as a sum of the contributions from each of the modes of energy associated with the physical properties of a sample. A brief review of some of these contributing phenomena is given below.

For temperatures below 40 K, the vibrational motion of the atoms in a crystalline solid can be represented by the harmonic-lattice model,[34, 67] where $C_{Lat} = \sum B_n T^n$ with n = 3, 5, 7, 9, ... The lattice contribution to the heat capacity is generally much larger than other contributing phenomena at temperatures higher than 10 K, but below this temperature the lattice heat capacity is small enough that other contributions are more easily extracted. Magnetic ordering can be observed as spin waves[34] which show a $T^{3/2}$ dependence for ferro- and ferrimagnetism and T^3 for antiferromagnetism. If there is

anisotropy in an ordered ferro- or ferrimagnet the spin wave spectrum will have a gap, which is similar to the gap induced by a magnetic field.[55, 56] The heat capacity for the ferrimagnetic spin waves (C_{fsw}) for an $H = 0$ gap can be represented by

$$C_{fsw} = B_{fsw} T^{3/2} e^{-\Delta/T}$$

where B_{fsw} is a constant proportional to molar volume and the spin-wave stiffness constant, and Δ represents the spin-wave gap in units of Kelvin. Conduction electrons also contribute to the heat capacity with a linear dependence expressed as γT, yet a linear term has also been observed in nonstoichiometric oxide insulators.[54, 68, 69] In the case of nonstoichiometric insulators the linear term has been attributed to localized electronic states associated with oxygen vacancies.[69] As discussed previously, superparamagnetic contributions will also make a sizeable contribution to the linear term.[42, 43]

2.4.3 Fits of 13 nm Magnetite Load 1

The low-temperature heat capacity of 13 nm magnetite Load 1 is shown in Figure 2.4, which has an upturn below 1 K. To represent this upturn, a term of the form AT^{-2} was included in fitting 13 nm magnetite Load 1. Also, 13 nm magnetite is a crystalline solid and the lattice vibrations will be represented by $C_{Lat} = \sum B_n T^n$ as discussed previously. Because bulk magnetite is a ferrimagnet, some fits included a $T^{3/2}$ term to test whether this behavior persists on the nanoscale. However magnetite nanoparticles have shown anisotropic behavior,[51-53] and fits were also made using the spin gap term $C_{fsw} = B_{fsw} T^{3/2} e^{-\Delta/T}$. Many fits were made with and without the linear term γT, and it was found that those fits which did not use a linear term gave high RMS values or were not physically meaningful. Also, if nanocrystalline magnetite has spin-glass behavior as discussed previously, it can be fit using $C = \gamma T + B_2 T^2$, and fits were made including this expression as well. An extensive variety of fits were made using permutations of these different terms, but Table 2.4 only provides a summary of the best fits of the heat capacity of 13 nm magnetite Load 1. These fits follow the general formula:

$$C = \gamma T + \sum_{n=3,5,7} B_n T^n + B_{fsw} T^{3/2} e^{-\Delta/T} + B_2 T^2 \quad (1)$$

where setting any of the coefficients in this expression equal to zero results in the removal of the corresponding term. All fits were done in the temperature range 0.5 to 10 K.

Table 2.4. A summary of the fits of the heat capacity of nanocrystalline magnetite Load 1. Units are in mJ, K, and mole.

Parameters	Fit-1	Fit-2	Fit-3	Fit-4
γ	3.461(9)	4.119(7)	3.722(2)	3.313(4)2
B_3	0.586(6)	0.669(8)	0.702(4)	0.613(0)
B_5	0.00210(0)	1.65(8) x 10-4	3.71(0) x 10-5	6.50(6) x 10-4
B_{fsw}	75.7(7)	-0.770(7)		
Δ	21.6(3)			
A	0.283(1)	0.280(7)	0.287(4)	0.324(0)
B_2T^2			0.411(0)	
RMS (%)	2.54	2.76	2.75	2.94

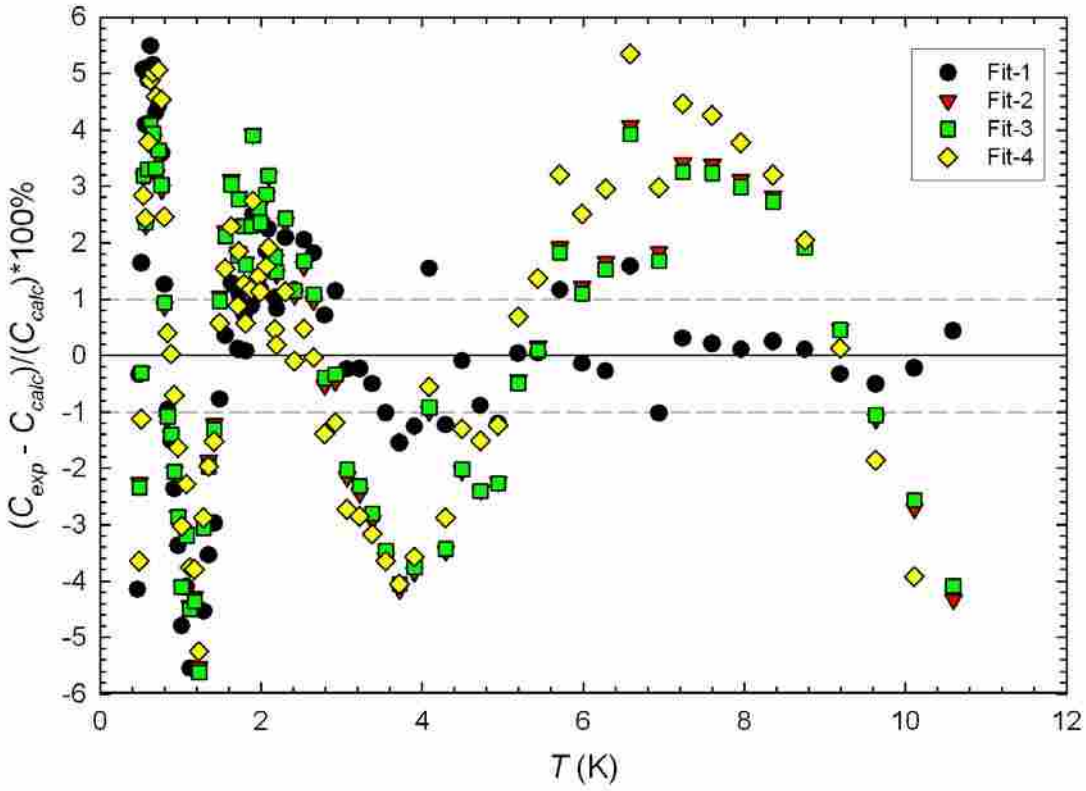

Figure 2.9. Plot of the percent deviation of the calculated heat capacity of the fits shown in Table 2.4.

Before a discussion of its physical meaning can be given, it is necessary to determine which fitting expression in Table 2.4 is the most accurate representation of the heat capacity of 13 nm magnetite Load 1. Fit-2 can immediately be rejected because of the negative value it has for B_{fsw}, which is physically meaningless. This leaves a comparison of Fits 1,3 and 4, which is more difficult given the similar RMS values for each of these fits. A more detailed comparison of the accuracy of each of these fits can be seen in the deviation of the respective fits from the experimentally measured heat capacity of 13 nm magnetite Load 1 found in Figure 2.9. It can be observed in this figure that all three fits display a systematic deviation below 2 K which suggests that none of the fits accurately represent the heat capacity of 13 nm magnetite Load 1 below this temperature. This can be seen graphically in the comparison of the fits with the experimental heat capacity as shown in Figure 2.10, and it is probable that the AT^{-2} term does not sufficiently represent the upturn. Rather, there is some other contributing phenomenon that is not included in any of the fits.

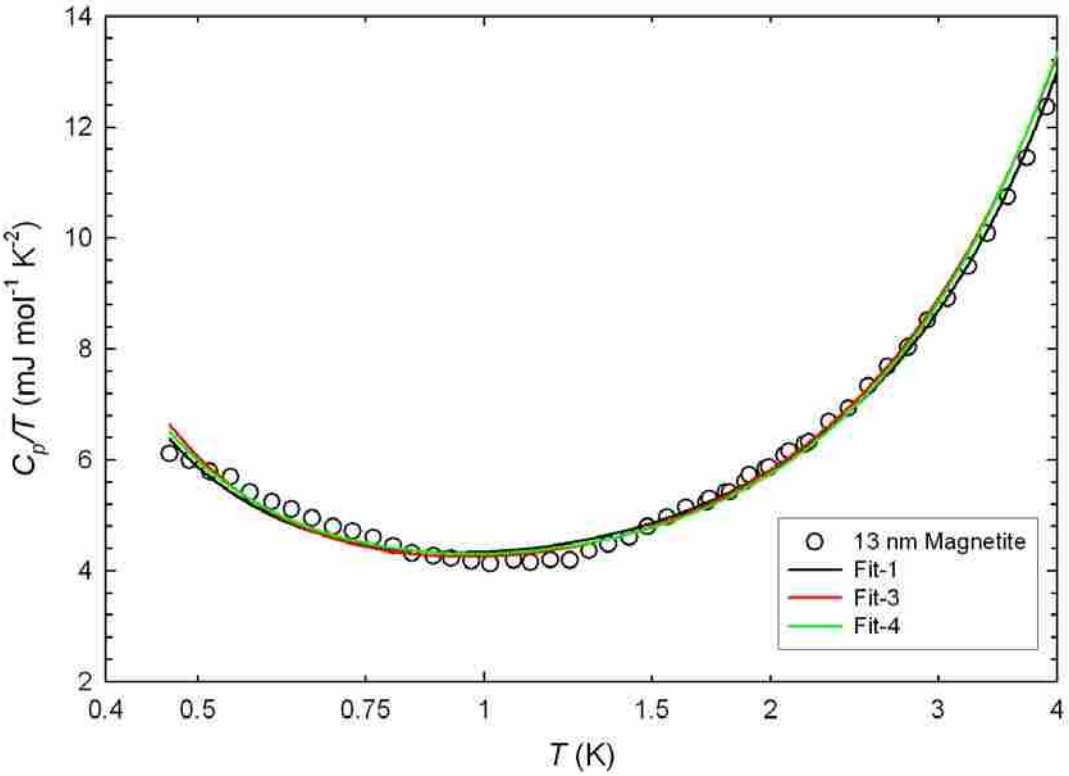

Figure 2.10. A comparison of various fits with the heat capacity of 13 nm magnetite Load 1 below $T = 2$ K. Details of these Fits are provided in Table 2.4.

In spite of the poor representation of the heat capacity below 2 K, above this temperature the deviations of Fit-1 show a random behavior in Figure 2.9 while Fits-3 and 4 have a systematic deviation. A random deviation corresponds to a good, physical representation of the heat capacity in this temperature range. Also, Fit-1 shows a small degree of error in this temperature range with most points within 1% of the experimental measurements while the other fits deviate as much as 5%. The three fits are compared graphically to experimental data in the temperature range 5 to 10 K in Figure 2.11 where it can be seen that Fits-3 and 4 drop below the heat capacity of 13 nm magnetite until 6 K and then begin to have a positive deviation. In contrast Fit-1 matches the shape of the heat capacity curve without any noticeable deviations. With a lower degree of error at temperatures above 2 K and a random deviation from experimental measurements, Fit-1 is the best physical representation of the heat capacity of 13 nm magnetite Load 1.

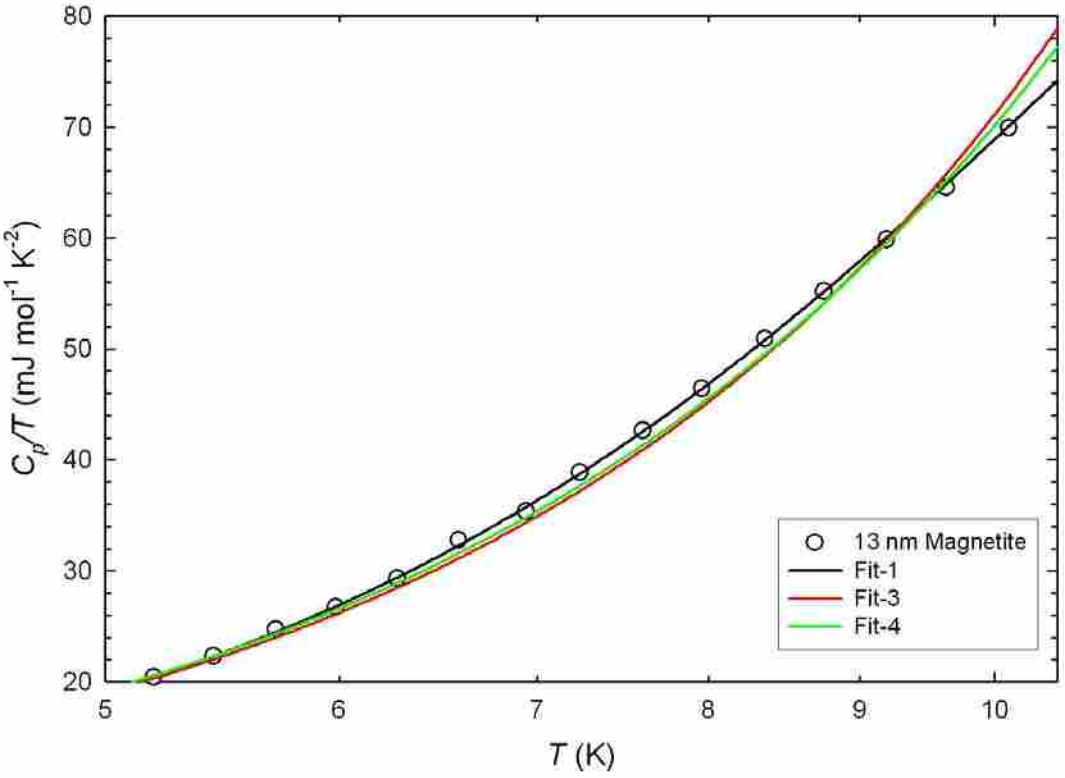

Figure 2.11. A comparison of various fits with the heat capacity of 13 nm magnetite Load 1 from 2 K to 10 K. Details of these Fits are provided in Table 2.4.

2.4.4 Physical Meaning of 13 nm Magnetite Load 1

With the evidence supporting Fit-1 as the most accurate representation of the heat capacity of 13 nm magnetite, the physical meaning of this expression can be discussed. Fit-1 consists of a variety of meaningful terms including γT, AT^{-2}, and $B_{fsw}T^{3/2}e^{-\Delta/T}$. The use of a gap parameter agrees with the conclusions of other studies which have shown that magnetite nanoparticles display anisotropy.[49, 52, 53] However, the linear term and the upturn are not readily interpreted, and an analysis of Fit-1 and its meaning are given below.

2.4.5 The Lattice Heat Capacity

Although nanocrystalline magnetite has not been shown to have antiferromagnetic behavior, it is still useful to show that the T^3 term originates with the lattice. Unfortunately, Koenitzer *et al.* did not provide a summary of their fits of bulk magnetite,[48] however low-temperature fits do exist for other iron oxides, some of which are nanoparticles. Recent measurements of hematite (α-Fe_2O_3) in our lab (unpublished) showed B_3 to have a value of 0.0832 $mJ \cdot mol^{-1} \cdot K^{-4}$ for the bulk and a 13 nm sample to have a value of 0.0982 $mJ \cdot mol^{-1} \cdot K^{-4}$. Fits of antiferromagnetic goethite[54] (α-FeOOH) were able to separate the lattice from the antiferromagnetic contributions, and goethite had a value of 0.100 $mJ \cdot mol^{-1} \cdot K^{-4}$ for B_3 while the antiferromagnetic coefficient B_{asw} was about ten time larger with a value of 1.16 $mJ \cdot mol^{-1} \cdot K^{-4}$. This observation for goethite is consistent with antiferromagnets which show the spin wave contribution to be ten to twenty times larger than the lattice contribution.[34] For 13 nm magnetite, the value of 0.587 $mJ \cdot mol^{-1} \cdot K^{-4}$ obtained from Fit-1 for B_3 is almost six times as large as those for other iron oxides. However, it is important to remember that this represents the molar heat capacity of Fe_3O_4 where there are three times as many Fe atoms as FeOOH and one and half times as many as Fe_2O_3, and consequently more heat is required in the lattice vibrational contributions of 13 nm magnetite. Also, the value of B_3 for 13 nm magnetite does not show the magnitude consistent with most antiferromagnets, and such behavior is unlikely in nanocrystalline magnetite.

2.4.6 The Linear Term, γT

The linear term in heat capacity models is generally due to an electronic contribution.[34] However in the case of magnetite the low-temperature phase is insulating and thus ideally has no electronic contribution. A comparison of the γT term to that calculated for other iron oxides can provide insight into the origin of the linear term in the heat capacity of 13 nm magnetite. Koenitzer *et al.* modeled the heat capacity of pure Fe_3O_4 and a second unstoichiometric sample with the formula $Fe_{2.9951}O_4$.[48] Both samples did not require the use of a linear term even though a linear term has been observed in many unstoichiometric oxide insulators.[54, 68, 69] The presence of a linear contribution to the heat capacity of 13 nm magnetite when the bulk has no linear contribution suggests that there is some physical property at the nanoscale that is not observed in the bulk.

Table 2.5. A comparison of the linear term of several nanocrystalline samples of anatase and rutile polymorphs of TiO_2 with that of 13 nm magnetite.

Sample	γ (per mole sample) $mJ \cdot mol^{-1} \cdot K^{-2}$	γ (per mole H_2O) $mJ \cdot mol^{-1} \cdot K^{-2}$
7 nm Antase $TiO_2 \cdot 0.677H_2O$	0.594	0.8774
7 nm Antase $TiO_2 \cdot 0.532H_2O$	0.656	1.2331
7 nm Anatase $TiO_2 \cdot 0.379H_2O$	0.688	1.8153
7 nm Rutile $TiO_2 \cdot 0.361H_2O$	0.508	1.4072
7 nm Rutile $TiO_2 \cdot 0.296H_2O$	0.564	1.9054
7 nm Rutile $TiO_2 \cdot 0.244H_2O$	0.499	2.0451
13 nm Magnetite ($Fe_3O_4 \cdot 0.735H_2O$)	3.462	4.7102

The large water component of the 13 nm magnetite particles could possibly be the source of a glassy linear term.[34] To evaluate this possibility, Table 2.5 shows a comparison between the linear terms of 13 nm magnetite from this study and nanocrystalline polymorphs of TiO_2 which have been measured with different water contents. The heat capacity of these TiO_2 samples has been published and discussed in detail,[70-73] but the low-temperature fits have not yet been published. An inspection of Table 2.5 shows that for the TiO_2 polymorphs the values of γ fall within the range 0.5-0.7 $mJ \cdot mol^{-1} \cdot K^{-2}$. Assuming that the linear term is associated only with the water, it can be observed that the value of γ actually increases with decreasing hydration. If the linear contribution were associated with the glass-like behavior of water adsorbed onto the

surface of the TiO_2 nanoparticles, the linear term would be expected to increase with hydration. This suggests that the linear term does not stem from glass-like behavior in the water adsorbed onto the surface. In 13 nm magnetite, the linear term is almost seven times larger than that of the TiO_2 polymorphs which suggests that it originates with some other physical phenomenon.

When compared to other conducting metals, the heat capacity of elemental iron has a relatively large linear contribution of 5.02 $mJ \cdot mol^{-1} \cdot K^{-2}$.[34] This value is similar in magnitude to that of 13 nm magnetite which has a value of 3.46 $mJ \cdot mol^{-1} \cdot K^{-2}$. While these values are similar, the linear contribution of iron metal shows that the heat capacity of free electrons is generally large.[34] It is unlikely that the linear term for 13 nm magnetite Load 1 stems from an electronic contribution. This can be supported by the observation that as temperature decreased the time for 13 nm magnetite to reach thermal equilibrium increased. Thermal conductivity has been shown to be directly related to conduction electrons,[74] and long equilibrium times in 13 nm magnetite correspond to low thermal conductivity. In turn, low thermal conductivity suggests that the sample is an insulator, and that the linear contribution to the heat capacity does not stem from electronic phenomena. Furthermore, the comparison of the linear term for 13 nm magnetite to that of Fe would suggest a large number of conduction electrons in 13 nm magnetite. This is extremely unlikely given the information available which shows that magnetite is an insulator at low temperature.

As discussed previously, a linear term can stem from localized electronic states due to oxygen vacancies. This can be seen in a 37 nm sample of goethite, which had a significant amount of oxygen vacancies (8.3 %) and a γ value of 0.23 $mJ \cdot mol^{-1} \cdot K^{-2}$.[54] The linear contribution in Fit-1 is 15 times larger than that of goethite, which means that either there are a significant number of oxygen vacancies in13 nm magnetite or there is some other physical property that contributes to its heat capacity. In short, the linear contribution in Fit-1 is too large to originate solely from localized electronic states associated with oxygen vacancies; there must be some other source for the linear term.

Recent heat capacity measurements (not yet published) of a 13 nm hematite sample in our lab have also been modeled with linear term of 1.02 $mJ \cdot mol^{-1} \cdot K^{-2}$. This large linear term is in spite of a band gap of 2.2 eV for nanocrystalline hematite. Like

nanocrystalline magnetite, hematite nanoparticles have also been characterized with superparamagnetic behavior, and a linear term was not observed in the heat capacity of the bulk (not published for bulk hematite) for either material. As Livingston and Bean[43] put forth, superparamagnetic particles can make a measurable contribution to the linear temperature coefficient of the heat capacity. There are very few heat capacity studies of superparamagnetic materials, yet this model is supported experimentally by Triplett and Phillips[42] who observed a γ value of 13.3 $mJ \cdot mol^{-1} \cdot K^{-2}$ in the heat capacity of $Ni_{0.62}Rh_{0.38}$, a sample which was shown to be consistent with the superparamagnetic behavior of ferromagnetic clusters. As stated previously, magnetite nanoparticles have been shown to be superparamagnetic through many studies,[35-38] and it is more likely that the linear contribution to the heat capacity of 13 nm magnetite Load 1 originates for the most part from superparamagnetic behavior.

2.4.7 The Upturn and the Meaning of AT^{-2}

Nuclear hyperfine contributions are a common origin of an upturn in heat capacity data near 0 K,[34] and the upturn in the measurements of Load 1 may stem from a hyperfine contribution. The only isotope of iron with a nuclear moment is ^{57}Fe which has an abundance of 2.19%.[75] The nuclear hyperfine contribution to heat capacities is modeled by $D(H/T)^2$, and the nuclear moment is $0.09024\mu_N$ with a spin of ½, which corresponds to $D = 5.953 \times 10^{-7}$ mJ/(mole·T).[34] Equating the hyperfine model to the AT^{-2} term we can derive the relationship $H = (A/D)^{1/2}$, where H represents the internal nuclear magnetic field. Using the value of 0.2831 for A obtained in Fit-1, H is calculated to be 689.5 T. This value is too large to be physically meaningful and suggests that the upturn is not related to a nuclear hyperfine contribution. Additionally no upturn is observed in the heat capacity of bulk magnetite,[48] which suggests that nuclear hyperfine contributions are not significant in the heat capacity of magnetite.[48] The origin of the upturn is still unclear, however an upturn is observed in the heat capacity of superparamagnetic $Ni_{0.62}Rh_{0.38}$ measured by Triplett and Phillips,[42] which was surpressed when the heat capacity was measured in an external magnetic field. This agrees with heat capacity models which explain that anomalies can arise from the splitting of the energy levels of

superparamagnetic particles by an anisotropy field,[43] and perhaps the upturn in the heat capacity of 13 nm magnetite Load 1 can be attributed to its superparamagnetic behavior.

2.4.8 Claims of Spin Glass Behavior

The claim that nanocrystalline magnetite samples can be characterized as a spin glass[44] needs to be addressed. Fit-3 attempts to model the heat capacity of 13 nm magnetite using the model put forth by Fogle *et al.*[47] of $C = \gamma T + B_2 T^2$. While Fit-3 gives an RMS value of 2.75% the deviations in Figure 2.9 show a systematic distribution rather than a random behavior, which suggests the fit is not a physical representation. Also, no anomaly associated with a superparamagnetic to spin-glass transition is observed in the heat capacity, and it is unlikely that there is spin-glass behavior in 13 nm magnetite.

2.4.9 The Heat Capacity of 13 nm Magnetite Load 2 Below 15 K

The heat capacity of nanocrystalline magnetite Load 2 (Figure 2.12) was more difficult to fit due to a thermally dependent variation in an anomaly found below 4 K. The thermal history of this sample shown in Table 2.6 helps to understand why this anomaly is inconsistent. Some regularity can be seen in this region with Series 1-4 showing good agreement and Series 5-8 also having consistency. Interestingly, Series 11 and 13 show similar behavior while Series 12 has a large anomaly that was not reproduced. Each of these groups of measurements were made after heating the sample to temperatures close to 40 K. This suggests that like the Verwey transition, cooling rate and history are important variables in the low-temperature behavior of magnetite nanoparticles.

Table 2.6. Thermal history of 13 magnetite Load 2.

Series	Date	*T* Start	*T* finish
1	5/25/2009	1.65	11.097
2	5/26/2009	8.75	38.88
3	5/27/2009	1.732	10.599
4	5/28/2009	9.194	37.71
5	6/1/2009	1.732	10.608
6	6/2/2009	0.451	2.284
7	6/3/2009	0.472	2.176
8	6/4/2009	1.732	5.437
9	6/5/2009	35.99	51.92
10	6/5/2009	51.00	58.99
11	6/8/2009	0.472	2.178
12	6/9/2009	0.446	2.278
13	6/10/2009	0.472	2.176

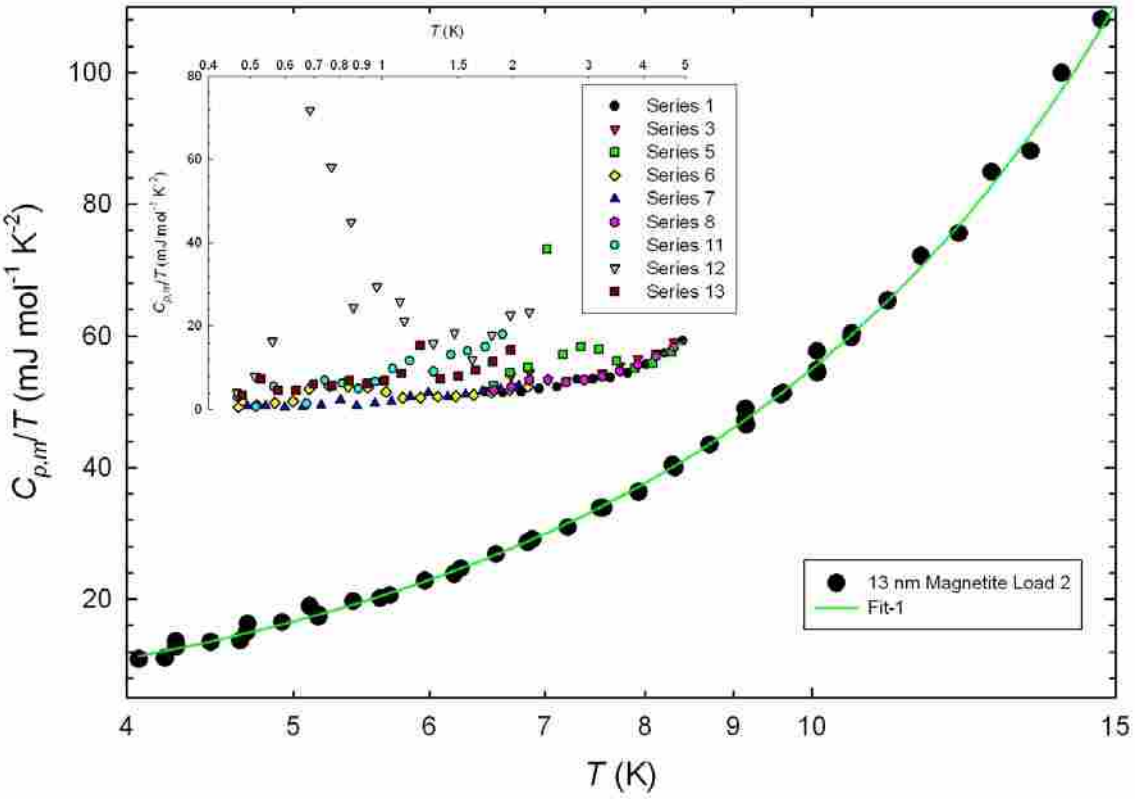

Figure 2.12. Plot of measured heat capacity against temperature for nanocrystalline magnetite Load 2. The inset shows the data below $T = 5$. The solid line represents Fit-1 of the data.

2.4.10 Fits of 13 nm Magnetite Load 2

Above a temperature of ~ 4 K the data is reproducible as the lattice contribution begins to increase, and heat capacity data from Load 2 was fit in the temperature range 4-14 K. A summary of the fits of Load 2 can be found in Table 2.7. These fits were performed in the same manner as those of Load 1 except no term was included to represent an upturn. A linear term combined with a spin-wave resulted in a negative γ value rendering such an expression meaningless. Yet a linear term was successfully applied in Fit-3, and a spin-wave in Fits 2 and 4. Often the need for extra lattice terms (ie. T^5, T^7, T^9…) implies that a contribution to the total specific heat is not being modeled well by the fitting expression. For 13 nm magnetite Load 2, a T^5 term (Fit-2) was needed in order for an expression using a spin-wave to approach the accuracy of Fit-1, which suggests that the gap parameter is better at modeling the heat capacity of Load 2 as it did not use the higher order lattice terms. As for the linear term used in Fit-3, an examination

of the deviations of these fits in Figure 2.13 provides some valuable insight. It can be seen that the deviation of Fit-3 is almost exactly the same as that of Fit-2, both of which are systematic. In contrast, the deviation of Fit-1 shows more random deviation suggesting a physically meaningful fit.

2.4.11 Physical Meaning of 13 nm Magnetite Load 2

Like Load 1, the heat capacity of 13 nm magnetite Load 2 included an anisotropy term for the ferrimagnetic spin-wave contribution which indicates there is a gap in the zero-field spin-wave spectrum. However the two data sets differed in that Load 2 did not require a linear term. This suggests that cooling rate has an effect on the linear contribution of the heat capacity of 13 nm magnetite.

Table 2.7. A summary of the parameters for Fits of the heat capacity of nanocrystalline magnetite Load 2. Units are in mJ, K, and mole.

Parameters	Fit-1	Fit-2	Fit-3	Fit-4
γ			2.03(6)	
B_3	0.381(6)	0.561(6)	0.588(1)	0.484(9)
B_5		$-4.47(7) \times 10^{-4}$	$-5.21(0) \times 10^{-4}$	
B_{fsw}	8.90(2)	1.20(1)		1.95(4)
Δ	5.17(7)			
RMS(%)	3.35	3.57	3.65	4.26

2.4.12 Summary

In summary, theoretical fits of the heat capacity of nanocrystalline magnetite at temperatures below 15 K suggest that magnetite nanoparticles have superparamagnetic properties with anisotropic behavior. This is shown through a large linear term and the need for an anisotropy term and gap parameter in order to accurately model the low-temperature heat capacity of 13 nm magnetite. This data does not support the claim that magnetite nanoparticles have super spin-glass behavior as no anomaly was observed at the T_f reported[44] for magnetite nanoparticles. A large discrepancy (> 7 $J \cdot mol^{-1} \cdot K^{-1}$) in the magnitude of the heat capacity around 50 K shows that the Verwey transition and magnetic character of 13 nm magnetite are dependent on cooling rate and thermal history.

Also, the disappearance of a peak at T_v and the broad anomaly at temperatures below 95 K indicate that the nature of the Verwey transition is dependent on crystal size.

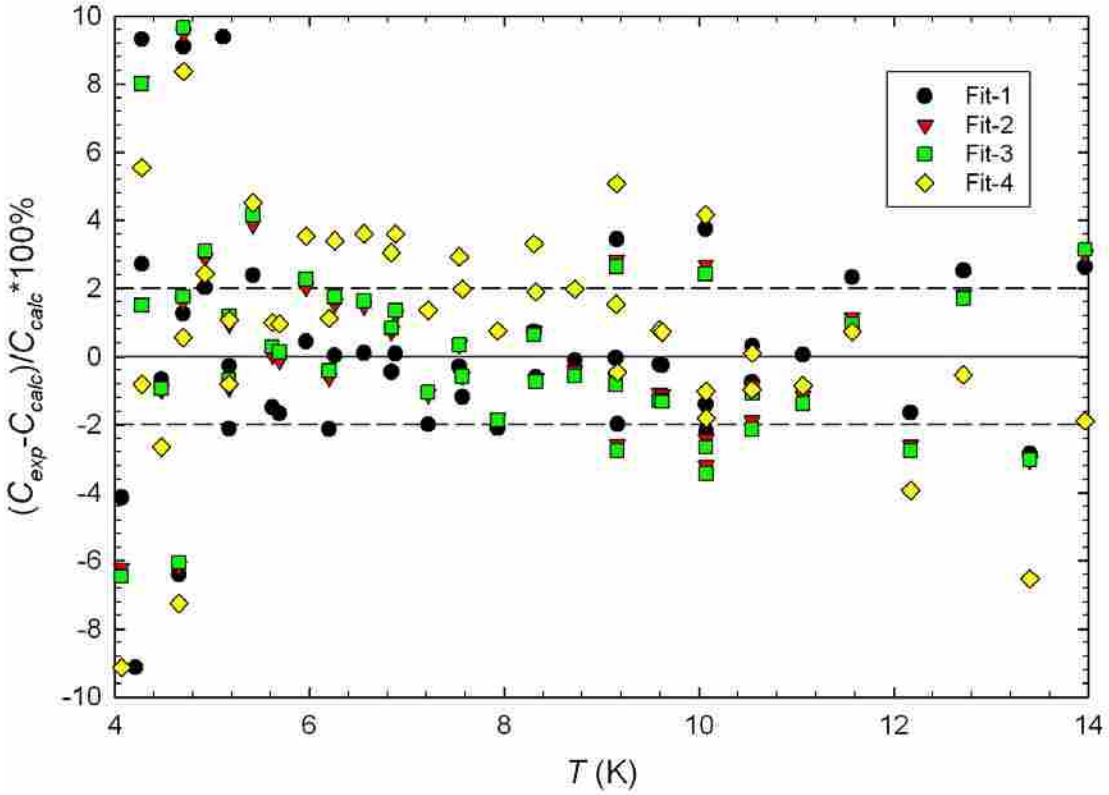

Figure 2.12. Deviation of the calculated heat capacity of 13 nm Magnetite Load 2. Units are in mJ, mole, and K.

References

1. Westrum, E. F. F.; Groenvold, F., *J. Chem. Thermodyn.* **1969,** *1* (6), 543-57.
2. Iizumi, M.; Koetzle, T. F.; Shirane, G.; Chikazumi, S.; Matsui, M.; Todo, S., *Acta Crystallogr., Sect. B* **1982,** *B38* (8), 2121-33.
3. Verwey, E. J. W.; Haayman, P. W., *Physica (The Hague)* **1941,** *8*, 979-87.
4. Chiba, K.; Matsui, M.; Chikazumi, S., *Kotai Butsuri* **1974,** *9* (8), 465-70.
5. Chikazumi, S.; Chiba, K.; Matsui, M.; Akimitsu, J.; Todo, S., **1974,** *1, Pt. 1*, 137-41.
6. Verwey, E. J. W., *Nature (London, U. K.)* **1939,** *144*, 327-8.
7. Verwey, E. J. W.; Haayman, P. W.; Romeijn, F. C., *J. Chem. Phys.* **1947,** *15*, 181-7.

8. Garcia, J.; Subias, G., *J. Phys.: Condens. Matter* **2004,** *16* (7), R145-R178.
9. Kozlowski, A.; Kakol, Z.; Tarnawski, Z., *Acta Phys. Pol., A* **2007,** *111* (4), 537-547.
10. Leonov, I.; Yaresko, A. N., *J. Phys.: Condens. Matter* **2007,** *19* (2), 021001/1-021001/3.
11. Piekarz, P.; Parlinski, K.; Oles, A. M., *Phys. Rev. Lett.* **2006,** *97* (15), 156402/1-156402/4.
12. Piekarz, P.; Parlinski, K.; Oles, A. M., *J. Phys.: Conf. Ser.* **2007,** *92*, No pp given.
13. Piekarz, P.; Parlinski, K.; Oles, A. M., *Phys. Rev. B: Condens. Matter Mater. Phys.* **2007,** *76* (16), 165124/1-165124/16.
14. Shchennikov, V. V.; Ovsyannikov, S. V., *J. Phys.: Condens. Matter* **2009,** *21* (27), 271001/1-271001/4.
15. Evans, B. J.; Westrum, E. F., Jr., *Phys. Rev. B* **1972,** *[3]5* (9), 3791-3.
16. Takai, S.; Akishige, Y.; Kawaji, H.; Atake, T.; Sawaguchi, E., *J. Chem. Thermodyn.* **1994,** *26* (12), 1259-66.
17. Shepherd, J. P.; Koenitzer, J. W.; Sandberg, C. J.; Aragon, R.; Honig, J. M., *Mol. Cryst. Liq. Cryst.* **1984,** *107* (1-2), 191-4.
18. Gmelin, E.; Lenge, N.; Kronmueller, H., *Philos. Mag. B* **1984,** *50* (3), L41-L44.
19. Westrum, E. F., Jr.; Bartel, J. J., **1975,** *2*, 19-26.
20. Rigo, M. O.; Mareche, J. F.; Brabers, V. A. M., *Philos. Mag. B* **1983,** *48* (5), 421-30.
21. Shepherd, J. P.; Aragon, R.; Koenitzer, J. W.; Honig, J. M., *Phys. Rev. B: Condens. Matter Mater. Phys.* **1985,** *32* (3), 1818-19.
22. Kozlowski, A.; Kakol, Z.; Kim, D.; Zalecki, R.; Honig, J. M., *Z. Anorg. Allg. Chem.* **1997,** *623* (1), 115-118.
23. Kozlowski, A.; Kakol, Z.; Zalecki, R.; Honig, J. M., *J. Magn. Magn. Mater.* **1995,** *140-144* (Pt. 3), 2083-4.
24. Miyahara, Y., *J. Phys. Soc. Jpn.* **1972,** *32* (3), 629-34.
25. Bartel, J. J. Heat capacity determination of the effect of dopants upon the metal-nonmetal transition in magnetite and synthetic iron(II, III) oxide. 1974.
26. Tabis, W.; Tarnawski, Z.; Kakol, Z.; Krol, G.; Kolodziejczyk, A.; Kozlowski, A.; Fluerasu, A.; Honig, J. M., *J. Alloys Compd.* **2007,** *442* (1-2), 203-205.
27. Gmelin, E.; Lenge, N.; Kronmueller, H., *Phys. Status Solidi A* **1983,** *79* (2), 465-75.
28. Shepherd, J. P.; Koenitzer, J. W.; Aragon, R.; Sandberg, C. J.; Honig, J. M., *Phys. Rev. B: Condens. Matter Mater. Phys.* **1985,** *31* (2), 1107-13.
29. Matsui, M.; Todo, S.; Chikazumi, S., *J. Phys. Soc. Jpn.* **1977,** *42* (5), 1517-24.
30. Aragon, R.; Rasmussen, R. J.; Shepherd, J. P.; Koenitzer, J. W.; Honig, J. M., *J. Magn. Magn. Mater.* **1986,** *54-57* (3), 1335-6.
31. Aragon, R.; Shepherd, J. P.; Koenitzer, J. W.; Buttrey, D. J.; Rasmussen, R. J.; Honig, J. M., *J. Appl. Phys.* **1985,** *57* (8, Pt. 2A), 3221-2.
32. Shepherd, J. P.; Koenitzer, J. W.; Aragon, R.; Spalek, J.; Honig, J. M., *Phys. Rev. B: Condens. Matter Mater. Phys.* **1991,** *43* (10-B), 8461-71.
33. Korolev, V. V.; Arefyev, I. M.; Blinov, A. V., *J. Therm. Anal. Calorim.* **2008,** *92* (3), 697-700.

34. Gopal, E. S. R., *Specific Heats at Low Temperatures (International Cryogenics Monograph Series)*. Plenum Press: New York, 1966; p 226
35. Bremholm, M.; Felicissimo, M.; Iversen, B. B., *Angew. Chem., Int. Ed.* **2009,** *48* (26), 4788-4791, S4788/1-S4788/12.
36. Kim, M.-J.; Choa, Y.-H.; Kim, D. H.; Kim, K. H., *IEEE Trans. Magn.* **2009,** *45* (6), 2446-2449.
37. Maity, D.; Kale, S. N.; Kaul-Ghanekar, R.; Xue, J.-M.; Ding, J., *J. Magn. Magn. Mater.* **2009,** *321* (19), 3093-3098.
38. Tueysuez, H.; Salabas, E. L.; Weidenthaler, C.; Schueth, F., *J. Am. Chem. Soc.* **2008,** *130* (1), 280-287.
39. Joensson, P. E., *Adv. Chem. Phys.* **2003,** *128*, 191-248.
40. Bean, C. P.; Livingston, J. D., *J. Appl. Phys.* **1959,** *30*, 120S-129S.
41. Bienias, J. A.; Moody, D. E., *Physica B + C (Amsterdam)* **1977,** *86-88 B+C, pt. 1*, 541-2.
42. Triplett, B. B.; Phillips, N. E., *Phys. Lett. A* **1971,** *37* (5), 443-4.
43. Livingston, J. D.; Bean, C. P., *J. Appl. Phys.* **1961,** *32* (10), 1964-1966.
44. Suzuki, M.; Fullem, S. I.; Suzuki, I. S.; Wang, L.; Zhong, C.-J., *Phys. Rev. B: Condens. Matter Mater. Phys.* **2009,** *79* (2), 024418/1-024418/7.
45. Fibich, M.; Riess, I.; Ron, A., *J. Magn. Magn. Mater.* **1978,** *7*, 262-4.
46. Caudron, R.; Costa, P.; Lasjaunias, J. C.; Levesque, B., *J. Phys. F* **1981,** *11* (2), 451-6.
47. Fogle, W. E.; Boyer, J. D.; Fisher, R. A.; Phillips, N. E., *Phys. Rev. Lett.* **1983,** *50* (22), 1815-18.
48. Koenitzer, J. W.; Keesom, P. H.; Honig, J. M., *Phys. Rev. B: Condens. Matter Mater. Phys.* **1989,** *39* (9), 6231-3.
49. Williams, W.; Muxworthy, A. R.; Paterson, G. A., *J. Geophys. Res., [Solid Earth]* **2006,** *111* (B12), B12S13/1-B12S13/9.
50. Erin, K. V., *Opt. Spectrosc.* **2009,** *106* (6), 858-862.
51. Mazo-Zuluaga, J.; Restrepo, J.; Munoz, F.; Mejia-Lopez, J., *J. Appl. Phys.* **2009,** *105* (12), 123907/1-123907/10.
52. Thakur, M.; De, K.; Giri, S.; Si, S.; Kotal, A.; Mandal, T. K., *Los Alamos Natl. Lab., Prepr. Arch., Condens. Matter* **2006**, 1-21, arXiv:cond-mat/0604119.
53. Vargas, J. M.; Lima, E., Jr.; Zysler, R. D.; Duque, J. G. S.; De Biasi, E.; Knobel, M., *Eur. Phys. J. B* **2008,** *64* (2), 211-218.
54. Majzlan, J.; Navrotsky, A.; Woodfield, B. F.; Lang, B. E.; Boerio-Goates, J.; Fisher, R. A., *J. Low Temp. Phys.* **2003,** *130* (1/2), 69-76.
55. Niira, K., *Phys. Rev.* **1960,** *117*, 129-33.
56. Fisher, R. A.; Bouquet, F.; Phillips, N. E.; Franck, J. P.; Zhang, G.; Gordon, J. E.; Marcenat, C., *Phys. Rev. B: Condens. Matter Mater. Phys.* **2001,** *64* (13), 134425/1-134425/9.
57. Wang, Q.; Liu, Y.; Wang, J.; Zhang, X., *Beijing Ligong Daxue Xuebao* **1994,** *14* (2), 200-5.
58. Gao, D.; Wang, J., *Sichuan Shifan Daxue Xuebao, Ziran Kexueban* **1997,** *20* (6), 94-97.
59. Clarke, R. G.; Groth, R. H.; Duzak, E. J. Absorbent for carbon dioxide and water. 3141729, 19600711., 1964.

60. Dry, M. E.; Leuteritz, G. M.; Zyl, W. J. V., *J. S. Afr. Chem. Inst.* **1963,** *16* (1), 15 21.
61. Nerlov, J.; Hoffmann, S. V.; Shimomura, M.; Moller, P. J., *Surf. Sci.* **1998,** *401* (1), 56-71.
62. Nishizawa, K.; Kodama, T.; Tabata, M.; Yoshida, T.; Tsuji, M.; Tamaura, Y., *J. Chem. Soc., Faraday Trans.* **1992,** *88* (18), 2771-3.
63. Shaikhutdinov, S.; Weiss, W., *J. Mol. Catal. A: Chem.* **2000,** *158* (1), 129-133.
64. Stevens, R.; Boerio-Goates, J., *J. Chem. Thermodyn.* **2004,** *36* (10), 857-863.
65. Lashley, J. C.; Hundley, M. F.; Migliori, A.; Sarrao, J. L.; Pagliuso, P. G.; Darling, T. W.; Jaime, M.; Cooley, J. C.; Hults, W. L.; Morales, L.; Thoma, D. J.; Smith, J. L.; Boerio-Goates, J.; Woodfield, B. F.; Stewart, G. R.; Fisher, R. A.; Phillips, N. E., *Cryogenics* **2003,** *43* (6), 369-378.
66. Takai, S.; Atake, T.; Koga, Y., *Thermochim. Acta* **1994,** *246* (1), 1-10.
67. Phillips, N. E., *Crit. Rev. Solid State Sci.* **1971,** *2* (4), 467-553.
68. Boerio-Goates, J.; Stevens, R.; Lang, B.; Woodfield, B. F., *J. Therm. Anal. Calorim.* **2002,** *69* (3), 773-783.
69. Coey, J. M. D.; Von Molnar, S.; Torressen, A., *J. Less-Common Met.* **1989,** *151*, 191-4.
70. Boerio-Goates, J.; Li, G.; Li, L.; Walker, T. F.; Parry, T.; Woodfield, B. F., *Nano Lett.* **2006,** *6* (4), 750-754.
71. Levchenko, A. A.; Li, G.; Boerio-Goates, J.; Woodfield, B. F.; Navrotsky, A., *Chem. Mater.* **2006,** *18* (26), 6324-6332.
72. Li, G.; Li, L.; Boerio-goates, J.; Woodfield, B. F., *J. Mater. Res.* **2003,** *18* (11), 2664-2669.
73. Li, G.; Li, L.; Boerio-Goates, J.; Woodfield, B. F., *J. Am. Chem. Soc.* **2005,** *127* (24), 8659-8666.
74. Powell, R. W.; Ho, C.-Y.; Liley, P. E., *Natl. Stand. Ref. Data Ser. (U. S., Natl. Bur. Stand.)* **1966,** *No. 8*, 165 pp.
75. Lide, D. R., *CRC Handbook of Chemistry and Physics, 83rd Edition*. 2002; p 2664 pp.

Chapter 3

Heat Capacity, Third-law Entropy, and Low-Temperature Physical Behavior of Bulk Hematite (α-Fe_2O_3).

3.1 Introduction

Hematite (α-Fe_2O_3) is considered to be the most thermodynamically stable iron oxide,[1] and like other iron oxides, hematite displays unique magnetic properties.[2-4] Below a Néel temperature of 950 K, hematite adopts a spin structure containing two ferromagnetic sublattices. These ferromagnetic sublattices are antiferromagnetically coupled to each other, and their moments are aligned perpendicular to the basal plane of hematite's hexagonal setting. The two sublattices have a slight canting toward each other which produces a small, net moment. Below 260 K (T_M) the magnetic moments realign themselves parallel to the *c* axis of the hexagonal structure in a first order spin reorientation called the Morin transition. The net magnetic moment is lost in this process, and bulk hematite transforms from a ferromagnet to an antiferromagnet. T_M has been shown through magnetization measurements to decrease with particle size,[2, 3] and the Morin transition has been shown to disappear altogether in samples of mesoporous[6] and nanocrystalline[2] hematite. This suggests that the spin-flip transition in hematite has a thermodynamic dependence, which can be investigated through calorimetric techniques including heat capacities.

Magnetic studies of solids can be complemented through the measurement of heat capacities.[7] As a bulk property, the heat capacity depends on all the energetic states available to a material at a given temperature, and contributions from these various states can often be separated. Magnetic contributions to heat capacities can originate from a number of sources including transitions from one type of magnetism to another as well as the presence of magnetic spin-waves. While atomic vibrations in the lattice make the largest contributions to heat capacities at most temperatures,[7] below 10 K the lattice heat capacity is small enough that contributions from other sources (including spin waves) are

more easily discerned. Hence, the measurement of heat capacities below 10 K becomes important in the study of magnetic materials.

Heat capacities can also be used to generate third-law entropies that, when combined with thermochemical measurements, yield relative free energies of compounds.[8] In turn, free energies give information about the phase stabilities of materials relative to each other.

The heat capacity of bulk hematite was first measured by Parks and Kelley[9] in 1926 over four narrow regions from 90 K to 290 K. In 1958, Westrum and Gronvold[5] improved upon these measurements covering the range 5 K to 350 K. No anomaly in the heat capacity due to the Morin transition was observed in this study or in another later series of measurements in 1985 by Jayasuriya *et al.*[10] While Jayasuriya did not provide any values for the entropy of hematite, Westrum and Gronvold[5] calculated the entropy of hematite at 298.15 K to be 87.400 $J \cdot mol^{-1} \cdot K^{-1}$.

Although heat capacity measurements for hematite exist as low as 5 K, there are only a few points which makes it difficult to accurately model this data using theoretical fits. To characterize the magnetic behavior of hematite through heat capacity, it is necessary to obtain measurements at lower temperatures and with a greater density of points. This data can be used to investigate spin wave contributions which can provide details on the magnetic coupling in bulk hematite at low temperatures. The spin wave contributions can then help determine the extent of the Morin transition and the change to an antiferromagnet at low-temperatures.

With the goal of studying magnetic coupling in hematite, we report the heat capacity of hematite in the range 2-300 K measured using a Quantum Design physical properties measurement system (PPMS). This data was fit to theoretical functions below 10 K, and the results of these fits are discussed. Third law entropies were also calculated and a comparison is made with previously calculated values.

3.2 Experimental

A 1 g sample of nanocrystalline hematite prepared using the method of Liu *et al.*[11] was sintered at 1200°C for 48 hours in an alumina dish. The powder was then slowly cooled to 500°C at a rate of 10°/min before removing it from the furnace. The XRD

spectrum for this sample is shown in Figure 3.1 over the range 25-75^{o}. The peaks are narrow indicating large crystal size, and the sample is characterized as bulk. Brunauer Emmet Teller (BET) surface area measurements for this sample also confirm that sintering the sample has resulted in grain growth with the change in surface area going from 59.03 m^2/g for the nanopowder to 0.0187 m^2/g. The chemical purity of this sample was analyzed using a Perkin-Elmer inductively coupled plasma optical emission spectrometer (ICP-OES) Optima 4300 DV. A sample solution for ICP was prepared by dissolving two samples (129.0 and 168.6 mg) of the hematite powder in 50.0 mL of 5% HNO_3. Qualitative analysis of this sample revealed the presence of Al, Ca, Cr, Mn, and Mg. Quantitative analysis using standard concentrations of these species showed the total

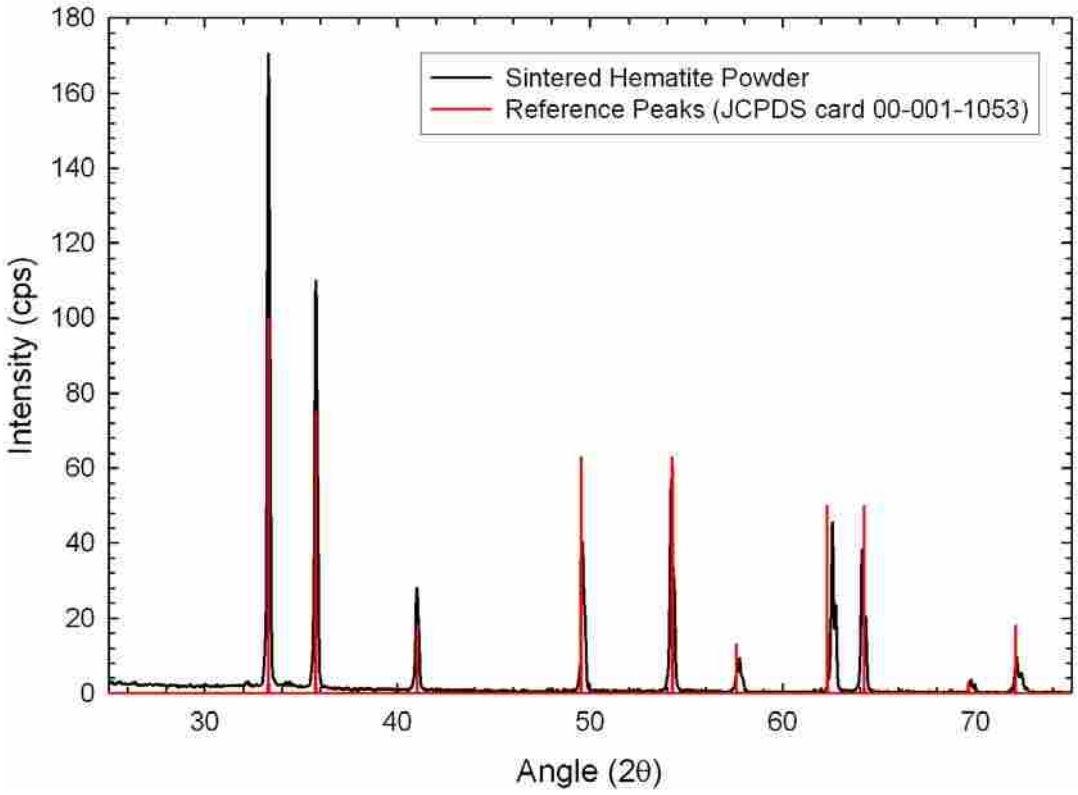

Figure 3.1. Powder X-ray diffraction spectrum of sintered hematite powder.

impurities to be less than 0.082 % of the sample mass making the sample 99.918 % pure on a metals basis.

We have developed new methods of measuring the heat capacity of powdered samples using the Quantum Design Physical Properties measurement system (PPMS) with an accuracy of ± 1% from 22 K to 300 K and ± (2-5) % below 22 K, and this accuracy corresponds to both conducting and non-conducting samples. Details of this method will be published elsewhere. In general, sample mounting consists of combining the sample with Apiezon N grease in a copper cup which is then compressed into a pellet using a stainless steel die. The copper cup is formed from a foil of 0.025 mm thickness and 99.999 % purity while the pellet has a 2.8 mm diameter and height of 3.5 mm. The heat capacity of the grease, copper, and addenda are measured as a background which can be subtracted from measurements including the sample. The heat capacity of the sintered hematite was measured for two samples (33.25 and 28.57 mg) in the range 2 to 350 K using the PPMS.

3.3 Results

Heat capacity measurements for the two samples are given separately (Tables 2.1 and 2.2) with the 33.25 mg sample referred to as *Series* 1 and the 28.57 mg sample as *Series* 2. This data can be seen graphically with a comparison to that of Westrum and Gronvold in Figure 2.2, and an inset on this figure shows these graphs below 10 K. The relative accuracy of the PPMS measurements can be seen by their deviation from the measurements of Westrum and Gronvold[5] in Figure 2.3.

As with the measurements published by Jayasuriya *et al*[10]. as well as those by Westrum and Gronvold,[5] no anomaly is observed in the heat capacity measured using PPMS. Above 30 K the PPMS measurements are within ±0.8% (dashed reference lines in Figure 3) while below this temperature the data show much larger deviations. There are two reasons for the large deviations at lower temperatures. First, the heat capacity at low temperatures is small, and consequently even small deviations will be a much larger percent of the heat capacity. The second reason for the larger deviations in the heat capacity comes from the greater degree of error for the measurements by Westrum (5%) and the PPMS (2%) at temperatures lower than 10 K.

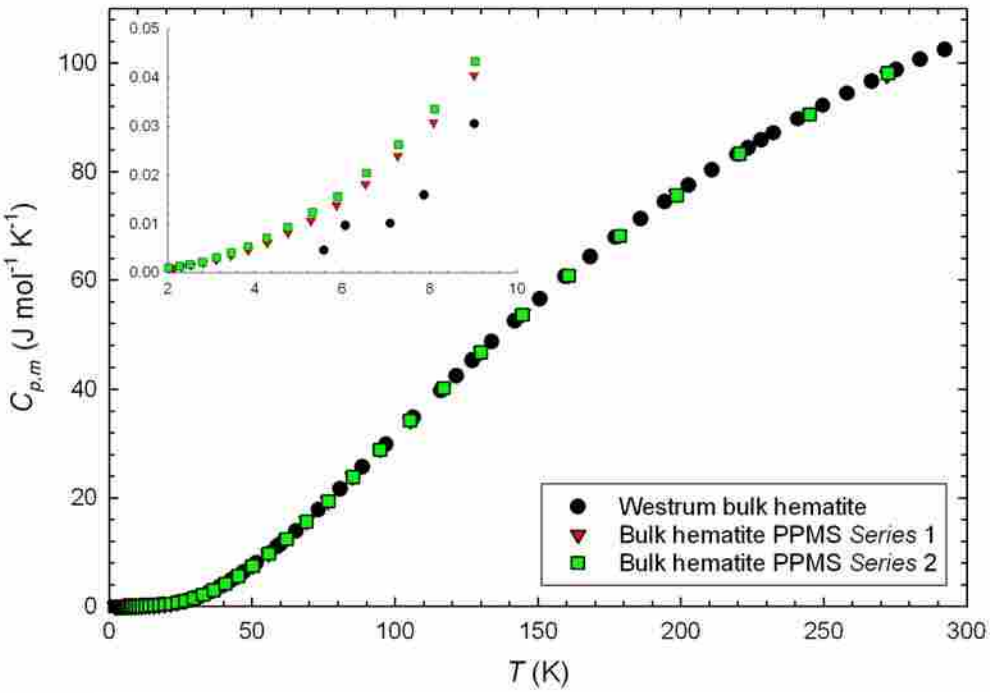

Figure 3.2. The heat capacity of hematite measured using PPMS with a comparison to measurements by Westrum and Gronvold.[5]

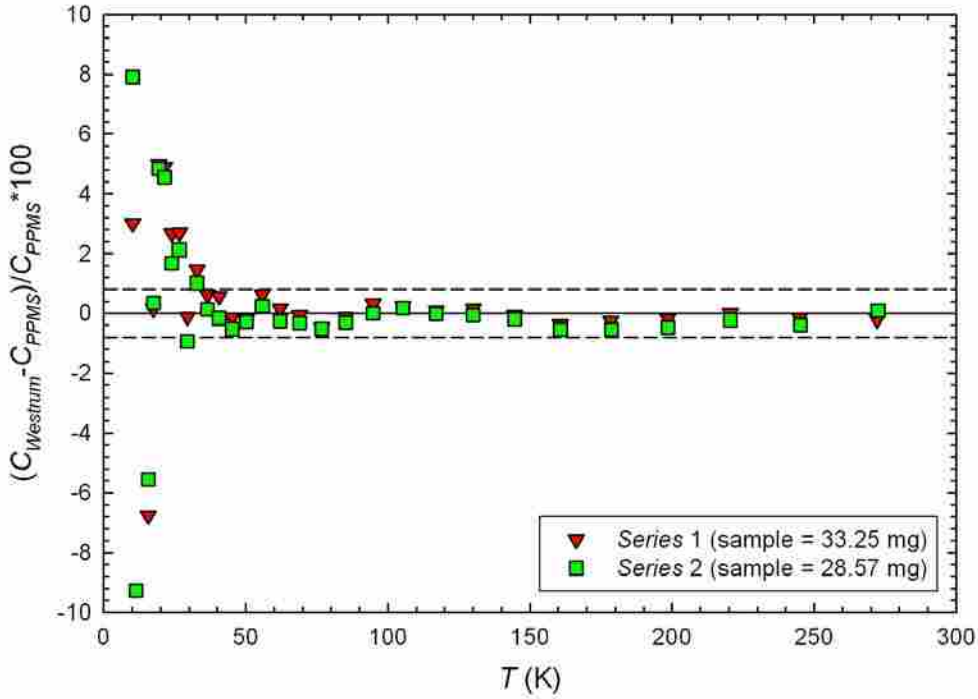

Figure 3.3. Percent deviation of the heat capacity measured by PPMS from measurements by Westrum and Gronvold.[5]

Table 3.1. Molar heat capacity of hematite (α-Fe_2O_3) *Series* 1. M = 159.69 g·mol^{-1}

T / K	$C_{p,m}$ / (J • K^{-1} • mol^{-1})	T / K	$C_{p,m}$ / (J • K^{-1} • mol^{-1})
1.9541	0.00070104	26.594	1.0593
2.1567	0.00093836	29.495	1.5099
2.3181	0.00115	32.823	2.1561
2.5461	0.0014856	36.516	3.032
2.8188	0.0019405	40.597	4.1877
3.1219	0.0025902	45.138	5.6233
3.4585	0.003456	50.197	7.4647
3.8503	0.0045692	55.788	9.7205
4.2841	0.006133	62.034	12.463
4.755	0.0080633	68.977	15.665
5.2823	0.01059	76.67	19.414
5.8708	0.01379	85.232	23.87
6.5297	0.018178	94.744	28.898
7.2662	0.023863	105.29	34.294
8.0867	0.030711	117.04	40.288
9.0149	0.040392	130.07	46.896
10.176	0.054913	144.59	53.709
11.395	0.074045	160.65	60.907
12.666	0.099194	178.51	68.285
14.074	0.13228	198.45	75.828
15.676	0.18189	220.54	83.465
17.441	0.25158	245.04	90.728
19.331	0.35724	272.19	97.802
21.478	0.50603	302.42	104.51
23.916	0.73218		

Table 3.2 Molar heat capacity of hematite (α-Fe_2O_3) *Series* 2. M = 159.69 g·mol^{-1}

T / K	$C_{p,m}$ / (J • K^{-1} • mol^{-1})	T / K	$C_{p,m}$ / (J • K^{-1} • mol^{-1})
1.9042	0.00076921	26.548	1.0469
2.0321	0.00089922	29.519	1.5018
2.2840	0.0012784	32.838	2.1501
2.5220	0.0016728	36.532	3.0214
2.8041	0.0022341	40.610	4.1605
3.1213	0.0030526	45.150	5.6065
3.4652	0.0040369	50.199	7.4583
3.8467	0.0053558	55.802	9.6894
4.2680	0.0070385	62.039	12.413
4.7556	0.0093363	68.975	15.625
5.3130	0.012390	76.682	19.409
5.8904	0.015619	85.239	23.827
6.5481	0.020407	94.760	28.814
7.2886	0.026202	105.28	34.265
8.1128	0.033507	117.04	40.247
9.0343	0.043294	130.04	46.777
10.224	0.058732	144.57	53.620
11.411	0.077078	160.72	60.834
12.680	0.10093	178.60	68.124
14.088	0.13779	198.53	75.641
15.700	0.18486	220.58	83.282
17.426	0.25149	245.13	90.538
19.324	0.35634	272.48	98.155
21.493	0.50565	302.78	106.92
23.926	0.72611		

3.4 Discussion

3.4.1 Contributions to the Heat Capacity of Hematite

Modeling heat capacity data with theoretical functions at low temperatures (< 15 K) can provide valuable information about the magnetic, electronic, and vibrational properties of a sample.[7] The total heat capacity can be viewed as a sum of the energetic contributions from the various physical properties of a material. At temperatures above 10 K, the largest contribution to heat capacity stems from lattice vibrations which are modeled by an odd-powers fit to the equation:[12]

$$C_{Lat} = \sum_{n=3,5,7\ldots} B_n T^n \,. \quad (1)$$

Magnetic contributions will also have a temperature-dependence with $T^{3/2}$ for ordered ferro- and ferrimagnets and T^3 for antiferromagnets.[7]

Conduction electrons contribute to the heat capacity in a linear fashion with γT representing the electronic heat capacity in most cases.[7] In addition to conducting solids, a linear term is generally observed in many oxide materials that are not fully stoichiometric or which contain oxygen vacancies or dislocations.[13] For example, non-conducting oxides requiring a linear term include α-FeOOH (goethite),[13] crystalline pure SiO_2 zeolites,[14] and hydrous potassium aluminosilicate[15] (muscovite) where the linear term has been attributed by Coey *et al.*[15] to localized electronic states associated with oxygen vacancies.

3.4.2 Fits of Bulk Hematite

As seen in the characterization of this sample by XRD, bulk hematite is an ordered solid which will have a significant lattice contribution of the form $C_{Lat} = \sum B_n T^n$. Magnetic characterization of bulk hematite generally shows that below the Morin transition hematite is an antiferromagnet which is represented with a T^3 term. However in some conditions samples of hematite have shown ferromagnetic behavior at temperatures as low as 2 K, and consequently some fits were made using a $T^{3/2}$ term. As other oxide samples have included a linear term, fits were also made using γT to check whether the linear term made a significant improvement in representing the heat capacity of bulk hematite.

The heat capacity of bulk hematite in the temperature range 2 to 10 K was fit with a wide variety of fitting expressions which consisted of different combinations of the above terms. A summary of a number of different fits are given in Table 3.3 for bulk hematite which follow the expression:

$$C = \gamma T + \sum_{n=3,5,7} B_n T^n + B_{fsw} T^{3/2} . \quad (2)$$

Equation 2 can be viewed as a generalized formula that is modified by setting any coefficient equal to zero. In cases where a coefficient is zero, its corresponding term will be omitted from the equation.

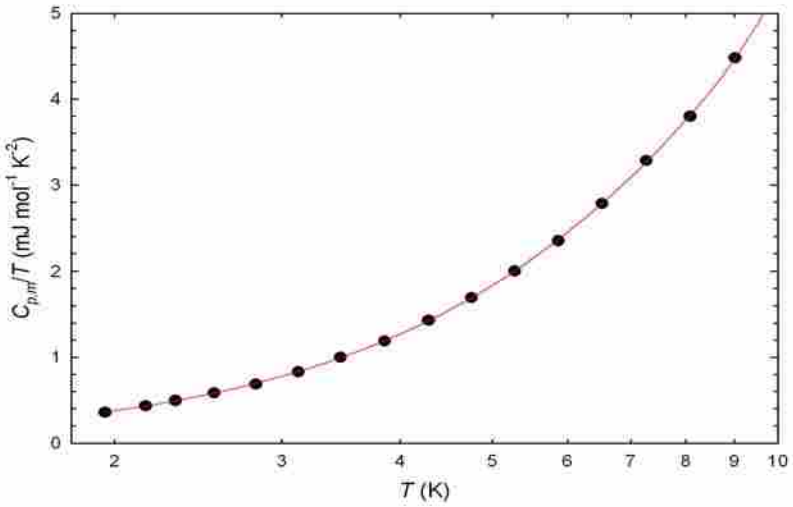

Figure 3.4. Low-temperature fit of bulk hematite heat capacity. Circles are experimental data. Red line is the fit.

Table 3.3. Parameters for equation 3. Units are in mJ, mole, and K.

Parameter	Fit-1	Fit-2	Fit-3	Fit-4
γ		4.5994E-02	-15.446	
B_3 (α)	0.083190	8.5981E-02	0.38144	9.4175E-02
B_5	-5.8426E-04	-6.2920E-04	2.280	-8.7321E-04
B_7	2.6530E-06	2.9055E-06		4.6191E-06
B_{fsw}	0.039629		10.079	
RMS%	0.74	0.83	3.34	2.25

Before a discussion can be given of the thermophysical properties of bulk hematite it is necessary to determine which of the fits described in Table 3.3 is the best. Upon immediate inspection it can be seen that Fit-3 has a negative value for γ, which is physically meaningless. However Fit-3 was included in Table 3.3 because it can still provide some valuable insight, which will be discussed later on. A comparison of the %RMS values for the remaining fits shows that Fit-4 has a %RMS of 2.25 which significantly larger value than 0.74 and 0.83 for Fits 1 and 2 respectively. This suggests that Fit-4 is missing some contribution that can more accurately represent the heat capacity of bulk hematite. The %RMS values for Fits 1 and 2 are too similar to allow one to determine which is the best fit, and more information will be necessary.

A graph of these two fits and experimentally measured data can be found in Figure 3.5 where it can be seen that both fits match the experimental heat capacity well.

To facilitate the comparison of the fits, the percent deviation of Fits 1, 2, and 4 from the experimentally measured heat capacity of hematite are shown in Figure 3.5.
Fit-4 shows a large degree of error compared to Fits 1 and 2, which display a random deviation about zero. This indicates that a lattice contribution alone is insufficient to correctly model the heat capacity of hematite. The similar deviations of Fits 1 and 2 as well as their low %RMS values make it difficult to conclude whether the linear term or the ferromagnetic spin wave makes the best fit.

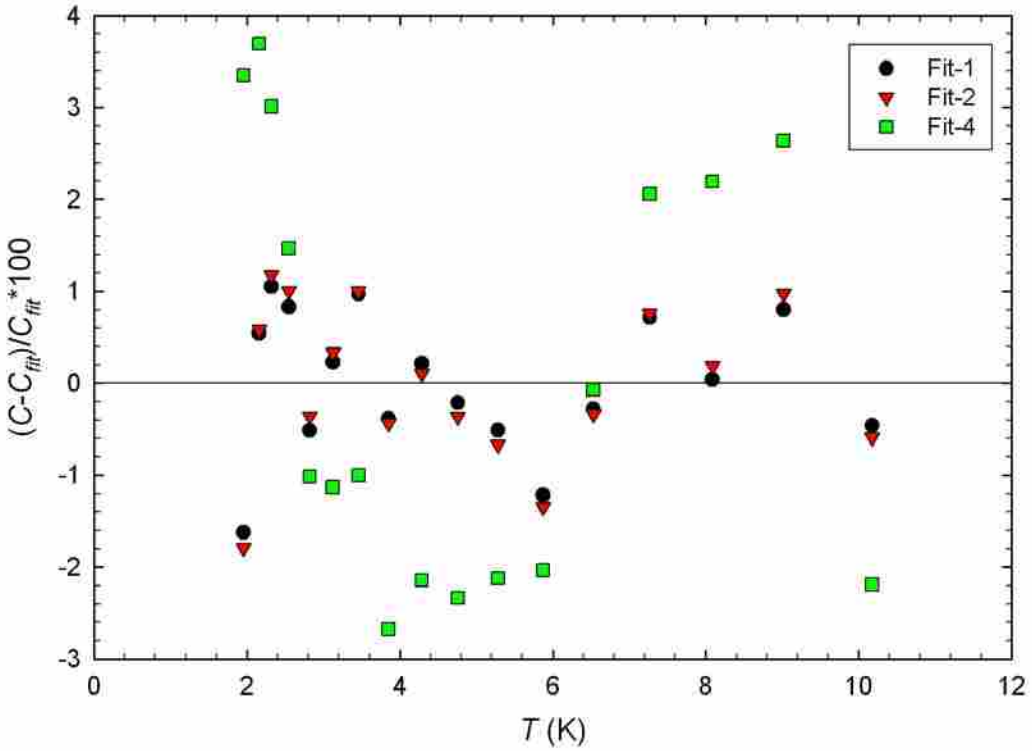

Figure 3.5. Percent deviation of fits from the experimentally measured heat capacity of hematite.

It is important to note that Fit-3 included both a linear term and a ferromagnetic spin wave, yet was physically meaningless. Likewise other fits that used both terms gave similar results. This suggests that either hematite has ferromagnetic coupling at low temperatures or there are electronic contributions due to oxygen deficiencies, but not both. To determine which fit is the best, it is useful to compare more basic fitting expressions that use similar terms which allows one to see the effects of a given term on the fit of the heat capacity. When bulk hematite is fit to the expression $C = \gamma T + B_3 T^3$ a

%RMS of 8.84 is obtained while a fit to $C = B_{fsw}T^{3/2} + B_3T^3$ gave a %RMS of 4.26. This suggests that the heat capacity of hematite has contributions from a ferromagnetic spin wave and that Fit-1 is more accurate since such a term can model the heat capacity with approximately half as much error as a linear term. Furthermore the use of a spin wave is more likely since some samples of hematite have shown ferromagnetic behavior at low temperatures.

Since hematite is an antiferromagnet below T_M, the use of a ferromagnetic spin wave is surprising. Yet as mentioned previously, under certain conditions hematite has been shown to have ferromagnetic behavior as low as 2 K. A variety of techniques have been employed in the study of the magnetic properties of hematite including neutron diffraction,[6] magnetometry,[2] and Mossbauer spectroscopy.[16] These studies have shown that small particle size and porous samples of hematite do not undergo the spin-flip transition and retain their ferromagnetic behavior at low temperatures. The bulk sample used in these studies was prepared by sintering nanocrystalline hematite, which may suggest a reason for its observed magnetic properties. The sample characterization clearly shows grain growth, which eliminates the explanation of small particle size. However the characterization of bulk hematite was not so clear with respect to the porosity of the sample. BET surface area measurements were unable to provide a pore size, and the low surface are suggests that the sample is not very porous. The use of a spin wave in the fitting expression for this bulk hematite sample suggests that there are other conditions in which bulk hematite does not undergo the spin-flip transition and will have ferromagnetic properties at low-temperatures. One of these conditions may be that this sample is polycrystalline, and heat capacity studies of a single crystal of bulk hematite would be useful.

Although ferromagnetic behavior has been observed in this bulk hematite sample, hematite has generally been characterized as antiferromagnetic.[2, 6] These two types of magnetism will not be displayed simultaneously, and it is important to determine whether or not the T^3 term has an antiferromagnetic contribution. This can be accomplished by examining the contributions to the heat capacity from the T^3 term which can stem from a combination of lattice vibrations and antiferromagnetic coupling.[7] Generally, the antiferromagnetic contributions are ten to twenty times larger than the lattice component

at low-temperatures.[7] This can be seen in a comparison of the low-temperature heat capacity of antiferromagnetic $MnCO_3$ and nonmagnetic $CaCO_3$.[7] These two samples have a similar lattice contribution but the contribution of T^3 in $MnCO_3$ is many times that of $CaCO_3$. In the case of hematite, other iron oxides make good candidates for such a comparison. While the heat capacity of many iron oxides has been measured below 10 K,[13, 17, 18] the only published study to give an extensive analysis of the low-temperature heat capacity involved α-FeOOH (goethite).[13] Fits of goethite at low temperatures were able to separate the contributions of lattice vibrations from antiferromagnetic contributions. These fits give a value of ~ 0.1 for B_3 while the antiferromagnetic parameter B_{asw} has a value of 1.16, which is about ten times larger. The antiferromagnetic term for goethite was coupled to an anisotropic gap parameter which does not give the best comparison to antiferromagnetism. However this bulk hematite and goethite do have similar lattice terms where B_3 for hematite is 0.083 and goethite has a value of 0.1. Other recent low-temperature fits (unpublished) in our lab of ferrimagnetic 13 nm magnetite gave a value of 0.587 for B_3 which is about 6 times as large as that of bulk hematite. The similarity between the lattice contributions of goethite and the T^3 dependence of hematite suggests that antiferromagnetic coupling does not exist in hematite at low-temperatures. Also, the large size of B_3 for 13 nm magnetite compared to that of bulk hematite agrees with this conclusion since 13 nm magnetite is ferrimagnetic.

3.4.3 Thermodynamic Functions of Hematite

The standard molar thermodynamic functions, $C_{p,m}$, $\Delta^T_0 H^\circ_m$, $\Delta^T_0 S^\circ_m$, and $\Phi^\circ_m=(\Delta^T_0 S^\circ_m-\Delta^T_0 H^\circ_m/T)$ scaled by the ideal gas constant R are reported for *Series* 1 (Table 3.4) and *Series* 2 (Table 3.5). The values have been generated at smoothed temperatures by fitting a combination of orthogonal polynomials to the experimental results for the two series which were merged with the low-temperature fits. The parameters for these fits as well as their temperature range can be found in Tables 3.6 and 3.7, respectively. The standard molar entropy at 298.15 K was calculated to be 87.32 ± 2 $J{\cdot}mol^{-1}{\cdot}K^{-1}$ for *Series* 1 and 87.27 ± 2 $J{\cdot}mol^{-1}{\cdot}K^{-1}$ for *Series* 2, which are in good agreement with the value of 87.40 ± 0.2 $J{\cdot}mol^{-1}{\cdot}K^{-1}$ (originally 20.889 $cal{\cdot}deg^{-1}{\cdot}mole^{-1}$) calculated by Westrum and Gronvold.[5]

Table 3.4. Standard thermodynamic functions of Hematite (α-Fe_2O_3) *Series* 1 where $\Phi = \Delta S - \Delta H/T$, M = 159.69 g·mol^{-1}, $p°$ = 100 kPa, and R = 8.3145 J·K^{-1}·mol^{-1}.

T/K	$C_{p,m}/R$	$\Delta_0^T S_m^o/R$	$\Delta_0^T H_m^o/RT$	Φ_m^o/R
2.0	9.11E-05	3.66E-05	2.52E-05	1.14E-05
2.5	0.00017	6.46E-05	4.56E-05	1.90E-05
3.0	0.00028	0.0001	7.48E-05	2.98E-05
3.5	0.00043	0.00016	0.00011	4.41E-05
4.0	0.00061	0.00023	0.00016	6.25E-05
4.5	0.00084	0.00031	0.00023	8.54E-05
5.0	0.00111	0.00041	0.0003	0.00011
5.5	0.00142	0.00053	0.00039	0.00015
6.0	0.00177	0.00067	0.00049	0.00018
6.5	0.00216	0.00083	0.0006	0.00023
7.0	0.00259	0.001	0.00073	0.00028
7.5	0.00307	0.0012	0.00087	0.00033
8.0	0.0036	0.00141	0.00102	0.00039
8.5	0.00419	0.00165	0.00119	0.00046
9.0	0.00483	0.00191	0.00137	0.00053
9.5	0.00555	0.00219	0.00157	0.00061
10	0.00633	0.00249	0.00179	0.0007
11	0.00813	0.00318	0.00228	0.00089
12	0.01025	0.00397	0.00286	0.00111
13	0.01275	0.00489	0.00352	0.00137
14	0.0157	0.00594	0.00428	0.00166
15	0.01917	0.00714	0.00515	0.00198
16	0.02327	0.0085	0.00616	0.00234
17	0.02809	0.01005	0.0073	0.00275
18	0.03371	0.01181	0.00861	0.0032
19	0.04024	0.01381	0.0101	0.00371
20	0.04776	0.01606	0.01179	0.00427
25	0.10296	0.03206	0.02398	0.00808
30	0.19245	0.05819	0.04409	0.0141
35	0.31879	0.09687	0.07388	0.023
40	0.48026	0.14961	0.11423	0.03538
45	0.67256	0.21701	0.16533	0.05168

Table 3.4 continued

T/K	$C_{p,m}/R$	$\Delta_0^T S_m^o/R$	$\Delta_0^T H_m^o/RT$	Φ_m^o/R
50	0.89066	0.29895	0.22676	0.07219
55	1.13	0.39491	0.29784	0.09706
60	1.3867	0.50412	0.37777	0.12635
65	1.6583	0.62575	0.46575	0.16001
70	1.9425	0.75898	0.56102	0.19797
75	2.2377	0.90301	0.6629	0.24011
80	2.5425	1.0571	0.7708	0.28631
85	2.8541	1.2205	0.88417	0.33641
90	3.1688	1.3926	1.0023	0.39027
95	3.4846	1.5724	1.1247	0.44772
100	3.7999	1.7591	1.2506	0.50859
110	4.4236	2.1507	1.5107	0.63992
120	5.0337	2.5618	1.7791	0.78283
130	5.6269	2.9883	2.0523	0.93598
140	6.2012	3.4264	2.3282	1.0982
150	6.7555	3.8732	2.6051	1.2683
160	7.2887	4.3264	2.8812	1.4452
170	7.8	4.7837	3.1557	1.6281
180	8.2883	5.2435	3.4274	1.8162
190	8.7531	5.7043	3.6955	2.0087
200	9.1945	6.1645	3.9595	2.2049
210	9.6127	6.6234	4.2189	2.4045
220	10.009	7.0797	4.4731	2.6067
230	10.384	7.533	4.722	2.811
240	10.74	7.9824	4.9654	3.0171
250	11.077	8.4278	5.2032	3.2246
260	11.398	8.8686	5.4353	3.4333
270	11.702	9.3045	5.6619	3.6427
273.15	11.794	9.4407	5.732	3.7087
280	11.989	9.7353	5.8827	3.8525
290	12.258	10.161	6.098	4.0628
298.15	12.465	10.503	6.2693	4.2342
300	12.509	10.581	6.3077	4.273

Table 3.5. Standard thermodynamic functions of Hematite (α-Fe_2O_3) *Series* 2 where $\Phi = \Delta S - \Delta H/T$, M = 159.69 g·mol^{-1}, $p°$ = 100 kPa, and R = 8.3145 J·K^{-1}·mol^{-1}.

T/K	$C_{p,m}/R$	$\Delta_0^T S_m^o/R$	$\Delta_0^T H_m^o/RT$	Φ_m^o/R
2.0	1.05E-04	3.92E-05	5.59E-05	1.12E-05
2.5	1.97E-04	7.18E-05	1.30E-04	1.99E-05
3.0	3.27E-04	1.19E-04	2.59E-04	3.22E-05
3.5	4.99E-04	1.81E-04	4.64E-04	4.88E-05
4.0	7.14E-04	2.61E-04	7.65E-04	7.02E-05
4.5	9.72E-04	3.60E-04	1.18E-03	9.68E-05
5.0	1.27E-03	4.78E-04	1.74E-03	1.29E-04
5.5	1.61E-03	6.14E-04	2.46E-03	1.67E-04
6.0	1.99E-03	7.71E-04	3.36E-03	2.10E-04
6.5	2.41E-03	9.46E-04	4.46E-03	2.60E-04
7.0	2.86E-03	1.14E-03	5.78E-03	3.16E-04
7.5	3.36E-03	1.36E-03	7.33E-03	3.78E-04
8.0	3.90E-03	1.59E-03	9.14E-03	4.46E-04
8.5	4.50E-03	1.84E-03	1.12E-02	5.21E-04
9.0	5.16E-03	2.12E-03	1.37E-02	6.02E-04
9.5	5.88E-03	2.42E-03	1.64E-02	6.89E-04
10	6.67E-03	2.74E-03	1.95E-02	7.84E-04
11	8.46E-03	3.46E-03	2.71E-02	9.93E-04
12	1.06E-02	4.28E-03	3.66E-02	1.23E-03
13	1.31E-02	5.22E-03	4.84E-02	1.50E-03
14	1.60E-02	6.30E-03	6.29E-02	1.81E-03
15	1.95E-02	7.52E-03	8.06E-02	2.14E-03
16	2.36E-02	8.91E-03	1.02E-01	2.52E-03
17	2.83E-02	1.05E-02	1.28E-01	2.94E-03
18	3.39E-02	1.22E-02	1.59E-01	3.41E-03
19	4.03E-02	1.42E-02	1.96E-01	3.93E-03
20	4.76E-02	1.65E-02	2.40E-01	4.50E-03
25	1.02E-01	3.24E-02	6.01E-01	8.34E-03
30	1.91E-01	5.83E-02	1.32E+00	1.44E-02
35	3.17E-01	9.68E-02	2.58E+00	2.32E-02
40	4.78E-01	1.49E-01	4.55E+00	3.55E-02
45	6.69E-01	2.16E-01	7.41E+00	5.18E-02

Table 3.5 continued

T/K	$C_{p,m}/R$	$\Delta_0^T S_m^o/R$	$\Delta_0^T H_m^o/RT$	Φ_m^o/R
50	8.87E-01	2.98E-01	1.13E+01	7.22E-02
55	1.13E+00	3.94E-01	1.63E+01	9.70E-02
60	1.38E+00	5.02E-01	2.26E+01	1.26E-01
65	1.66E+00	6.24E-01	3.02E+01	1.60E-01
70	1.94E+00	7.57E-01	3.91E+01	1.97E-01
75	2.23E+00	9.00E-01	4.96E+01	2.40E-01
80	2.54E+00	1.05E+00	6.15E+01	2.86E-01
85	2.85E+00	1.22E+00	7.50E+01	3.36E-01
90	3.16E+00	1.39E+00	9.00E+01	3.89E-01
95	3.48E+00	1.57E+00	1.07E+02	4.47E-01
100	3.79E+00	1.76E+00	1.25E+02	5.07E-01
110	4.42E+00	2.15E+00	1.66E+02	6.38E-01
120	5.03E+00	2.56E+00	2.13E+02	7.81E-01
130	5.62E+00	2.98E+00	2.66E+02	9.34E-01
140	6.19E+00	3.42E+00	3.25E+02	1.10E+00
150	6.74E+00	3.87E+00	3.90E+02	1.27E+00
160	7.27E+00	4.32E+00	4.60E+02	1.44E+00
170	7.78E+00	4.77E+00	5.35E+02	1.62E+00
180	8.27E+00	5.23E+00	6.16E+02	1.81E+00
190	8.73E+00	5.69E+00	7.01E+02	2.00E+00
200	9.17E+00	6.15E+00	7.90E+02	2.20E+00
210	9.59E+00	6.61E+00	8.84E+02	2.40E+00
220	9.98E+00	7.06E+00	9.82E+02	2.60E+00
230	1.04E+01	7.52E+00	1.08E+03	2.81E+00
240	1.07E+01	7.96E+00	1.19E+03	3.01E+00
250	1.11E+01	8.41E+00	1.30E+03	3.22E+00
260	1.14E+01	8.85E+00	1.41E+03	3.43E+00
270	1.17E+01	9.29E+00	1.53E+03	3.63E+00
273.15	1.18E+01	9.42E+00	1.56E+03	3.70E+00
280	1.21E+01	9.72E+00	1.64E+03	3.84E+00
290	1.24E+01	1.01E+01	1.77E+03	4.05E+00
298.15	1.27E+01	1.05E+01	1.87E+03	4.23E+00
300	1.28E+01	1.06E+01	1.89E+03	4.26E+00

Table 3.6. Parameters for fits of the heat capacity of hematite *Series* 1. Units are in J, mole, and K.

Powers	Temperature Ranges	Coefficients
	$0 \leq T\,(\mathrm{K}) \leq 9.9$	
1		3.620950E-05
3		8.870109E-05
5		-7.995470E-07
7		6.075500E-09
9		-1.718381E-11
	$9.9 \leq T\,(\mathrm{K}) \leq 76.0$	
0		1.584123E-01
1		-6.904413E-02
2		1.225543E-02
3		-1.034390E-03
4		5.035171E-05
5		-1.270369E-06
6		1.855010E-08
7		-1.597010E-10
8		7.566424E-13
9		-1.527721E-15
	$76.0 \leq T\,(\mathrm{K}) \leq 305.0$	
0		4.333282E+01
1		-2.573582E+00
2		6.278703E-02
3		-7.023903E-04
4		4.793339E-06
5		-2.057930E-08
6		5.401251E-11
7		-7.903096E-14
8		4.933786E-17

Table 3.7. Parameters for fits of the heat capacity of hematite *Series* 2. Units are in J, mole, and K.

Powers	Temperature Range	Coefficients
	$0 \le T\,(\mathrm{K}) \le 8.8$	
1		0.02240755
3		0.10821692
5		-1.2005184E-03
7		9.4876256E-06
9		-2.7659340E-08
	$8.8 \le T\,(\mathrm{K}) \le 70.5$	
0		-147.96760
1		78.264648
2		-17.338673
3		2.2562558
4		-0.17394824
5		8.57955848E-03
6		-2.6730764E-04
7		5.3604435E-06
8		-6.9249393E-08
9		5.5748589E-10
10		-2.5449416E-12
11		5.0308269E-15
	$70.5 \le T\,(\mathrm{K}) \le 305.0$	
0		22597.43858
1		-1401.29387
2		34.8330425
3		-0.335129448
4		1.8792126E-03
5		-6.2542054E-06
6		1.1345043E-08
7		-8.5828132E-12

References

1. Cornell, R. M.; Schwertmann, U.; Editors, *The Iron Oxides: Structure, Properties, Reactions, Occurrence and Uses*. VCH: Weinem, 1996; p 573.
2. Bahl, C. R. H. *The magnetic properties of antiferromagnetic nanoparticles: NiO and alpha -Fe2O3*; Information Service Department,Riso National Laboratory,Roskilde,Den.: 2006; pp i-vi,1-100.
3. Carbone, C.; Di Benedetto, F.; Sangregorio, C.; Marescotti, P.; Pardi, L. A.; Sorace, L., *J. Phys. Chem. C* **2008,** *112* (27), 9988-9995.
4. Lee, J. D., *Phys. Rev. B: Condens. Matter Mater. Phys.* **2004,** *70* (17), 174450/1-174450/6.
5. Gronvold, F.; Westrum, E. F., Jr., *J. Am. Chem. Soc.* **1959,** *81*, 1780-3.
6. Hill, A. H.; Jiao, F.; Bruce, P. G.; Harrison, A.; Kockelmann, W.; Ritter, C., *Chem. Mater.* **2008,** *20* (15), 4891-4899.
7. Gopal, E. S. R., *Specific Heats at Low Temperatures (International Cryogenics Monograph Series)*. Plenum Press: New York, 1966; p 226
8. Ott, J. B.; Boerio-Goates, J., *Chemical Thermodynamics: Principles and Applications*. 2000; p 360 pp.
9. Parks, G. S.; Kelley, K. K., *J. Phys. Chem.* **1926,** *30*, 47-55.
10. Jayasuriya, K. D.; Stewart, A. M.; Campbell, S. J., *J. Phys. Chem. Solids* **1985,** *46* (5), 625-9.
11. Liu, S.; Liu, Q.; Boerio-Goates, J.; Woodfield, B. F., *J. Adv. Mater. (Covina, CA, U. S.)* **2007,** *39* (2), 18-23.
12. Phillips, N. E., *Crit. Rev. Solid State Sci.* **1971,** *2* (4), 467-553.
13. Majzlan, J.; Navrotsky, A.; Woodfield, B. F.; Lang, B. E.; Boerio-Goates, J.; Fisher, R. A., *J. Low Temp. Phys.* **2003,** *130* (1/2), 69-76.
14. Boerio-Goates, J.; Stevens, R.; Lang, B.; Woodfield, B. F., *J. Therm. Anal. Calorim.* **2002,** *69* (3), 773-783.
15. Coey, J. M. D.; Von Molnar, S.; Torressen, A., *J. Less-Common Met.* **1989,** *151*, 191-4.
16. Morup, S.; Frandsen, C.; Bodker, F.; Klausen, S. N.; Lefmann, K.; Lindgard, P.-A.; Hansen, M. F., *Hyperfine Interact.* **2003,** *144/145* (1-4/1-4), 347-357.
17. Majzlan, J.; Lang, B. E.; Stevens, R.; Navrotsky, A.; Woodfield, B. F.; Boerio-Goates, J., *Am. Mineral.* **2003,** *88* (5-6), 846-854.
18. Koenitzer, J. W.; Keesom, P. H.; Honig, J. M., *Phys. Rev. B: Condens. Matter Mater. Phys.* **1989,** *39* (9), 6231-3.

Chapter 4

Size-Dependence of the Heat Capacity and Thermodynamic Properties of Hematite (α-Fe_2O_3)

4.1 Introduction

Hematite (α-Fe_2O_3) is considered to be the most stable form of iron oxide, and can be found naturally in rocks, mud, and water systems.[2, 3] The catalytic, electronic, and magnetic properties of hematite have been extensively investigated leading to a wide variety of applications. Some technologies that employ hematite include gas sensors, electrode materials in lithium secondary batteries, catalysts, magnetic recording media, and optical and electromagnetic devices as well as water splitting treatments.[3-7] In addition to its many applications, the use of hematite is attractive owing to its nontoxicity, low processing cost, and high resistance to oxidative change.[7, 8]

Studies involving hematite have begun to focus on the size-dependence of its chemical and physical properties, and a comparison of bulk and nanoscale behavior reveals significant changes in the properties of hematite. Some studies[9, 10] have concluded that small particle size may alter the energy positions of the electronic states that define the semiconductor band gap, yet a recent study suggests no change in the electronic properties of hematite.[11] The magnetic behavior of nanocrystalline hematite has also been shown to deviate from that of bulk hematite.[12-26] At room temperature bulk hematite is weakly ferromagnetic, but below 260 K (T_M) hematite undergoes a first order spin reorientation called the Morin transition. The net magnetic moment is lost in this process, and bulk hematite transforms into an antiferromagnet. In contrast, magnetization studies on nanocrystalline and mesoporous samples of hematite show that no spin reorientation occurs upon cooling, and ferromagnetic behavior persists as low as 2 K.[7] Many studies also show that hematite nanoparticles display superparamagnetic properties.[8-10]

In addition to magnetic and electronic measurements, thermodynamic studies of nanosystems provide sophisticated characterization and a more quantitative approach to phase stability. A comprehensive thermodynamic study of the many iron oxides and iron oxyhyrdoxides (FeOOH) has been undertaken by Navrotsky and coworkers[11-19] who have recently published a summary of current thermodynamic understanding of these materials.[11] This work has included the measurement of heat capacities and thermochemical measurements which can be used to obtain the standard Gibbs free energy of formation at 298.15 K, and bulk hematite has been shown to be the most stable iron oxide with a Gibbs free energy of formation of -744.4 ± 1.3 kJ/mol. In these studies, the importance of particle size and degree of hydration has been a key point in determining the energetics of the iron oxide polymorphs.[11] Surface enthalpy (whether comparing wet or dry surfaces) has been shown to be much higher for the anhydrous phases (oxides) than for any of the hydrous phases (oxyhyrdoxides). A lower surface enthalpy allows oxyhydroxides to exist with larger surface areas and to be thermodynamically more competitive at smaller particle sizes.[11] This can be seen in the dehydration reaction from goethite (α-FeOOH) to hematite ($2FeOOH = Fe_2O_3 + H_2O$) where smaller particle sizes allow goethite to persist to temperatures more than 100 K higher than those calculated by bulk thermodynamic relationships.[11] Another observation of surface enthalpy measurements is that materials with the highest surface enthalpy are stabilized by the adsorption of water.[11] As metastability of the bulk phase increases its surface enthalpy decreases, which has been seen as possibly a close to universal trend and not just with the iron oxides.[20] The decrease of surface enthalpy with increasing metastability of the bulk polymorphs leads to crossovers in free energy of the polymorphs at the nanoscale.[11] This has been seen in the iron oxides as γ-Fe_2O_3 (maghemite) becomes stable with respect to hematite at the nanoscale, and there are complex crossovers for the FeOOH polymorphs as well.[11] This phenomenon emphasizes the need to consider nanoscale phenomena when studying phase stability and reactivity. In general, the thermodynamics of different polymorphs at the nanoscale depends on the energetics of the bulk polymorphs, the particle size, and the extent of hydration.[11]

Size driven thermodynamic differences among iron oxide phases must be taken into account if the formation, stability, and transformation of these materials in geologic,

environmental, and industrial settings are to be understood and predicted.[11] Heat capacity measurements of nanocrystalline hematite can aid in this understanding as they can provide information about the density of vibrational states as well as the electronic and magnetic properties of solids.[27, 30] Heat capacities can also be used to generate third-law entropies that, when combined with thermochemical measurements, yield relative free energies of the nanoparticles. In turn, free energies give information about the phase stabilities of the particles relative to each other and to their parent bulk materials.

The heat capacity of bulk hematite was first measured by Parks and Kelley in 1926 over four narrow regions from 90 K to 290 K.[27, 28, 31] In 1958, Westrum and Gronvold improved upon these measurements covering the range from 5 K to 350 K.[6] No anomaly in the heat capacity due to the Morin transition was observed in this study or in another later series of measurements in 1985 by Jayasuriya *et al.*[21] While Jayasuriya did not provide any values for the entropy of hematite, Westrum and Gronvold calculated the entropy of hematite at 298.15 K to be 87.40 $J \cdot mol^{-1} \cdot K^{-1}$. Recently, the heat capacity of nanocrystalline hematite was measured in the temperature range 253 to 283 K with a reported accuracy of ± 1.5%.[22] Because of its small temperature range, this data is insufficient to calculate the entropy associated with nanocrystalline hematite; however, the authors state that their research purpose was to study the magnetocaloric effect in nanosystems, and thus thermodynamic calculations and physical modeling of heat capacity were not within their scope.

While the heat capacity of nanocrystalline hematite has not been adequately measured, heat capacity measurements for several metal and metal oxide nanoparticle systems are available.[27, 34-39] It was previously accepted that the heat capacity of nanoparticles exceeds that of their bulk counterparts with the larger heat capacity being attributed to the increase of surface atoms, which have different vibrational modes than interior atoms.[23, 24, 25] More recently, a careful study regarding the origin of the excess heat capacity in nanoparticles was carried out by Boerio-Goates *et al.*[4] on anatase and rutile polymorphs of TiO_2. The heat capacity of 7 nm TiO_2 nanoparticles decreased proportionally with the degree of hydration, and the excess heat capacity was shown to be caused by water adsorbed onto the surface of the nanoparticles. When the contributions of the adsorbed water were subtracted from the heat capacity it was shown that, within

experimental error, the bare small particle heat capacity was the same as that of the bulk. Also, the water showed two types of behavior. Layers of water closer to the surface of the nanoparticles had a low heat capacity due to tight binding while outer layers were similar to liquid water. These studies by Boerio-Goates *et al.* agree with the conclusions of Navrotsky *et al.*[11] that the degree of hydration must be taken into account when studying the thermodynamic properties of nanosystems.

This work aims to complement the thermodynamic studies of the iron oxides undertaken by Navrotsky *et al.* Like the measurements carried out on nanocrystalline TiO_2 polymorphs[4] this study will compare the thermodynamic properties of nanocrystalline hematite to those of the bulk material. This study provides the heat capacity of a hematite powder with an average crystal size of 13 nm in the temperature range 1.5 to 350 K. A comparison to new bulk hematite data measured from 2 to 300 K (to be published separately) is made with a discussion on the effects of water adsorbed onto the surface of nanocrystalline hematite.

4.2 Experimental

Nanocrystalline hematite was prepared through a solid state reaction following the method described by Liu *et al.*[26] Solid NH_4HCO_3 was combined with 99.99% pure $Fe(NO_3)_3 \cdot 9H_2O$ in a 3:1 Fe^{3+}:HCO_3^- molar ratio. The mixture of the two dry powders turned into a wet slurry which rapidly produced bubbles of CO_2(g). The mixture was continuously ground (15-30 minutes) in an alumina mortar until the evolution of bubbles ceased. A dark brown solid precipitated in this slurry which was dried in air at 50°C for 20 hours. The solid powder was then rinsed with water using a vacuum filtration flask, transferred to a pyrex dish, then calcined in air at 270°C for 45 minutes.

The sample was characterized by powder x-ray diffraction (XRD) on a Scintag Diffractometer (Cu-Kα radiation, λ = 1.54176 nm) at a scanning rate of 0.1 2θ/min and a power of 15 kW over the range 25 to 70°. The resulting pattern (Figure 4.1) showed the product to be pure hematite in agreement with JCPDS card number 00-001-1053. Using the full peak width at half the maximum intensity and the Scherrer formula, the average crystallite diameter was calculated to be 13 nm.

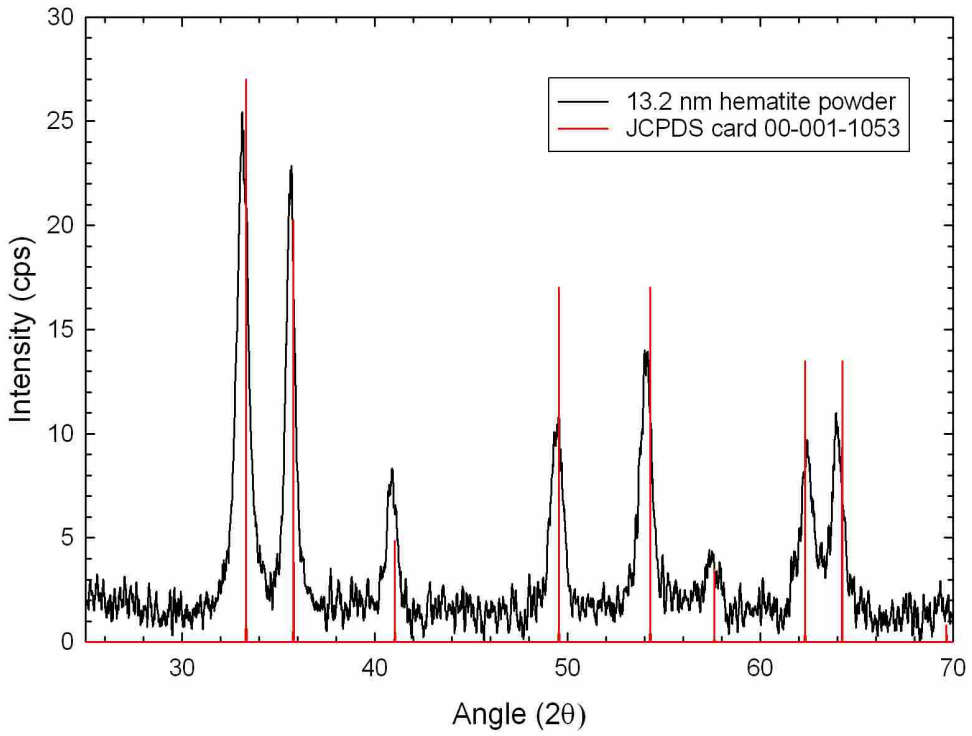

Figure 4.1. Powder X-ray Diffraction spectrum of hematite powder.

A sample was prepared for transmission electron microscopy (TEM) by dispersing a small amount of hematite powder in ethanol and grinding with an agate mortar and pestle. The mixture was allowed to rest for 24 hours in a glass test tube before drawing off the supernatant. A drop of this suspension was then placed on a copper grid with 3 nm carbon backing and microscopy images were acquired using a Tecnai F30 TEM. Micrographs of the hematite powder are shown in Figures 4.2a and 4.2b. Figure 4.2a, which show the particles at 200 kx magnification gives an idea of the size dispersion and morphology. The particles are roughly spherical, and most have a diameter of ~ 10 nm. Figure 4.2b shows these particles at 310 kx where ordered atomic planes can be seen, indicating that these particles are highly crystalline in agreement with the results of XRD.

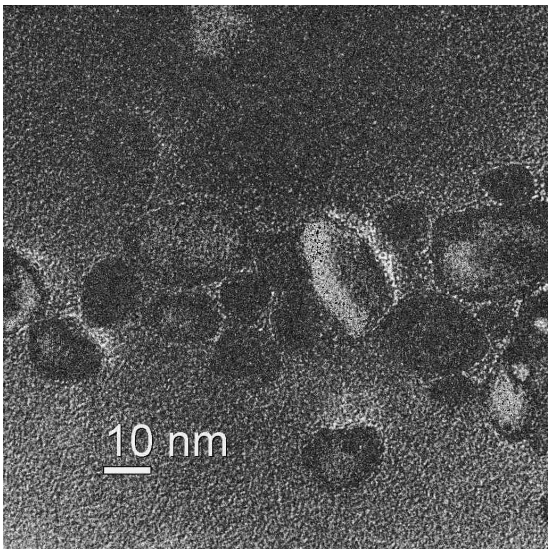

Figure 4.2a. Transmission electron micrograph of hematite nanoparticles At 200 kx magnification

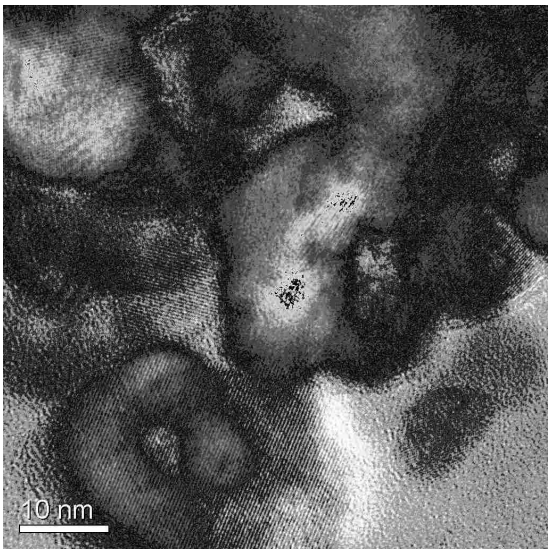

Figure 4.2b. Transmission electron micrograph of hematite nanoparticles At 310 kx magnification

Brunauer Emmett Teller (BET) surface area measurements were performed using a nitrogen adsorption isotherm on a Micromeritics Tristar 3020. The nano-hematite powder was found to have a surface area of 59.0 m^2/g. A spherical particle size equivalent can be calculated from surface area measurements using the formula:

$$d(nm) = \frac{6}{SA * \rho} * 1000,$$

where ρ is the density of the sample. Approximating the density of the nanopowder to be that of bulk hematite (5.25 g/cm^3) the particle size is calculated to be 19.4 nm. This formula assumes the particles to have cubic shape, however if a spherical particle is assumed then this value can be multiplied by the ratio of the surface area of a sphere to that of a cube (0.523), which gives a value of 10.1 nm, which is in much better agreement with the results from XRD and TEM.

Anlaysis of chemical impurities was performed using a Perkin-Elmer inductively coupled plasma optical emission spectrometer (ICP-OES) Optima 4300 DV. A sample solution for ICP was prepared by dissolving two samples (129.0 and 168.6 mg) of the hematite powder in 50.0 mL of 5% HNO_3. Qualitative analysis of this sample revealed the presence of Al, Ca, Cr, Mn, and Mg. Quantitative analysis using standard concentrations of these species showed the total impurities to be less than 0.082% of the

sample mass making the sample 99.918% pure on a metals basis. An analysis of carbon, nitrogen, and hydrogen by combustion at Galbraith Laboratories showed the nitrogen residue from the NH_4HCO_3 to be 68 ppm while the carbon and hydrogen contents were less than 0.5%.

Thermal gravimetric analysis (TGA) of the sample was carried out in corundum crucibles using a Netzsch 409 system. The sample was heated at a rate of 8.0°C/min to 1000°C in He(g) resulting in a 2.80% mass loss. Assuming all the mass lost to be water, this equates to a percent mass of hydrogen of 0.313%, which agrees well with the Galbraith results of less than 0.5%. With a detailed characterization the chemical formula of the hematite nanopowder used in this study is represented as $Fe_2O_3 \cdot 0.248H_2O$ with a molecular weight of 164.156 g/mol.

The sample was prepared for adiabatic calorimetry by compressing the powder into pellets of 3/8" diameter which were then broken and placed in the calorimetric vessel described by Stevens and Boerio-Goates.[27] This container was evacuated and refilled with 0.080 mmoles of dry He(g). The calorimeter was then sealed by pressing a 0.7620 g gold gasket against a stainless steel knife edge located at the top of the vessel. Heat capacity measurements were made on this system over the temperature range 30 to 350 K.

The heat capacity of this sample was also measured in the temperature range 0.5 to 38 K using the semi-adiabatic calorimeter described by Lashley *et al.*[28] This was done using a 0.1906 g sample wrapped in a 0.0841 g copper foil (99.999% pure) to provide greater thermal conductivity. The copper and hematite nanopowder were compressed into a pellet of 3/8" diameter and 1/8" thickness which was then attached to the sample platform of the apparatus by using Apiezon N grease. The contributions of the copper, grease, and addenda were subtracted to obtain the molar heat capacity of nanocrystalline hematite.

4.3 Results

Experimental results for the molar heat capacity $C_{p,m}$ of the nanocrystalline hematite powder are given in Table 4.1 along with the temperature increments ΔT for each heat capacity measurement. Figure 4.3 shows the results graphically with a

comparison to two bulk data sets measured by PPMS as well as the heat capacity of bulk hematite measured by Westrum and Gronvold.[6] The heat capacity divided by temperature

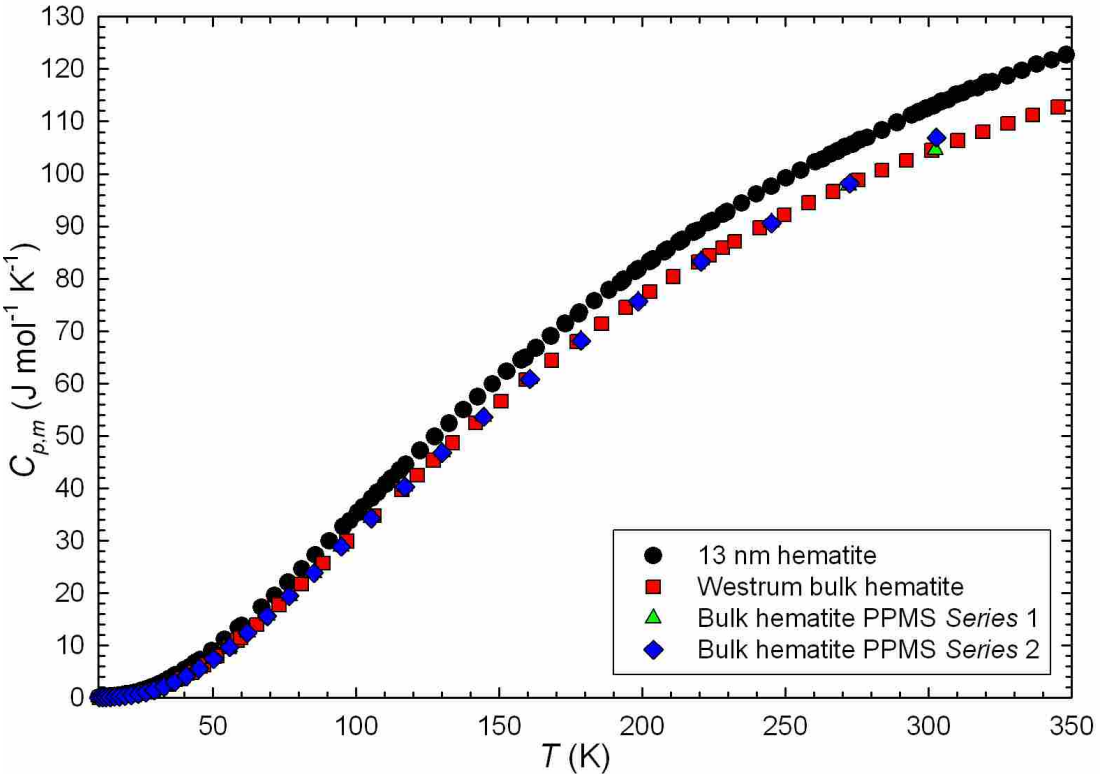

Figure 4.3. Heat Capacity of 13 nm hematite compared to the bulk including measurements by Westrum.[6]

is shown in the temperature range 1.5 to10 K in Figure 4.4.

It can be seen in these graphs that, like other nanomaterials, the heat capacity of nanocrystalline hematite is larger than that of the bulk. Also, the spin-flip transition at T_M is not observed in the heat capacity of nanocrystalline hematite. However, no anomaly was observed in the heat capacity of bulk hematite as well.[6, 21] Another feature in this data is seen in the region from 4 to 7 K where there is a small, broad anomaly. A discussion of the physical implications of the features observed in the heat capacity of nanocrystalline hematite is given below.

The heat capacity was experimentally measured as low as 0.5 K, but an examination of the data by plotting C/T vs T^2 (Figure 4.5) showed an inflection at T = 1.3 K at which point the data began to trend towards negative values. Attempts to fit the heat capacity of nanocrystalline hematite including these points resulted in large degrees of error, and it was determined that data below 1.3 K did not achieve thermal equilibrium

during the measurement process.

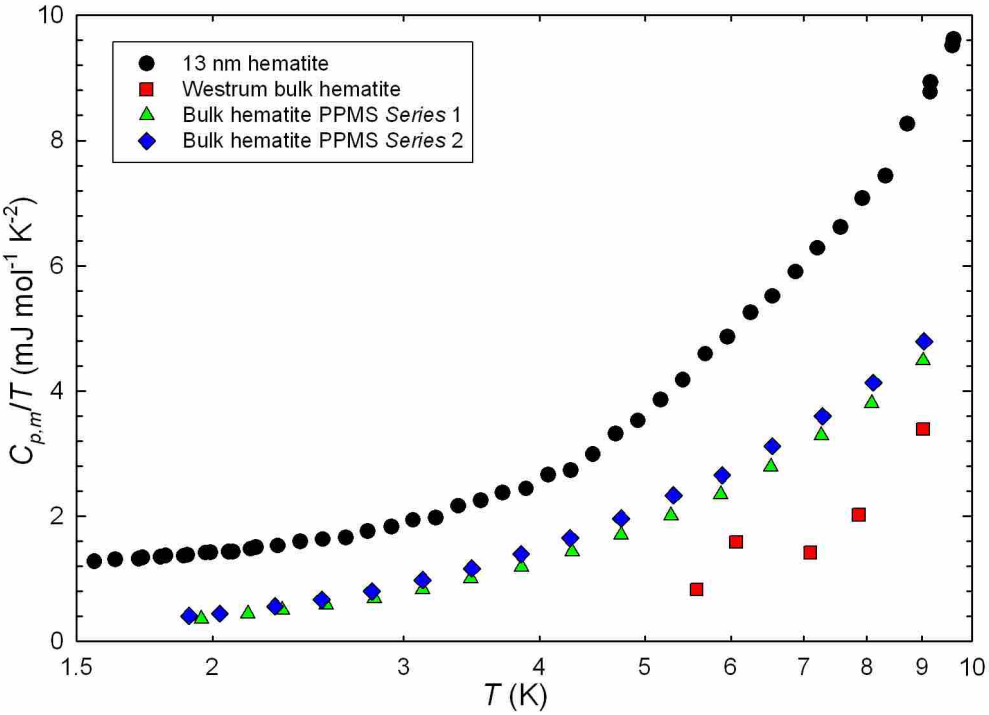

Figure 4.4. Heat capacity of 13 nm hematite below 10 K. Temperature is shown on a log scale. A comparison is made to the bulk including measurements by Westrum.[6]

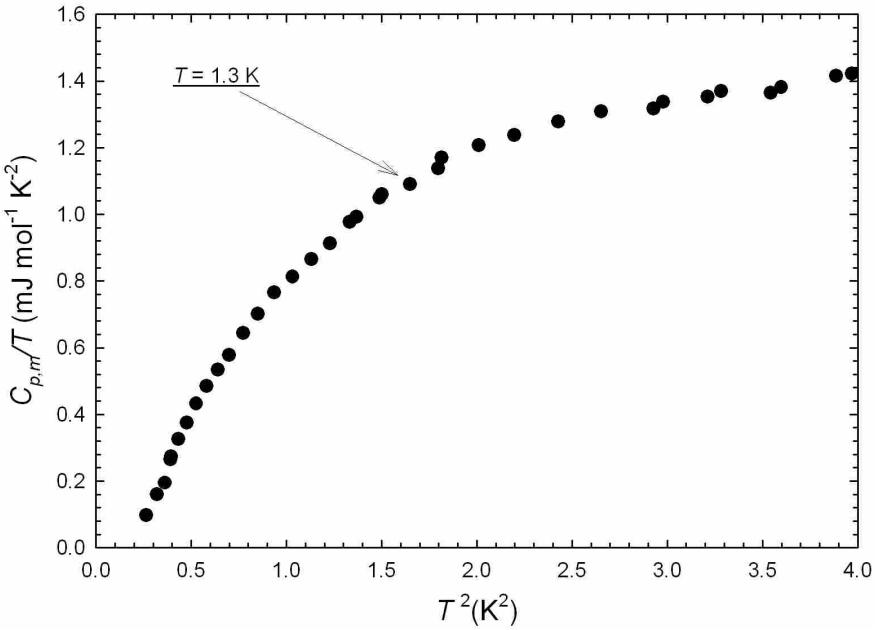

Figure 4.5. A graph of C/T vs T^2 which shows a trend in the data where the heat capacity begins to drop towards negative values at $T^2 = 1.8$ ($T = 1.3$ K).

Table 4.1. Experimental heat capacity of nanocrystalline hematite.
$M = 164.156\ g \cdot mol^{-1}$

T/K	$C_{p,m}$ (J mol^{-1} K^{-1})	ΔT/K	T/K	$C_{p,m}$ (J mol^{-1} K^{-1})	ΔT/K
	Series 1		40.15	5.396	3.57
159.13	64.866	2.82	43.91	6.769	3.95
163.08	66.801	5.09		*Series* 11	
168.18	69.052	5.09	41.99	5.859	3.43
173.28	71.343	5.10	45.62	7.280	3.75
177.77	73.225	3.88	49.61	8.942	4.24
	Series 2		54.08	11.135	4.69
192.39	79.228	5.12	59.05	13.386	5.22
197.50	81.318	5.11		*Series* 12	
202.62	83.259	5.12	1.726	0.002622	0.166
207.75	85.126	5.13	1.897	0.002977	0.185
212.88	86.969	5.13	2.088	0.003394	0.199
218.01	88.857	5.13	2.298	0.003988	0.220
223.14	90.638	5.14	2.528	0.004683	0.240
228.28	92.283	5.14	2.781	0.005564	0.266
	Series 3		3.060	0.006745	0.292
219.40	89.20	5.11	3.368	0.008285	0.323
224.52	91.03	5.14		*Series* 13	
229.65	92.74	5.14	9.157	0.09291	0.875
234.79	94.41	5.14	10.073	0.11885	0.964
239.94	96.09	5.14	11.082	0.15264	1.060
245.08	97.63	5.15	12.191	0.19559	1.164
250.23	99.22	5.15	13.404	0.25298	1.270
255.38	100.68	5.15	14.740	0.32877	1.414
260.53	102.23	5.15	16.222	0.41833	1.559
265.68	103.70	5.16	17.845	0.56851	1.705
270.83	105.12	5.16	19.632	0.75521	1.880
275.99	106.43	5.16	21.601	0.99091	2.065
	Series 4		23.761	1.33421	2.266
263.07	102.817	5.40	26.119	1.77470	2.464
268.34	104.287	5.15	28.712	2.34062	2.738
273.50	105.659	5.16	31.578	3.10029	3.010
278.66	106.883	5.17	34.730	4.09817	3.311
283.82	108.345	5.15	37.552	4.93222	2.352
288.97	109.750	5.16		*Series* 14	
294.14	111.168	5.17	1.812	0.002819	0.173
299.30	112.446	5.16	1.992	0.003221	0.190
304.46	113.746	5.17	2.193	0.003749	0.207
309.62	115.080	5.17	2.411	0.004362	0.231
314.78	116.255	5.18	2.654	0.004985	0.251
319.95	117.371	5.17	2.923	0.006086	0.280

T/K	$C_{p,m}$ (J mol^{-1} K^{-1})	Δ*T*/K	*T*/K	$C_{p,m}$ (J mol^{-1} K^{-1})	Δ*T*/K
	Series 5		3.212	0.007206	0.307
296.58	111.778	5.25	3.534	0.009041	0.336
301.78	112.954	5.16	3.887	0.010769	0.366
306.94	114.080	5.17	4.275	0.013272	0.407
312.11	115.455	5.16	4.701	0.017728	0.448
	Series 6		5.170	0.022685	0.491
317.23	116.357	5.11	5.684	0.029664	0.543
322.37	117.499	5.17	6.258	0.037346	0.594
327.54	118.725	5.17	6.883	0.046173	0.657
332.71	119.710	5.17	7.570	0.056935	0.717
337.88	120.881	5.17	8.327	0.070361	0.790
343.05	121.706	5.17	9.152	0.091213	0.871
348.23	122.697	5.17	10.066	0.115613	0.962
353.41	123.683	5.17		*Series* 15	
	Series 7		9.618	0.1051	0.921
60.08	13.824	9.50	10.580	0.1347	1.005
67.01	17.274	4.35	11.637	0.1732	1.110
71.54	19.555	4.72	12.795	0.2251	1.206
76.28	22.039	4.75	14.068	0.2892	1.342
81.05	24.610	4.79	15.477	0.3777	1.481
85.87	27.239	4.83	17.032	0.4961	1.631
90.72	29.910	4.87	18.741	0.6542	1.792
95.61	32.646	4.90	20.622	0.8588	1.972
100.53	35.339	4.93	22.684	1.1514	2.164
105.47	38.038	4.95	24.942	1.5389	2.367
110.43	40.766	4.97	27.419	2.0477	2.601
115.41	43.479	4.99	30.145	2.6922	2.858
	Series 8		33.149	3.5614	3.172
97.87	33.802	4.39	36.140	4.5749	2.842
102.54	36.431	4.95		*Series* 16	
107.49	39.181	4.96	1.347	0.001791	0.127
112.46	41.860	4.98	1.482	0.002085	0.141
117.45	44.531	5.00	1.628	0.002422	0.157
122.46	47.181	5.01	1.792	0.002754	0.175
127.47	49.832	5.02	1.972	0.003172	0.189
132.50	52.410	5.04	2.169	0.003644	0.208
137.55	54.939	5.05		*Series* 17	
142.60	57.439	5.06	1.418	0.001945	0.139
147.66	59.898	5.06	1.558	0.002264	0.143
152.73	62.287	5.08	1.711	0.002560	0.165
	Series 9		1.883	0.002921	0.179
157.82	64.487	5.03	2.070	0.003370	0.197

T/K	$C_{p,m}$ (J mol^{-1} K^{-1})	Δ*T*/K	*T*/K	$C_{p,m}$ (J mol^{-1} K^{-1})	Δ*T*/K
162.88	66.732	5.09		*Series* 18	
167.97	69.077	5.09	3.700	0.009972	0.362
173.07	71.383	5.10	4.075	0.012323	0.386
178.17	73.645	5.11	4.480	0.015204	0.427
183.28	75.730	5.11	4.928	0.019739	0.468
188.39	77.781	5.12	5.419	0.025729	0.517
193.51	79.806	5.12	5.960	0.032922	0.566
198.63	81.777	5.12	6.556	0.041086	0.626
203.75	83.657	5.13	7.211	0.051480	0.683
208.88	85.606	5.13	7.928	0.063731	0.755
214.01	87.424	5.13	8.721	0.081892	0.834
	Series 10		9.592	0.10372	0.917
31.01	2.566	2.41	10.552	0.13197	1.010
36.77	4.261	3.19			

4.4 Discussion

4.4.1 The Morin Transition

The absence of an anomaly in the region of the Morin transition is not surprising since the transition was not observed in the heat capacity of bulk hematite.[29, 32] Various studies have placed the temperature of the Morin transition where the sample changes from ferromagnetic to antiferromagnetic at 250 K.[7, 21] It has been suggested that the heat capacity shows no sign of transition in this region because either it does not involve any appreciable entropy increment or that it is spread out over a rather broad temperature range.[6] Although the Morin transition has not shown a significant contribution to the heat capacity of hematite, low-temperature fits can help determine whether or not a magnetic transition has occurred. The following discussion is an analysis of the physical properties of 13 nm hematite that are extracted from low-temperature theoretical fits.

4.4.2 Thermophysical Properties of Nanocrystalline Hematite

Modeling heat capacity data with theoretical functions at low temperatures (< 15 K) can provide valuable information about the magnetic, electronic, and vibrational properties of a sample.[29] The total heat capacity can be viewed as a sum of the energetic contributions from the various physical properties of a material. At temperatures above 10 K, the largest contribution to heat capacity stems from lattice vibrations which are modeled by an odd-powers fit to the equation:

$$C_{Lat} = \sum_{n=3,5,7...} B_n T^n \text{ .}^{30} \quad (1)$$

Magnetic contributions will also have a temperature-dependence with $T^{3/2}$ for ordered ferro- and ferrimagnets and T^3 for antiferromagnets. If there is a significant amount of anisotropy the spin-wave spectrum will have a gap,[45, 46] which is similar to the gap induced by a magnetic field. Gaps in magnetic solids require the use of the term $C_{fsw} = B_{fsw} T^{3/2} e^{-\Delta/T}$ for ferro- and ferrimagnets and $C_{asw} = B_{asw} T^3 e^{-\Delta/T}$ for antiferromagnets, where Δ is the gap parameter given in units of K. Fits are made by combining some of these models, and a physically meaningful expression that represents the heat capacity of nanocrystalline hematite can be obtained.

Conduction electrons contribute to the heat capacity in a linear fashion with γT representing the electronic heat capacity in most cases.[29] In addition to conducting solids, a linear term is generally observed in many oxide materials that are not fully stoichiometric or which contain oxygen vacancies or dislocations.[29] For example, non-conducting oxides requiring a linear term include α-FeOOH (goethite),[1] crystalline pure SiO_2 zeolites,[31] and hydrous potassium aluminosilicate[32] (muscovite) where the linear term has been attributed by Coey *et al.*[31] to localized electronic states associated with oxygen vacancies.

Superparamagnetic effects[33, 34] can also contribute to the heat capacity. Superparamagnetism occurs in nanoparticles that consist of a single magnetic domain with a diameter between 3 and 50 nm. Unlike the effects of paramagnetism which are usually observed above the Curie temperature, superparamagnetism occurs below this point. This magnetic behavior is characterized by the entire nanoparticle acting as a single magnetic moment which can randomly flip direction under the influence of temperature. Superparamagnetism can be manifest as a dipolar contribution to the heat capacity due to the interaction of each spin cluster with the dipolar field created by all the other neighbors. [35, 36] This dipolar field depends on the spin configuration of the neighboring spins, which is dependent on the overall magnetization, and in the absence of a magnetic field the probability distribution of the internal fields is centered at zero. The heat capacity of ideal superparamagnets frequently exhibits an upturn in the heat capacity at temperatures lower than 1 K as shown in reports by Triplett and Phillips.[33] Livingston

and Bean[34] proposed that superparamagnetic effects might make a measurable contribution to γ under optimal conditions which include small particle size and positive anisotropy energy. This model is limited by its neglect of interactions between particles, yet a linear term has been observed in other superparamagnetic systems.[33]

4.4.3 Fits of the Heat Capacity of 13 nm Hematite

The presence of a small anomaly in the heat capacity ranging from 4 to 7 K presented some difficulties in modeling the thermophysical behavior of nanocrystalline hematite. Attempts to model this data with a Schottky (2-level system) or a magnetic spin gap produced physically meaningless results with parameters having negative values. The points in the region of the anomaly were omitted in subsequent fits, which were done in the range 1.4 to 15 K. This approach was successful, and the heat capacity of nanocrystalline hematite is expressed as:

$$C_{p,m} = \gamma T + B_3 T^3 + B_5 T^5 \quad (2).$$

Table 4.2 contains the parameters for this expression (Fit-1) as well as those for other fits of the heat capacity of nanocrystalline hematite. An inspection of this table shows that Fits 2 and 3 do not accurately represent the heat capacity of 13 nm hematite as seen by their high %RMS values. Fits 1 and 4 have a similar %RMS, but Fit-4 has a small negative value for B_{fsw}. A negative parameter is physically meaningless, but this value is small enough that the spin-wave contribution be approximated to be zero. Consequently, Fit-4 has the same expression as that of Fit-1, which suggests that Fit-1 gives the most accurate representation of the heat capacity of 13 nm hematite. Support for this conclusion can also be seen in the deviation of the various fits (Figure 4.6) which shows that only Fit-1 has a random distribution about zero in the given temperature range. Also, the low-temperature heat capacity of nanocrystalline hematite is compared with Fit-1 in Figure 4.7 where it can be seen that this fit agrees well with experimental measurements except in the region of the anomaly from 4 to 8 K.

Table 4.2. A summary of fits of low-temperature heat capacity of 13 nm hematite. Units are in mJ, mole, and K.

Parameter	Fit-1	Fit-2	Fit-3	Fit-4
B_3	0.098187	0.087202	0.070020	0.10080
B_5	-5.9318E-05		4.3157E-05	-6.9112E-05
γ	1.0235	0.82085		1.1129
B_{fsw}		0.17695	0.79806	-0.070675
%RMS	1.47	2.35	4.84	1.42

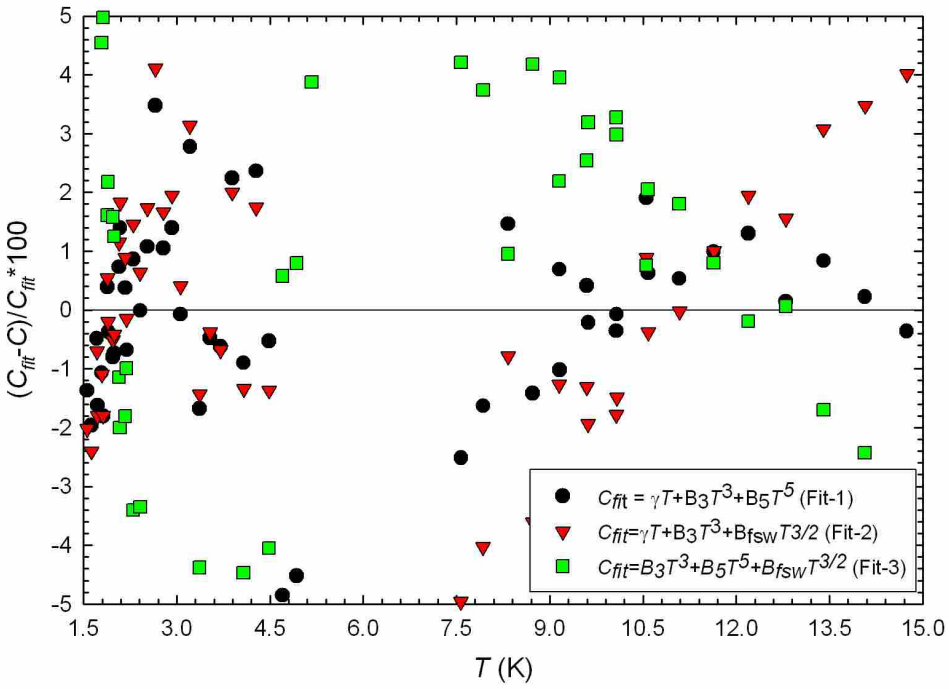

Figure 4.6. Deviation of Fits 1-3 from the low-temperature experimental heat capacity of 13 nm hematite.

4.4.4 Physical Meaning of Fit-1

Fit-1 included terms for the lattice heat capacity and a linear contribution, but no ferromagnetic spin wave. This is surprising since several studies indicated that nanocrystalline hematite did not undergo the spin-flip transition to antiferromagnetic behavior, but that it retained ferromagnetic behavior as low as 2 K.[7, 9, 37-41] One possible explanation for this observation is that the sample has transformed to antiferromagnetic which would be manifest in the use of a T^3 term. A second explanation is that the ferromagnetic spin wave contribution is so small that it does not make a significant difference in the fitting expression, yet this is unlikely since Fits 2 and 3 show that B_{fsw} can be large but not accurately represent the heat capacity data. Another possibility is that 13 nm hematite does not order magnetically at low temperatures. An analysis of the T^3

contribution is necessary in order to determine whether or not there is antiferromagnetic ordering in 13 nm hematite.

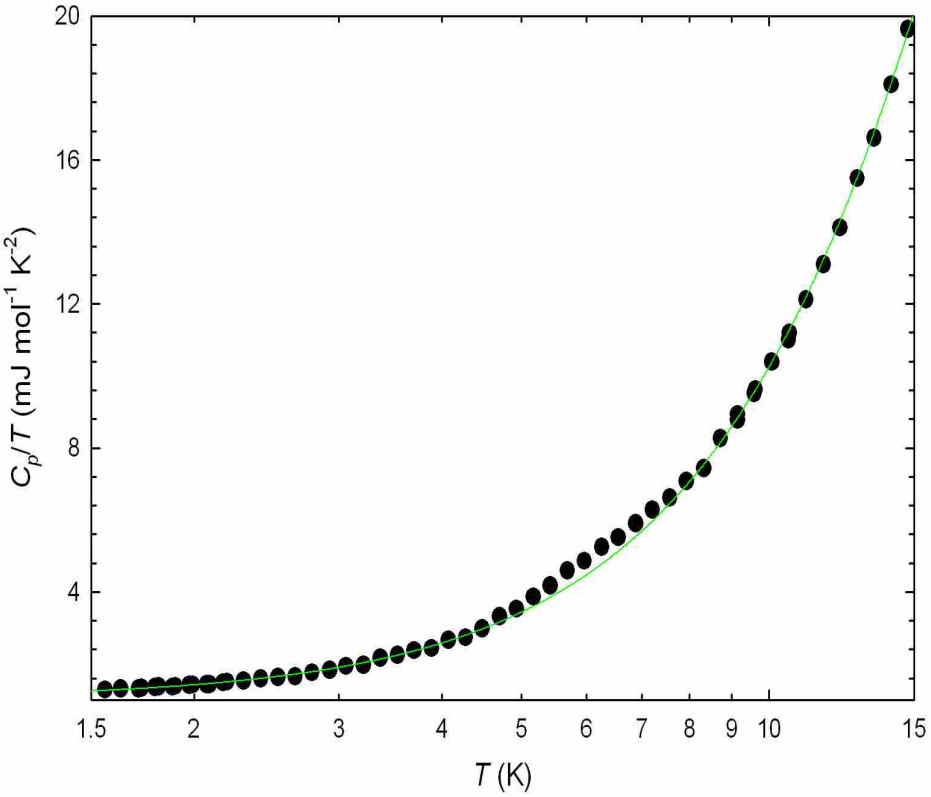

Figure 4.7. Low-temperature heat capacity of nanocrystalline hematite shown on a log scale. The line represents a fit of the lattice.

4.4.5 Analysis of the T^3 Dependence

Generally, antiferromagnetic contributions are ten to twenty times larger than the lattice component at low-temperatures.[29] This can be seen in a comparison of the low-temperature heat capacity of antiferromagnetic $MnCO_3$ and nonmagnetic $CaCO_3$.[29] These two samples have a similar lattice contribution but the contribution of T^3 in $MnCO_3$ is many times that of $CaCO_3$. In the case of 13 nm hematite, other iron oxides make good candidates for such a comparison. Table 4.3 shows a list of iron oxides that have been fit at low-temperatures with their respective lattice components and magnetic behavior. It can be seen that 13 nm hematite has a similar lattice contribution to those of bulk hematite and goethite (α-Fe3O4). Bulk hematite was also shown to have a ferromagnetic spin wave while goethite (α-FeOOH) had an anisotropic antiferromagnetic contribution.

The similarity and small size of these lattice components suggests that the T^3 dependence in 13 nm hematite stems from the lattice heat capacity with no antiferromagnetic spin wave. This can also be seen in the much larger lattice contribution of 13 nm magnetite (Fe3O4) which had no antiferromagnetic spin wave component. This conclusion implies that 13 nm hematite has no significant contribution from antiferromagnetic or ferromagnetic ordering.

Table 4.3. A comparison of some fit parameters of various Iron oxides. Units of these parameters are in mJ, mole, and K. Information for Goethite was taken from Majzlan *et al.*[1] while 13 nm Magnetite, Lepidocrocite, Akaganéite, and Bulk Hematite are unpublished work from our lab.

Sample	γ	B_3	B_{fsw}	B_{asw}	Magnetic Term
13 nm Hematite	1.02	0.098			None
Bulk Hematite		0.083	0.040		Ferromagnetic
37 nm Goethite (α-FeOOH)	0.23	0.10		1.2	Anisotropic Antiferromagnetic
13 nm Magnetite (Fe_3O_4)	3.46	0.59	75.8		Anisotropic Ferrimagnetic
30 nm Lepidocrocite (γ-FeOOH)	0.35	0.496		9.65	Anisotropic Antiferromagnetic
34 nm Akaganéite (β-FeOOH)	0.47	0.218		0.514	Anisotropic Antiferromagnetic

4.4.6 Analysis of the Linear Term

The most common use of a linear term represents an electronic contribution, yet nanocrystalline hematite is a semiconductor with a band gap of 2.2 eV.[42] As mentioned previously a linear term has been seen for non-conducting oxides that had oxygen vacancies.[1] This phenomenon was observed in the low-temperature heat capacity of goethite, which has a similar band gap of 2.5 eV.[43] As seen in Table 4.4, nanocrystalline hematite has a value of 1.02 $mJ \cdot mol^{-1} \cdot K^{-2}$ for γ which is significantly larger than the linear contribution for the iron oxyhydroxides. The significant difference in these values suggests that the linear term in Fit-1 does not originate from localized electronic states associated with oxygen vacancies.

Magnetic studies at low-temperatures of hematite nanoparticles have shown superparamagnetic behavior,[8] and it is likely that the linear term stems from a superparamagnetic contribution. To the best of our knowledge no heat capacity studies have been performed by any other groups on superparamagnetic nanosystems. Triplett and Phillips reported a γ value of 13.3 $mJ \cdot mol^{-1} \cdot K^{-2}$ for the bulk compound $Ni_{0.62}Rh_{0.38}$, which was shown to have anomalous behavior consistent with superparamagnetic clusters.[33] However in this study no mention was made of the relationship of the linear term with superparamagnetic behavior, although Livingston and Bean[34] had already suggested such a relationship. Instead it was assumed that all of the linear term was due to the electronic specific as $Ni_{0.62}Rh_{0.38}$ was a conducting solid. The electronic contribution to the heat capacity of Ni metal is 7.28 $mJ \cdot mol^{-1} \cdot K^{-2}$ while Rh metal has value of 4.89 $mJ \cdot mol^{-1} \cdot K^{-2}$.[29] By multiplying the value of Ni by 0.62 and that of Rh by 0.38 then adding them together, the electronic contribution to the heat capacity of $Ni_{0.62}Rh_{0.38}$ can be estimated to be 6.37 $mJ \cdot mol^{-1} \cdot K^{-2}$. This value is well below 13.3 $mJ \cdot mol^{-1} \cdot K^{-2}$ as reported by Triplett and Phillips, and it is possible that the linear contribution in their studies had a superparamagnetic component. Estimates of the linear term like that made for $Ni_{0.62}Rh_{0.38}$ are more accurate for conducting alloys that are not superparamagnetic. This can be seen in CuZn[44] which has a linear contribution of 0.69 $mJ \cdot mol^{-1} \cdot K^{-2}$ while our method of estimating the linear term predicts a value of 0.66 $mJ \cdot mol^{-1} \cdot K^{-2}$. Likewise, $Ni_{0.47}Cu_{0.53}$ had a value of 3.10 $mJ \cdot mol^{-1} \cdot K^{-2}$ while our estimate was 3.20 $mJ \cdot mol^{-1} \cdot K^{-2}$.[45] Recently, the heat capacity of superparamagnetic, non-conducting 13 nm magnetite was measured in our lab (unpublished) which had a large value of 3.46 $mJ \cdot mol^{-1} \cdot K^{-2}$ for the linear term. As an electrical insulator the linear term in 13 nm magnetite is too large to be associated with the electronic heat capacity, and it is more likely due to its superparamagnetic properties. Likewise, several studies suggest that nanocrystalline hematite is superparamagnetic[8-10, 37, 40, 46] and it is likely that the linear term stems from superparamagnetic effects.

4.4.7 Effects of Uncompensated Surface Spins

To understand the anomaly found between 4 and 7 K, the calculated heat capacity from Fit-1 was subtracted from experimentally measured data and the excess heat

capacity is shown in Figure 4.8. This anomaly has a sharp rise beginning at 4 K and peaking at 6 K before slowly declining to a minimum at 10 K.

Studies of nanocrystalline hematite using SQUID (superconducting quantum interference device) magnetometry reveal the presence of uncompensated surface spins of Fe^{3+} ions.[12, 14, 24] A simple Ising model[29] gives the magnetic entropy per mole of a system as $S_M = R\ln(2s + 1)$, where s is the spin quantum number. If a two-level system is assumed then the entropic contribution per mole of magnetic spin will be $R\ln 2$.[29]

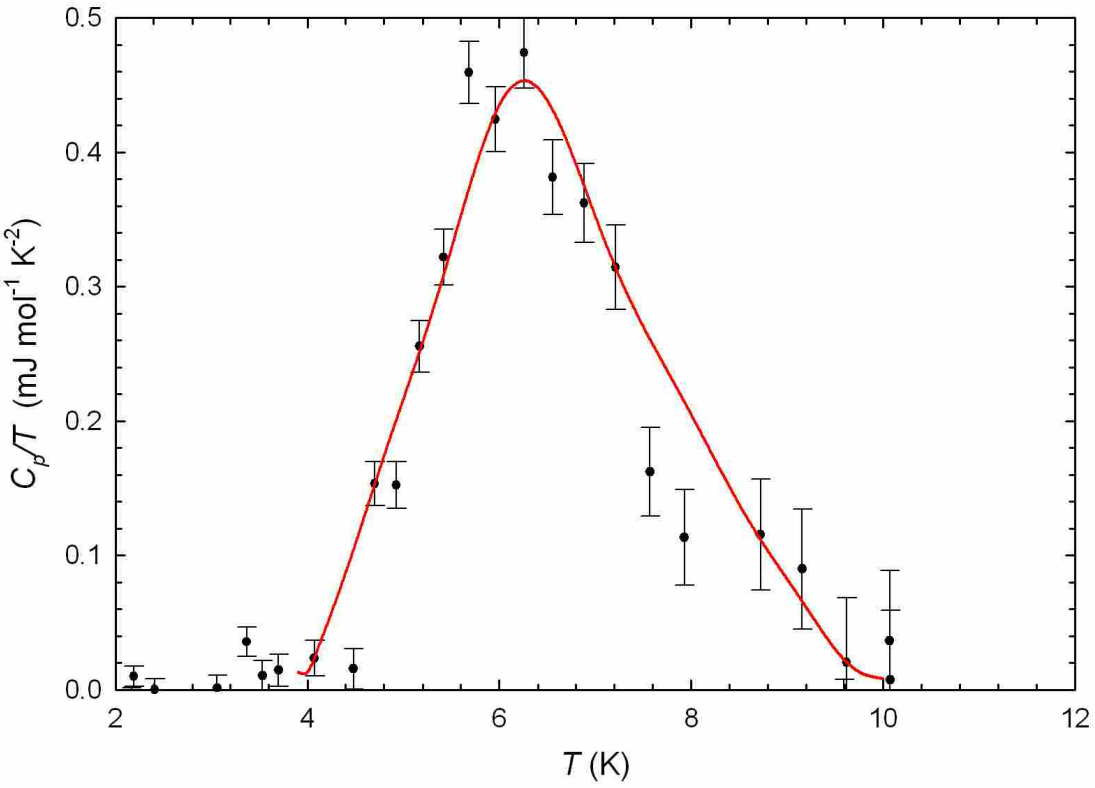

Figure 4.8. Anomalous heat capacity of nanocrystalline hematite due to uncompensated surface spins. The vertical bars show the degree of error in each point while the solid red line shows the orthogonal fit of the anomaly.

The spin concentration can be found by comparing the molar entropy of magnetic spins to the entropic contribution from the anomaly found in the heat capacity of nanocrystalline hematite. The anomaly was fit by hand which data was subsequently fit with an orthogonal polynomial and can be seen by the red line in Figure 4.8. The entropy

of the magnetic transition was calculated by integrating C_{fit}/T over the temperature range 4 to 10 K, and the entropy per mole of $Fe_2O_3 \cdot 0.248H_2O$ was found to be 1.312 $mJ \cdot mol^{-1} \cdot K^{-1}$. By dividing the entropy of transition by $R\ln 2$, the spin concentration was calculated to be 2.3 x 10^{-4} moles spin/mol $Fe_2O_3 \cdot 0.248H_2O$. Another way to interpret this value is that there are only about 2 uncompensated spins for every 10,000 Fe_2O_3. Assuming the unit cell of 13 nm hematite to be similar to that of the bulk, there are approximately 648 Fe atoms on the surface of each nanoparticle. From the surface spin calculation there are only 5.1 spins per nanoparticle meaning that only 0.8 % of the surface iron atoms have uncompensated spins. Such a small concentration agrees with the assumption that the anomaly is due to uncompensated surface spins.

4.4.8 Effects of Surface Water

Studies by both Navrotsky *et al.*[11] and Boerio-Goates *et al.*[4] have shown that the degree of hydration has a significant effect on the thermodynamic properties of nanoparticles.[4] Since characterization has shown a significant amount of water in this sample and the molar heat capacity of 13 nm hematite is in excess of the bulk hematite, the effects of water on the heat capacity of nanocrystalline hematite should also be considered. In the case of TiO_2 polymorphs studied by Boerio-Goates *et al.*, it was found that the heat capacity of the bare nanoparticle (contributions of water subtracted) was equal to that of the parent bulk material. By assuming that nanocrystalline hematite will behave in a similar manner, the heat capacity of adsorbed water can be obtained by subtracting contributions equal to bulk hematite from the experimentally measured heat capacity of 13 nm α-$Fe_2O_3 \cdot 0.248H_2O$. Fits of the heat capacity of bulk hematite were obtained from recent measurements (to be published separately) in our lab. The heat capacity of water adsorbed onto the surface of nanocrystalline hematite was obtained by subtracting that of bulk hematite and dividing the resultant heat capacity by the moles of water (0.248) per mole Fe_2O_3.

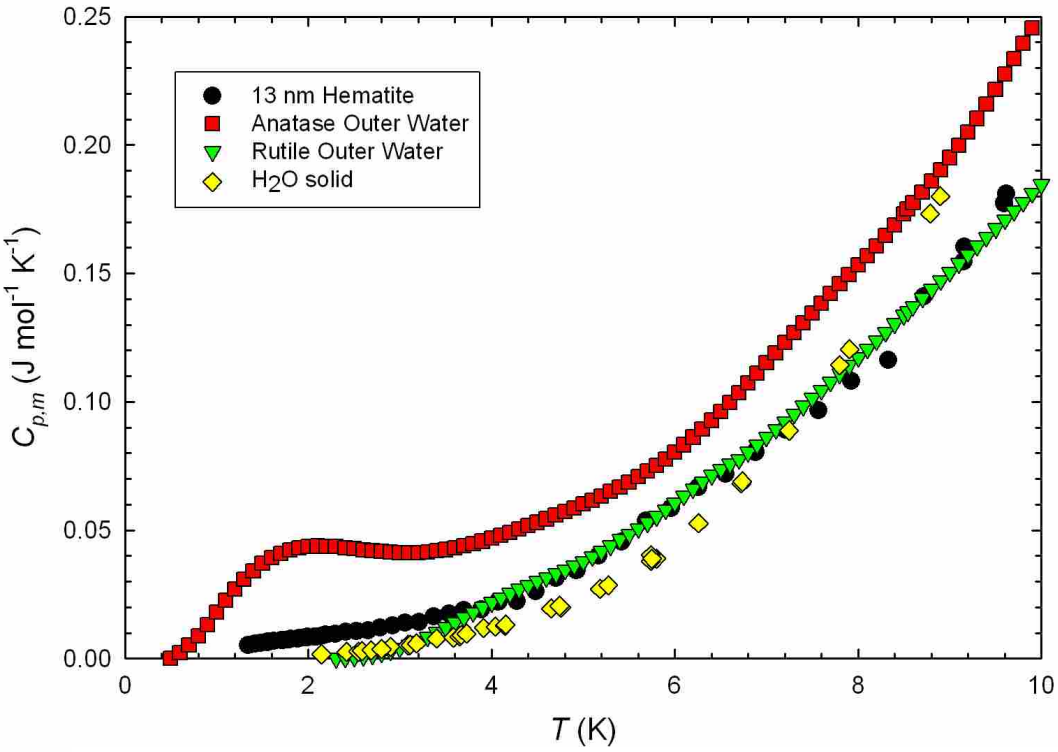

Figure 4.9a. Comparison of the heat capacity of H_2O on nanocrystalline hematite to that on TiO_2 polymorphs[4] and ice[4, 5] at temperatures below 10 K.

The calculated heat capacity of water on the surface of nanocrystalline hematite can be seen in Figure 4.9. Included in this figure are plots of water on the surface of TiO_2, as well as the heat capacity of solid ice.[4, 5] In this figure "outer water" on TiO_2 refers to the heat capacity of samples with the highest degree of hydration: $TiO_2 \cdot 0.677H_2O$ for anatase and $TiO_2 \cdot 0.361H_2O$ for rutile. Conversely, "inner water" refers to the removal of significant amounts of adsorbed water on the TiO_2 polymorphs with samples having the chemical formula $TiO_2 \cdot 0.379H_2O$ for anatase and $TiO_2 \cdot 0.244H_2O$ for rutile. To facilitate the comparison between the water on TiO_2 polymorphs and that on nanocrystalline hematite, a summary of the water contents and surface coverage of these samples can be seen in Table 4.4.

It can be seen that nanocrystalline hematite has a surface coverage similar to that of the inner layer of rutile, yet Figure 4.9b shows that the heat capacity of water on nanocrystalline hematite is higher. This can be explained by hydration enthalpy measurements reported by Navrotsky *et al.* for nanocrystalline TiO_2 polymorphs[47] and

also nanocrystalline hematite.[11] These measurements show that as the number of H_2O/nm^2 decreases, the enthalpy of hydration approaches 150 kJ/mol for nano-TiO_2 polymorphs while that of nanocrystalline hematite approaches 100 kJ/mol. In both cases the nanoparticles hold onto the inner layers of water tenaciously, but TiO_2 has a higher propensity to hold onto its water. This difference in water binding is manifest in the heat capacity curves shown in Figure 9b where the inner water on nano-rutile has a smaller heat capacity than that on nanocrystalline hematite in spite of the similar degrees of hydration.

Table 4.4. A comparison of the surface hydration of nanaparticulate rutile and anatase polymorphs with that of nanocrystalline hematite. Values for TiO_2 polymorphs were taken from Boerio-Goates *et al.*[4] except H_2O/nm^2 which were calculated from the other values.

	TiO2 anatase "outer water"	TiO2 anatase "inner water"	TiO2 rutile "outer water"	TiO2 rutile "inner water	13 nm Hematite
***SA* (BET) m^2/g**	250	250	104	104	56.1
moles H_2O per mole sample	0.677	0.379	0.361	0.244	0.248
***M* (g/mol)**	92.062	86.694	86.369	84.262	164.156
H_2O/nm^2	17.7	10.5	24.2	16.8	16.2

Further evidence that the heat capacity of surface water decreases with tighter binding is seen when the heat capacity of inner water on anatase is compared to that of rutile. Anatase has both a lower heat capacity and surface coverage (about 6 H_2O/nm^2 less) than rutile, and according to the measurements of Navrotsky *et al.*[11, 47] the lower surface coverage corresponds to a higher magnitude of hydration enthalpy. In other words the inner water of anatase is bound more tightly than that of rutile because the surface coverage is lower. Overall, these results agree well with the conclusions of Navrotsky *et al.* and Boerio-Goates *et al.*[4] that the degree of hydration must be taken into account when studying the thermodynamic properties of nanosystems.

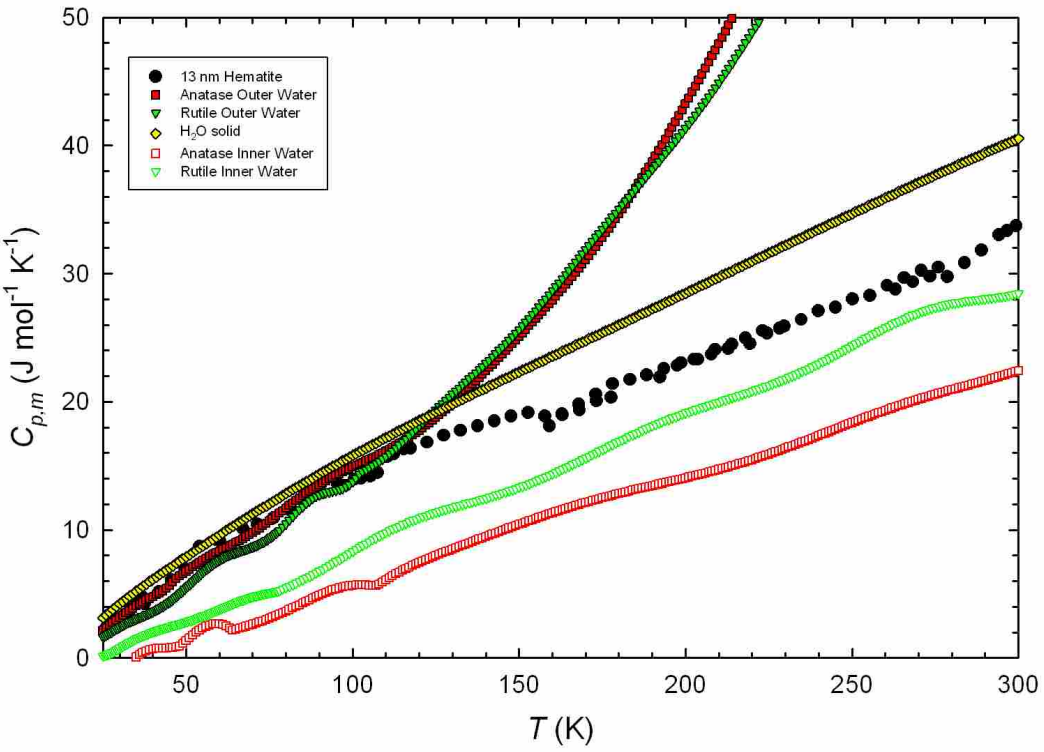

Figure 4.9b. Comparison of the heat capacity of H_2O on nanocrystalline hematite to that on TiO_2 polymorphs[4] and ice[4, 5] in the range 0-300 K.

A second observation in the heat capacity of the surface water of nanocrystalline hematite is seen in Figure 4.9b where the heat capacity of water on the surface of hematite is higher than that of H_2O(s) below 7 K. This is probably less an effect of the water and has more to do with the contributions from uncompensated surfaces spins discussed previously. These magnetic contributions were not part of the bulk hematite heat capacity subtracted from the experimentally measured heat capacity of nanocrystalline hematite, and thus would still be present in the residual heat capacity attributed to water.

4.4.9 Thermodynamic Functions of Nanocrystalline Hematite

The standard molar thermodynamic functions, $C^{\circ}_{p,m}$, $\Delta^{T}_{0}H^{\circ}_{m}$, $\Delta^{T}_{0}S^{\circ}_{m}$, and $\Phi^{\circ}_{m}=(\Delta^{T}_{0}S^{\circ}_{m}-\Delta^{T}_{0}H^{\circ}_{m}/T)$ scaled by the ideal gas constant R are reported in Table 4.5 for nanocrystalline hematite (α-$Fe_2O_3 \cdot 0.248H_2O$). They have been generated at smoothed

temperatures by fitting a combination of orthogonal polynomials and Fit-1 (given in Table 4.6) to the experimental results for nanocrystalline hematite.

Table 4.5. Standard thermodynamic functions of nanocrystalline hematite ($Fe_2O_3 \cdot 0.248H_2O$) where $\Phi_m^o = \Delta_0^T S_m^o - \Delta_0^T H_m^o / T$, M = 164.156 g · mol^{-1}, p° = 100 kPa, and R = 8.3145 J · K^{-1} · mol^{-1}

T/K	$C_{p,m}^o / R$	$\Delta_0^T S_m^o / R$	$\Delta_0^T H_m^o / RT$	Φ_m^o / R
1.5	0.00022445	0.00019792	0.00010228	0.00079522
2.0	0.00034044	0.00027764	0.00014667	0.0010889
2.5	0.00049156	0.00036910	0.00019988	0.0014070
3.0	0.00068640	0.00047523	0.00026407	0.0017557
3.5	0.00093341	0.00059886	0.00034138	0.0021408
4.0	0.0012408	0.0007429	0.00043392	0.0025687
4.5	0.0016169	0.0009100	0.00054380	0.0030448
5.0	0.0020693	0.0011031	0.00067307	0.0035753
5.5	0.0026059	0.0013248	0.00082372	0.0041662
6.0	0.0032339	0.0015777	0.00099774	0.0048223
6.5	0.0039604	0.0018646	0.0011970	0.0055502
7.0	0.004792	0.002188	0.001424	0.006355
7.5	0.005736	0.002550	0.001679	0.007243
8.0	0.006797	0.002953	0.001965	0.008218
8.5	0.007982	0.003400	0.002283	0.009287
9.0	0.009295	0.003893	0.002636	0.010453
9.5	0.010758	0.004434	0.003024	0.011723
10	0.012321	0.005025	0.003450	0.013102
11	0.015816	0.006359	0.004411	0.016201
12	0.019880	0.007905	0.005526	0.019780
13	0.024606	0.009678	0.006808	0.023868
14	0.030086	0.011698	0.008270	0.028498
15	0.036413	0.013984	0.009930	0.033705
16	0.043678	0.016560	0.011807	0.039518
17	0.05197	0.01945	0.01392	0.04599
18	0.06136	0.02268	0.01629	0.05316
19	0.07195	0.02628	0.01894	0.06105
20	0.08379	0.03026	0.02188	0.06974
25	0.16388	0.056892	0.041665	0.12661
30	0.28210	0.096624	0.071338	0.21024
35	0.43930	0.15142	0.11222	0.32593
40	0.6327	0.2223	0.1648	0.4780
45	0.8569	0.3095	0.2290	0.6693
50	1.1062	0.4125	0.3041	0.9015
55	1.3747	0.5304	0.3891	1.1750
60	1.6581	0.6621	0.4829	1.4894

Table 4.5 continued

T/K	$C^o_{p,m}/R$	$\Delta^T_0 S^o_m/R$	$\Delta^T_0 H^o_m/RT$	Φ^o_m/R
65	1.9536	0.8064	0.5846	1.8438
70	2.2591	0.9623	0.6933	2.2368
75	2.5732	1.1288	0.8081	2.6667
80	2.8943	1.3051	0.9284	3.1318
85	3.2200	1.4903	1.0536	3.6307
90	3.5478	1.6837	1.1831	4.1623
95	3.8800	1.8839	1.3158	4.7240
100	4.2122	2.0914	1.4523	5.3140
110	4.8756	2.5240	1.7335	6.5730
120	5.5234	2.9761	2.0224	7.9300
130	6.1478	3.4431	2.3160	9.3720
140	6.7477	3.9207	2.6112	10.8880
150	7.324	4.406	2.906	12.471
160	7.879	4.897	3.200	14.108
170	8.414	5.390	3.491	15.793
180	8.928	5.886	3.779	17.521
190	9.422	6.382	4.063	19.283
200	9.894	6.878	4.343	21.075
210	10.342	7.371	4.618	22.893
220	10.768	7.862	4.888	24.730
230	11.171	8.350	5.152	26.586
240	11.554	8.833	5.411	28.455
250	11.918	9.313	5.664	30.334
260	12.267	9.787	5.911	32.221
270	12.601	10.256	6.153	34.114
273.15	12.704	10.403	6.228	34.711
280	12.926	10.720	6.389	36.010
290	13.238	11.179	6.620	37.908
298.15	13.485	11.550	6.804	39.455
300	13.540	11.633	6.846	39.806
310	13.826	12.081	7.066	41.697
320	14.095	12.525	7.282	43.596
330	14.342	12.963	7.492	45.487
340	14.572	13.395	7.697	47.374
350	14.797	13.820	7.897	49.254

Table 4.6. Summary of fits used for calculations of thermodynamic functions of nanocrystalline hematite (α-$Fe_2O_3 \cdot 0.248H_2O$). Units are in J, mole, and K.

Power	Range	Coefficient
	0.47 to 9.35 K	
1		1.0235E-03
3		9.8187E-05
5		-5.9318E-08
	9.35 to 94.1 K	
0		-0.052008
1		6.5792E-03
2		1.4609E-03
3		-1.7071E-04
4		1.4695E-05
5		-3.8101E-07
6		4.7122E-09
7		-2.8880E-11
8		7.0689E-14
	94.1 to 350 K	
0		183.16
1		-8.7099
2		0.17696
3		-1.8567E-03
4		1.1764E-05
5		-4.6340E-08
6		1.1089E-10
7		-1.4751E-13
8		8.3608E-17

4.5 Summary

The heat capacity of a nanocrystalline hematite sample with an average crystallite size of 13 nm was measured from 1.4 to 350 K. No anomaly was observed for the Morin transition, and, like other nanomaterials, this heat capacity was shown to be larger than the bulk. The effects of hydration on the heat capacity of hematite nanopowder were also investigated by subtracting contributions equal to the heat capacity of bulk hematite from that of nanocrystalline hematite to yield the heat capacity of water adsorbed onto the surface of the nanoparticles. Previous heat capacity studies of TiO_2 polymorphs showed that as the water surface coverage decreased the corresponding heat capacity also

decreased. This was attributed to tighter binding of "inner layers" of water to the surface of the nanoparticles, which agrees well with hydration enthalpy studies by Navrotsky *et al.* A similar effect is seen in the heat capacity of water adsorbed on hematite nanoparticles where the heat capacity is lower than that of solid H_2O. However, the heat capacity of water on nanocrystalline hematite was higher than that of the nanocrystalline TiO_2 polymorphs. This is explained by hydration enthalpy measurements which show that TiO_2 nanoparticles have a higher affinity for binding water than nanocrystalline hematite. The results of this study agree well with the conclusions that the more tightly bound the water the lower the corresponding heat capacity.

The experimental heat capacity of nanocrystalline hematite was fit in the range 1.5 to 15 K, omitting a small anomaly in the middle of this region. This fit required a linear term which is attributed to the superparamagnetism of nanocrystalline hematite. No term for a ferromagnetic spin wave was required in fitting this data in spite of magnetization studies indicating ferromagnetic ordering as low as 2 K.

A small anomaly was observed in the region 4 to 7 K, which was attributed to uncompensated spins of the Fe^{3+} ions on the surface of the nanoparticles. The heat capacity of the anomaly was obtained by subtracting the lattice contributions from the experimental measurements of nanocrystalline hematite. The spin concentration was obtained by dividing the entropy of this anomaly by $R\ln 2$, and was found to be 2.3×10^{-4} moles spin/mol $Fe_2O_3 \cdot 0.248H_2O$.

References

1. Majzlan, J.; Navrotsky, A.; Woodfield, B. F.; Lang, B. E.; Boerio-Goates, J.; Fisher, R. A., *J. Low Temp. Phys.* **2003,** *130* (1/2), 69-76.
2. Cornell, R. M.; Schwertmann, U.; Editors, *The Iron Oxides: Structure, Properties, Reactions, Occurrence and Uses*. VCH: Weinem, 1996; p 573.
3. Schwertmann, U., *NATO ASI Ser., Ser. C* **1988,** *217* (Iron Soils Clay Miner.), 267-308.
4. Boerio-Goates, J.; Li, G.; Li, L.; Walker, T. F.; Parry, T.; Woodfield, B. F., *Nano Lett.* **2006,** *6* (4), 750-754.

5. Smith, S. J.; Lang, B. E.; Liu, S.; Boerio-Goates, J.; Woodfield, B. F., *J. Chem. Thermodyn.* **2007,** *39* (5), 712-716.
6. Gronvold, F.; Westrum, E. F., Jr., *J. Am. Chem. Soc.* **1959,** *81*, 1780-3.
7. Hill, A. H.; Jiao, F.; Bruce, P. G.; Harrison, A.; Kockelmann, W.; Ritter, C., *Chem. Mater.* **2008,** *20* (15), 4891-4899.
8. Bahl, C. R. H. *The magnetic properties of antiferromagnetic nanoparticles: NiO and alpha -Fe2O3*; Information Service Department,Riso National Laboratory,Roskilde,Den.: 2006; pp i-vi,1-100.
9. Carbone, C.; Di Benedetto, F.; Sangregorio, C.; Marescotti, P.; Pardi, L. A.; Sorace, L., *J. Phys. Chem. C* **2008,** *112* (27), 9988-9995.
10. Lee, J. D., *Phys. Rev. B: Condens. Matter Mater. Phys.* **2004,** *70* (17), 174450/1-174450/6.
11. Navrotsky, A.; Mazeina, L.; Majzlan, J., *Science (Washington, DC, U. S.)* **2008,** *319* (5870), 1635-1638.
12. Majzlan, J.; Navrotsky, A.; Schwertmann, U., *Geochim. Cosmochim. Acta* **2004,** *68* (5), 1049-1059.
13. Bomati-Miguel, O.; Mazeina, L.; Navrotsky, A.; Veintemillas-Verdaguer, S., *Chem. Mater.* **2008,** *20* (2), 591-598.
14. Majzlan, J.; Grevel, K.-D.; Navrotsky, A., *Am. Mineral.* **2003,** *88* (5-6), 855-859.
15. Majzlan, J.; Koch, C. B.; Navrotsky, A., *Clays Clay Miner.* **2008,** *56* (5), 526-530.
16. Majzlan, J.; Lang, B. E.; Stevens, R.; Navrotsky, A.; Woodfield, B. F.; Boerio-Goates, J., *Am. Mineral.* **2003,** *88* (5-6), 846-854.
17. Majzlan, J.; Mazeina, L.; Navrotsky, A., *Geochim. Cosmochim. Acta* **2007,** *71* (3), 615-623.
18. Mazeina, L.; Navrotsky, A., *Clays Clay Miner.* **2005,** *53* (2), 113-122.
19. Mazeina, L.; Navrotsky, A., *Chem. Mater.* **2007,** *19* (4), 825-833.
20. Navrotsky, A., *J. Chem. Thermodyn.* **2006,** *39* (1), 2-9.
21. Jayasuriya, K. D.; Stewart, A. M.; Campbell, S. J., *J. Phys. Chem. Solids* **1985,** *46* (5), 625-9.
22. Korolev, V. V.; Arefyev, I. M.; Blinov, A. V., *J. Therm. Anal. Calorim.* **2008,** *92* (3), 697-700.
23. Barron, T. H. K.; Berg, W. T.; Morrison, J. A., *Proc. R. Soc. London, Ser. A* **1959,** *250*, 70-83.
24. Zhang, H.; Banfield, J. F., *Nanostruct. Mater.* **1998,** *10* (2), 185-194.
25. Terwilliger, C. D.; Chiang, Y.-M., *J. Am. Ceram. Soc.* **1995,** *78* (8), 2045-55.
26. Liu, S.; Liu, Q.; Boerio-Goates, J.; Woodfield, B. F., *J. Adv. Mater. (Covina, CA, U. S.)* **2007,** *39* (2), 18-23.
27. Stevens, R.; Boerio-Goates, J., *J. Chem. Thermodyn.* **2004,** *36* (10), 857-863.
28. Lashley, J. C.; Lang, B. E.; Boerio-Goates, J.; Woodfield, B. F.; Darling, T. W.; Chu, F.; Migliori, A.; Thoma, D., *J. Chem. Thermodyn.* **2002,** *34* (2), 251-261.
29. Gopal, E. S. R., *Specific Heats at Low Temperatures (International Cryogenics Monograph Series)*. Plenum Press: New York, 1966; p 226
30. Phillips, N. E., *Crit. Rev. Solid State Sci.* **1971,** *2* (4), 467-553.
31. Boerio-Goates, J.; Stevens, R.; Lang, B.; Woodfield, B. F., *J. Therm. Anal. Calorim.* **2002,** *69* (3), 773-783.

32. Coey, J. M. D.; Von Molnar, S.; Torressen, A., *J. Less-Common Met.* **1989,** *151*, 191-4.
33. Triplett, B. B.; Phillips, N. E., *Phys. Lett. A* **1971,** *37* (5), 443-4.
34. Livingston, J. D.; Bean, C. P., *J. Appl. Phys.* **1961,** *32* (10), 1964-1966.
35. Bean, C. P.; Livingston, J. D., *J. Appl. Phys.* **1959,** *30*, 120S-129S.
36. Joensson, P. E., *Adv. Chem. Phys.* **2003,** *128*, 191-248.
37. Bodker, F.; Hansen, M. F.; Koch, C. B.; Lefmann, K.; Morup, S., *Phys. Rev. B: Condens. Matter Mater. Phys.* **2000,** *61* (10), 6826-6838.
38. Cromphaut, C.; Resende, V. G.; Grave, E.; Vandenberghe, R. E., *Hyperfine Interact.* **2009,** *191* (1-3), 167-171.
39. Gee, S. H.; Hong, Y. K.; Sur, J. C.; Erickson, D. W.; Park, M. H.; Jeffers, F., *IEEE Trans. Magn.* **2004,** *40* (4, Pt. 2), 2691-2693.
40. Klausen, S. N.; Lefmann, K.; Lindgard, P. A.; Clausen, K. N.; Hansen, M. F.; Bodker, F.; Morup, S.; Telling, M., *J. Magn. Magn. Mater.* **2003,** *266* (1-2), 68-78.
41. Klausen, S. N.; Lefmann, K.; Lindgard, P. A.; Kuhn, L. T.; Bahl, C. R. H.; Frandsen, C.; Moerup, S.; Roessli, B.; Cavadini, N.; Niedermayer, C., *Phys. Rev. B: Condens. Matter Mater. Phys.* **2004,** *70* (21), 214411/1-214411/6.
42. Gilbert, B.; Frandsen, C.; Maxey, E. R.; Sherman, D. M., *Phys. Rev. B: Condens. Matter Mater. Phys.* **2009,** *79* (3), 035108/1-035108/7.
43. Sherman, D. M., *Geochim. Cosmochim. Acta* **2005,** *69* (13), 3249-3255.
44. Veal, B. W.; Rayne, J. A., *Phys. Rev.* **1962,** *128*, 551-5.
45. Chakrabarti, D. Transport properties of chromium-aluminum solid solution alloys. 1970.
46. Bodker, F.; Morup, S., *Europhys. Lett.* **2000,** *52* (2), 217-223.
47. Levchenko, A. A.; Li, G.; Boerio-Goates, J.; Woodfield, B. F.; Navrotsky, A., *Chem. Mater.* **2006,** *18* (26), 6324-6332.

Chapter 5

Heat Capacity Studies of the Iron Oxyhydroxides Akaganéite (β-FeOOH) and Lepidocrocite (γ-FeOOH)

5.1 Introduction

Iron oxides exist as several different polymorphs[2-5] which can be divided into two groups: anhydrous (oxides) and hydrous (oxyhyrdoxides). The more common anhydrous forms include hematite (α-Fe_2O_3), maghemite (γ-Fe_2O_3), magnetite (Fe_3O_4), and wüstite ($Fe_{(1-x)}O$) with magnetite and wüstite containing both ferrous and ferric iron. Goethite (α-FeOOH), lepidocrocite (γ-FeOOH), and akaganéite (β-FeOOH) comprise the majority of the hydrous polymorphs with these compounds often containing excess water. One of the most hydrated forms is ferrihydrite ($Fe(OH)_3$) which exists only as poorly crystalline particles smaller than ~ 8 nm.[6-8] With such a diverse and complex collection of polymorphs, it is difficult to predict and understand which phases form under specified conditions.[9-11] Thermodynamic studies can help to understand which polymorphs are stable and which metastable as well as when and how they transform. Recently, thermodynamic studies have begun to focus on the iron oxyhydroxides seeking to understand their relative stabilities and reactivities.[1, 10, 13-19] Goethite has been well studied through heat capacity and enthalpy measurements, and has been characterized as the most stable of the iron oxyhydroxide polymorphs. In spite of this, there is still some information that is needed for lepidocrocite and akaganéite. A brief review of the physical properties and current thermodynamic understanding of these two materials is given below.

5.1.1 Heat Capacity and Physical Properties of Lepidocrocite

Lepidocrocite (γ-FeOOH) is the second most common phase of FeOOH after goethite.[5] Similar to goethite, lepidocrocite is orthorhombic and is isostructural to Boehmite (γ-AlOOH). The name comes from the Greek word lepidos meaning flake,

which is a fitting description as this solid is layered.[23] The second half of the word comes from krokoeis meaning saffron-colored, but orange is a more common description. Lepidocrocite is naturally formed as an oxidation product of Fe^{2+} in biomes, soils, and rust.[2, 5] It is paramagnetic at room temperature, but becomes antiferromagnetic at its Néel temperature of 77 K and has a slightly smaller band gap than goethite at 2.4 eV.[24-26] With slow crystallization, plates of lepidocrocite of 0.5-1.0 μm in length, 0.1-0.2 μm wide, and < 0.1 μm thick can be grown.[3, 5] Its thermodynamic properties have been studied, with the low-temperature heat capacity for lepidocrocite in the temperature range 10 K to 300 K first published by Majzlan *et al.* in 2003.[1] The sample used in this study had an average crystallite size of 30 nm as determined by powder x-ray diffraction (XRD), and the small particle size creates the effect of a broad anomaly in the heat capacity around the Néel transition at 68 K. Mössbauer spectroscopy studies by Murad and Schwertmann[27] found that antiferromagnetic and paramagnetic lepidocrocite co-exist over a large temperature range, which is consistent with the observation of a broad anomaly in the heat capacity. Majzlan reported the standard entropy for lepidocrocite to be 65.1 ± 0.2 $J \cdot mol^{-1} \cdot K^{-1}$. After the enthalpy of formation was obtained, the Gibbs free energy of formation was calculated to be – 480.1 ± 1.4 $kJ \cdot mol^{-1}$, showing lepidocrocite to be less thermodynamically stable than goethite under standard conditions.[1, 13]

5.1.2 Heat Capacity and Physical Properties of Akaganéite

Akaganéite, (β-FeOOH) is scarcely found in nature.[2, 5] It mostly occurs in chloride-rich environments such as hot brines or in acid mine waters and has a brown to bright yellow color. In contrast to the other FeOOH phases, it has a structure based on body centered cubic close packing of the anions and necessarily includes trace levels of chloride.[28, 29] It is classified in the monoclinic crystallographic system and patterned after the hollandite ($BaMn_8O_{16}$) structure, which is less dense than those of goethite and lepidocrocite and contains one tunnel per unit cell. These tunnels are the location of a significant amount of zeolitic water as well as the chloride anions. Akaganéite has a Néel temperature that lies close to room temperature at 290 K,[28, 30, 31] and thus it is called either a paramagnet or antiferromagnet under ambient conditions. Akaganéite is a

semiconductor like goethite and lepidocrocite although with a smaller band gap of 2.12 eV.[32]

The earliest measurements of the heat capacity of akaganéite appear in the dissertation of B. Lang for two samples of akaganéite with varying degrees of hydration.[12] These measurements were performed adiabatically using a microcalorimeter in the range 12 K to 320 K. No noticeable anomaly could be seen in the heat capacity, but an inflection was observed that put the Néel temperature between 290 and 295 K. The resulting entropy was combined with enthalpy values from the literature, and the standard Gibbs free energy was reported as -481.7 ± 1.3 kJ·mol^{-1}. More recently, Wei *et al.* reported the heat capacity from 78 to 390 K of two akaganéite samples with rod and spindle shapes, respectively.[21]

These measurements are significantly lower than those of Lang by several J·mol^{-1}·K^{-1}, and there are several reasons for this disagreement. First Wei *et al.* characterized their samples using thermal gravimetric analysis, but failed to use this analysis to quantify the degree of hydration. Instead, their data is reported for a molecular formula of FeOOH. Also, Wei *et al.* used small sample amounts which were less than 1 cm^3 in a calorimeter which was approximately 6 cm^3. Generally, accurate heat capacity measurements are dependent upon the sample making a significant contribution to the overall heat capacity (that of the sample + the calorimeter).[33] When the contributions of the sample are not large enough, the resultant heat capacity measurements can be lower than their true value, and the lower heat capacity measurements by Wei *et al.* suggests that not enough sample was used in their studies. On the other hand, measurements of copper, benzoic acid, and sapphire standards with the instrumentation used by Lang showed a systematic positive deviation from the reference values which increased with temperature.[12, 34] This behavior suggests that there is a heat leak in the instrumentation which usually results in the measurement of heat capacities larger than their true value. To compensate for this heat leak, Lang applied a correction to samples measured on his system which may not be as reproducible as originally assumed. These discrepancies between existing heat capacity measurements make it important that new measurements be made in order to assess which of the two reports, if any, is more accurate.

5.1.3 Scope

The studies of Majzlan *et al.*[1, 13] have obtained the heat capacity, enthalpy of formation, and the Gibbs free energy of formation of lepidocrocite which have provided a better understanding of its relative stability. However, the heat capacity measurements of Majzlan *et al.* do not provide data below 5 K where such measurements are more amenable to theoretical modeling. Also, at lower temperatures, the adiabatic technique employed by Majzlan *et al.* is less accurate with an error of ±2% for $T < 13.8$ K and ±1% for 13.8 K < T < 25 K.[35] The accuracy and data range of Majzlan *et al.* is can reliably calculate the entropy of the sample, but cannot explain the microscopic origin of the heat capacity. From a quantum mechanical perspective heat capacities can provide information about the vibrational density of states, magnetic ordering, and electronic properties of a material,[33] but this is generally accomplished through fitting the heat capacity data to theoretical functions at temperatures below 10 K. In order to understand the microscopic origins and the physical properties associated with the heat capacity of lepidocrocite, measurements below 10 K will need to be made at lower temperatures and in greater quantity. This study provides the heat capacity of lepidocrocite measured by a semi-adiabatic pulse method in the temperature range 0.8 to 38 K which was used to study the physical and thermodynamic properties of lepidocrocite by fitting it to theoretical functions below 10 K.

The previous discussion suggests that there is some uncertainty and disagreement in the available heat capacity measurements of akaganéite. In order to evaluate the reliability of these measurements the heat capacity of an akaganéite sample supplied by Lang[12] was measured using semi-adiabatic calorimetry as well as a relaxation technique on a Quantum Design Physical Properties Measurement system (PPMS). The combined heat capacity of these two techniques provides the heat capacity of akaganéite in the temperature range 0.8 to 302 K. These measurements are compared to those of Lang and Wei *et al.* and a discussion is given of the relative accuracy of the three sets of measurements. Fits were made of the heat capacity of akaganeite below 15 K, and a corresponding analysis of their meaning is given. Through classical thermodynamic relationships, heat capacity measurements can be used to calculate third law entropies,

which can be combined with thermochemical measurements to calculate free energies.[11, 33] In turn, free energies can provide information about the relative stabilities of the various iron oxide polymorphs as well as help predict the outcome of chemical reactions. The third law entropy at 298.15 K and thermodynamic functions have been calculated for the hydrated form of akaganéite.

5.2 Experimental

The sample of akaganéite was synthesized by dissolving 40.1 g of $FeCl_3 \cdot 6H_2O$ in 1.5 L of water and hydrolyzed in a plastic flask for 8 days at 40 to 50°C. The resulting precipitate was decanted and dialyzed for two weeks, then dried at 40°C. The amount of water present in the sample was determined by measuring the mass loss of the sample after it was heated to 1100°C for 12 hours. Part of the mass loss is attributed to the decomposition of akaganéite to hematite:

$$\beta\text{-}FeOOH_{(s)} \rightarrow \tfrac{1}{2}\ \alpha\text{-}Fe_2O_{3(s)} + \tfrac{1}{2}H_2O_{(g)}.$$

From the reaction stoichiometry, water given off by this reaction should account for 10.14% of the mass loss. Thus, any additional mass loss is from water in the tunnels or water adsorbed on the particle surfaces. The water content of this sample was found to be 0.652 moles of water per FeOOH unit.

In addition to the water analysis, it is important to know the amount of chloride residing in the tunnels, since Cl^- is always present in akaganéite, serving to stabilize the molecular framework.[29] The Cl^- content was measured using liquid ion chromatography, and this akaganéite sample was found to contain 0.34% chlorine by mass, or 0.0096 moles of Cl^- per mol of FeOOH. This translates to roughly 7.5% of the possible chlorine sites being occupied. Thus, the resulting formula for this sample of akaganéite is $\beta\text{-}FeOOH \cdot 0.652H_2O \cdot 0.0096Cl^-$, where the charge is balanced by an equivalent number of hydrogen ions in the lattice.

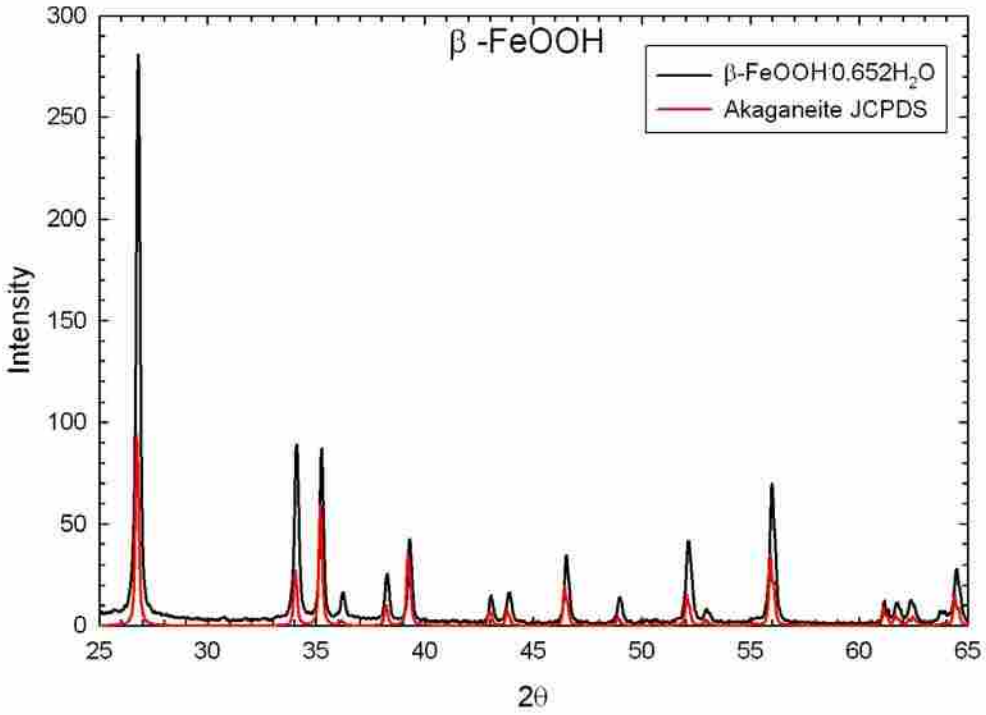

Figure 5.1. Powder X-ray Diffraction Pattern of the Akaganéite Sample used in this study. The red lines are the reference peaks found on JCPDS card 00-008-0093.

The sample was analyzed by powder X-ray diffraction (XRD) at room temperature on a Scintag Diffractometer (Cu-Kα radiation, λ = 0.154176 nm) at a scanning rate of 0.10 2θ/min and a power of 15 kW. The resulting powder pattern (Figure 5.1) was consistent with that of akaganéite, and no identifiable structural or chemical impurities were observed. From the peak widths at half the maximum height, the average size of the particles was estimated to be 34 nm. However, BET analysis indicated that this akaganéite sample had a surface are of 22.30 ± 0.28 m^2/g. This surface area is consistent with particles of an average size of 100 nm (assuming the akaganéite particles are rods). Thus, to determine the true nature of the akaganéite particle crystal sizes the sample was examined using a transmission electron microscope (TEM), revealing that the akaganéite particles are rods ranging between 25 and 80 nm in diameter and between 400 and 500 nm in length (Figure 5.2). The discrepancy in the average crystal size measurements from the XRD peaks indicates that the larger akaganéite crystals have multiple domains.

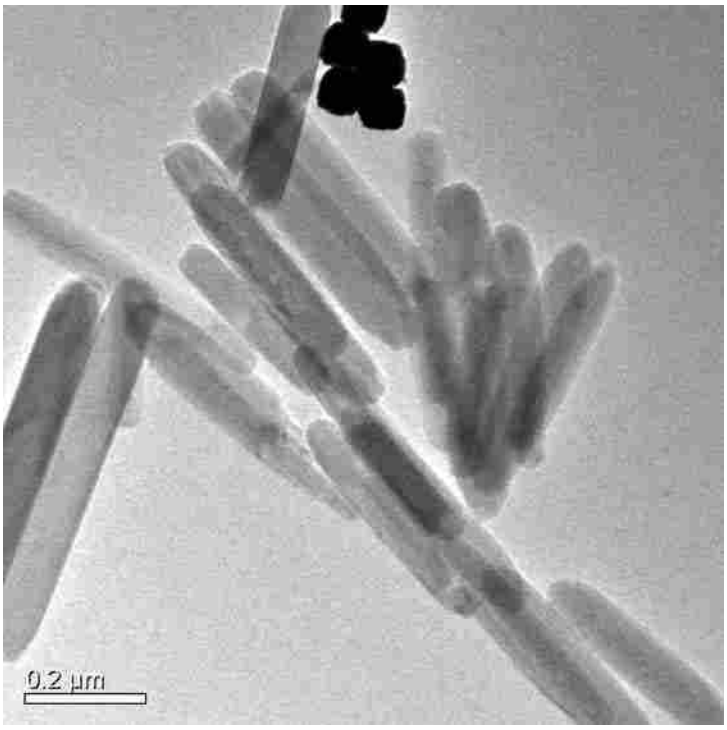

Figure 5.2. Transmission Electron Micrograph of Akaganeite sample reveals a rod-like shape.

The synthesis and characterization of the lepidocrocite sample used in this study have been described by Majzlan *et al.*[1] XRD showed only peaks corresponding to lepidocrocite, and the sample was found to be of adequate chemical purity with negligible amounts of aluminum and 200 ppm Cl^-. The sample had an average crystallite size of 30 nm, and after water was quantified the sample formula was calculated to be $FeOOH \cdot 0.087H_2O$.

The heat capacity of the lepidocrocite and akaganéite samples was measured in the temperature range 0.8 to 38 K using the semi-adiabatic calorimeter described by Lashley *et al.*[36] A lepidocrocite sample of 0.1206 g and an akaganéite sample of 0.1149 g were respectively wrapped in a copper foil (99.999% pure) to provide greater thermal conductivity. For each measurement, the copper and sample were compressed into a pellet of 3/8" diameter and 1/8" thickness which was then attached to the sample platform of the apparatus by using Apiezon N grease. The contributions of the copper, grease, and addenda were subtracted to obtain the molar heat capacity of the respective samples. The accuracy of this technique has been reported elsewhere to be within ±0.25%.[19, 36]

We have developed new methods of measuring the heat capacity of powdered samples using the Quantum Design Physical Properties measurement system (PPMS) with an accuracy of ± 1% from 22 K to 300 K and ± (2-5) % below 22 K, and this accuracy corresponds to both conducting and non-conducting samples. Details of this method will be published elsewhere. In general, sample mounting consists of combining the sample with Apiezon N grease in a copper cup which is then compressed into a pellet using a stainless steel die. The copper cup is formed from a foil of 0.025 mm thickness and 99.999 % purity while the pellet has a 2.8 mm diameter and height of 3.5 mm. The heat capacity of the grease, copper, and addenda are measured as a background which can be subtracted from measurements including the sample. The heat capacity of a 13.96 mg sample of akaganéite was measured in the range 2 to 350 K using the PPMS.

5.3 Results

The low-temperature heat capacity of lepidocrocite measured by semi-adiabatic calorimetry can be found in Table 5.1. This data is compared to that of Majzlan *et al.*[1] in Figure 5.3 where it can be seen that the two sets of measurements agree well over the temperature range 15 to 35 K. Below 15 K, Majzlan's measurements show less precision while above 35 K the semi-adiabatic measurements are consistently larger. The disagreement in these two regions can be explained by the relative accuracies of the two techniques for each region. Above 35 K the semi-adiabatic pulse technique begins to lose its accuracy due to radiative heat loss,[36] which will add a positive error to heat capacity measurements. As discussed previously, the adiabatic method used by Majzlan *et al.* has an error of ±2% below 14 K while the measurements below 14 K in this study have an error of ±0.25%. From this comparison, it can be seen that the heat capacity measured by the semi-adiabatic pulse technique is more accurate at temperatures below 15 K while the adiabatic pulse method becomes better at temperatures above 35 K. In the region of overlap between 15 and 35 K, the techniques have similar accuracies (~ 0.5%) which can be seen in the agreement between the two sets of measurements.

Table 5.2 contains the results of the measurements of β-$FeOOH{\cdot}0.652H_2O$ measured by semi-adiabatic calorimetry in the temperature range 0.8 to 38 K while Table 5.3 lists the measurements using the PPMS which were made from 2 K to 302 K. This

data is compared to that of Lang[12] as well as that of Wei *et al.*[21] in Figure 5.4. The data of Wei *et al.* is shown only for the rod-shaped samples which were found to be of a more similar size and shape to the sample used in this study. The first curve representing the measurements of Wei *et al.* is the data as it was published, while the second curve has been adjusted for water content according to the TGA curve published with their measurements. This curve shows a total mass loss of 18.82% which corresponds to a value of 0.469 moles H_2O per mole FeOOH. In both cases, the heat capacity reported by Wei *et al.* is much lower than the other two curves except at room temperature where the hydrated form approaches the heat capacity measured by the PPMS.

Table 5.1. The heat capacity of lepidocrocite (γ-FeOOH·0.087H_2O) measured by the semi-adiabatic technique. M = 90.419 g/mol.

T/K	$C_{p,m}$ (J mol^{-1} K^{-1})	ΔT/K	T/K	$C_{p,m}$ (J mol^{-1} K^{-1})	ΔT/K
	Series 1		2.6600	0.0094136	0.255
0.84062	0.000426639	0.0799	2.9279	0.011683	0.283
0.92489	0.000603259	0.0885	3.2214	0.014530	0.311
1.0142	0.000757346	0.101	3.5456	0.017801	0.343
1.1161	0.0010306	0.109	3.9013	0.022111	0.368
1.2280	0.0012863	0.116	4.2884	0.027358	0.411
1.3519	0.0016472	0.128	4.7158	0.033756	0.452
1.4835	0.0021836	0.144	5.1883	0.042053	0.497
1.6317	0.0027153	0.160	5.7080	0.051822	0.546
1.7990	0.0034718	0.169	6.2809	0.062769	0.598
1.9783	0.0044167	0.186	6.9085	0.077422	0.655
2.1766	0.0056637	0.205	7.5967	0.095210	0.723
	Series 2		8.3538	0.11756	0.795
0.88354	0.00052259	0.0822	9.1909	0.14330	0.880
0.97038	0.00069704	0.0923	10.110	0.17642	0.963
1.0659	0.00082556	0.104		*Series* 6	
1.1737	0.0011435	0.110	9.1957	0.14507	0.885
1.2897	0.0014696	0.121	10.105	0.17822	0.988
1.4162	0.0019125	0.138	11.109	0.22180	1.091
1.5591	0.0024520	0.148	12.222	0.27898	1.198
1.7147	0.0031368	0.163	13.451	0.34614	1.266

1.8859	0.0039958	0.181	14.790	0.43492	1.413
2.0738	0.0050436	0.199	16.270	0.54491	1.560
	Series 3		17.906	0.70763	1.708
1.7298	0.0032671	0.167	19.699	0.90398	1.883
1.9019	0.0041321	0.187	21.670	1.1408	2.065
2.0931	0.0052018	0.200	23.834	1.4353	2.270
2.3028	0.0065310	0.223	26.205	1.7825	2.474
2.5333	0.0081938	0.244	28.817	2.2701	2.737
2.7888	0.010222	0.268	31.691	2.9007	3.007
3.0696	0.012743	0.294	34.859	3.7445	3.327
3.3766	0.015811	0.326	37.686	4.5595	2.310
3.7148	0.019546	0.354		*Series* 7	
4.0857	0.024238	0.391	9.6561	0.15817	0.931
4.4941	0.029830	0.427	10.623	0.19165	0.998
4.9432	0.037216	0.474	11.680	0.24454	1.105
5.4381	0.046237	0.518	12.832	0.31401	1.221
5.9802	0.056912	0.571	14.114	0.38860	1.352
6.5789	0.068992	0.630	15.534	0.48418	1.491
7.2379	0.084574	0.688	17.094	0.61500	1.625
7.9606	0.10437	0.758	18.808	0.77344	1.799
8.7527	0.12852	0.825	20.688	0.99888	1.953
9.6261	0.15768	0.921	22.749	1.2661	2.188
10.591	0.19350	1.011	25.025	1.6113	2.367
	Series 4		27.514	2.0592	2.616
1.8155	0.0038884	0.177	30.253	2.6142	2.868
1.9954	0.0048338	0.198	33.269	3.3248	3.166
2.1958	0.0060414	0.217	36.265	4.2164	2.831
2.4184	0.0075588	0.234			

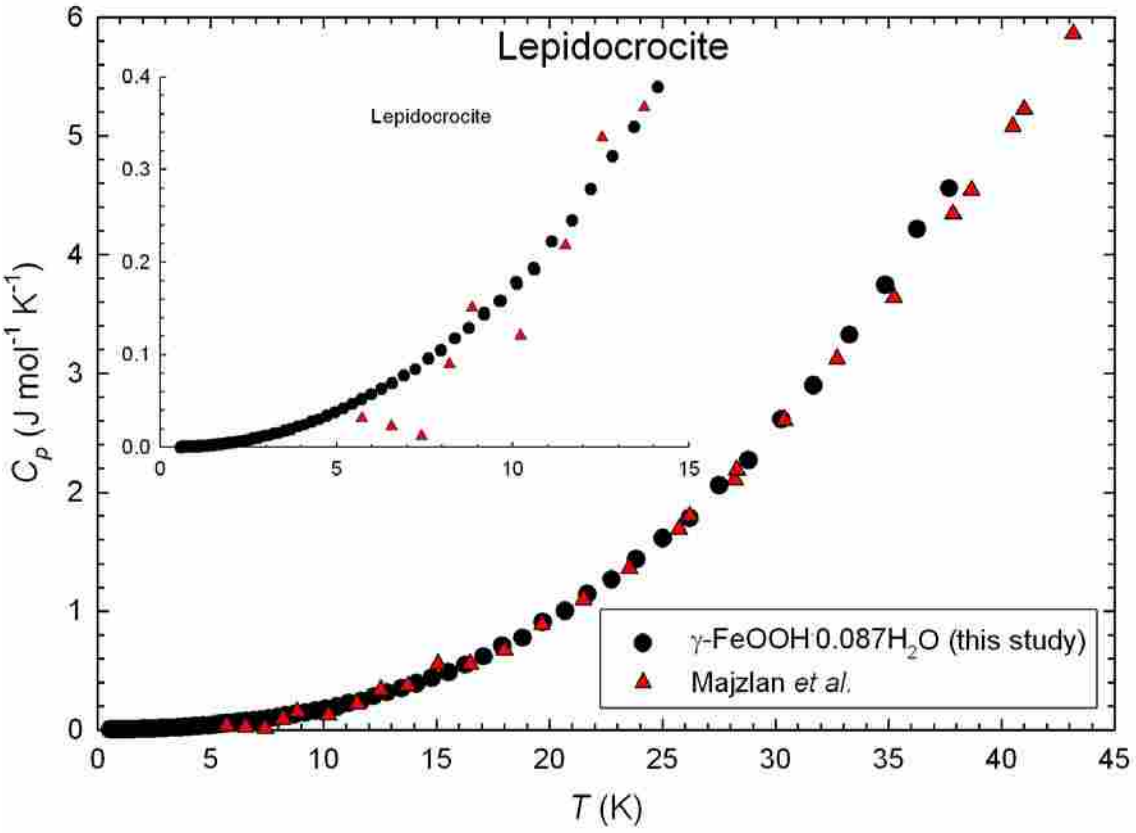

Figure 5.3. The heat capacity of γ-FeOOH.0.087H_2O measured by semi-adiabatic calorimetry with a comparison to the published results of Majzlan *et al.*[1] The inset shows the two sets of data below 15 K where the measuements by Majzlan *et al*. are less accurate.

Table 5.2. Heat capacity of akaganéite (β-FeOOH.0652H_2O) measured by PPMS. M = 100.938 g/mol.

***T*/K**	**$C_{p,m}$ (J mol^{-1} K^{-1})**	***T*/K**	**$C_{p,m}$ (J mol^{-1} K^{-1})**
1.9511	0.0027952	43.574	7.2632
2.1502	0.0034414	48.398	8.9758
2.1740	0.0035248	53.734	10.988
2.4775	0.0046700	59.680	13.342
2.7382	0.0057887	66.269	15.992
3.0453	0.0086081	73.597	19.009
3.3861	0.010683	81.724	22.527
3.7901	0.013951	90.759	26.526
4.1824	0.018113	100.79	30.731

4.6589	0.023885	110.89	34.884
5.1762	0.031398	120.95	38.943
5.7522	0.042266	131.05	43.009
6.4174	0.055520	141.11	46.937
7.1683	0.074280	151.27	50.570
7.9362	0.097755	161.37	54.235
8.8251	0.13064	171.46	57.710
10.011	0.18367	181.60	61.081
11.154	0.24657	191.74	64.321
12.391	0.32814	201.85	67.477
13.763	0.43387	211.96	70.610
15.262	0.56343	222.07	73.830
16.894	0.74357	232.16	76.768
18.753	0.99051	242.25	79.526
20.940	1.2989	252.29	82.335
23.204	1.6862	262.38	84.733
25.775	2.1916	272.53	86.989
28.587	2.8248	282.60	88.839
31.775	3.6221	292.58	90.349
35.327	4.6255	302.65	91.588
39.237	5.8419		

Table 5.3 contains the heat capacity of akaganéite measured from 0.8 to 38 K by semi-adiabatic calorimetry, and this data can be seen with a comparison to the measurements of Lang[12] as well as those made on the PPMS in Figure 5.5. One key observation of this figure is the good agreement among all three measurements in the temperature range 20 to 40 K. At these temperatures, the heat leak reported by Lang was generally small and thus the accuracy of the heat capacity was better.[34] However, as the temperature increases the heat capacity measured by Lang deviates to much higher values than that measured by PPMS. As discussed previously, independent measurements of the heat capacity of reference materials copper, benzoic acid, and sapphire using the instrument employed by Lang all displayed positive deviations from the reference values of the heat capacity.[12, 34] Lang attributed this excess heat capacity to a heat leak which was approximated to be consistent for all measurements. Such an approximation does not account for the thermal diffusivity of the sample being measured, and it may be less accurate for samples that require more time to reach thermal equilibrium. It is possible

that the heat capacity of akaganéite measured by Lang is higher than its true value just as the heat capacity of reference materials measured by Lang were consistently high. It should be noted that recent measurements of the heat capacity of bulk hematite using the techniques described previously for PPMS were found to be within ±0.8% of measurements of a different bulk hematite sample by Westrum and Gronvold[37] which were reported to have an error of

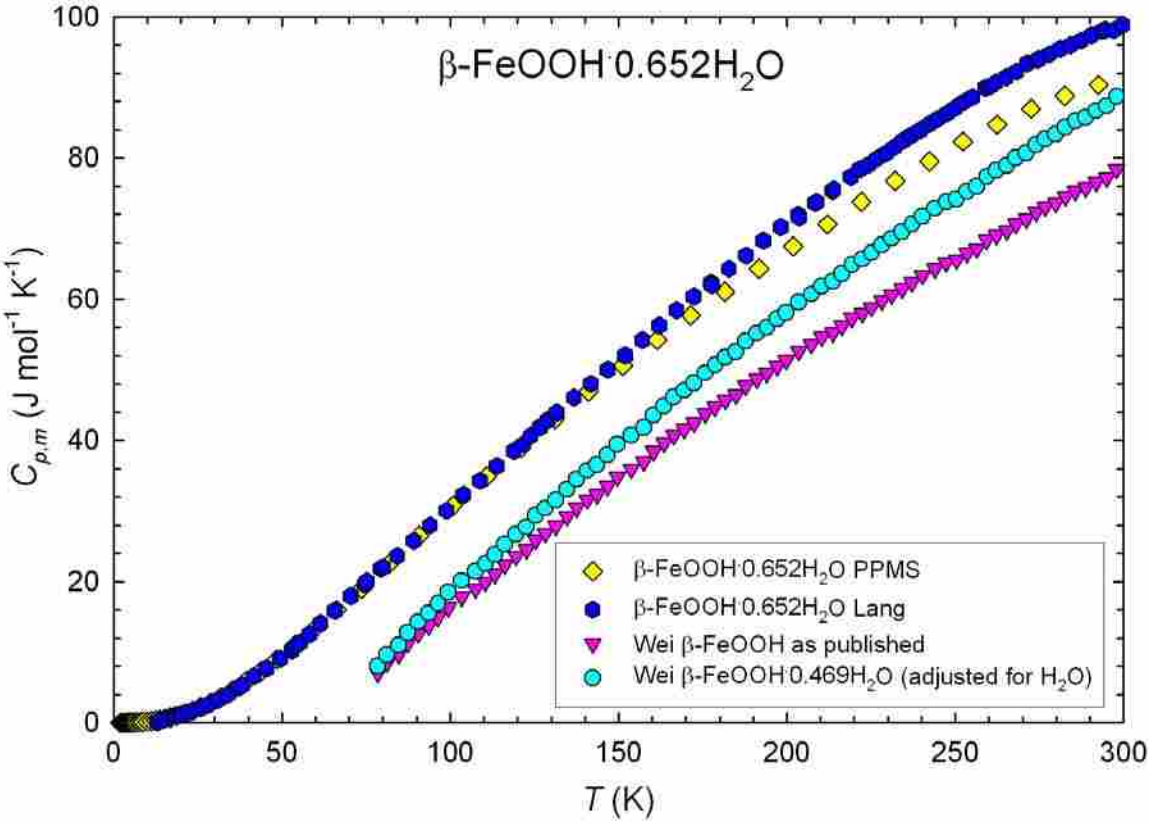

Figure 5.4. Comparison of heat capacity of akaganéite measurements from this work (PPMS), Wei *et al.*,[21] and Lang.[12, 22]

±0.1%. As the heat capacity of akaganéite measured by PPMS followed the same technique, this suggests that the measurements made in this study are more accurate than those reported by Lang.[12] It is believed also that the heat capacity of akaganéite reported by Wei *et al.*[21] is also of poor accuracy even when corrected for water content. This is mainly due to the use of a small sample size as discussed previously.

Table 5.3. Heat capacity of akaganéite (β-FeOOH.0652H_2O) measured using a semi-adiabatic pulse technique. M = 100.938 g/mol.

T/K	$C_{p,m}$ (J mol^{-1} K^{-1})	ΔT/K	T/K	$C_{p,m}$ (J mol^{-1} K^{-1})	ΔT/K
	Series 1		8.3548	0.065242	0.79051
1.7309	0.0021273	0.16587	9.1880	0.086798	0.87599
1.9019	0.0026345	0.18584	10.109	0.11557	0.96492
2.0926	0.0032424	0.20027		*Series* 4	
2.3028	0.0039827	0.22109	0.88143	0.00030872	0.08566
2.5341	0.0047923	0.24335	0.96974	0.00043910	0.09273
2.7890	0.0057909	0.26678	1.0660	0.00056833	0.10145
3.0686	0.0069513	0.29531	1.1722	0.00081904	0.11093
3.3772	0.0083321	0.32448	1.2884	0.0010514	0.12392
3.7147	0.010046	0.35250	1.4199	0.0013185	0.13825
4.0853	0.012130	0.38947	1.5614	0.0016438	0.14296
4.4938	0.014570	0.42740	1.7143	0.0020771	0.16053
4.9431	0.018463	0.47403	1.8855	0.0025523	0.17824
5.4381	0.023291	0.51823	2.0738	0.0031291	0.19696
5.9818	0.028973	0.57249		*Series* 5	
6.5799	0.035415	0.62937	9.1919	0.088554	0.87974
7.2385	0.044980	0.69266	10.111	0.11692	0.95965
7.9600	0.057604	0.75761	11.119	0.15733	1.0564
8.7533	0.075882	0.83486	12.230	0.21347	1.16624
9.6268	0.10066	0.91584	13.448	0.28412	1.27466
10.588	0.13696	1.0134	14.789	0.38497	1.41219
	Series 2		16.272	0.51713	1.55313
0.92452	0.00036683	0.08875	17.904	0.68887	1.71631
1.01561	0.00050552	0.09788	19.701	0.92568	1.87959
1.11785	0.00069610	0.10643	21.676	1.2130	2.06845
1.22826	0.00092624	0.11694	23.843	1.6013	2.2642
1.35105	0.0011608	0.12667	26.211	2.0892	2.47291
1.48258	0.0014537	0.14094	28.814	2.706	2.73419
1.63184	0.0018395	0.15687	31.689	3.4947	3.0136
1.79645	0.0022950	0.17016	34.863	4.4745	3.3361
1.97571	0.0028295	0.18799	37.686	5.3739	2.3303
2.17424	0.0034451	0.20804		*Series* 6	
	Series 3		9.6512	0.10305	0.92699
1.997	0.0028892	0.18996	10.617	0.13560	1.0095

2.417	0.0043830	0.23292	11.674	0.18616	1.11245
2.661	0.0052746	0.25395	12.835	0.24407	1.2172
2.928	0.0063323	0.2807	14.117	0.33283	1.3538
3.223	0.0076468	0.3094	15.531	0.44835	1.4834
3.546	0.0090038	0.33763	17.088	0.59691	1.6366
3.900	0.010919	0.3697	18.803	0.80565	1.7998
4.290	0.013178	0.41041	20.687	1.0667	1.9791
4.718	0.015815	0.44922	22.756	1.4027	2.1674
5.191	0.020303	0.49474	25.021	1.8483	2.3734
5.7094	0.025398	0.54338	27.508	2.3921	2.6180
6.2806	0.031147	0.59889	30.250	3.1313	2.8756
6.9086	0.038552	0.65764	33.274	4.0068	3.1790
7.5987	0.049345	0.72213	36.274	4.9618	2.8340

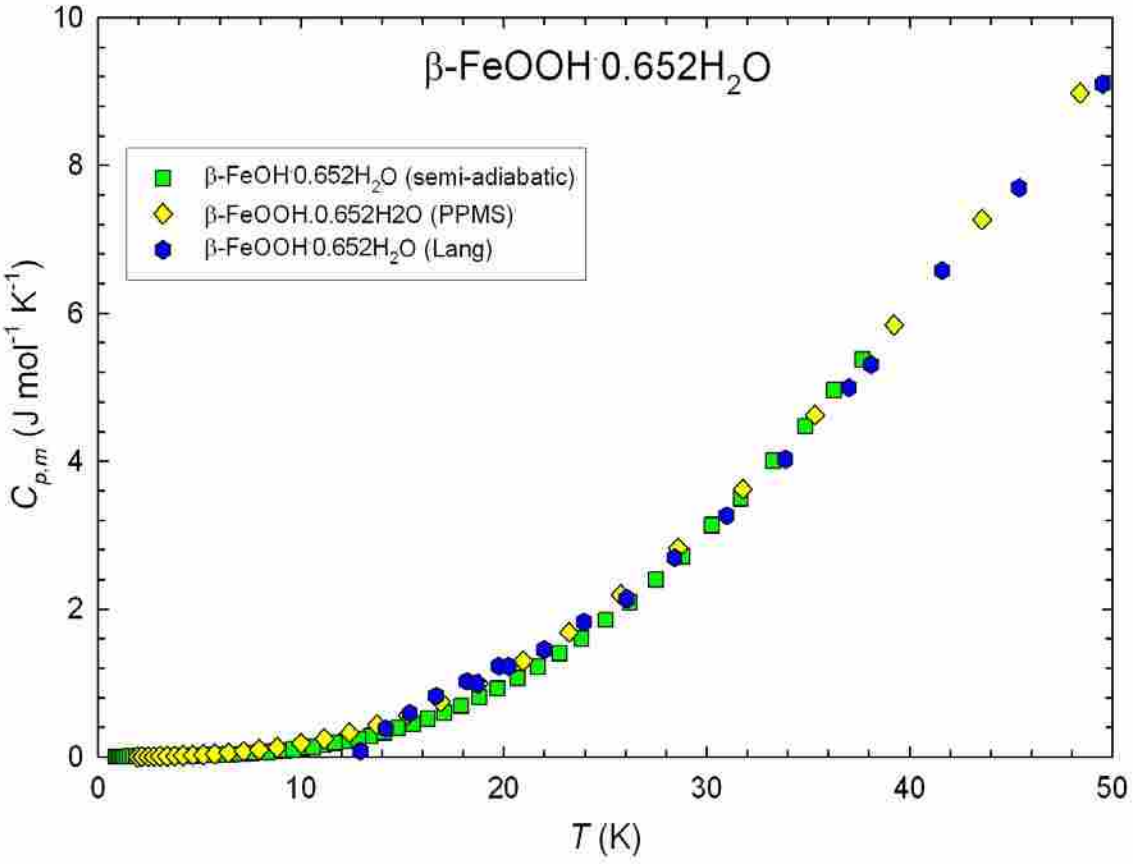

Figure 5.5. Comparison of the heat capacity of akaganéite measured in this study by PPMS and semi-adiabatic calorimetry to that measured by Lang[12] at temperatures below 50 K.

5.4 Discussion

5.4.1 The Heat Capacity of Lepidocrocite (γ-FeOOH·0.087H_2O) and Akaganéite (β-FeOOH·0.652H_2O) below 15 K

Modeling heat capacity data with theoretical functions at low temperatures (< 15 K) can provide valuable information about the magnetic, electronic, and vibrational properties of a sample.[33] The total heat capacity can be viewed as a sum of the energetic contributions from the various physical properties of a material. At temperatures above 10 K, the largest contribution to heat capacity stems from lattice vibrations which are modeled by an odd-powers fit to the equation:

$$C_{Lat} = \sum_{n=3,5,7\ldots} B_n T^n \text{ .}^{38} \quad (1)$$

Magnetic contributions will also have a temperature-dependence with $T^{3/2}$ for ordered ferro- and ferrimagnets and T^3 for antiferromagnets.[33] If there is a significant amount of anisotropy the spin-wave spectrum will have a gap, which is similar to the gap induced by a magnetic field.[39] Gaps in magnetic solids require the use of the term $C_{fsw} = B_{fsw} T^{3/2} e^{-\Delta/T}$ for ferro- and ferrimagnets and $C_{asw} = B_{asw} T^3 e^{-\Delta/T}$ for antiferromagnets, where Δ is the gap parameter given in units of K.[17, 40]

Conduction electrons contribute to the heat capacity in a linear fashion with γT representing the electronic heat capacity in most cases.[33] In addition to conducting solids, a linear term is generally observed in many oxide materials that are not fully stoichiometric or which contain oxygen vacancies or dislocations. For example, non-conducting oxides requiring a linear term include α-FeOOH (goethite),[17] crystalline pure SiO_2 zeolites,[41] and hydrous potassium aluminosilicate[42] (muscovite) where the linear term has been attributed by Coey *et al.* to localized electronic states associated with oxygen vacancies.[42]

5.4.2 Fits of the Heat Capacity of Lepidocrocite

Because lepidocrocite is antiferromagnetic below 77 K,[5, 25, 26, 43] initial fits were tried using the lattice heat capacity $C_{Lat} = \sum_{n=3,5,7\ldots} B_n T^n$, but the results were well outside of the experimental error of the heat capacity measurements. When a linear term was

included the fits showed improvement, but were still a poor representation of the heat capacity of lepidocrocite. Fits of a similar compound, goethite (α-FeOOH), at low temperatures required the anisotropic gap parameter $C_{asw} = B_{asw}T^3e^{-\Delta/T}$ as well as a linear term.[17] Following the method used for goethite the heat capacity of lepidocrocite was fit according to the expression:

$$C = \gamma T + \sum_{n=3,5,7...} B_n T^n + B_{asw}T^3e^{-\Delta/T} \quad (2)$$

This is expression was successful in modeling the heat capacity of lepidocrocite and a summary of the various fits using Equation 2 can be found in Table 5.4. Fits 1 through 3 can be seen with a comparison to the experimentally measured heat capacity of lepidocrocite in Figure 5.6.

Table 5.4. Summary of the fits of the heat capacity of lepidocrocite following Equation 2. Units are in mJ, mole, and K.

Parameter	Fit-1	Fit-2	Fit-3	Fit-4
B_3	0.49625	0.61265	0.68270	0.54439
B_5	-9.7094E-03	-0.021880	-0.033766	-0.014504
B_7		5.1268E-05	1.7030E-04	3.6857E-05
B_9			-4.2145E-07	-4.6288E-08
γ	0.35257	0.17212	0.092661	0.27461
B_{asw}	9.6474	7.6244	6.9065	6.0955
Δ	27.092	18.207	14.723	20.903
%RMS	0.833	0.364	0.227	0.527
Range (K)	0 to 10	0 to 10	0 to 10	0 to 15

It can be seen from by the low values for the %RMS in this table that these fits model the heat capacity of lepidocrocite well even when they are extended to 15 K. The curves shown in Figure 5.6 show generally good agreement between the fits and the experimental data, with Fit-1 showing some small deviations. This provides strong support for the use of the antiferromagnetic spin gap, which suggests that the sample has anisotropic behavior.

A linear term was also needed to accurately model the heat capacity of lepidocrocite. In the case of non-conducting oxides a linear term can stem from localized

electronic states associated with oxygen vacancies[42] or originate from localized vibrations of loosely bound particles trapped in defects.[17, 39] Trapped particles will act as a three dimensional particle in a box with each particle occupying its own box. Goethite was observed to have a linear term, but the origin was ambiguous with both oxygen vacancies or trapped particles given as plausible explanations.[17] The sample was shown to have a large discrepancy between its surface area as measured by BET (21 m^2/g) and that calculated from XRD (38 m^2/g) which suggests the presence of planar defects (interfaces) between the crystallites. These defects would act as the box where particles could potentially be trapped. Like goethite, lepidocrocite has a large discrepancy between its surface area as measured by BET (23 m^2/g) and that calculated by XRD (50 m^2/g),[1] and localized vibrations is one possible explanation for the linear term observed in the heat capacity of lepidocrocite.

As mentioned earlier another possible explanation for the linear term could be localized electronic states associated with oxygen vacancies. This was also explained for goethite in which the presence of excess water suggests the existence of Fe^{3+} vacancies.[17] Goethite and lepidocrocite have similar amounts of excess water with goethite having the formula α-$FeOOH.0.083H_2O$ and lepidocrocite having 0.087 moles H_2O per mole of FeOOH. Also, both samples have a similar linear term with goethite having a value of ~ 0.2 $mJ \cdot mol^{-1} \cdot K^{-2}$ and lepidocrocite Fit-3 having a value of ~ 0.1 $mJ \cdot mol^{-1} \cdot K^{-2}$. These similar values suggest that the linear term in the two polymorphs stems from the same contributing phenomenon, but localized electronic states or localized vibrations are both plausible explanations.

5.4.3 Fits of the Heat Capacity of Akaganéite.

The process of fitting the heat capacity of akaganéite below 15 K was identical to that of lepidocrocite. In both cases, the use of only the lattice contribution $C_{Lat} = \sum_{n=3,5,7...} B_n T^n$ resulted in poor fits of the heat capacity, and a linear term significantly improved these fits, which still exhibited considerable error. Like lepidocrocite and goethite, akaganéite is also antiferromagnetic,[28, 30, 31] and a gap parameter was necessary in order to obtain an accurate representation of its heat capacity. The heat capacity of

akaganéite was fit to Equation 2 and a summary of the various fits can be found in Table 5.5. The low values for the %RMS suggest that like the other FeOOH polymorphs a linear term and anisotropic spin gap accurately represent the heat capacity of akaganéite.

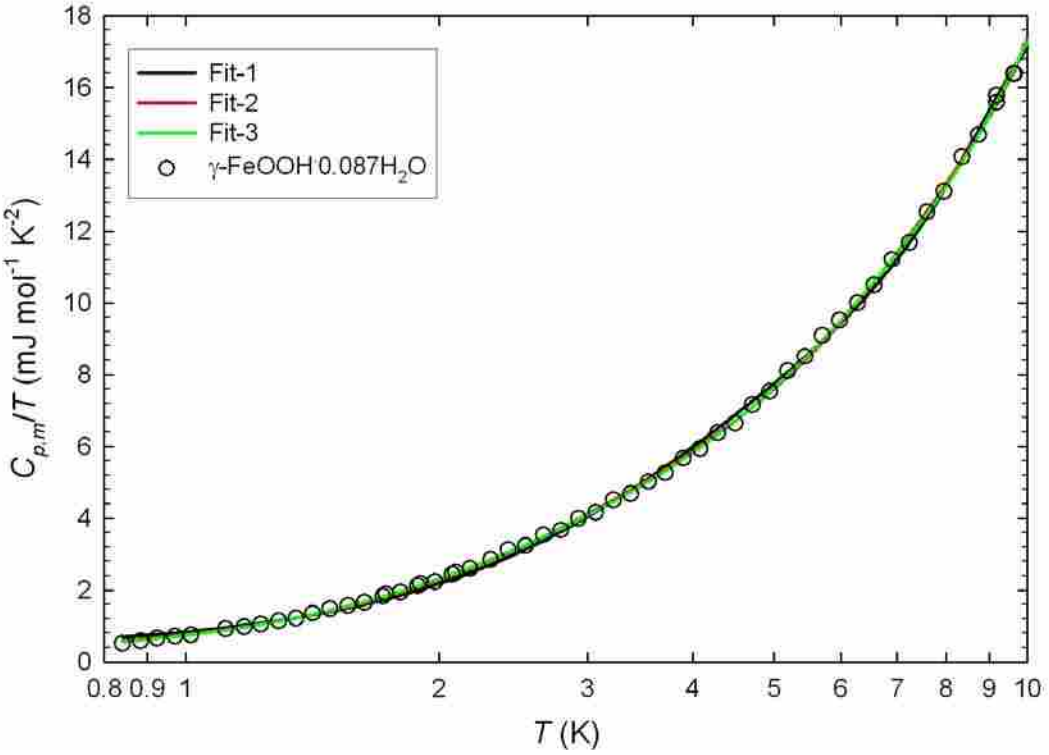

Figure 5.6. The Heat Capacity of Lepidocrocite in the Temperature Range 0-10 K with a comparison to Fits 1 to 3 from Table 5.4. Temperature is shown on a log scale.

Further support is seen in Figure 5.7 which compares Fits 1 through 3 to the experimentally measured heat capacity of akaganéite. It can be seen in this graph that the fits show generally good agreement with the experimental measurements with Fit-3 showing the best agreement.

The linear term of akaganéite is similar to those of lepidocrocite and goethite having a value in Fit-3 of 0.14 $mJ \cdot mol^{-1} \cdot K^{-2}$. However akaganéite has a water content of 0.652 moles H_2O per mole of FeOOH which is about 7.5 times more than the other FeOOH polymorphs. Some of this water occupies the tunnels in the lattice which could also be a good site for localized vibrations of trapped particles.[28, 29, 44] However with so many more potential boxes (one per unit cell) for these trapped particles, the linear term

of akaganéite is similar in value to those of the other FeOOH polymorphs. Yet a structure with more potential sites for trapped particles would be expected to result in a larger linear contribution to the heat capacity. This suggests that that the linear term in the three FeOOH polymorphs is more likely due to localized electronic states due to oxygen vacancies.

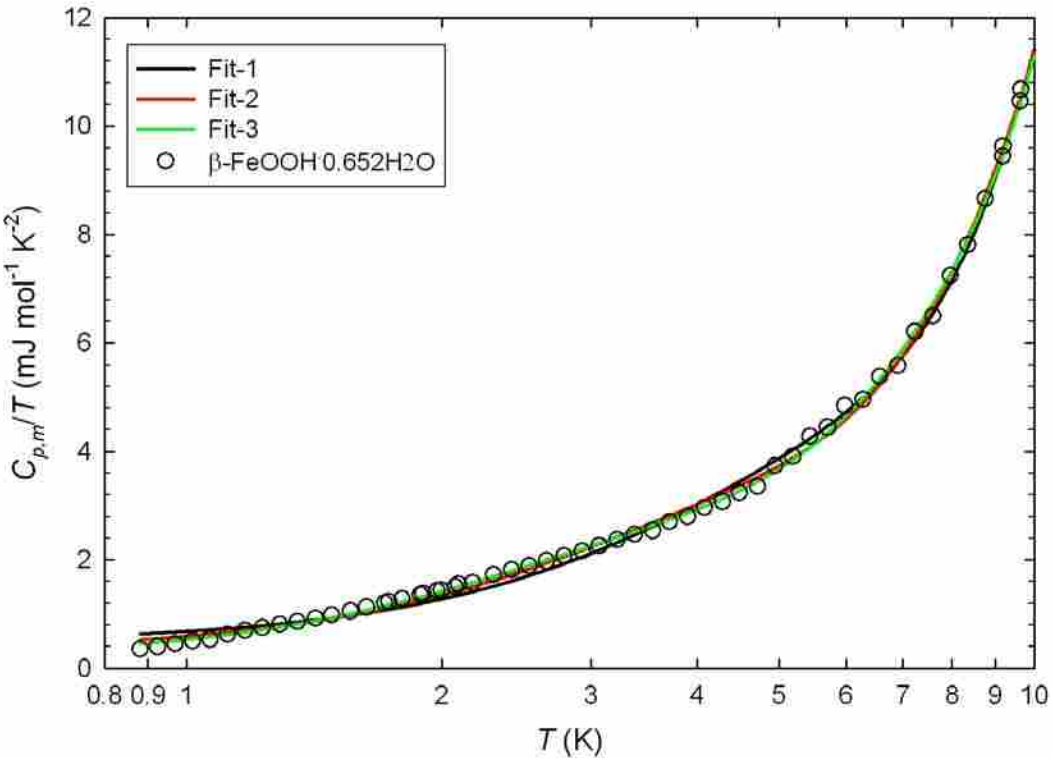

Figure 5.7. The Heat Capacity of Akaganeite in the temperature range 0-10 K with a comparison to Fits 1through 3 found in Table 5.5. Temperature is shown on a log scale.

5.4.4 The Heat Capacity of Anhydrous Akaganéite

Figure 5.8 shows a comparison between the heat capacity of hydrated akaganéite measured by PPMS and that of lepidocrocite and goethite. It can be seen in this figure that akaganéite is significantly larger which can be attributed to its greater degree of hydration. In order to provide a comparison between the heat capacity of anhydrous akaganéite and that of the other FeOOH polymorphs, the heat capacity of the water on akaganéite was approximated the same as that of solid H_2O. The heat capacity of ice was represented by a combination of orthogonal polynomials from 0 to 40 K using the

Table 5.5. Summary of the fits of the heat capacity of lepidocrocite following Equation 2. Units are in mJ, mole, and K.

Parameter	Fit-1	Fit-2	Fit-3	Fit-4
B_3	0.21842	0.30387	0.41319	0.24840
B_5	-3.9057E-03	-1.0557E-02	-2.4649E-02	-6.1156E-03
B_7		1.7037E-05	1.0147E-04	8.9913E-06
B_9			-2.0165E-07	-6.2570E-09
γ	0.46809	0.30064	0.14487	0.40678
B_{asw}	5.14220	5.51200	6.41550	4.21520
Δ	29.056	20.754	15.588	23.836
%RMS	1.50	1.03	0.624	1.13
Range (K)	0 to 12	0 to 12	0 to 12	0 to 20

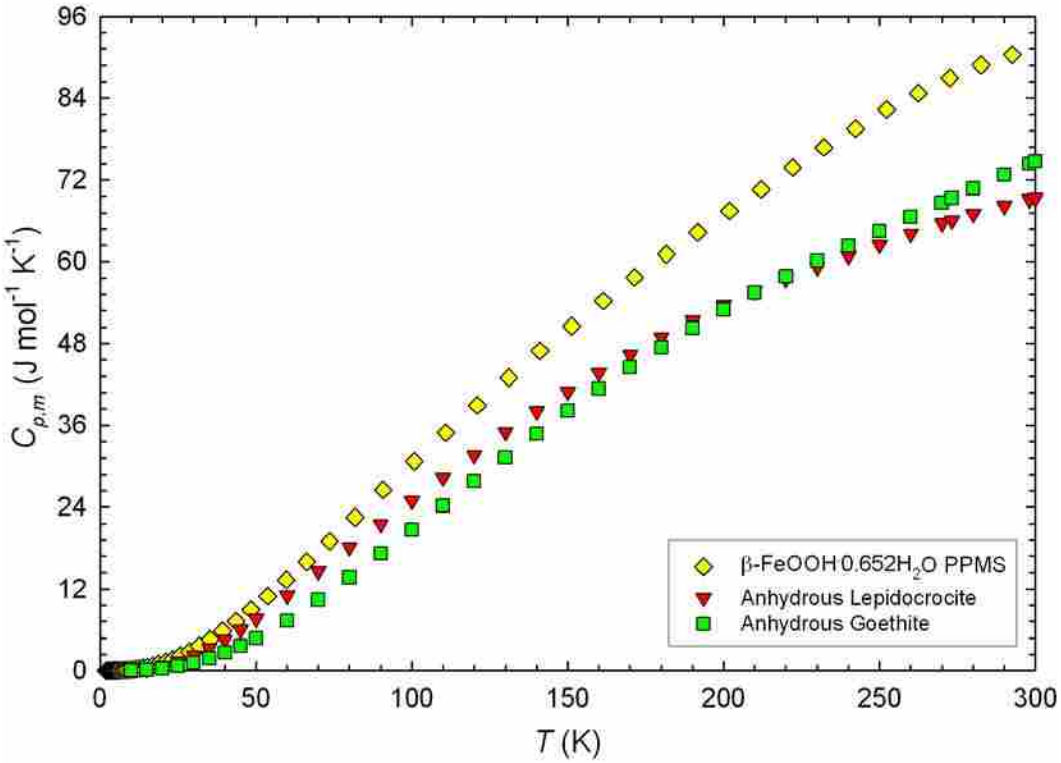

Figure 5.8. A comparison of the heat capacity of hydrated akaganéite from this study to that of anhydrous lepidocrocite and goethite reported by Majzlan *et al.*[1]

measurements of Smith *et al.*[19] and from 40 to 300 K using a Debye-Einstein fit of other various measurements.[18, 20, 22] Calculated values of the heat capacity of ice were multiplied by 0.652 and subsequently subtracted from the heat capacity of akaganéite at smoothed temperatures. The results can be seen in Figure 5.9 with a comparison to the heat capacity of anhydrous goethite and lepidocrocite. The calculated heat capacity of anhydrous akaganéite using the ice approximation has several negative values (shown in the inset) at low temperatures, but above 40 K it begins to resemble the other FeOOH polymorphs.

The estimate that the water on akaganéite has the same heat capacity as that of ice is probably too high as seen by the negative values at low temperatures. Heat capacity studies of water on nanocrystalline TiO_2 polymorphs[45] and nanocrystalline hematite

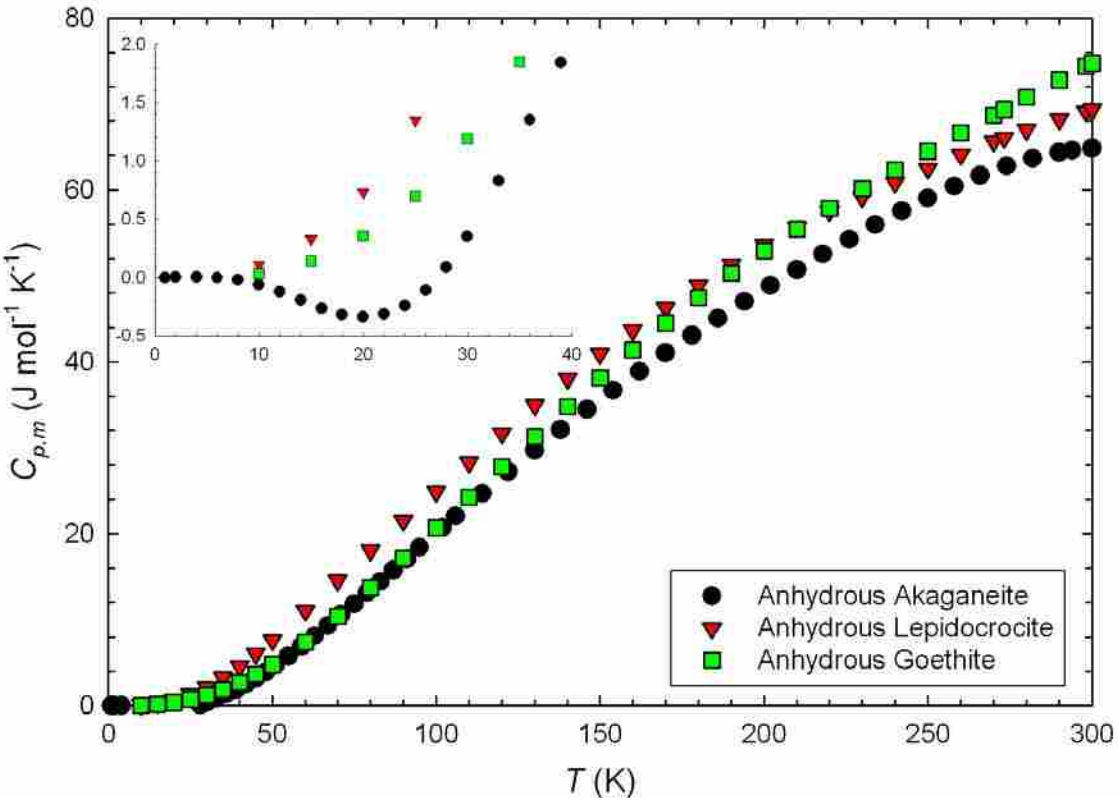

Figure 5.9. The heat capacity of anhydrous akaganéite calculated by approximating the heat capacity of the adsorbed water to be equal to that of solid H_2O.[20] A comparison is given to lepidocrocite and goethite.[1] The Inset shows the curves below 40 K.

(unpublished) show that the heat capacity of adsorbed water depends upon the proximity of the water to the surface of the nanoparticles. In the case of TiO_2, the heat capacity was

measured for nanoparticles with varying degrees of hydration, and it was found that the water on the less hydrated samples had a much lower heat capacity. This can be attributed to the tighter binding of inner layers[9, 10, 45] of water to the surface of the nanoparticles while the outer layers have more degrees of freedom which correspond to a higher heat capacity. In general, the heat capacity of water adsorbed onto the surface of both TiO_2 and hematite nanoparticles did not equal that of solid H_2O. In spite of the poor estimate of the heat capacity of water on akaganéite, the anhydrous sample shows relatively good agreement with the other FeOOH polymorphs, and it is possible that some of the water on akaganéite behaves in a similar manner to solid H_2O. Reliable heat capacity studies of akaganéite with varying degrees of hydration would be useful in providing a better understanding of the heat capacity of water on the surface of akaganéite which could then enable a more accurate calculation of the heat capacity of anhydrous akaganéite.

5.4.5 Thermodynamic Functions of Akaganéite (β-FeOOH·0.652H_2O)

To calculate thermodynamic functions for akaganéite the semi-adiabatic measurements were combined with the PPMS data. A graph of the two sets of measurements can be seen in Figure 5.5 where below 30 K the PPMS data is higher than that of the semi-adiabatic. Since the semi-adiabatic technique has a better accuracy (±0.5%) in this region, the PPMS (±2%) data below 30 K was not included in the thermodynamic calculations of akaganéite.

The standard molar thermodynamic functions, $C_{p,m}$, $\Delta^{T}_{0}H^{\circ}_{m}$, $\Delta^{T}_{0}S^{\circ}_{m}$, and $\Phi^{\circ}_{m}=(\Delta^{T}_{0}S^{\circ}_{m}-\Delta^{T}_{0}H^{\circ}_{m}/T)$ scaled by the ideal gas constant R are reported in Table 5.6 for hydrated akaganéite (β-FeOOH·0.652H_2O). They have been generated at smoothed temperatures by fitting a combination of orthogonal polynomials (given in Table 5.7) to the experimental results for akaganéite. These polynomials include the data below 15 K as they are more convenient in the calculation of the entropy. Although they are not physically meaningful, these polynomials are a good statistical representation of the heat capacity as can be seen by their respective %RMS values as shown in Table 5.7. The standard molar entropy of hydrated akaganéite is calculated to be 81.8 ± 2 J·mol^{-1}·K^{-1}, which is somewhat larger than 59.2 ± 0.2 J·mol^{-1}·K^{-1} for goethite[1] and 65.1 ± 0.2

$J \cdot mol^{-1} \cdot K^{-1}$ for lepidocrocite.[1] This is most likely due to the contribution from the water in the entropy calculated for akaganéite while the other polymorphs are anhydrous. With a better understanding of the behavior of water on the surface of akaganéite, a more reliable comparison can be made between the stability of akaganéite and the other iron oxyhydroxides.

Table 5.6. Smoothed heat capacity and thermodynamic functions of akaganéite (β-$FeOOH \cdot 0.652H_2O$). $\Phi = \Delta S - \Delta H/T$, M = 100.938 g/mol, p° = 100 kPa, and R = 8.3145 $J \cdot K^{-1} \cdot mol^{-1}$.

T (K)	$C_{p,m} / R$	$\Delta S / R$	$\Delta H / RT$	Φ / R
1.0	5.7694E-05	9.0543E-06	8.2229E-06	6.9131E-06
1.5	0.00018219	5.4659E-05	4.4372E-05	8.5532E-05
2.0	0.00034975	0.00012880	9.8711E-05	0.00025021
2.5	0.00056332	0.00022912	0.00016967	0.00049425
3.0	0.00080209	0.00035266	0.00025493	0.00081255
3.5	0.0010643	0.00049556	0.00035142	0.0011984
4.0	0.0013772	0.00065735	0.00045938	0.0016460
4.5	0.0017708	0.00084141	0.00058240	0.0021535
5.0	0.0022526	0.0010522	0.00072463	0.0027234
5.5	0.0028097	0.0012924	0.00088835	0.0033600
6.0	0.0034280	0.0015631	0.0010738	0.0040675
6.5	0.0041128	0.0018640	0.0012808	0.0048489
7.0	0.0048965	0.0021966	0.0015103	0.0057067
7.5	0.0058278	0.0025653	0.0017661	0.0066442
8.0	0.0069524	0.0029761	0.0020540	0.0076667
8.5	0.0082974	0.0034368	0.0023807	0.0087818
9.0	0.0098669	0.0039544	0.0027519	0.0099987
9.5	0.011654	0.0045348	0.0031724	0.011328
10	0.013656	0.0051825	0.0036457	0.012779
11	0.018366	0.0066970	0.0047622	0.016087
12	0.024098	0.0085335	0.0061276	0.020004
13	0.030907	0.010724	0.0077646	0.024604
14	0.038907	0.013300	0.0096960	0.029960
15	0.048213	0.016293	0.011946	0.036144
16	0.058913	0.019739	0.014540	0.043227
17	0.071046	0.023667	0.017500	0.051278

18	0.084617	0.028105	0.020844	0.060367
19	0.099614	0.033076	0.024590	0.070556
20	0.11602	0.038596	0.028745	0.081907
25	0.22024	0.074964	0.055978	0.15786
30	0.36661	0.12740	0.094953	0.26979
35	0.54591	0.19714	0.146335	0.42231
40	0.73296	0.28222	0.207962	0.61744
45	0.93434	0.37996	0.277287	0.85377
50	1.1509	0.48951	0.353707	1.1291
55	1.3789	0.60981	0.436466	1.4413
60	1.6162	0.73990	0.524830	1.7882
65	1.8610	0.87890	0.618161	2.1679
70	2.1114	1.0259	0.715846	2.5783
75	2.3656	1.1803	0.817343	3.0175
80	2.6225	1.3412	0.922124	3.4838
85	2.8808	1.5078	1.0297	3.9753
90	3.1392	1.6798	1.1398	4.4905
95	3.3967	1.8565	1.2518	5.0278
100	3.6528	2.0372	1.3654	5.5856
110	4.1574	2.4092	1.5964	6.7574
120	4.6490	2.7920	1.8304	7.9957
130	5.1253	3.1831	2.0657	9.2910
140	5.5854	3.5799	2.3007	10.635
150	6.0296	3.9804	2.5346	12.022
160	6.4588	4.3833	2.7665	13.443
170	6.8747	4.7874	2.9960	14.895
180	7.2787	5.1919	3.2228	16.372
190	7.6724	5.5960	3.4466	17.871
200	8.0566	5.9994	3.6676	19.388
210	8.4321	6.4016	3.8855	20.920
220	8.7981	6.8023	4.1005	22.464
230	9.1533	7.2013	4.3126	24.018
240	9.4949	7.5982	4.5214	25.581
250	9.8192	7.9924	4.7269	27.151
260	10.121	8.3834	4.9286	28.725
270	10.396	8.7707	5.1262	30.302
273.15	10.475	8.8917	5.1874	30.800
280	10.635	9.1532	5.3188	31.881
290	10.832	9.5300	5.5056	33.461

298.15	10.956	9.8320	5.6530	34.746
300	10.979	9.8998	5.6857	35.038

Table 5.7. A summary of the orthogonal polynomials used in the calculation of smoothed heat capacity and thermodynamic functions of akaganéite.

Powers	Temperature Range	Coefficients
	$1.0 \leq T$ (K) ≤ 11.56	
0		0.01447
1		-0.06487
2		0.12163
3		-0.12642
4		0.08298
5		-0.03620
6		0.01087
7		-0.002295
8		0.0003451
9		-3.708E-05
10		2.82E-06
11		-1.482E-07
12		5.116E-09
13		-1.043E-10
14		9.511E-13
	%RMS = 1.24	
	$11.56 \leq T$ (K) $\leq$ 41.11	
0		-1.019E+00
1		1.218E+00
2		-4.855E-01
3		1.007E-01
4		-1.271E-02
5		1.058E-03
6		-6.034E-05
7		2.408E-06
8		-6.764E-08
9		1.329E-09

10	-1.782E-11
11	1.554E-13
12	-7.921E-16
13	1.790E-18
%RMS = 0.659	
$41.11 \leq T\,(\mathrm{K}) \leq 300$	
0	-4.547E-01
1	-5.633E-02
2	7.117E-03
3	-4.408E-05
4	8.035E-08
5	2.347E-10
6	-1.126E-12
7	1.181E-15
% RMS = 0.141	

Acknowledgements

Portions of the experimental section were written by Dr. Brian Lang and Stacey Smith provided valuable help with the fitting of akaganéite.

References

1. Majzlan, J.; Lang, B. E.; Stevens, R.; Navrotsky, A.; Woodfield, B. F.; Boerio-Goates, J., *Am. Mineral.* **2003,** *88* (5-6), 846-854.
2. Schwertmann, U., *NATO ASI Ser., Ser. C* **1988,** *217* (Iron Soils Clay Miner.), 267-308.
3. Schwertmann, U.; Cornell, R. M., *Iron Oxides in the Laboratory, 2nd Edition*. 2000; p 154
4. Sundman, B., *J. Phase Equilib.* **1991,** *12* (2), 127-40.
5. Cornell, R. M.; Schwertmann, U.; Editors, *The Iron Oxides: Structure, Properties, Reactions, Occurrence and Uses*. VCH: Weinem, 1996; p 573.
6. Jambor, J. L.; Dutrizac, J. E., *Chem. Rev. (Washington, D. C.)* **1998,** *98* (7), 2549-2585.
7. Jansen, E.; Kyek, A.; Schafer, W.; Schwertmann, U., *Appl. Phys. A: Mater. Sci. Process.* **2002,** *74* (Suppl., Pt. 2), S1004-S1006.
8. Penn, R. L., *Science (Washington, DC, U. S.)* **2007,** *316* (5832), 1704-1705.
9. Navrotsky, A., *J. Chem. Thermodyn.* **2006,** *39* (1), 2-9.

10. Navrotsky, A.; Mazeina, L.; Majzlan, J., *Science (Washington, DC, U. S.)* **2008,** *319* (5870), 1635-1638.
11. Ott, J. B.; Boerio-Goates, J., *Chemical Thermodynamics: Principles and Applications*. 2000; p 360 pp.
12. Lang, B. E. Specific Heat and Thermodynamic Properties of Metallic Systems: Instrumentation and Analysis. 2005.
13. Majzlan, J.; Grevel, K.-D.; Navrotsky, A., *Am. Mineral.* **2003,** *88* (5-6), 855-859.
14. Majzlan, J.; Koch, C. B.; Navrotsky, A., *Clays Clay Miner.* **2008,** *56* (5), 526-530.
15. Majzlan, J.; Mazeina, L.; Navrotsky, A., *Geochim. Cosmochim. Acta* **2007,** *71* (3), 615-623.
16. Majzlan, J.; Navrotsky, A.; Schwertmann, U., *Geochim. Cosmochim. Acta* **2004,** *68* (5), 1049-1059.
17. Majzlan, J.; Navrotsky, A.; Woodfield, B. F.; Lang, B. E.; Boerio-Goates, J.; Fisher, R. A., *J. Low Temp. Phys.* **2003,** *130* (1/2), 69-76.
18. Giauque, W. F.; Stout, J. W., *J. Am. Chem. Soc.* **1936,** *58*, 1144-50.
19. Smith, S. J.; Lang, B. E.; Liu, S.; Boerio-Goates, J.; Woodfield, B. F., *J. Chem. Thermodyn.* **2007,** *39* (5), 712-716.
20. Flubacher, P.; Leadbetter, A. J.; Morrison, J. A., *J. Chem. Phys.* **1960,** *33*, 1751-5.
21. Wei, C.; Wang, X.; Nan, Z.; Tan, Z., *J. Chem. Eng. Data* **2009,** *55* (1), 366-369.
22. Haida, O.; Matsuo, T.; Suga, H.; Seki, S., *J. Chem. Thermodyn.* **1974,** *6* (9), 815-25.
23. Ewing, F. J., *J. Chem. Phys.* **1935,** *3*, 420-4.
24. Morris, R. V.; Lauer, H. V., Jr.; Lawson, C. A.; Gibson, E. K., Jr.; Nace, G. A.; Stewart, C., *J. Geophys. Res., B* **1985,** *90* (B4), 3126-44.
25. Hall, P. G.; Clarke, N. S.; Maynard, S. C. P., *J. Phys. Chem.* **1995,** *99* (15), 5666-73.
26. Hirt, A. M.; Lanci, L.; Dobson, J.; Weidler, P.; Gehring, A. U., *J. Geophys. Res., [Solid Earth]* **2002,** *107* (B1), EPM5/1-EPM5/9.
27. Murad, E.; Schwertmann, U., *Mineral. Mag.* **1984,** *48* (349), 507-11.
28. Murad, E., *Clay Miner.* **1979,** *14* (4), 273-83.
29. Cai, J.; Liu, J.; Gao, Z.; Navrotsky, A.; Suib, S. L., *Chem. Mater.* **2001,** *13* (12), 4595-4602.
30. Barrero, C. A.; Garcia, K. E.; Morales, A. L.; Kodjikian, S.; Greneche, J. M., *J. Phys.: Condens. Matter* **2006,** *18* (29), 6827-6840.
31. Chambaere, D.; De Grave, E., *J. Magn. Magn. Mater.* **1984,** *42* (3), 263-8.
32. Sherman, D. M., *Geochim. Cosmochim. Acta* **2005,** *69* (13), 3249-3255.
33. Gopal, E. S. R., *Specific Heats at Low Temperatures (International Cryogenics Monograph Series)*. Plenum Press: New York, 1966; p 226
34. Lang, B. E.; Boerio-Goates, J.; Woodfield, B. F., *J. Chem. Thermodyn.* **2006,** *38* (12), 1655-1663.
35. Stevens, R.; Boerio-Goates, J., *J. Chem. Thermodyn.* **2004,** *36* (10), 857-863.
36. Lashley, J. C.; Lang, B. E.; Boerio-Goates, J.; Woodfield, B. F.; Darling, T. W.; Chu, F.; Migliori, A.; Thoma, D., *J. Chem. Thermodyn.* **2002,** *34* (2), 251-261.
37. Gronvold, F.; Westrum, E. F., Jr., *J. Am. Chem. Soc.* **1959,** *81*, 1780-3.
38. Phillips, N. E., *Crit. Rev. Solid State Sci.* **1971,** *2* (4), 467-553.

39. Fisher, R. A.; Bouquet, F.; Phillips, N. E.; Franck, J. P.; Zhang, G.; Gordon, J. E.; Marcenat, C., *Phys. Rev. B: Condens. Matter Mater. Phys.* **2001,** *64* (13), 134425/1-134425/9.
40. Niira, K., *Phys. Rev.* **1960,** *117*, 129-33.
41. Boerio-Goates, J.; Stevens, R.; Lang, B.; Woodfield, B. F., *J. Therm. Anal. Calorim.* **2002,** *69* (3), 773-783.
42. Coey, J. M. D.; Von Molnar, S.; Torressen, A., *J. Less-Common Met.* **1989,** *151*, 191-4.
43. Lee, G. H.; Kim, S. H.; Choi, B. J.; Huh, S. H.; Chang, Y.; Kim, B.; Park, J.; Oh, S. J., *J. Korean Phys. Soc.* **2004,** *45* (4), 1019-1024.
44. Childs, C. W.; Goodman, B. A.; Paterson, E.; Woodhams, F. W. D., *Aust. J. Chem.* **1980,** *33* (1), 15-26.
45. Boerio-Goates, J.; Li, G.; Li, L.; Walker, T. F.; Parry, T.; Woodfield, B. F., *Nano Lett.* **2006,** *6* (4), 750-754.

Chapter 6

The Effects of Imidazole, MOPS, and Cysteine Buffers on the Reconstitution of the Iron Core of Horse Spleen Ferritin

6.1 Introduction

The use of proteins as a template for the production of nanomaterials is an emerging and promising aspect of biochemical engineering.[1, 2] Research in materials science has assimilated the concepts of biology on a basic level, and now faces the challenge of carrying this knowledge over to applied materials. Facilitating discovery in this discipline is attractive for many reasons. For example, protein cages are among just a few nanoplatforms capable of simultaneous control over size, shape, and biocompatibility.[3] Studies have shown that, in nature, protein interactions not only direct nucleation of inorganic materials, but also control the crystal type, face, and size, even of metastable forms, all in aqueous solutions and at ambient conditions.[1, 3] Furthermore, protein cages yield products which are already dispersed in solution and thus avoid the problem of agglomeration common in other production methods. Proteins are also attractive because they are amenable to alterations in functionality through both chemical and genetic means.

Ferritin, the biological protein for iron storage,[4] has been more extensively studied as a nanoplatform than any other protein, and not without success. Mn(O)OH, Mn_3O_4, Co(O)OH, Co_3O_4, $Cr(OH)_3$, $Ni(OH)_3$, In_2O_3, FeS, CdS, CdSe, and ZnSe have all been synthesized within the ferritin protein cage.[1, 5-12] Metallic nanoparticles such as Pd, Ag, and CoPt have also been synthesized within ferritin by pre-incubation of the protein with a metal salt and subsequent chemical reduction by a strong reducing agent.[3] Compounds

formed in ferritin have shown promise in catalysis, electrochemistry, and targeted drug delivery and bioimaging.[1, 3, 5, 12]

Ferritin is a spherical protein cage with an outer diameter of 12 nm and an interior cavity of 8 nm.[4] The shell is composed of 24 subunits that self-assemble generating channels of 4 Å in diameter, eight of which are hydrophilic. Ferritin has been observed to contain as many as 4500 iron atoms although naturally the average is closer to 2000. These iron atoms form a ferric oxyhydroxide core in the center of the ferritin cavity that most resembles ferrihydrite.[13-15] The solid iron core can be chemically removed through chemical reduction followed by chelation and dialysis.[16, 17]

It has been shown that chemical species in solution such as buffers and salts can greatly affect iron uptake in ferritin for *in vitro* reactions.[18] Studies by Cutler *et al.*[19] concluded that, in general, cations slow the rate of iron loading into ferritin by competing with Fe^{2+} for negatively charged amino acids. Specific anions such as halides and sulfate had no effect. On the other hand phosphate and its tetrahedral oxo-anion analogs have been shown to stimulate the rate of iron loading into ferritin.[20-23] Pâques *et al*.[24] studied the effects of buffer, ionic strength, pH, and temperature upon the rate of core formation in ferritin. This study involved the buffers 4-morpholinoepropanesulphonic acid (MOPS), 4-morpholineethanesulphonic acid (MES), and imidazole. At lower pH's the authors concluded that there was little difference in the rates for these buffers, but at a pH of 7.0 imidazole showed much smaller rates of iron formation. These authors also observed an inhibition of ferritin core formation with increasing ionic strength which is consistent with the findings of Cutler *et al*.[19] as to the general effects of cations and anions.

Oxidative damage to apoferritin results in the termination of core formation and presents a serious problem when trying to maximize the number of iron atoms introduced into the protein.[4, 25] In the natural process of core formation, Fe^{2+} is oxidized at the ferroxidase center and subsequently solidifies in the central cavity. If the Fe^{2+} were to be oxidized before entering the protein's channels,[26] hydroxyl radicals[27] would be produced through the well-known Fenton reaction. The production of these radicals damages the ferritin protein and prevents iron core formation.[28]

Although Pâques[24] and his coworkers theorized that complexing ions like imidazole inhibit core formation, complexing ions may prevent the premature oxidation

of Fe^{2+}. Pâques *et al.* suggested that inhibition was due to the binding of complexing ions to the active site of apoferritin and did not discuss the idea of oxidative damage. This study revisits the effects of buffers on iron loading in ferritin with the aim of maximizing iron content in ferritin. A report is given of the effects of MOPS, imidazole, and cysteine.

6.2 Experimental

6.2.1 Preparation of Apoferritin

Native horse spleen ferritin (HoSF) obtained from Sigma-Aldrich was treated according to established methods to make apoferritin.[29] As obtained HoSF in saline solution was dialyzed for 24 hours against 1% thioglycolic acid and 0.25 M sodium acetate ($NaC_2H_3O_2$) at 4°C. This process was repeated with an addition of 100 mg/L of 2,2' bipyridyl (bipy) which chelates Fe^{2+} forming the red $[Fe(bipy)_3]^{2+}$ complex. The HoSF was then dialyzed twice with 5 g/L sodium bicarbonate ($NaHCO_3$) at 4°C. The apoferritin solution was then dialyzed several times with H_2O at 4°C to remove ionic species from the solution. Dialysis with H_2O was terminated when Na, S, C, and Fe could not be detected in the rinsing solution.

6.2.2 Study of Core Formation in MOPS, Cysteine, and Imidazole

Kinetic studies on the iron-loading in ferritin were carried out on an Agilent 8453 UV-Vis spectrometer equipped with a magnetic stirring motor, and changes in the absorbance at 310 nm were monitored. Imidazole ($C_3H_4N_2$), cysteine ($HO_2C_2H_3N$), and MOPS solutions (0.05 M) were prepared and the pH adjusted to 7.5 by the addition of NaOH for MOPS and cysteine and HNO_3 for imidazole. A 0.010 M Fe^{2+} solution was prepared by the combination of 49.7 mg $Fe(NH_4)_2(SO_4)_2 \cdot 6H_2O$ with 5 mL of 1 mM HCl and 5 mL of H_2O. Reaction solutions were prepared in a cuvette with 1.8 mL of buffer and 20 µL of 1.2 x 10^{-5} M apoferritin and a Teflon coated stir bar. Absorbance was measured over time at 310 nm, and once a baseline was established 40 µL of 0.010 M Fe^{2+} was quickly injected into the cuvette. The absorbance measurements were continued for 10 minutes.

6.2.3 Preparation and Characterization of Reconstituted Ferritin in MOPS and Imidazole

A reconstituted ferritin sample was prepared in the presence of imidazole buffer. Imidazole (1.65 g) was combined with apoferritin in a 350 mL solution. The pH was adjusted to 7.5 by the addition of HNO_3(aq). An Fe^{2+} solution was prepared by dissolving 2.01 g $Fe(NH_4)_2(SO_4)_2 \cdot 6H_2O$ in 880 mL H_2O with 0.475 mL 1 M HCl. The Fe^{2+} solution was slowly titrated into the apoferritin solution at room temperature under constant stirring, and the pH was monitored and maintained at 7.5 by the addition of NaOH(aq). As the titration progressed the solution turned to a dark brownish-red. After ~ 16 hours, a small amount of solid began to form and the reaction was stopped. The solid was removed by centrifugation, and the ferritin solution was transferred to a dialysis bag. The ferritin was dialyzed at 4°C with water to remove all salts and impurities. The water from each round of dialysis was analyzed for S, Na, C, and Cl^-. The Na was analyzed by atomic absorption spectrometry (AA), while S and C were analyzed using inductively coupled plasma optical emission spectrometry (ICP-OES), and the Cl^- was quantified using ion chromatography (IC). Once the levels of these species were below detection limits the ferritin solution was removed and lyophilized. The mass of the recovered product was 435.7 mg. The iron content of this powder was analyzed by ICP-OES and the crystallinity of the core was characterized by powder X-ray diffraction (XRD) using a Scintag Diffractometer (Cu-Kα radiation, λ = 1.54176 nm) at a scanning rate of 0.1 2θ/min and a power of 15 kW over the range 10 to 85°.

A second ferritin sample was prepared in a MOPS solution. An apoferritin solution (24 mL) was combined with 3.139 g MOPS, 0.4383 g NaCl, and 150 mL H_2O. The pH of this solution was adjusted to 7.5 by the addition of NaOH(aq). A Fe^{2+} solution was prepared by dissolving 312.8 mg $Fe(NH_4)_2(SO_4)_2 \cdot 6H_2O$ in 138 mL of 1 mM HCL. The two solutions were combined in the same manner as the imidazole reaction with constant stirring and maintenance of the pH at 7.5. The reaction was stopped after ~ 8 hours when the mixture began to get cloudy due to protein precipitation. The solid was removed by centrifugation and the buffer exchanged to water by dialysis which also removed any salts. Rinsing was terminated after the impurities were no longer detected by the same methods described in the preparation of the imidazole sample. The solution

was then lyophilized yielding 0.176 g, and the powder was analyzed using ICP-OES and XRD.

6.3 Results and Discussion

Iron loading into ferritin was monitored by following the absorbance at 310 nm in the various buffers and the results are shown in Figure 6.1. The curve representing the reaction in MOPS is characterized by a sigmoidal shape which has been described previously by Xu and Chasteen.[30, 31] This shape is due to two different iron loading reactions. The first occurs at low iron content in ferritin where Fe^{2+} is oxidized at the ferroxidase center. As a core begins to form inside ferritin, Fe^{2+} can be oxidized on the surface of the growing mineral core. As the surface area of the core increases, iron oxidation also increases resulting in the sigmoidal shape. Conversely, the curve representing the reaction in imidazole rises exponentially before reaching a plateau. This behavior suggests that the iron is entering the ferritin protein and reacting at an accelerated rate. Interestingly, the reaction in cysteine never reaches the final level of absorbance observed in the other reactions in spite of a sharp rise at the beginning. The reaction in cysteine was repeated in the absence of ferritin and the results can be seen in Figure 6.2. In this curve the absorbance rises almost instantaneously then decays to a constant absorbance. This suggests that the cysteine initially complexes with all the iron and then progresses to an equilibrium between iron bound to ferritin and an $Fe(cysteine)_x$ complex in solution. Because of this equilibrium, cysteine was not selected in preparing powdered samples of reconstituted ferritin.

Table 6.1 shows the ICP-OES results for iron content in the imidazole and MOPS samples. The iron content is reported in two ways. The first number describes the moles of iron found in one gram of the lyophilized powder while the second quantifies the number of iron atoms in one ferritin protein. This second number is found if we assume a formula of FeOOH for the mineral core and that the rest of the mass is the apoferritin protein which has a molecular weight of 450 kDa.[4]

Table 6.1. Iron content for the two ferritin powders determined by ICP-OES.

Sample	Moles Fe/gram sample	Moles Fe/protein
Imidazole Ferritin	$4.12(4) \times 10^{-3}$	2956
MOPS Ferritin	$2.82(0) \times 10^{-3}$	1693

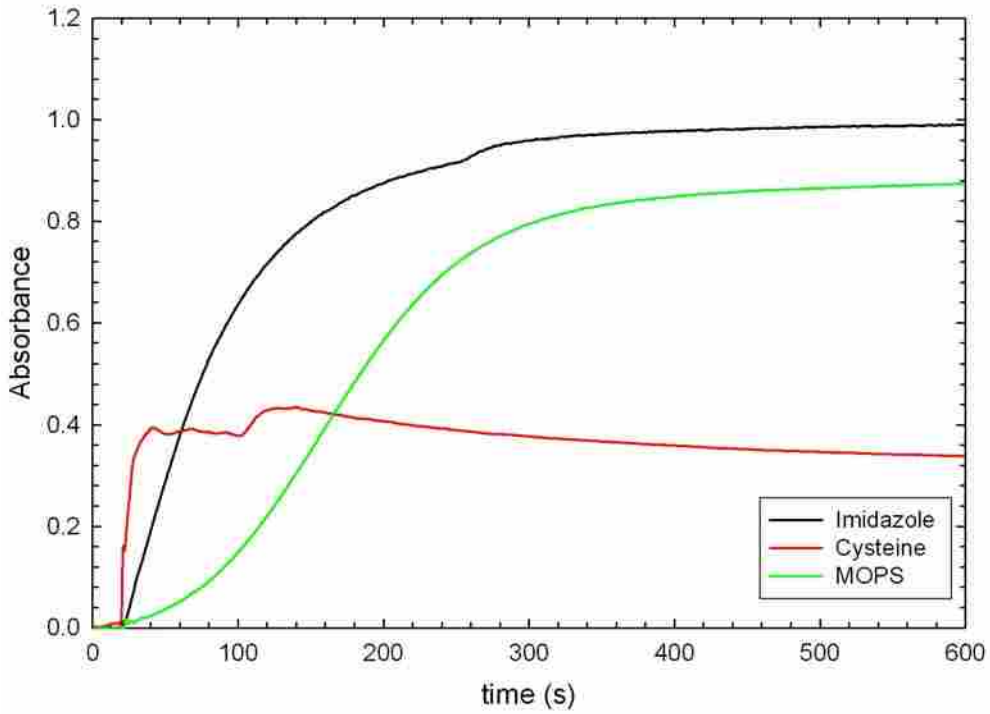

Figure 6.1. The absorbance at 310 nm over time as a probe of core formation. The reaction was initiated by injecting a Fe^{2+} solution into the solution in the cuvette under constant stirring.

In this table, the imidazole sample shows a higher iron content of 2956 Fe/protein while the MOPS sample has 1693. The higher iron content in the imidazole sample is consistent with the exponential rise shown in the UV-Vis experiments. These results contradict those of Pâques *et al.*[24] who concluded that at a pH of 7.0 and high ionic strength, imidazole inhibits core formation. However, the reactions in the present study were carried out at a pH of 7.5 which is somewhat higher, and it is possible that there is a crossover in pH where imidazole is less inhibitory. Such a crossover could explain the difference between the two studies.

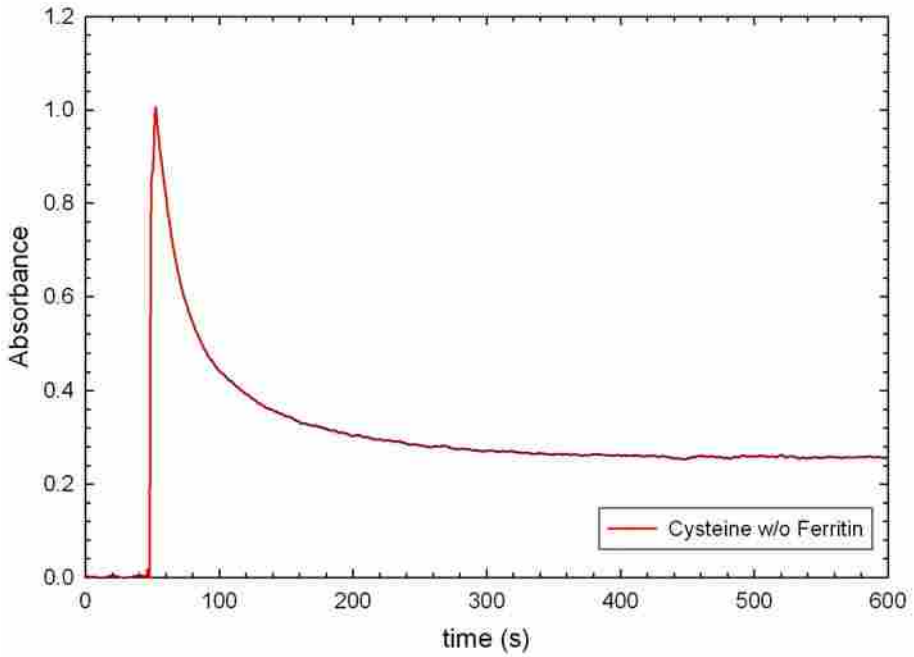

Figure 6.2. The absorbance at 310 nm of Fe^{2+} ion injected into a cysteine solution in the absence of apoferritin.

An XRD spectrum in the range 5 to 85° for a lyophilized sample of apoferritin can be found in Figure 6.3. Two reflections are observed at 2θ values of 9.72°, and 19.80°. After the second peak the spectrum decays with no other features. This spectrum can be seen as a background in the XRD spectra of the two reconstituted ferritin powders found in Figures 6.4 and 6.5, respectively. Figure 6.4 shows the XRD spectrum from the sample prepared in imidazole with the reference peaks for the reflections of six-line ferrihydrite found in JCPDS card 00-029-0712.[32] In addition to the apoferritin background, the XRD of this sample shows peaks which correspond to 6-line ferrihydrite. The two broad peaks located around 35° and 63° indicate that while 6-line ferrihydrite is present, it is mixed with the less-ordered 2-line ferrihydrite, which displays only two broad reflections at these angles.[32] Figure 6.5 contains the XRD spectrum for the ferritin sample reconstituted in MOPS. The smaller amount of sample produces the effect of a lower intensity, however some key features can be discerned. The spectrum has the characteristic curve of the apoferritin XRD spectrum which interferes with the pattern of the iron core. In spite of this interference a definite broad peak is observed ranging from 57 to 66° which corresponds with 2-line ferrihydrite. Other possible peaks are found

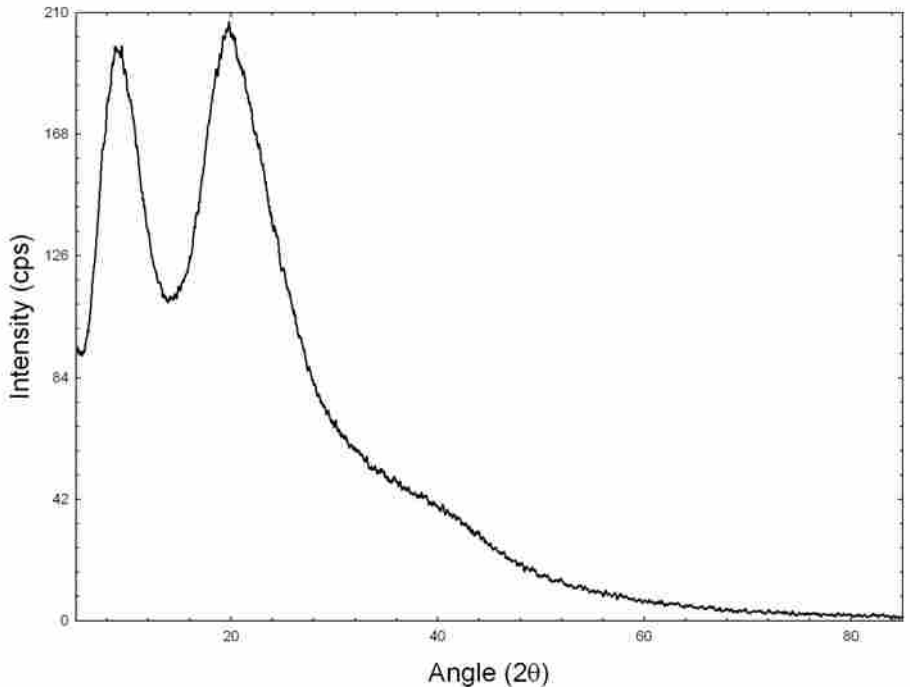

Figure 6.3. Powder X-ray Diffraction (XRD) spectrum of lyophilized apoferritin powder.

at 35°, 46°, and 53°. Peaks at these locations suggest that 6-line ferrihydrite is beginning to form. A comparison of the two spectra reveals that the core of ferritin prepared in imidazole has greater order as seen by the more distinct peaks in its XRD spectrum.

6.4 Conclusion

In conclusion buffer effects on the formation of the ferritin core were studied by measuring the absorbance at 310 nm over time using UV-Vis spectroscopy. Complexation by cysteine may inhibit the uptake of iron as experiments without ferritin showed a sharp rise followed by a slow decay to a constant absorbance. Iron uptake in imidazole was exponential and leveled quickly while reactions in MOPS were slower and had a sigmoidal character. This evidence points to imidazole facilitating the introduction of iron into the ferritin protein. Quantitative analysis of iron in lyophilized samples

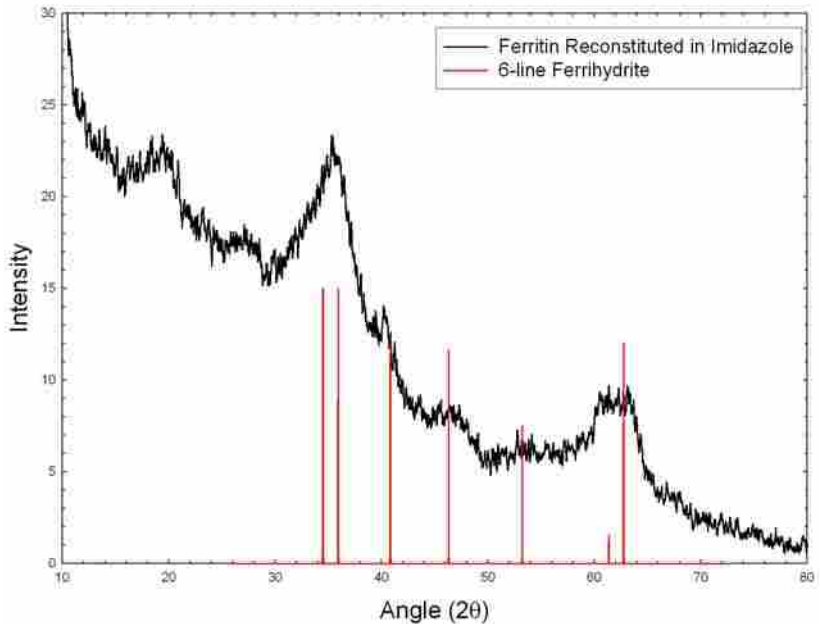

Figure 6.4. XRD spectrum of a ferritin sample reconstituted in imidazole. The red lines represent the standard pattern for 6-line ferrihydrite.

revealed a greater number of iron atoms could be introduced into ferritin using imidazole than could be achieved in the presence of MOPS. XRD spectra of these samples shows a cleaner spectrum with more diffuse peaks for the sample prepared in imidazole. The spectrum of the sample reconstituted in imidazole was found to most likely to have a core consisting of a mixture of 2-line and 6-line ferrihydrite. The greater number of iron atoms introduced into the ferritin protein suggests that imidazole stabilizes Fe^{2+}, keeps it in the solution for a longer duration, and prevents the damage to the ferritin protein by free radicals. These results also suggest that, in addition to the effects of chemical species on the rate of core formation, buffers and salts can affect the final size of the iron core in ferritin.

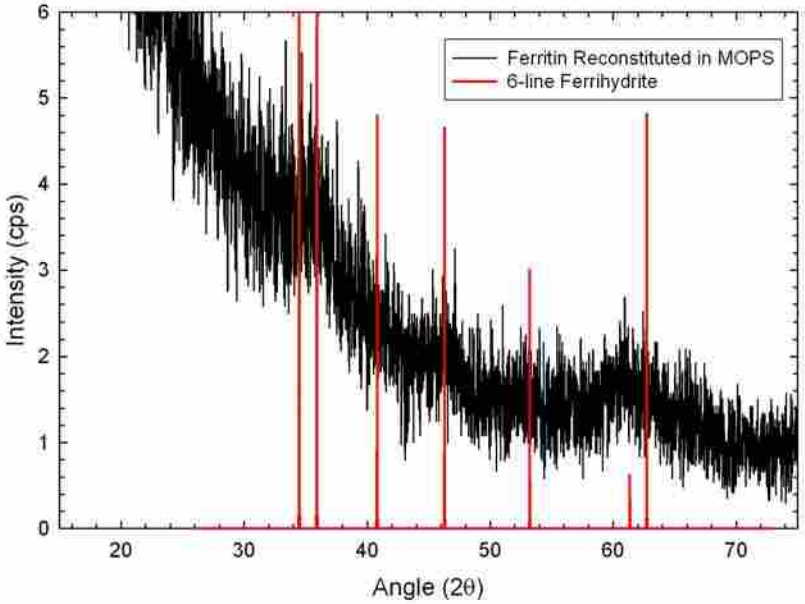

Figure 6.5. XRD spectrum of ferritin reconstituted in MOPS. The red lines represent the standard pattern for 6-line ferrihydrite.

References

1. Katz, E.; Willner, I., *Angewandte Chemie, International Edition* **2004,** *43* (45), 6042-6108.
2. Iwahori, K.; Yamashita, I., *Recent Res. Dev. Biotechnol. Bioeng.* **2005,** *7*, 41-68.
3. Uchida, M.; Klem, M. T.; Allen, M.; Suci, P.; Flenniken, M.; Gillitzer, E.; Varpness, Z.; Liepold, L. O.; Young, M.; Douglas, T., *Advanced Materials (Weinheim, Germany)* **2007,** *19* (8), 1025-1042.
4. Arosio, P.; Ingrassia, R.; Cavadini, P., *Biochim. Biophys. Acta, Gen. Subj.* **2009,** *1790* (7), 589-599.
5. Bulte, J. W.; Douglas, T.; Mann, S.; Frankel, R. B.; Moskowitz, B. M.; Brooks, R. A.; Baumgarner, C. D.; Vymazal, J.; Strub, M. P.; Frank, J. A., *Journal of magnetic resonance imaging JMRI* **1994,** *4* (3), 497-505.
6. Dominguez-Vera, J. M.; Colacio, E., *Inorg. Chem.* **2003,** *42* (22), 6983-6985.
7. Douglas, T.; Dickson, D. P. E.; Betteridge, S.; Charnock, J.; Garner, C. D.; Mann, S., *Science (Washington, D. C.)* **1995,** *269* (5220), 54-7.
8. Gerion, D.; Pinaud, F.; Williams, S. C.; Parak, W. J.; Zanchet, D.; Weiss, S.; Alivisatos, A. P., *Journal of Physical Chemistry B* **2001,** *105* (37), 8861-8871.
9. Iwahori, K.; Yoshizawa, K.; Muraoka, M.; Yamashita, I., *Inorg. Chem.* **2005,** *44* (18), 6393-6400.
10. Meldrum, F. C.; Heywood, B. R.; Mann, S., *Science (Washington, DC, United States)* **1992,** *257* (5069), 522-3.
11. Yamashita, I.; Hayashi, J.; Hara, M., *Chemistry Letters* **2004,** *33* (9), 1158-1159.

12. Sanchez, P.; Valero, E.; Galvez, N.; Dominguez-Vera, J. M.; Marinone, M.; Poletti, G.; Corti, M.; Lascialfari, A., *Dalton Transactions* **2009,** (5), 800-804.
13. Allen, M.; Douglas, T.; Nest, D.; Schoonen, M.; Strongin, D., *ACS Symp. Ser.* **2005,** *890* (Nanotechnology and the Environment), 226-229.
14. Gorham, N. T.; Pierre, T. G. S.; Chua-Anusorn, W.; Parkinson, G. M., *J. Appl. Phys.* **2008,** *103* (5), 054302/1-054302/5.
15. Kim, S.-W.; Seo, H.-Y.; Lee, Y.-B.; Park, Y. S.; Kim, K.-S., *Bull. Korean Chem. Soc.* **2008,** *29* (10), 1969-1972.
16. Joo, M. S.; Tourillon, G.; Sayers, D. E.; Theil, E. C., *Biol. Met.* **1990,** *3* (3-4), 171-5.
17. Granick, S.; Michaelis, L., *J. Biol. Chem.* **1943,** *147*, 91-7.
18. Yang, X.; Chasteen, N. D., *Biochem. J.* **1999,** *338* (3), 615-618.
19. Cutler, C.; Bravo, A.; Ray, A. D.; Watt, R. K., *J. Inorg. Biochem.* **2005,** *99* (12), 2270-2275.
20. Cheng, Y. G.; Chasteen, N. D., *Biochemistry* **1991,** *30* (11), 2947-53.
21. Aitken-Rogers, H.; Singleton, C.; Lewin, A.; Taylor-Gee, A.; Moore, G. R.; Le Brun, N. E., *JBIC, J. Biol. Inorg. Chem.* **2004,** *9* (2), 161-170.
22. Orino, K.; Kamura, S.; Natsuhori, M.; Yamamoto, S.; Watanabe, K., *BioMetals* **2002,** *15* (1), 59-63.
23. Polanams, J.; Ray, A. D.; Watt, R. K., *Inorg. Chem.* **2005,** *44* (9), 3203-3209.
24. Paques, E. P.; Paques, A.; Crichton, R. R., *Eur. J. Biochem.* **1980,** *107* (2), 447-53.
25. Orino, K.; Lehman, L.; Tsuji, Y.; Ayaki, H.; Torti, S. V.; Torti, F. M., *Biochem. J.* **2001,** *357* (1), 241-247.
26. Rohrer, J. S.; Frankel, R. B.; Papaefthymiou, G. C.; Theil, E. C., *Inorg. Chem.* **1989,** *28* (17), 3393-5.
27. Yoon, J. H.; Kang, J. H., *Bull. Korean Chem. Soc.* **2009,** *30* (7), 1644-1646.
28. Linder, M. C.; Kakavandi, H. R.; Miller, P.; Wirth, P. L.; Nagel, G. M., *Arch. Biochem. Biophys.* **1989,** *269* (2), 485-96.
29. Treffry, A.; Harrison, P. M., *Biochem. J.* **1978,** *171* (2), 313-20.
30. Hanna, P. M.; Chen, Y.; Chasteen, N. D., *J. Biol. Chem.* **1991,** *266* (2), 886-93.
31. Xu, B.; Chasteen, N. D., *J. Biol. Chem.* **1991,** *266* (30), 19965-70.
32. Drits, V. A.; Sakharov, B. A.; Salyn, A. L.; Manceau, A., *Clay Miner.* **1993,** *28* (2), 185-207.